Investigation into the Feasibility of Implementing Piezoelectric Patches for Sensing and Actuation of Structural Components

by

Mark Jason Riley

Submitted
in partial fulfillment of the requirements
for the degree of

Doctor of Philosophy

Major Subject: Civil Engineering
At

Dalhousie University

Halifax, Nova Scotia **September, 2005**

© Copyright by Mark Riley, 2005

Library and Archives Canada

Published Heritage Branch

395 Wellington Street
Ottawa ON K1A 0N4
Canada

Bibliothèque et Archives Canada

Direction du Patrimoine de l'édition

395, rue Wellington
Ottawa ON K1A 0N4
Canada

Your file Votre référence
ISBN: 0-494-13053-9
Our file Notre référence
ISBN: 0-494-13053-9

NOTICE:
The author has granted a non-exclusive license allowing Library and Archives Canada to reproduce, publish, archive, preserve, conserve, communicate to the public by telecommunication or on the Internet, loan, distribute and sell theses worldwide, for commercial or non-commercial purposes, in microform, paper, electronic and/or any other formats.

The author retains copyright ownership and moral rights in this thesis. Neither the thesis nor substantial extracts from it may be printed or otherwise reproduced without the author's permission.

AVIS:
L'auteur a accordé une licence non exclusive permettant à la Bibliothèque et Archives Canada de reproduire, publier, archiver, sauvegarder, conserver, transmettre au public par télécommunication ou par l'Internet, prêter, distribuer et vendre des thèses partout dans le monde, à des fins commerciales ou autres, sur support microforme, papier, électronique et/ou autres formats.

L'auteur conserve la propriété du droit d'auteur et des droits moraux qui protège cette thèse. Ni la thèse ni des extraits substantiels de celle-ci ne doivent être imprimés ou autrement reproduits sans son autorisation.

In compliance with the Canadian Privacy Act some supporting forms may have been removed from this thesis.

While these forms may be included in the document page count, their removal does not represent any loss of content from the thesis.

Conformément à la loi canadienne sur la protection de la vie privée, quelques formulaires secondaires ont été enlevés de cette thèse.

Bien que ces formulaires aient inclus dans la pagination, il n'y aura aucun contenu manquant.

Canada

DALHOUSIE UNIVERSITY

To comply with the Canadian Privacy Act the National Library of Canada has requested that the following pages be removed from this copy of the thesis:

Preliminary Pages
- Examiners Signature Page
- Dalhousie Library Copyright Agreement

Appendices
- Copyright Releases (if applicable)

TABLE OF CONTENTS

List of Figures

List of Tables

List of Abbreviations and Symbols

a	dilation factor in wavelet analysis
A	Extensional stiffness matrix
b	Translation of origin for wavelet analysis
B	Coupling stiffness matrix
c	Component from EMD sifting process
$[c^E]$	Piezoelectric stiffness matrix
C_s	Capacitance of charge amplifier
Cov	Covariance
CC	Correlation coefficient, used as a damage index
COV	Coefficient of variation
D	Bending stiffness matrix, and electrical displacement
DI	Differential data acquisition channel set-up
e	Piezoelectric charge coefficients
E	Electric field
ε^o	Neutral axis strain
ε^S	Permittivity of piezoelectric material at constant strain
ε_x	Axial strain in the x direction
ε_y	Axial strain in the y direction
F(k)	Fourier spectrum
FRF	Frequency response function

FRP	Fiber reinforced polymer
ϕ	Electric potential
γ_s	In-plane shear strain
h	z-coordinate of a laminate layer
h_k	z-coordinate to the top surface of the laminate layer
h_{k-1}	z-coordinate to the bottom surface of the laminate layer
h_{ik}	kth component of the ith EMD sifting process
i	Numerical value of the square root of –1
I_{3x3}	Identity matrix of size 3x3
κ	Curvature
m	Mean of envelope in EMD
M_x	Bending moment per unit length in the x-direction
M_y	Bending moment per unit length in the y-direction
M_s	Twisting moment per unit length
MAPD	Mean absolute percent deviation, used as a damage index
n	Number of components from EMD
N	Number of data points
N_x	Normal force per unit length in the x-direction
N_y	Normal force per unit length in the y-direction
N_s	Shear force per unit length
NDE	Non destructive evaluation
O()	Order of ()

p	Distributed external load
φ^*	Basic wavelet transform
Q	Electric Charge
[Q]	Stiffness matrix
r	Residual of the EMD process
R_S	Rotational matrix relating strain in the piezoelectric directions to the global axis directions
R_T	Rotational matrix relating stress in the piezoelectric directions to the global axis directions
RMSD	Root mean square deviation, used as a damage index
S	Piezoelectric strain, and Stress outputs from NISA
SE	Single ended data acquisition channel set-up
S^0	Neutral axis strain in a piezoelectric material
SD	Standard deviation
SAD	Sum of absolute differences
SSD	Sum of square differences
SHM	Structural health monitoring
σ	Axial in-plane stress
σ_x	Standard deviation of baseline signature
σ_y	Standard deviation of subsequent signatures
t	Time, and thickness
T_{11}	Piezoelectric stress in the x-direction

T_{22}	Piezoelectric stress in the y-direction
T_{12}	Piezoelectric shear stress in the x-y plane
τ	In-plane shear stress
u	Displacement in the x-direction
v	Displacement in the y-direction
w	Displacement in the z-direction
$W(a,b,X,\varphi)$	Energy from wavelet transform
Ω	Domain of piezoelectric sensor
x_i	Signature of baseline measurement
x_n	Time history response for Fourier transform
x_{2n}	Even terms in Fourier transform
x_{2n-1}	Odd terms in Fourier transform
x(t)	Time history data for EMD
$x^*(t)$	Resulting decomposed response from EMD
$\bar{x}$	Mean of baseline signature
X(t)	Time history data for wavelet analysis
y_i	Signature of subsequent measurement
$\bar{y}$	Mean of subsequent signature
z	Distance of laminate layer to neutral axis
z_{mk}	Distance from center of laminate layer to mid-plane of the laminate

Acknowledgements

I wish to express my thanks and appreciation to my supervisor, Dr. Farid Taheri, for all the encouragement, support, and guidance he has given me over the past five years. I would also like to thank Defence Research Development Canada (DRDC), formerly known as Defence Research Establishment Atlantic (DREA), along with National Science and Engineering Research Council of Canada (NSERC) for their financial support during the coarse of this investigation.

For helping me develop my experimental equipment and test specimens I would like to thank Mr. Mark MacDonald, Mr. Brian Leikens, Mr. Blair Nickerson, and Mr. Marc Leblanc for their assistance. I would like to express thanks to Mr. Peter Jones, Mr. Chris Hill, and Mr. Joe Isenor for loaning me equipment when it was required.

I would also like to thank Mr. Nader Cheraghi and Mr. Khaled Shahin for helping with the testing procedures.

To my mother, father, and brothers I would like to say thank you for all the support and encouragement through all my years.

Last but not least, to my lovely wife Leeann, who over the last seven years has given me nothing but love, encouragement, and understanding, you have meant more to me than you would ever know. Finally to my son Jack, who has allowed me to have fun and laugh everyday since his arrival, I thank you.

To all the above, I would like to express great thanks for making this work possible.

Abstract

Within this thesis there are three distinct studies related to the implementation of piezoelectric materials. These include a study on the vibration suppression capabilities of self-sensing piezoelectric patches, damage detection of pipe joints, followed by a study on the effects of embedding piezoelectric patches into fiber reinforced laminate plates. Due to the unusual nature of this thesis involving three such distinct applications, attempts will be made to switch the mindset of the reader when a new field is being introduced in this thesis.

An overview of the field of smart materials and structures are investigated in the first two chapters of this report. These chapters will provide the reader with the information required to fully appreciate the different aspects of smart materials and their desirable and practical applications. These chapters will also introduce the reader to the different topics and practical engineering issues, such as vibration suppression, damage detection, and the influence of embedding sensors into fiber reinforced polymer composites, followed by synopses of some of the works conducted to date.

Chapter 3 of this thesis provides the results from an experimental investigation into the capabilities of small piezoelectric patches for vibration suppression of FRP plates, as well as PVC piping. The efficiency of both surface bonded and embedded piezoelectric sensors/actuators was investigated for laboratory scale FRP plates. It was found that dramatic vibration suppression was achievable in the FRP plates with the use of a simple control system, and the comparison of the results for the embedded actuator relative to the surface bonded actuator showed excellent correlation to the linear theory. However, it was not possible to effectively suppress the vibration in the PVC pipes examined.

Chapter 4 is designed to switch the focus of the reader from vibration suppression to damage detection applications. Within this chapter, methods of data measurement, signal processing, data analysis, and damage evaluation methods are detailed. This chapter will provide the reader with the fundamental information required to appreciate how damage detection systems operate.

Chapter 5 provides the results of an extensive experimental investigation using a state of the art damage detection system that was developed to determine joint load loss in adhesively bonded as well as mechanically fastened pipes with the use of piezoelectric sensors. Within these investigations the effects of sensor location, damage location, loading locations and support conditions were studied. It was found that the proposed damage detection method/system could effectively determine the presence of damage as well as giving a quantitative measure of the amount of damage present.

The aim of the initial sections of Chapter 6 is to again switch the mindset of the reader to focus on the third distinct study in this thesis, which is the influence of an embedded piezoelectric sensor on the integrity of a host FRP plate. This is followed by the results of an extensive finite element investigation that addressee the influence of factors such as the laminate lay-up orientation, embedding interface of the sensor, plate curvature, piezoelectric material properties, and the dimensions of the piezoelectric patch. It was found that the lay-up orientation, plate curvature, and sensor thickness had a substantial influence on the stress distribution in the plate, where the sensor properties, width, and length showed minimal effects.

Chapter 1

Introduction

1.1 Preface

The field of smart materials has been recognized as one of the most rapidly growing fields in engineering today. The technology innovations appearing in engineering materials, sensors, and actuators have been instrumental in the growth. The most commonly used terminologies used in the field of smart materials and structures include adaptive, sensory, controlled, active, and intelligent. Figure 1-1 shows how these different terminologies of smart systems overlap as defined by Clark et al. (1998).

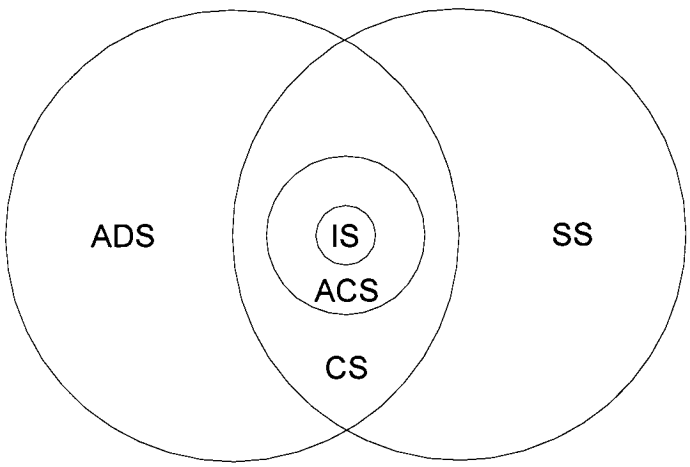

ADS = Adaptive Structure

SS = Sensory Structure

CS = Controlled Structure

ACS = Active Structure

IS = Intelligent Structure

Figure 1-1: Diagram Defining Intelligent Structure Hierarchy (Clark et al., 1998)

Adaptive structures are those that have distributed actuators throughout while sensory structures possess sensors throughout. Adaptive and sensory structures would be the basic grass roots of smart structures, while the rest would be combinations of these two systems. Controlled structures are structures that possess sensors and actuators and have some kind of controlling or suppression capabilities. Wada et al. (1990) defined active structures as those that serve some function in the load bearing properties of the system. Intelligent structures would be the most advanced system that would employ feedback from the sensors to the actuators, in order to control the system.

With the use of piezoelectric and other smart materials growing at an extraordinary rate over the past decade, the scope of the investigations has been expanding. Applications such as vibration control, shape control, and damage detection have been investigated in varying levels with most smart materials. However, in vibration control and damage detection applications piezoelectric materials have been leading the way. Some of the reasons for this include: full range of sizes available, ease of implementation, relatively lower cost, and linear behavior to name a few. With the increase in the use of smart materials, fiber-reinforced laminated polymer composites (FRP) have also become a very attractive structural material. This is mainly due to their high strength/weight and stiffness/weight ratios, as well as their ability to host smart materials directly within their structure.

Most research carried out in this field involves structures with very large life-cycle costs such as aerospace and military structures. Recently, studies have started to expand to the oil and gas industry involving offshore structures and pipeline systems. With the expansion of the field the biggest challenge in implementing smart materials is to fully understanding their capabilities as well as their limitations, which is addressed within this thesis.

1.2 Motivation

With the life cycle cost associated with aerospace, military, and oil and gas industries, it is of paramount importance to have smart systems to monitor these structures, detect any flaws and reduce unfavorable responses in these systems. Leading the way in the field of smart materials are piezoelectric materials, which can be easily implemented as sensors and actuators.

The work in this field to date has included extensive research on vibration control of structures made of FRP, as well as other materials. This has been performed experimentally, as well as computationally. In most of these applications several small piezoelectric patches, large piezoelectric patches or layers are implemented leading to large costs. Therefore an investigation into the applicability or extension of small self-sensing actuators to sense problems in such structures, and/or controlling them needs further exploration.

Applications involving damage detection has now become one of the most investigated areas of research. This includes investigations into health monitoring of beams, trusses, plates, frames, bridges, offshore platforms, other large civil engineering structures, aerospace structures, and various structures made of FRP. However, with all the works performed, there have been very few investigations into health monitoring of pipeline joints. Pipe joints are located in many different engineering systems such as water distribution, sewer systems, offshore recovery, as well as onshore oil and gas systems to name a few. In general, when one joint in the system fails, the entire network has to be shut down to fix the problem, which is a very costly process. Therefore, it is of paramount importance to locate and fix any degradation in such systems before a catastrophic failure could occur.

Moreover, with the growth in the use of smart materials, the need to determine their effects on the integrity of the host structure is required. For instance, there have been a

small number of investigations into the effects created by embedding piezoelectric sensors into FRP plates, such as stress concentrations. The available studies have focused on examining the influence of a patch on a structure subject to axial tension, and no bending applications have been investigated. Since most systems undergo flexure, the effects of embedding piezoelectric patches in flexural specimens need to be studied. Also, in most structures the desirable location is near an edge, which in laminated composites is a location of susceptibility. Therefore, research on the influence of embedded elements near the edge of structural components subjected to bending is required.

1.3 Objectives

This thesis explores a wide range of applications involving piezoelectric materials, which include monitoring and actuation for vibration suppression, health monitoring and damage detection, as well as an investigation into the effects of embedding piezoelectric patches into laminate plates, subjected to bending. These investigations are aimed at implementing user-friendly methods to determine the feasibility of implementing relatively small piezoelectric patches for smart structure applications.

The first objective was to determine the applicability and feasibility of these small piezoelectric patches to reduce the free vibration damping time in laminate plates as well as PVC piping through experimental investigations. The capabilities of self-sensing actuation and embedded patches were also explored.

The next objective was to develop a user-friendly procedure to determine the presence of damage in pipe systems. This included the development of a very efficient and low cost experimental system, as well as an easily implemented data processing algorithm.

The final objective was to determine the effects of embedding piezoelectric patches into FRP laminate plates. This investigation looks at several factors that may influence the

stress concentrations in the laminate, such as the lay-up orientation, plate curvature, piezoelectric sensor size, and the piezoelectric material properties.

1.4 Layout of Thesis

This thesis is divided into 7 chapters. In Chapter 2 an extensive literature review of past studies into the application of piezoelectric patches is presented. It starts with an extensive look into past vibration control practices. It is followed up with an extensive look at damage detection practices and methods used in the past. The final survey is of the work performed on the influence of embedding piezoelectric patches into laminated composites. Details of the current investigation into the suppression of free vibration in laminate plates as well as PVC cylindrical shells, is provided in Chapter 3. This involved implementing self-sensing piezoelectric patches, as well as a comparison of the efficiency of an embedded piezoelectric sensor/actuator to suppress the free vibration in a FRP plate with that of a surface bonded sensor/actuator. Chapter 4 shows the methods of data monitoring, analysis, processing, and evaluation for damage detection using smart materials. The capabilities of the proposed vibration based health monitoring and damage detection system for pipe joints are shown in Chapter 5. These are shown through the results of an extensive experimental investigation of damage detection in adhesively bonded PVC pipe joints as well as mechanically fasted joints of PVC and cast iron piping. This involves studying the ability of the system to monitor the system response and quantitatively determining the degree of damage as well as the use of different damage indices. Chapter 6 provides the results for an extensive finite element investigation into the effects of embedding piezoelectric patches into FRP laminated composites. This study involves investigating the influence of the layer orientation, piezoelectric patch dimensions, embedding interface characteristics, as well as plate curvature (i.e. two-way and one-way plate bending). The summary and conclusions of the findings as well as recommendations for the future work are presented in Chapter 7, followed by references and appendices.

1.5 Contributions

With the works that were conducted within this thesis several potential contributions to the engineering field were given. These contributions include the findings through experimental determination of the efficiency of embedded piezoelectric patches to suppress vibrations in FRP plates in comparison to surface bonded patches.

A robust technique for detecting and determining damage in both adhesively bonded and mechanically fastened pipe joints was also developed. The developed method was able to determine the presence of damage as well as provide a quantitative measure of the degree of damage. Also the influence of several system parameters, such as support conditions, position of damage, loading location, and sensor location were investigated to evaluate the capabilities of the developed damage detection system. The findings will enhance the present state of the art in structural health monitoring systems.

The results of the study on the effects of embedding piezoelectric sensors in FRP plates subjected to bending also revealed useful and practical information. The study provides the knowledge of what influence most practical parameters create on the host laminates, when such sensors are embedded in them. This in turn allows the users to ensure the integrity of such structural components, and ensure their durability during their service life.

Chapter 2

Literature Review

2.1 Introduction

Over the past decade there has been extensive work performed in the field of smart materials and structures. Most of this research is focused on vibration control and damage detection with the use of piezoelectric materials. The following sections give a detailed literature review of past studies on vibration control and damage detection using piezoelectric materials. A review of past work on studying the influence of embedding piezoelectric materials in laminate composites will also be given.

2.2 Smart Materials

The field of smart materials and structures has been recognized as one of the most rapidly growing fields in engineering today. The technological innovations appearing in engineering materials, sensors, and actuators have been instrumental in the growth. In general, smart materials are referred to as:

- Materials that function as sensing and/or actuating materials
- Materials which have multiple responses to one stimulus in a coordinated fashion
- Passively smart materials with self-repairing or stand-by characteristics to withstand sudden changes
- Actively smart materials utilize feedback
- Smart Materials and systems reproduce biological functions in load bearing structural systems

Some of the most popular material systems being used for sensors and actuators today are piezoelectric materials, shape memory alloys (SMA), magnetostrictives materials,

electrorheological fluids and optical fibers. The following sections will give an overview of these materials.

The main purpose of a smart structure is to have the ability to respond to actions with a response. To perform this task, smart structures employ the use of many different materials as actuators and sensors. The sensor material should have the ability to feedback stimuli such as thermal, electrical, and magnetic signals to the motor system in order to change the thermomechanical properties of the structure. The actuator materials should have the ability to change the shape, stiffness, position, natural frequency, damping and other mechanical properties of the system in response to changes in temperature, electric field or magnetic field. The most popular materials being used for sensors and actuators are piezoelectric materials, shape memory alloys, magnetostrictives, electrorheological fluids, and optical fibers. The most common material used for both actuating and sensing in systems are piezoelectric materials. Shape memory alloys, magnetostrictives, and electrorheological fluids are primarily used for actuator materials although can be used as a sensory system. Where, optical fibers are limited to use as sensing materials. Among all these materials, piezoelectric materials are the most widely used mainly due to their fast electromechanical response, low power requirements and relatively high generative forces.

2.2.1 Piezoelectric Materials

There are three branches of piezoelectric materials. Naturally occurring materials such as quartz, topaz, cane sugar, and Rochelle salt all exhibit piezoelectric properties, although on a small scale, with quartz being the most widely used. The other two types of piezoelectric materials that are available are ceramics and polymers. The most common piezoceramic is Lead Zirconate Titanate (PZT) while polyvinylidene fluoride (PVDF) is the most common piezoelectric polymer. These piezoelectric materials are manufactured by polarizing the material in a given direction. This aligns the polarization direction of the crystals increasing the effects of an applied or measured stimulus. In most

applications a piezoceramic or piezoelectric polymer is used due to their improved properties over naturally occurring piezoelectric materials. In this report only polymer and ceramic piezoelectric materials will be considered.

Piezoelectric materials produce an electric field when subjected to a mechanical strain, which is known as the piezoelectric effect. In this case the piezoelectric element can be used as a sensor for stress or strain measurements and damage detection. If an electric charge is applied to the piezoelectric element it will produce a mechanical strain. This is known as the reverse piezoelectric effect and in this case, the piezoelectric material can be used as an actuator. Perfect collocation can occur when the same piezoelectric element is used for both sensing and actuating. When this is done, nonlinearities exist due to interactions of the sensing and actuating signals. This can be corrected when a proper bridge circuit is used to separate the sensing and actuating signals. In most cases when piezoelectric elements are used for both the sensing and actuating mechanisms, two closely spaced elements are used with one serving as a sensor and the other as the actuator.

In most applications the electric field is applied or measured through the thickness of the piezoelectric element which is referred to as the 3-direction. This leads to two of the piezoelectric modes, namely the 33-mode and the 31-mode. In these modes the measured or applied stimuli is in the poling direction and perpendicular to the poling direction respectively. A third mode that is employed is the 15-mode. This mode relates an applied or measured value to the shearing of the material. These modes of operation are further detailed in Section 2.3.

The most common piezoelectric elements are plates, disks, rings, rods, stacks (referred to as bulk elements) and films.

2.2.2 Shape Memory Alloys (SMA)

Shape memory alloys are a special class of metallic alloys that exhibit a shape recovery effect when heated. If the shape recovery is resisted by the structure, a large force will be generated by the SMA element. Shape memory alloys are used almost exclusively as an actuator material, for this reason the report will only look at the application of shape memory alloys as actuators. There are several materials that exhibit the shape recovery effect, such as copper, nickel, titanium and zinc alloys along with others. The most common of the shape memory alloys is a nickel-titanium alloy referred to as nitinol, which was first developed at Naval Ordinance Laboratory. The main characteristic of a shape memory alloy is that it has two solid phases, one above the transition temperature and one below. The low temperature composition of the SMA is the martensitic phase and the high temperature composition is the austenite phase. The transition temperature is the temperature in which the transformation between these phases takes place. The transition temperature for a SMA is dependent on the chemical composition of the alloy constituents and may vary from $-50^{o}C$ to $166^{o}C$.

The shape memory effect is simply described as an object that when in the low temperature martensitic phase is plastically deformed and the external force removed, it will regain its original shape when heated above its transition temperature. In most cases the heating of the shape memory alloy is done through resistive heating, where a current is applied through the element. As well as this mode of operation, shape memory alloys exhibit a superelastic effect. In this case, the SMA is used in an environment above its transition temperature, such that it is in an austenite phase. When the system is loaded, martensite is stress induced due to the deformation. When the loading is removed, the SMA immediately transforms to austenite, which causes the element to immediately return to its original undeformed shape.

The transformations between the austenite and martensite phases exhibit a hysteresis in the temperature that produces austenite upon heating and martensite upon cooling. The

amount of hysteresis is generally defined as the temperature difference between 50% austenite formation in heating and 50% martensite upon cooling and can have a value as large as 20-30°C. The hysteresis loop will be further investigated in the thermal properties section.

2.2.3 Magnetostrictive Materials

Magnetostrictives are materials that change dimensions when they are subjected to a magnetic field. Most ferromagnetic materials exhibit some level of magnetostriction, but alloying these materials with rare earth metals can lead to "giant" magnetostrictives that have improved characteristics. Within this class of giant magnetostrictives the most common is Terfenol-D, while new advancements are being made in manufacturing magnetostrictive composites. Due to the nature of magnetostrictive materials they can be implemented as actuators by applying a magnetic field, or sensors by measuring the magnetic field they generate.

In the use of magnetostrictives there are two effects that can be used for actuator and sensor applications. The first is the Joule effect that produces a change in the transverse and length directions for an applied magnetic field and the second is the Wiedemann effect that deals with the twisting/torque of the magnetostrictive material.

When a magnetic field is applied to the element, a transverse change in dimensions accompanies the length change produced by the Joule effect. This scenario would be used in the application of actuators to produce force or displacement from an applied magnetic field. The reciprocal effect, in which applying a stress to the material causes a change in its magnetization, is known as the Villari effect (also referred to as the magnetostrictive effect and magnetomechanical effect). The Villari effect is commonly used in magnetostrictive sensors.

The second magnetostrictive effect used in these devices is the Wiedemann effect, in which a twisting results from a helical magnetic field, which is often generated by passing a current through the magnetostrictive sample. The inverse to the Wiedemann effect, also known as the Matteuci effect, is used for magnetoelastic torque sensors, by measuring the magnetic field produced by the torque stress on the sensor.

The existence of both direct and reciprocal Joule and Wiedemann effects leads to two modes of operation for magnetostrictive transducers: (1) transferring magnetic energy to mechanical energy and (2) transferring mechanical energy to magnetic energy. The first mode is used in design of actuators for generating motion and/or force, and in design of sensors for detecting magnetic field states. The second mode is used in design of sensors for detecting motion and/or force, in design of passive damping devices, which dissipate mechanical energy as magnetic induced thermal losses.

In many devices, conversion between electrical and magnetic energies facilitates device use. This is most often accomplished by sending a current through a wire conductor to generate a magnetic field or measuring current induced by a magnetic field in a wire conductor to sense the magnetic field strength. Hence, most magnetostrictive devices are in fact electro-magneto-mechanical transducers.

Some of the earliest uses of magnetostrictive materials during the first half of this century include telephone receivers, hydrophones, magnetostrictive oscillators, torque-meters and scanning sonar. These applications were developed with nickel and other magnetostrictive materials that exhibit bulk saturation strains of up to 100 mL/L (units of microlength per unit length). As is the case with piezoelectric materials, magnetostrictives come in vary shapes and sizes such as plates, rods, and discs to name a few.

The major difference between magnetostrictive and piezoelectric materials is that piezoelectric materials strain in a linear manner with an applied electric field where magnetostrictives behave in a non-linear manner. Figure 2-1 shows the relationship of magnetostrictive and piezoelectric strain as a function of the applied field.

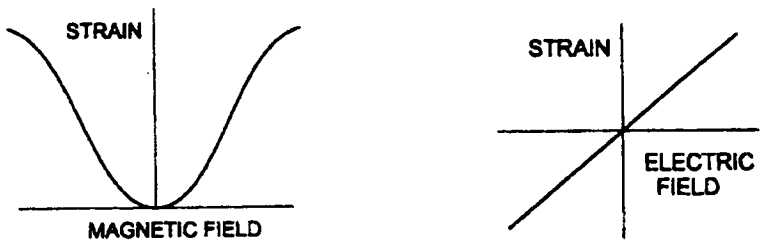

(a) (b)

Figure 2-1: Comparison of Strain Resulting from Applied Field (a) Magnetostrictive (b) Piezoelectric (Squire, 1999)

Although magnetostrictives are non-linear in nature most of the time they are modeled as linear systems. The only way that this can give representative results is if the magnetic field is kept within a small region of the full operational range. This results in a smaller usable strain range then the full -scale capabilities.

2.2.4 Electrorheological Fluids

Electrorheological (ER) fluids are a special class of fluids that transform into a gel like solid when an electric field is applied. This is a reversible process that is performed by dielectric particles in a non-polar liquid. When there is an electric field applied across the element, the dielectric particles align with the applied field resulting in a change in the rheological properties of the element with the main change being an increase in the viscosity of the material. Figure 2-2 shows the two forms of an ER fluid with and without the application of an electric field.

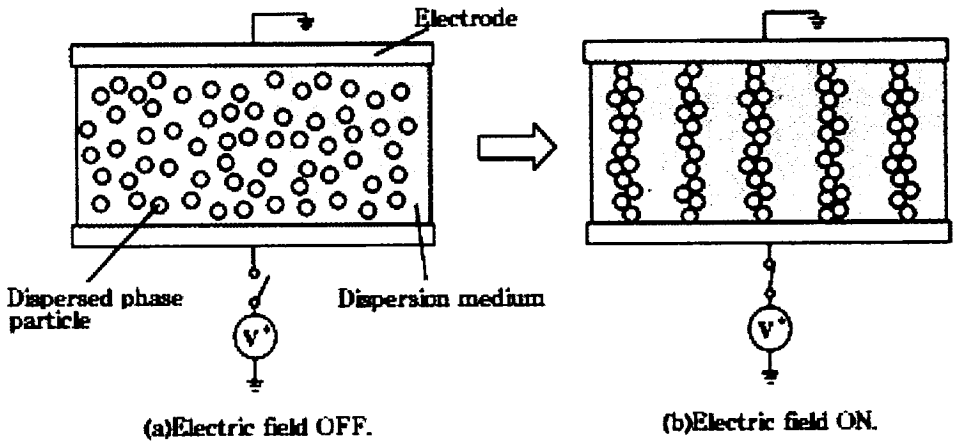

Figure 2-2: ER Fluid Element With and Without the Application of an Electric Field (Mechanism of ER Effect, 2001)

Unlike some of the other smart materials electrorheological materials cannot be implemented as sensors and actuators. Since the application of stress to the element will not cause the dielectric particles to align with the electrodes, ER materials cannot be implemented as sensors. Electrorheological fluids are implemented as semi-active control elements when used for structural control. They are considered as semi-active structures because structures composed of ER materials have the ability to control their stiffness and damping properties.

ER fluids behave like Newtonian fluids under no electric field conditions, but with the application of an electric field, ER fluids behave similarly to Bingham plastics, exhibiting a finite yield stress with the shear stress dependent on the shear rate. For electric field strengths on the order of 3 kV/mm, ER fluids solidify with static and dynamic yield stresses as high as 10 kPa and 5 kPa respectively. The fluid to solid transition of ER materials, which can be reversed in a mater of a few milliseconds, although not exactly reproducible, have been shown to be useful in many engineering applications. It is an attractive choice for use in devices such as brakes, clutches, hydraulic valves, dampers and engine mounts. This report is based on smart structures so only the application of dampers will be considered.

When ER materials are implemented as structural control applications they are generally used as confined layers in beams. This is mainly due to the fact that current ER materials do not have sufficient strength at acceptable electric fields to be implemented as actuators. This limits their capabilities in vibration control so they are generally used as shape control or damping materials.

ER fluids benefit from simple design, since no additional mechanical parts are needed. In order to make ER fluids widely applicable to commercial products, the electrorheological effect and the stability of the liquid must be improved. Furthermore, the range of operating temperatures and the strength in the solid state should be increased

2.2.5 Fiber Optic Sensors

Fiber optics are implemented as sensors by transmitting a light signal through the fiber and measuring the signal that is returned, with the change in the signal properties determining the effects at the site of the sensor. Fiber optic sensors generally have silica glass cores but for some specialized applications materials such as sapphire, fluoride glass and neodymium doped silica are implemented. A dielectric material that is referred to as the cladding surrounds the core. The cladding material must have a lower refraction index then the core material to satisfy Snell's Law for total propagation of the light along the core of the fiber. The cladding is then covered in a plastic, referred as the barrier, which gives the fiber protection and mechanical strength. Figure 2-3 illustrates the cross-sectional view of a typical fiber optic sensor.

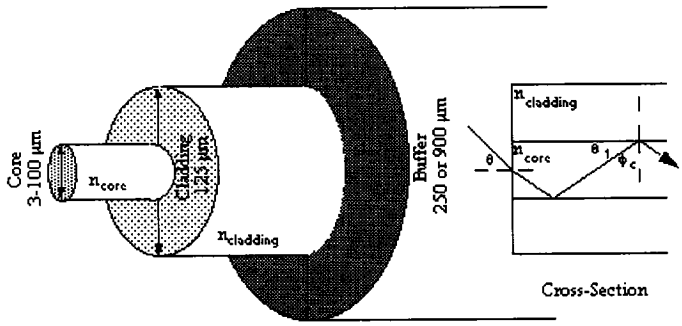

Figure 2-3: Cross-Section of Typical Fiber Optic Sensor (Future Fiber Technologies Pty. Ltd., 2001)

There are several ways in which fiber optic sensors are classified, which depend on how the signal is transmitted, what the fiber is measuring and whether the fiber is the sensor or just the transportation media.

There are four ways in which optical fiber sensors transmit the media to get the desired measurements. These are based on the light intensity, phase, frequency or the polarization, which are referred as intensiometric, interferometric, polarimetric, and modalmetric sensors respectively.

There are two modes associated with the different types of media measured. There are single mode fibers in which the light signal is transmitted directly down the fiber without refraction between the core and cladding and a multimode fiber that has the light signal refracted between the core and cladding. The single mode fibers have smaller core diameters, ~5-10 microns, compared to the multimode fibers which have core diameters of 50, 62.5, and 100 microns.

When classing the sensors on what they measure three classes are implemented. Physical sensors measure temperature, stress, etc., chemical sensors measure pH, gas analysis, etc. and bio-medical sensors measure blood flow, glucose content and so on. In all these types of applications intensiometric and interferometric sensors can be implemented.

The final classification of fiber optic sensors depends on whether the sensing takes place in the fiber itself or in a region outside the fiber. An extrinsic optical fiber sensor is one in which the measurements are taken in a region outside the optical fiber and the optical fiber is just a conduit to transmit the light to and from the sensing region. An intrinsic fiber optic sensor is one in which the physical properties of the optical fiber are changed. Fiber optic sensors can be designated as point sensors, which measures the disturbance in the optical fiber over a discrete localized region. If the sensor is capable of measuring fields continuously over their length they are known as distributed sensors and if the measurements are taken at various points along the length they are referred as quasi-distributed sensors.

2.3 Functionality of Piezoelectric Materials

Piezoelectric elements can be used as either a sensor and/or an actuator. To obtain perfect correlation of the data the same element is used as both a sensor and actuator. A single piezoelectric element that is used as a sensor and actuator does require a more advanced set-up, and will be described in a later section. The following sections describe the functionality of piezoelectric materials for use as sensors and actuators.

2.3.1 Piezoelectric Materials for Use as Sensors

When piezoelectric materials are used strictly as sensors, they are generally in the form of disks, plates or thin films. Disks and plates are generally used for strain sensing, where thin films are used generally for damage detection (i.e. composite delamination, matrix cracking).

If we distort a piezoelectric material compressing the molecular chains closer together, the material will expand in the dimension parallel with the chains. This will increase the distance between the free electrons and the bipolar molecules to reduce the force of attraction or repulsion while at the same time the side of the material having a surplus of free electrons will also become compressed to increase the similar charge repulsive force.

This causes a poling in the piezoelectric material, which results in a surface charge, known as the piezoelectric effect. The charge is generally transformed to a voltage, which is measured, and through the constitutive relationships of the material the strain in the structure can be determined. The different modes of a piezoelectric sensory element are dependent on the poling direction and the direction of the applied loading. The relationship required to determine the response of the element also depends on the measured characteristic. If the measured value is the charge, Q, then the charge coefficient "d" would be used to determine the response of the element. If the measured value is the voltage, V, then the voltage coefficient "g" would be used to determine or predict the response of the element. In bulk piezoelectric elements there are five modes in which they act as a sensor, they are namely two tension or compression modes, two shear modes and a bending mode.

The two tension modes are dependent on the direction of the applied load with respect to the poling direction. The first mode is with the applied loading parallel to the poling direction, which is related to the 33-mode of the material. The second tension mode is with the applied loading perpendicular to the poling direction. The response of this sensor is dependent on the 31-mode parameters of the material.

Analogous to the tension or compression modes of sensing, the two shear modes depend on the direction of the applied load with respect to the poling direction. Both shear modes of the piezoelectric element depend on the 15-mode of the piezoelectric element.
In the case of the bending mode sensory system, more than one piezoelectric element is required, where for tension, compression or shear sensing only one element is required. The bending mode response of a piezoelectric system depends on how the electrodes are connected (parallel or series) and the measured quantity. If you are measuring the charge produced on the surface of the elements, then the output does not depend on the configuration of the electrodes. If you are measuring the voltage produced by the applied

load, then the results will be different for the electrodes connected in series or parallel. All piezoelectric sensor modes of operation are shown in Figure 2-4.

2.3.2 Piezoelectric Materials for Use as Actuators

Piezoelectric actuators can generally be characterized by the piezoelectric coefficient that they exploit. These are based on the piezoelectric coefficients (also known as the "d" constant), which relate the direction of the applied electric field to the displacement or strain direction. They are 33-mode, 31-mode and 15-mode actuators, which are related to d_{33}, d_{31}, and d_{15} respectively.

The 33-mode actuator has a displacement in the direction of the electric field, which is applied in the materials polarized direction. The 31-mode actuator has a displacement in the perpendicular direction to the potential, which applied in the materials polarized direction. The strain that is achieved by a 33-mode actuator is about half of the 31-mode for the same electric potential due to the magnitude of the piezoelectric coefficients. Unlike the 33 and 31-mode actuators the 51-mode actuator requires the use of two piezoelectric elements, where the 33 and 31-modes only require one. The 15-mode uses the shear strain produced by an electric field applied in the materials polarized direction. The 51-mode (shear strain) actuator is not as common as the others because of the complexity of the manufacturing process.

Depending on the application of the actuator, plates, disks, rods, or stack actuators are most commonly employed. With the three different polarizations of piezoelectric materials three different actuator types can be produced. Utilizing the 33 or 31-mode actuators one can produce a parallel or transverse motor. With the use of a 15-mode actuator one can manufacture a shear motor. With the use of a stack of 31-mode actuators a bending motor can be manufactured. The application of the electric potential across the two outer electrodes of the stack allows one of the transducers to expand and the other to contract. This results in a bending displacement that is much larger than the

length displacement in either of the transducers. Figure 2-5 shows the functionality of the different types of piezoelectric actuators.

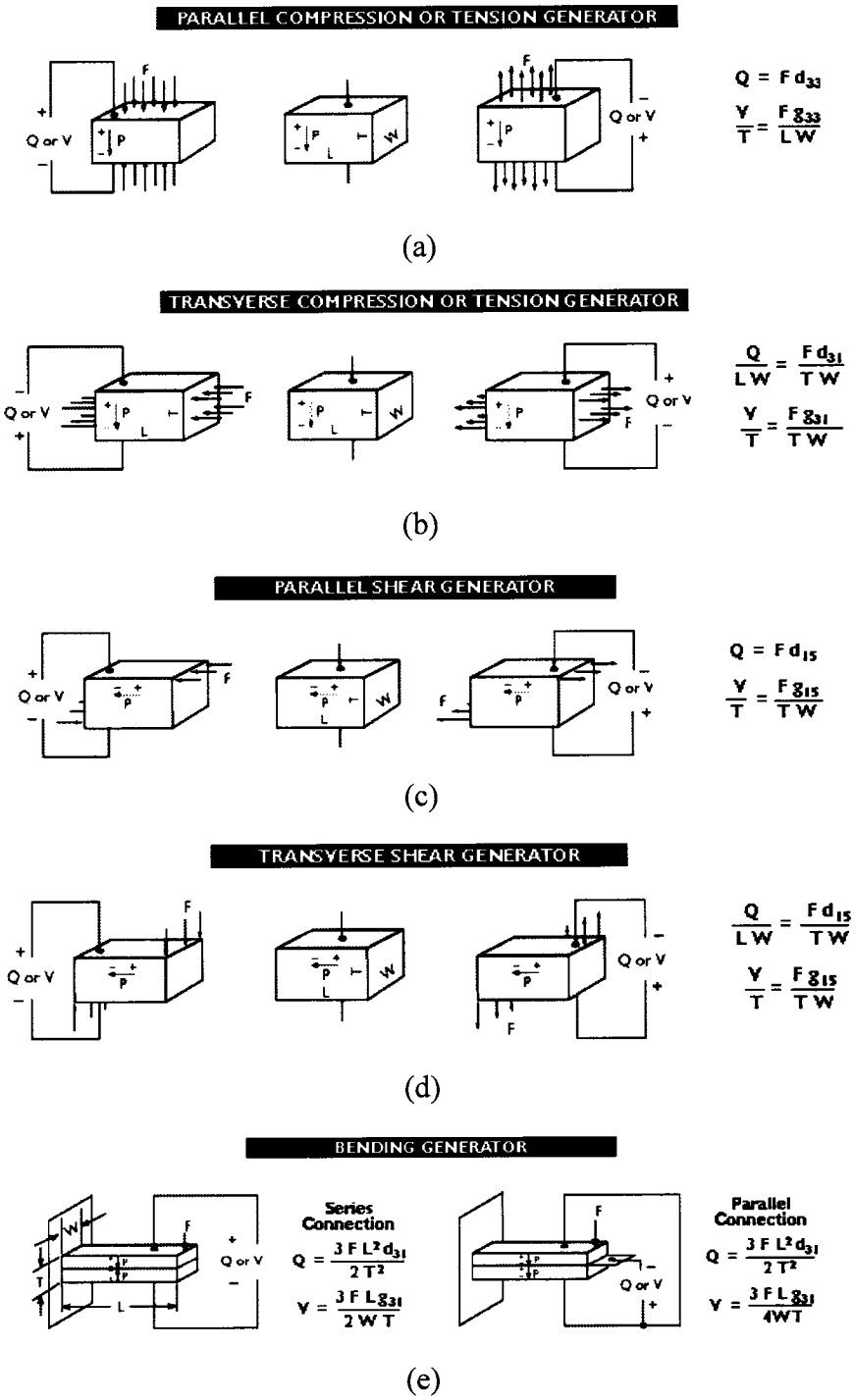

Figure 2-4: Functionality of Bulk Piezoelectric Sensors (Piezo Systems Inc., 2001)

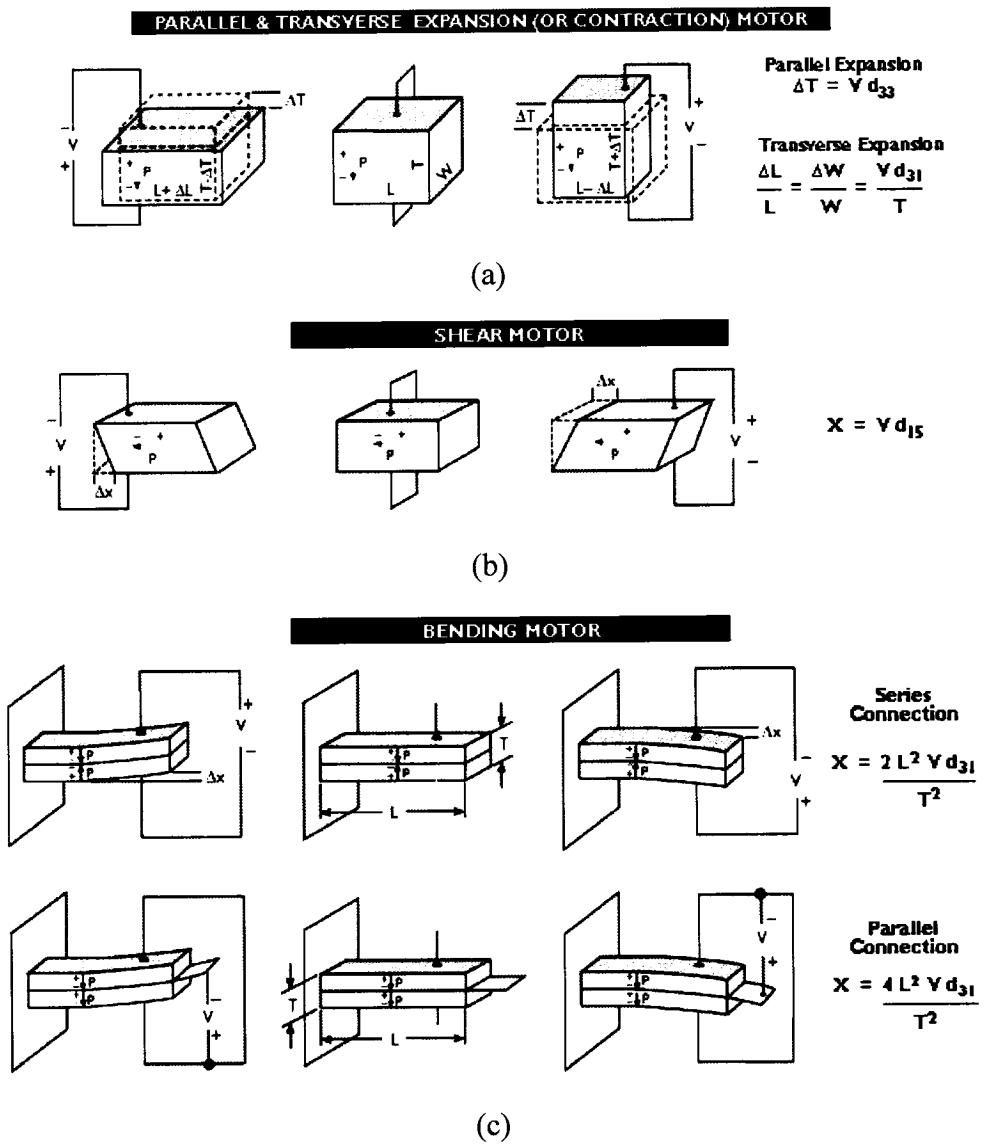

Figure 2-5: Functionality of Bulk Piezoelectric Actuators (Piezo Systems Inc., 2001)

If a large force is required, instead of using one large piezoelectric element, a stack actuator is commonly used. The stack actuator is a set of smaller piezoelectric elements bonded together with their electrode set up in series. This allows a greater force to be generated with an equivalent applied potential, for a device with smaller overall dimensions.

When a piezoelectric actuator is used for vibration control, it is implemented as an active control element. An active control system is one in which energy is added to the structure to control the unwanted stimuli. In the case of piezoelectric actuators anti-noise is implemented to control the system. The elements are placed such that when they are activated, they produce the same response as the vibration but at a phase difference of 180^{o}. This applied signal would sum with the vibration and result in a net vibration of zero. One of the difficulties that may arise from this type of control is if the control system fails. In the case of the control system shutting down completely, there would be no damping added to the system from the piezoelectric elements. A larger problem would result from a malfunction in the control system that would cause the noise from the piezoelectric elements to be in-phase with the unwanted vibrations. When the vibration and the noise from the actuators are summed, this may result in an unstable structure.

2.4 Advantage and Disadvantages of Smart Material

The following sections describe the advantages and disadvantages associated with the use of the various smart materials covered in the previous sections.

2.4.1 Piezoelectric Materials

Table 2-1 gives the advantages and disadvantages associated with piezoelectric materials.

Table 2-1: Advantages and Disadvantages Associated With Piezoelectric Materials

Advantages	Disadvantages
• Compact and light weight • High sensitivity • Linear behavior • Low power consumption, due to direct conversion of electric to mechanical energy • Operate over large temperature range • Fast Response • Repeatable nanometer and sub-nanometer sized steps at high frequency can be achieved • Not influenced by magnetic field • Excellent stability due to being a solid • High operational bandwidth • Can be used as sensor and actuator	• Brittle due to crystalline structure • Produce relatively small strains • Relatively weak in tension and shear • Material degrades with time • Can be depolarized if operated outside of operational range (i.e. excessive strain or applied voltage, above curie temperature)

From the smart materials described above, piezoelectrics are one of the only two materials that can be used as an actuator and sensory element; however, they are the only one that can be used as a self-sensing element. Therefore, for applications such as vibration they are a step above the other materials, since they allow for perfect collocation. However, piezoelectric elements produce the smallest force compared to magnetostrictives and shape memory alloys, therefore, they are limited to smaller amplitude vibrations. Another feature of piezoelectric actuators that make them favorable is their linear behavior. An advantage of piezoelectric sensors over other sensory elements is its ability to monitor multidirectional vibrations, due to the 1 and 2 directions of the material possessing the same properties. This makes piezoelectric sensors ideal for monitoring pipe vibrations where both longitudinal and circumferential modes are prevalent. Also, piezoelectric materials require relatively minimal amounts of peripheral equipment for use. Since they function on electric power they can be monitored with any data acquisition system and can be actuated easily with a computer.

A power amplifier is generally required, since actuation voltages are greater than 10 volts, which is the general maximum output from a computer board.

2.4.2 Shape Memory Alloys

Table 2-2 gives the advantages and disadvantages associated with the use of shape memory alloys.

Table 2-2: Advantages and Disadvantages Associated With Shape Memory Alloys

Advantages	Disadvantages
• Produce very large recovery stresses • Many shapes and sizes available • Manufactured to desired properties (i.e. both mechanical and operational) • Large recovery strains (up to 8%) • Good Ductility • Effective at low frequencies • Heating process can be done easily using resistive heating	• Slow reaction time • Can only operate at low frequencies for dynamic applications • Low energy efficiency • Influenced by large environmental temperature changes • Unweldable • Expensive for large applications • Nonlinear thermomechanical behavior (exhibit large hysteresis)

As stated earlier, shape memory alloys are limited to actuation applications. They could produce very large forces due to their large recovery strains, and can be actuated very easily. Shape memory alloys are not suitable for most vibration applications, limited to vibrations lower than 5 Hz, due to their slow response time through the heating and cooling process. However, they are very good for static or shape control applications such as buckling resistance. They also possess a large hysteresis and nonlinear behavior, which can make their behavior hard to predict over large operational levels.

2.4.3 Magnetostrictive Materials

Table 2-3 shows the advantages and disadvantages associated with the use of magnetostrictive materials.

Table 2-3: Advantages and Disadvantages Associated With Magnetostrictive Materials

Advantages	Disadvantages
• Quick response time • High curie temperature • Relatively high strain and force generation • No fatigue or aging effects • Large operational temperature range • Low voltage operation	• Low tensile strength • Brittle • Costly due to rare earth metals involved • Large magnetic field required • Non-linear response • Equipment intensive, required to produce magnetic field

Magnetostrictive materials are very similar to piezoelectric materials except they function with the use of a magnetic field not an electric field. They are a hybrid between piezoelectrics and shape memory alloys since they possess a very quick response time and high strain and force generation. The voltage requirement for magnetostrictives is very small but they are very equipment intensive due to the production of a magnetic field. Even though the behavior of magnetostrictives is non-linear over their full operational range they can be modeled as linear over small magnetic field levels. This however will reduce their strain recovery levels and decrease their advantage of large strain recovery over piezoelectric materials.

2.4.4 Electrorheological Fluids

Table 2-4 shows the advantages and disadvantages associated with the use of ER fluids.

Table 2-4: Advantages and Disadvantages Associated With Electrorheological Fluids

Electrorheological (ER) Fluids	
Advantages	Disadvantages
• Induce large shear stress • Quick response • Fairly good durability • Operational by AC and DC voltages	• Poor reproducibility • Produce small forces • Creep can be an issue • Power requirements increase as temperature increases • Low solid state strength • Abrasive behavior • Settlement of dielectric particles are an issue, resulting in limited functions

These materials have very few uses in their current form. There have been a few investigations in the past for shape control in sandwich beams, but they possess to many flaws such as poor reproducibility, small forces, and loss of functionality to be a competitor in the current smart material market.

2.4.5 Fiber Optic Sensors

Table 2-5 shows the advantages and disadvantages associated with the use of fiber optic sensors.

In the market of sensor technology the fiber optic sensor is a leading candidate. They possess many characteristics required by great sensors they however have not been studied to determine their full capabilities. In most cases they are very fragile, and to eliminate the possibility of failure must be embedded into materials or be isolated from untrained human contact.

Table 2-5: Advantages and Disadvantages Associated With Fiber Optic Sensors

Fiber Optic Sensors	
Advantages	Disadvantages
• Small size and light weight • High sensitivity • High spatial resolution • Corrosion resistant • Very wide frequency bandwidth response • Simultaneous sensing of several parameters • High tensile strength and fatigue life • Fast response time • Immunity to electromagnetic interference • Large operating temperature range	• May need to isolate sensor from unwanted parameters • Availability of optical sources • Cost and availability of suitable instrumentation • Long term stability is still relatively unknown

2.5 Vibration Control Applications

Vibration control has been extensively studied over the past decade, due to the increased capabilities of piezoelectric and other smart materials. In most of these applications, vibration suppression of flexible structures, such as aluminum and FRP plates, have been investigated. However, some work has been performed on larger structures, such as cylindrical shell structures, using either a large numbers of piezoelectric sensors and actuators or piezoelectric layers. A review of the works involving experimental vibration control will be presented in detail in the following section, followed by a tabular summary, containing brief explanations of the work conducted, of some computational investigations.

2.5.1 Experimental Investigations

Kang et al. (1996) investigated the optimal placement of piezoelectric sensors and actuators for vibration control of carbon-epoxy laminate plates. The investigation was

carried out on a cantilever plate for different lay-ups experimentally and numerically with the finite element method (FEM). The lay-ups were manufactured with fiber orientations given by $[\theta_4/0_2/90_2]_s$, where θ = 0,15,30,45,60,75, and 90 degrees. The set-up for the investigation included a collocated pair of piezoelectric patches bonded to the top and bottom surface of the plate. To determine the effectiveness of the control system a structural damping index, based on modal damping, was implemented. It was found that the optimal position of the collocated pair was at the root of the cantilever. It was also reported that the modal damping, which accounts for both the amplitude decay and settling time, would be a more appropriate performance index then the damping ratio, which represents only the amplitude decay in a single cycle.

Redmond and Barney (1997) investigated how piezoceramic stack actuators could be implemented to damp the vibration in stiff beams and plates. This technique is useful for applications requiring large actuation forces that cannot be produced by small bonded patches. In this work the methodology for stiff beams and thick plates was investigated and it was determined that the maximum modal control forces could be generated by placing the actuators at locations of peak modal strain and offsetting them from the neutral axis at a maximum distance. Experimental results showed that stack actuators could effectively be used to decrease the first mode damping by a factor greater than 6 for one actuator and 40 with the use of two actuators.

Han et al. (1997) developed analytical and simulation models, which calculated the sensor output history and control voltage history for a composite beam with piezoelectric sensors and actuators. The numerical models gave very good predictions for not only modal properties but also control characteristics. Experiments for active vibration control of the composite beam and plates was also performed using a digital controller composed of a PC and analogue–digital conversion card. A linear quadratic optimal control system was designed, in which the Kalman filter was used as an observer and the control gain was determined to minimize a linear quadratic performance index. The simultaneous

control for the first bending and torsion modes of composite plates has been successfully accomplished using the optimal vibration control method.

Yang and Bian (1996) studied experimentally the vibration suppression capabilities of embedded piezoelectric sensors and actuators. The modal parameters of two S-glass/epoxy laminated plates with lay-ups of $[0/90]_{6s}$ and $[45/-45]_{6s}$, were predicted by a finite element model and validated by experimental modal testing. Each specimen was embedded with six piezoelectric patches, with three located on each side of the neutral axis. The cutout method was used to embed the patches, which had a thickness of three laminate layers, in the third to fifth and eighth to tenth layers. Experiments showed that both the bending and torsional vibration modes could be effectively reduced by the velocity feedback from the embedded piezoelectric sensors and actuators.

Oshima et al. (1997) experimentally studied the possibility of implementing self-sensing actuators for vibration control in a cantilever beam. Self-sensing actuation was achievable with the use of a RC bridge circuit, which separated the sensor and actuator voltage present in the single piezoelectric element. This work used rigid piezoceramic layers bonded to the top and bottom surface of a cantilever plate. One layer was used for the control, and the other to vibrate the specimen. With a balanced bride circuit it was found that very good control could be achieved. However, the system was observed to have become unstable with an unbalanced bridge.

Tani et al. (1994 and 1995) showed the effectiveness of applying the $H_{infinity}$ control theory for vibration control in a cylindrical shell system. The cylindrical shell system consisted of a layer of plastic film and two piezoelectric film layers. A part of the piezoelectric film layers were used for actuation of the system. The analysis examined the vibration caused by periodic excitation. By applying the $H_{infinity}$ control theory to the cylindrical shell system, a numerical simulation and an experimental investigation of

vibration control was carried out. The problem was solved by means of the modal expansion method.

Qiu and Tani (1996) investigated the controllability of cylindrical shells under forced vibrations using distributed piezoelectric actuators and a hybrid control method. The shell was constructed from a polyester film with one piezoelectric film on each side. The electrodes on the surfaces of the piezoelectric films are divided into several parts, and two parts of the films are used as actuators. The shell was mounted vertically on a vibration table and excited by the horizontal motion of the table. A combination of μ-synthesis control and disturbance cancellation methods were used to develop the hybrid control scheme. Simulation and experiment were carried out with the hybrid control method showing more effective results than either of the individual control methods.

Grewal et al. (2000) studied reducing the fuselage noise caused by the propeller in a Dash-8 turboprop aircraft. This was performed experimentally on a full-scale aircraft. Three frames of the fuselage were used in this investigation. A total of 199 piezoelectric elements in total were bonded to the frame (with each individual frames containing 68, 62, and 69 piezoelectric elements, respectively). The piezoelectric elements were indeed attached to the framework of the plane and not the actual skin of the aircraft. The pressure field of the aircraft was simulated with four 12" loudspeaker units with a 200 W power rating. Along with the piezoelectric elements mounted on the framework, a total of 33 accelerometers were mounted on the shell of the fuselage to monitor the deflected shape. They observed that significant attenuation of both the fuselage vibration and cabin noise were achievable, with peak values of 16 dB in the fuselage vibration, and over 28 dB in the cabin noise. It was also noted that these reductions could be observed globally throughout the system.

2.5.2 Analytical Investigations

Table 2-6 provides a brief summary of some of the computational research investigations that have been performed on vibration control applications.

Table 2-6: Computational Studies of Vibration Control Applications

Authors (Year of Publication)	Details of Study
Koko et al. (1997)	Presented an integrated FE control methodology for the design and analysis of smart composite structures. The proposed method was implemented in a computer code called SMARTCOM. Results were produced for several examples.
Smith et al. (1998)	Studied the performance of optimal vibration control methods with FEM. The IMSC and LQR optimal control methods were modified for the analysis. The two methods were compared using the transient response of an aluminum strip with piezoelectric sensing and actuating patches. The results showed the maximum actuation voltage varies with control scheme, and they were smaller for the LQR method than the IMCS method.
Lim et al. (1997)	Presented a 3-D FE closed loop solution for active and active/passive damping of vibrating structures. To investigate the controllability of a structure two control methods were used based on charge and voltage. The results show that the method used shows significant reduction in the vibration oscillation.
Han and Lee (1998)	Used FEM to evaluate the closed loop performance of composite plates with distributed piezoelectric actuators using a layerwise displacement theory mechanics. By comparing the results obtained by this method with those available it was found that this approach could describe the smart composite plate more realistically.
Hwang et al. (1993)	Studied active vibration control of cantilevered laminated composite plates using piezoelectric actuators and sensors with FEM. The results from this investigation showed that the bending mode of a beam is most effectively damped with the actuators located at the root of the plate, while the outer edges give the best results for damping the torsional mode.

Table 2-6 continued	
Soares et al (1999)	Studied the behavior of composite plates with piezoelectric actuators and sensors with FE based on higher-order displacement fields. In order to maximize actuator efficiency, improve performance, and minimize the structure weight, a sensitivity and optimization technique was implemented. To show the performance of this method several simple examples were presented. It was found that the structural performance as well as weight reduction was achievable with the developed optimization scheme.
Chandrashekhara and Varadarajan (1997)	Investigated the adaptive shape control of FRP composite beams with integrated piezoelectric actuators using FE method based on a higher order shear deformation theory. Both open loop and closed loop control systems were investigated. To determine the optimal open loop actuator voltages a constrained optimization algorithm was used. It was found that the adaptive shape achieved by full sensor feedback and partial sensor feedback were nearly the same.
Wang and Vaicaitis (1998)	Performed an analytical investigation on active vibration and noise reduction in a double walled sandwich shell structure. A parametric study was also performed on the effects of actuator size and placement, control gains, and damping characteristics. The vibrations in the system were controlled using direct velocity feedback as well as sound pressure rate feedback. It was observed that the direct velocity feedback method provides significant control for frequency ranges with low modal densities. However, it is not effective in reducing noise transmission. The sound pressure rate feedback control method was very effective in reducing the noise transmission.
Saravana et al. (2000)	Analytically determined the damping ratio for boron/epoxy cylindrical shell with PVDF surface bonded layers. It was observed that for a given mode there is an optimal placement along the length of the shell for positioning the actuator/sensor pair, which varies from mode to mode. They also concluded that for a given set of laminae, the stacking sequence effects the active damping ratio of the cylindrical shell.
Sun and Tong (2001)	Performs simulations to show how active control of shell structures can be performed with discretely distributed piezoelectric surface bonded patches. It was observed from the simulations that the modal sensor can provide modal signals used for modal control even though its basic frequency is high. This is provided that the proper amounts, positions, and sizes of sensors and actuators are used. It was found that if the shell is partially covered with piezoelectric layers, the proposed method was suitable for vibration control of large shells.

2.6 Damage Detection Applications

In the past there have been several investigations into damage detection or health monitoring of various civil engineering structures. This includes investigations into beams, trusses, plates, frames, bridges, offshore platforms, other large civil engineering structures, aerospace structures, and composite structures. Most of the current nondestructive evaluation techniques involve periodic inspections involving ultrasonic equipment, that could be very costly, rigorous, and time consuming. With the use of piezoelectric materials damage detection can be achieved in real time, eliminating the need for periodic inspections. The following will detail the methods and techniques that are related to the scope of this thesis. For further information on a full range of damage detection systems and techniques the reader is directed to the work of Doebling et al. (1996), who provides an extensive literature review on the different methods and techniques for damage detection utilizing smart materials.

Tseng and Naidu (2002) performed an extensive investigation on the use of several statistical damage indices for detecting holes present in aluminum plates. An impedance-based method was used to determine the signatures of the response, and then damage indices were implemented to get an assessment of the damage. The damage indices used to evaluate the damage included the root mean square deviation (RMSD), mean absolute percentage deviation (MAPD), covariance (Cov), and correlation coefficient (CC). It was found that the RMSD and MAPD indices were most suitable for determining damage growth and location, where covariance and CC are more effective at determining increases in damage at a given location. They also determined the CC is a better method than the covariance since it is scaled to 1.

Caccese et al. (2004) investigated bolt load loss in hybrid composite-metal bolted connections. They investigated a composite panel that was bolted to a steel frame. A piezoelectric actuator located at the center of the panel was used to create a controlled input, while the response was monitored using shear accelerometers or dynamic strain

sensors located at the corners of the plate. They investigated three different approaches to determining bolt load loss, which involved low frequency modal analysis, high frequency transfer functions between the actuator and sensors, and high frequency transmittance functions between pairs of sensors. It was found that the modal analysis approach did not effectively produce results for bolt load loss until all bolts were loosened from their original preload, or one bolt is completely removed. The use of high frequency transfer functions showed promise in detection of bolt load loss, such that the damage index increased as the bolt was loosened. The transmittance function method showed very good damage detection capabilities and experimentally gave the most promising results.

Mickens et al. (2003) studied damage detection capabilities in aircraft wings using a frequency response function (FRF) damage index. In the experimental investigation an aircraft wing tip structure was made with screws replacing rivets for ease of damage simulation. There were four PZT patches bonded to the wing structure, with one in each quadrant. A periodic chirp signal was applied to one of the patches to load the system, while the other three patches were used to monitor the system. Several different degrees and locations of damage were tested to determine the full capabilities of this approach. It was shown that the FRF monitoring method was effective and had some advantages and limitations compared to other damage detection methods.

Lauwagie et al. (2002) studies the damage detection capabilities in beams using a laser vibrometer. In this paper the modal parameters of an undamaged beam were monitored and compared with the vibration behavior of the beam subjected to controlled damage. The beam was acoustically excited with a small loudspeaker and a Polytec Scanning Laser Doppler Vibrometer was used to measure the response of the beam to the excitation signal. The resonant frequencies were then compared to determine the state of damage.

Kessler et al. (2002) used a laser vibrometer to monitor the time response for damage detection in composite plates. The response of the laminate coupons with different degrees and types of damage were tested and modeled with FEM. To determine the presence of damage the natural frequencies of the specimens were compared. The models accurately predicted the response of the specimens at low frequencies, but coalescence of higher frequency modes made mode-dependant damage detection difficult for structural applications. The frequency response method was found to be reliable for detecting even small amounts of damage in a simple composite structure, however the potentially important information about damage type, size, location and orientation were lost using this method since several combinations of these variables can yield identical response signatures.

Giurgiutiu et al. (1998) presented results of an experimental investigation spot-welded lap-shear structural joints. The experiments studied structural heath monitoring, damage detection, and NDE by implementing the electro-mechanical impedance technique. The test specimens were instrumented with piezoelectric wafer transducers, and the base E/M impedance signature was recorded over the relevant frequency range. Fatigue testing was applied to initiate and propagate crack damage of controlled magnitude. A Euclidean norm based, same as the root mean square deviation (RMSD) damage index was used to evaluate the results. It was found that the damage index value increased as crack growth was observed.

Soh et al. (2000) performed a health monitoring study of a prototype reinforced concrete bridge. Piezoceramic patches were used to instrument the bridge. The patches were electrically excited at high frequencies, in the order of kHz, and the conductance was extracted as a function of the exciting frequency. The patches were scanned for the acquisition of this signature at various stages during the loading process. The signatures of the patches located in the vicinity of the damage were found to have undergone drastic changes, while those farther away were less affected. A non-parametric damage index,

RMSD, was used to quantify the deviation in signatures with respect to the baseline signature of the healthy state. The results showed the RMSD index correlated well with the damage progression in the structure.

Sun and Chang (2002) used the wavelet approach for damage assessment in a cantilever steel I-beam. The sum of absolute differences (SAD) and square sum of differences (SSD) between the wavelet package energies of the undamaged and damaged specimens were used to perform the damage assessment. The results showed that this method could perform very effectively for structural health monitoring applications.

Chiu et al. (2000) performed a numerical investigation into an impedance-based transfer function technique to determine the damage in a boron/epoxy patch on an aluminum host structure. It was found that impedance measurement technique could be effective in detecting damage, but the sensor/actuator must be located close to the damage region.

Park et al. (2001) studied an impedance based damage detection method along with self-healing bolted pipe joints. The impedance based damage detection approach uses the fact that the electrical impedance of the PZT sensors is related to the mechanical point impedance of the host structure. A model of a pipeline was constructed using 40mm diameter segmented pipes, flanges, elbows, and joints connected with more than 100 bolts. A PZT patch was bonded directly on each joint for evaluating the damage detection capabilities. It was found that the impedance signature of the sensors on the joints with damage gave good results.

Ritdumrongkul et al. (2003) studied damage detection in bolted joints of aluminum plating. The impedance-based method was used to determine the damage for varying bolt torque values, which ranged from 20 cN.m down to zero (completely loose). The bolt torques were so small due to the size of the bolts, which were 3mm. It was shown quantitatively that the degree of damage could be determined.

Yang et al. (2001) studied the use of damping and frequency measurements to monitor weak bond defects due to poor adherent surface preparation. The results of modal tests and shear tests are compared and discussed. The effects of dynamic excitation amplitudes on the modal parameters of such defective specimens were also investigated. A major conclusion was that monitoring of damping and frequencies was an effective means, however, damping measurement seems to be more reliable in some cases, for nondestructive detection of damage and/or degradation in adhesively bonded joints of composite structures. This work shows a fast, easy, and low cost method for structural health monitoring in composite bonded joints.

2.7 Influence of Embedding Piezoelectric Patches into FRP

Singh and Vizzini (1994) looked at the integrity of unidirectional laminated composites using an interlaced embedding technique under unidirectional tension. It was found that the interlacing technique could reduce the interlaminar normal stress up to 42% and the interlaminar shear stress up to 22% if the proper technique was implemented. It was also found that the actuation of the piezoelectric patch resulted in insignificant changes in the interlaminar stress. This means that the mere presence of the piezoelectric patch causes the increase in the interlaminar stresses.

Shukla and Vizzini (1996) experimentally studied the performance of interlacing lay-ups with embedded glass slides, used to simulate piezoelectric patch, on 24 ply unidirectional graphite/epoxy laminates. Their specimens where loaded using quasistatic uniaxial tension, with damage initiation and progression being monitored throughout the process. It was found that an inclusion equal to the thickness of eight plies reduced the ultimate strength by 72%. The onset of damage at and near the inclusion was delayed and the ultimate strength of the structure was increased substantially by distributing the discontinuity of the inclusion through the thickness via interlacing. It was also found that

interlacing the lay-up could increase the failure strength by a factor of two over the cutout method.

Mall (2002) investigated the effects on the monotonic and fatigue strength of graphite/epoxy tensile specimens with an embedded Active Control Experts (ACX) PZT patch. The difference between using an overlay and cutout embedding technique was also investigated. It was found that the tensile strength and the Young's modulus of the test specimens were not affected by the insertion of the PZT patch for either embedding technique. It was also found that the fatigue life/strength of the test specimens showed no degradation due to the embedded patch, with either embedding technique, and that the S-N curves were similar for all test specimens.

Shah et al. (1990) studied a smart laminated composite structure with embedded piezoelectric sensor layer. A quasi-three-dimensional finite element model was utilized to obtain the detailed state of stress in the vicinity of embedded piezoelectric layer in a laminated composite. Interlaminar stress distributions for a typical quasi-isotropic $[+45,-45,0,90]_s$ graphite/epoxy laminate were obtained with the piezoelectric layer placed at different interfaces. The numerical analysis results indicated that the placement of the piezoelectric layer did not alter the peak stress location. However, a compressive normal stress was observed in the region of the piezoelectric layer if the layer is placed at the [-/45/-45/-] interface. It was also observed that the addition of a glass layer adjacent to the piezoelectric layer results in the lowering of the interlaminar stresses.

Chapter 3

Vibration Suppression Applications

3.1 Introduction

The focus of this work was to investigate the feasibility of implementing self-sensing piezoelectric patches to monitor and suppress vibrations in laminate composite plates along with PVC piping.

3.2 Piezoelectric Materials

The piezoelectric patches that were used for these experiments were QP15N PZT QuickPack actuators available from Mide Technology Corporation, Cambridge, Ma. They are distributed prewired and insulated and are operated through a four-pin connector, as shown in Figure 3-1. The dimensions and characteristics of the piezoelectric patch are given in Table 3-1.

Figure 3-1: Piezoelectric Patch (Mide Technology Corporation, 2005)

Table 3-1: Characteristics of the Piezoelectric Patch

Device Size (in)	2.00x1.00x0.01
Active Element Size (in)	1.81x0.81x0.005
Device Weight (oz)	0.08
Device Capacitance (μF)	0.10
Full Scale Voltage Range (V)	±100
Full Scale Strain (με)	±225

3.3 Self-sensing Piezoelectric Patches

One of the major attractions of piezoelectric materials is their ability to be implemented as sensors and/or actuators. When one piezoelectric patch is implemented as a self-sensing element the required number of components will be halved. The process involved in implementing a single piezoelectric element as a sensor and actuator requires the separation of the resulting sensor signal and the incoming actuation signal. This can easily be done with the use of a resistor-capacitor bridge circuit as shown in Figure 3-2.

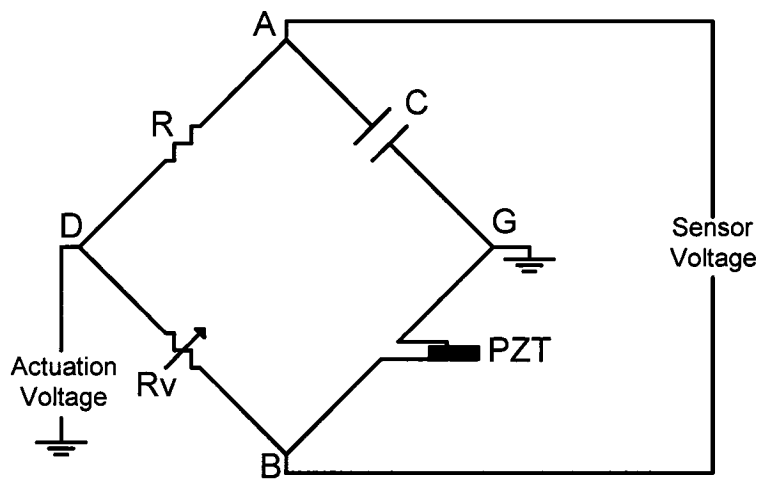

Figure 3-2: A Typical RC Bridge Implemented for Self-Sensing Actuation (Vera and Guemes 1998)

The components making up this circuit are a constant resistor, constant capacitor, variable resistor, and the piezoelectric patch itself. In order for this circuit to work for self-sensing applications the bridge must be balanced. To balance the circuit you minimize the output of the circuit, by adjusting the variable resistor, with a sinusoidal wave being input. If the bridge is correctly balanced, such that $R_V C_{PZT} = RC$, the voltage between A and B will contain only the sensor voltage, and the actuation voltage is applied across D and G. This circuit was constructed on a small electronic board with the addition of three BNC connectors as well as a cut-down circuit, which will be explained in detail in the next section, as shown in Figure 3-3.

(a) (b)

Figure 3-3: RC Bridge and Voltage Reduction Circuit (a) Top View (b) Front view

Where; A is the connector for applying the actuation voltage, B is the connector for the piezoelectric patch, C is the connector for monitoring the sensor voltage, D is the circuitry for the bridge circuit, and E is the voltage reduction circuitry.

3.4 Voltage Considerations

Due to the large values of the piezoelectric sensor voltage, and relatively low input capacity of the computer boards, the sensor signal had to be reduced before reaching the computer. This was done with a resistor T-circuit that reduced the sensor voltage to 6.5% of the actual value, bringing it below the required ±10 volt threshold. Conversely, in order to apply large voltage level to the actuator a power amplifier was implemented. The amplifier was a series 790A01 single channel power amplifier that is manufactured by PCB Piezotronics, Buffalo, NY. This amplifier has an adjustable gain with a maximum output capacity of ±200 volts at 50 mA.

3.5 Vibration Suppression of Fiber-Reinforced Laminate Plates

The experimental investigation into vibration suppression of laminate plates with surface bonded piezoelectric elements studied the influence of varying the feedback gain applied to the actuator. This was then performed for an embedded piezoelectric patch to determine the efficiency of an embedded patch vs. surface bonded patch.

3.5.1 Test Specimens

All test specimens were cut out of a single graphite/epoxy panel that was manufactured in the laboratory. The panel was manufactured with 12 unidirectional graphite fiber sheets using hand lay-up. The panel was then placed under a vacuum-seal and cured for a period of approximately 12 hours under 20 mm Hg vacuum. The vacuum is used to ensure the removal of air voids and gives a strong bond within the laminate. The resulting thickness of the panel was 3.61 mm. This panel was then cut into 304.8x76.2 mm test plates, as shown in Figure 3-4.

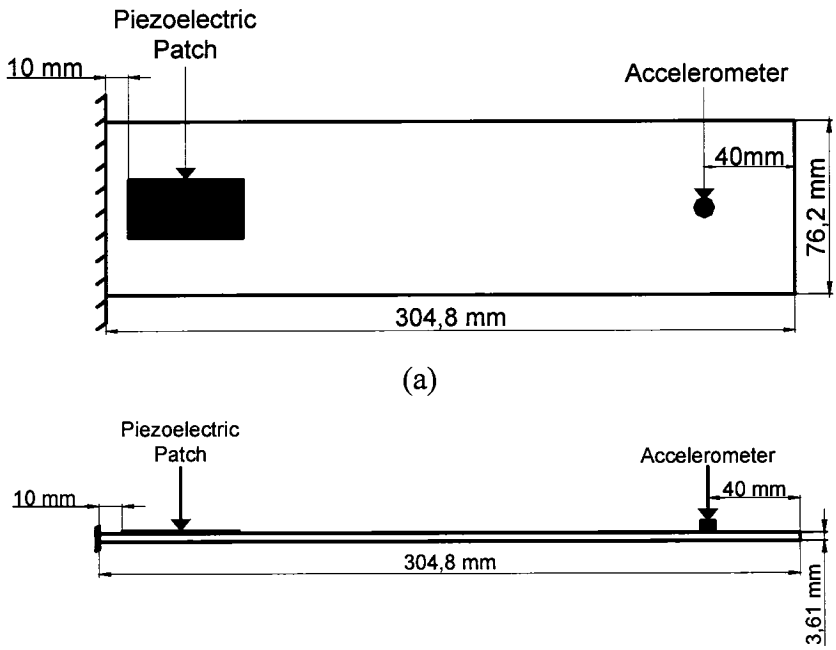

Figure 3-4: FRP Plate Test Specimen Dimensions, Piezoelectric Patch Location, and Accelerometer Location (a) Top View Dimensions (b) Front View Dimensions

There were two specimens cut to have a surface bonded piezoelectric patch and one with an embedded patch. Along with monitoring the piezoelectric sensor response an accelerometer, PCB Piezotronics mode number U353B15, was mounted near the free end of the plate, with the use of an adhesive wax, as shown above in Figure 3-4 above. This

was done to verify the reduction in the plate vibrations away from the self-sensing piezoelectric patch. The technique used to bond and embed the patch will be detailed in the next section.

3.5.2 Mounting of Piezoelectric Patches

3.5.2.1 Surface Bonding Procedure

The surface of the plate was initially sanded with a coarse sand paper to prepare it for bonding of the piezoelectric patch. This removes any imperfections in the surface as well as creates a rougher surface for increased bond adhesion. Once the area was sanded, the plate bonding surface as well as the piezoelectric patch surface were wiped with isopropyl alcohol to remove any foreign materials present, such as dust, which will decrease the strength of the bond. As soon as cleaning was complete, a two-part epoxy system, manufactured by West System, Bay City, MI., was applied to the surface of the plate as well as the piezoelectric patch. The patch was then placed in its correct position and taped down to hold it in place. On top of the piezoelectric patch there was a layer of porous Teflon followed by bleeder cloth, then a non-porous Teflon layer. These layers allow for the excess resin and air voids to escape from the bonding area of the patch. This was then placed under a vacuum seal for a period of approximately 12 hours under a pressure of 20 mm Hg. Once the epoxy had fully cured the vacuum seal was removed and the edges of the piezoelectric patch were visually inspected to determine the presence of a disbond.

3.5.2.2 Embedding Procedure

The piezoelectric patch that was embedded into the specimen was done so during the panel manufacturing process. Before embedding the patch into the lay-up the surfaces of the patch were wiped with isopropyl alcohol to remove any trace of dust. During the lay-up process the patch was placed at the desired location within the lay-up, which was between the second and third layers. The final two layers of the laminate were overlaid above the patch, which ensured consistency in the laminate. Once the panel was cured,

as described in the previous section, the plate with the embedded patch was cut out using a diamond blade on a table saw. Figure 3-5 shows a side view of the positioning of the piezoelectric patches for a surface bonded patch and the embedded patch.

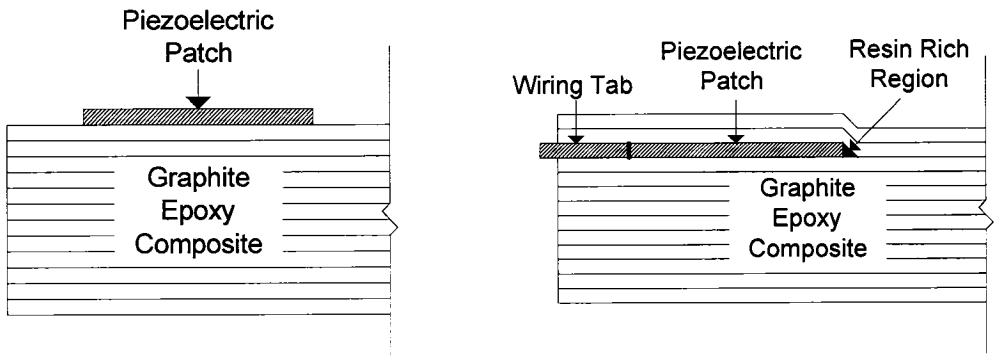

Figure 3-5: Location of Piezoelectric Sensor/Actuator (a) Surface Bonded Piezoelectric Patch (b) Embedded Piezoelectric Patch

3.5.3 Testing Apparatus and Equipment

3.5.3.1 Support Fixture

The testing fixture used to test the specimens is shown in Figure 3-6.

Where A is the bolts used to tighten the fixture to the massive steel frame foundation, B are the bolts that connect the upper and lower portion of the fixtures, C are the bolts that clamp the small steel plate down on the test specimen, D is the small steel plate that clamps down on the test specimen, and E is the location of the test specimen.

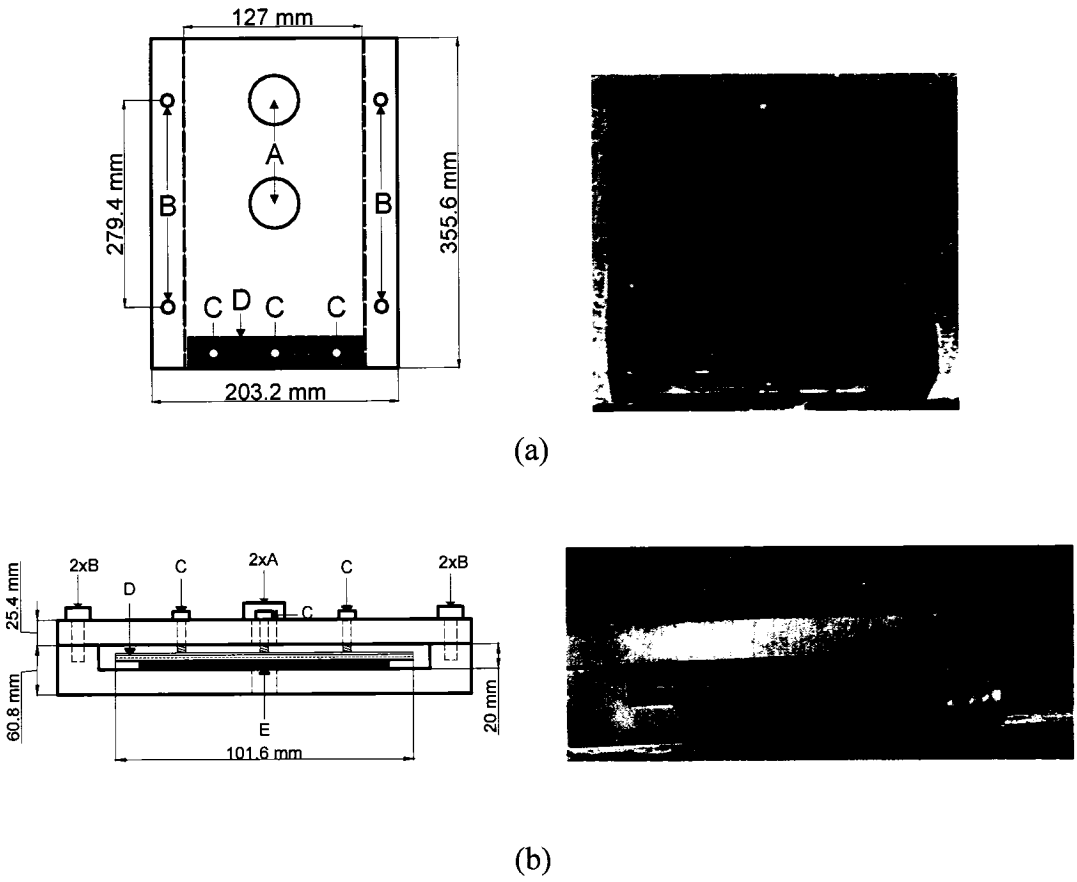

Figure 3-6: Support Fixture for Vibration Suppression in Laminate Plates (a) Top View (b) Front View

This fixture was securely fastened to a massive steel frame using 2-¾" bolts. The fixture had the center milled out such that the wiring from the piezoelectric patch could run through the fixture reducing the risk of damage to the sensors. The test specimens were clamped into the fixture by tightly fastening the three small bolts through the top of the fixture to a small steel plate. This steel plate then clamps down on the test specimen wedging it between the steel plate and the lower portion of the fixture.

3.5.3.2 Computer Data Acquisition System

There were two computer systems used to conduct these experiments. One was used to monitor and actuate the piezoelectric patch, while the other was used to monitor the impulse hammer and accelerometer.

The system used for monitoring and actuating the piezoelectric patches implemented the DT3010 data acquisition board, available from Data Translation. The DT3010 is a high-speed multifunction board, which contains 32SE/16DI analog input channels along with 2 analog output channels, all with 12-bit resolution. The throughput of the board is 1.25 MS/sec and 500 kS/sec for the input and output channels respectively. The input and output channels have a maximum operating range of ±10 volts. The software used in conjunction with this board was VEE Pro v6.0. This is a visual based program that is developed by Agilent Technologies (Palo Alto, CA.) with drivers provided by Data Translation Inc. (Marlboro, MA) to link directly to their data acquisition boards. The program developed was designed specifically for this experiment.

The data acquisition system used to monitor the accelerometer and impulse hammer used the DT24-EZ board, available from Data Translation Inc. (Marlboro, MA). The DT24-EZ is an input data acquisition board with 16SE/8DI analog input channels with 12-bit resolution. The throughput of the board is 100 KS/sec for a single channel or 80 KS/sec with channel scan. The maximum operating range of this board is ±10 volts. This board was operated with a LabVIEW program that was developed specifically for the application. Due to the incompatibility of the boards and LabVIEW a set of specific drivers had to be used, which was available from Data Translation in the form of DT-LV Link software.

With the use of visual based data acquisition programs the results can be graphically inspected to verify the test was fully captured, which is an advantage of these interfaces. However, the disadvantage of visual based programs is the maximum acquisition rate, which is reduced compared to codes written in languages such as C++.

3.5.4 Experimental Procedure

There were two sets of loading applied to the FRP plates. Statically displacing the free end of the plate and releasing it to induce free vibration conducted the first sets of tests, where the second set of tests were conducted with an impact load, using a PCB 086B01 impulse hammer. Along with the two different loading methods, tests were conducted with and without an accelerometer attached near the free end of the plate. Due to the number of different set-ups the tests are broken down into different series as shown in Table 3-2.

Table 3-2: Test Set-up Numbering System for Vibration Control of FRP Plates

Test Set-up Numbering	Set-up Description
Series 1	• Surface bonded piezoelectric patch • Initial displacement loading • No accelerometer attached
Series 2	• Surface bonded piezoelectric patch • Initial displacement loading • Accelerometer attached
Series 3	• Surface bonded piezoelectric patch • Impact loading • Accelerometer attached
Series 4	• Embedded piezoelectric patch • Initial displacement loading • No accelerometer attached
Series 5	• Embedded piezoelectric patch • Initial displacement loading • Accelerometer attached
Series 6	• Embedded piezoelectric patch • Impact loading • Accelerometer attached

3.5.4.1 Initial Displacement Test Procedure

For the first set of tests the LabVIEW program was started and the plate was released. The signal was monitored using single point value acquisition for all tests, to ensure consistent data acquisition between non-controlled and control tests. For control

applications this value was multiplied by a gain value and fed back to the piezoelectric patch, through the power amplifier, as an actuation voltage. For the testing program the operational frequency, where the operational frequency is a combination of both sampling and actuation, was found to be approximately 900 Hz. This is due to the single point acquisition, which is generally slower than multipoint acquisition, and the feedback portion of the program. 900 Hz. however, is adequate for the given application since all the excited frequencies are well below this value, with the first fundamental frequency of the plate being approximately 46 Hz. The accelerometer was monitored continuously for a period of 10 seconds at a rate of 10 kHz.

3.5.4.2 Impulse Loading Test Procedure

For these sets of tests the LabVIEW program was started and the plate was impacted with the impulse hammer near the free end of the plate as shown in Figure 3-7.

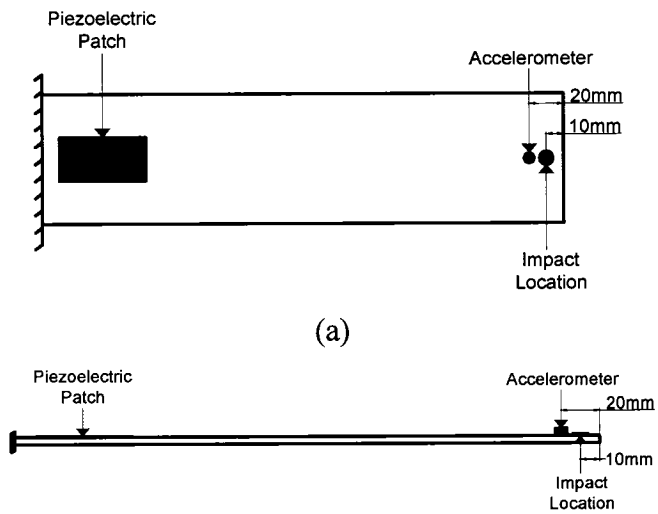

Figure 3-7: FRP Plate Set-up for Impact Loading (a) Top View (b) Front View

The accelerometer was monitored at a rate of 10 kHz but was found to produce incorrect results due to its close proximity to the impact load. Therefore the accelerometer results were ignored. The signal from the impulse hammer was monitored continuously for a

period of two seconds at a rate of 10 kHz. The piezoelectric patch was monitored and actuated with the same procedure as the initially displaced tests described above.

3.5.5 Control Test Method

In order to actuate the piezoelectric patches the sensor voltage was feedback to the patch after a gain was applied. Due to the limitations of the computer systems and software, a displacement based feedback control was used. This method involved applying a constant gain to the sensor voltage throughout the entire experiment.

3.5.6 Data Processing

All data processing of the results for these tests was performed with the use of codes developed in MATLAB. The processing that was required in the tests files is as follows:

- Removal of zero state data (i.e. determine test start and end points).
- Separation of the different data sets (i.e. piezoelectric sensor voltage and time). The accelerometer and impulse hammer results were written to separate files.
- Determination of the time for the individual points of the piezoelectric sensor.
- Store the results containing only appropriate test data to an output file.

3.5.6.1 Piezoelectric Sensor Response Data Processing

The following operations were performed in the piezosensor.m MATLAB code, which is documented in Appendix A.

The first step was to remove any offset that was present in the sensor response. It was determined through inspection that the last value in the data sets was equal to the offset in the data. Therefore, this value was subtracted from every value in the data to correct for the offset.

The removal of the zero state data included removing all the non-response data at the start and end of the test. The start of the test was determined by finding the position where the piezoelectric sensor response surpassed a set value, in these cases 0.5 volts. The test was then deemed to start 3 points before this value was surpassed, which was found by visually inspecting the results. The end of the test was determined by visually inspecting the free vibration of the plate. It was found that the vibration amplitude of the plate decayed to less than 1% of the maximum in under four seconds, so four seconds was taken as the test completion time.

Separation of the data sets was only required for the piezoelectric patch response files that contained both the piezoelectric sensor response as well as the time of the corresponding points. The accelerometer and hammer responses were continuously monitored so the time between data points would be consistent throughout the test. Knowing that the first half of the data contained the piezoelectric sensor response and the second half was the relative time of the individual data points allowed for easy separation.

One of the limitations of this data acquisition system is the inability of the system to determine the exact time of the single points being monitored, but does give a relative time. This is due to the computer only being able to update the time at a rate of 100 Hz in this case, which was limited by the operating system. Therefore, when monitoring with single point acquisition there will be several points that show the same time in the output file. This was resolved by assuming all the points that show the same time were monitored at the same rate. With this assumption, all that is required is the positions of the change in time, the magnitude of the change, and how many points were monitored during the constant time period. The time between the individual data points within a given set could then be determined by dividing the change in time by the number of points in that constant time set. With the use of a 'for' loop the time difference between every point was determined. However, this method would not assign change in time

values to the last few points that occur at the last recorded time. These points were assumed to have the same time between points as the last point calculated in the 'for' loop. However, this was not required since these last few points were removed as non-response data anyway.

3.5.6.2 Accelerometer and Impulse Hammer Response Processing

The following operations for the accelerometer and impulse hammer were performed with the accelerometer.m and hammer.m MATLAB codes documented in Appendix A.

The first step in these programs was to correct for any offset that may be present in the data. Selecting the last point in the data, which was found to be the value of the offset, and subtracting it from every value did this. The removal of the zero state data included removing all the non-response data at the start and end of the test. The start of the test was determined by finding the position where the accelerometer and impulse hammer voltages surpassed a set value, in these cases 0.1 volts. The test was then deemed to start 2 points before this value was surpassed, which was found by visually inspecting the results. The end of the test for the accelerometer response was found to be the same as the piezoelectric sensor. Therefore, four seconds of data from the start point of the accelerometer response were stored into a variable and written to an output file. The impulse hammer response was found to last for approximately 1.5 msec. However, the impulse hammer response was saved for a time period of 10 msec for display purposes.

3.5.7 Vibration Suppression of FRP Plates

Several factors were investigated to determine the efficiency of the proposed system for vibration suppression of the FRP plates. These included comparing the controllability of the plates with different feedback gains, different loading methods, and a comparison of the surface bonded actuator to an embedded actuator.

To determine the effectiveness of the tests conducted with voltage feedback the time required to reach 50 percent, 25 percent, and 10 percent of the non-controlled maximum signal strength was used. Figure 3-8 shows graphically how the envelopes for the non-controlled tests were done.

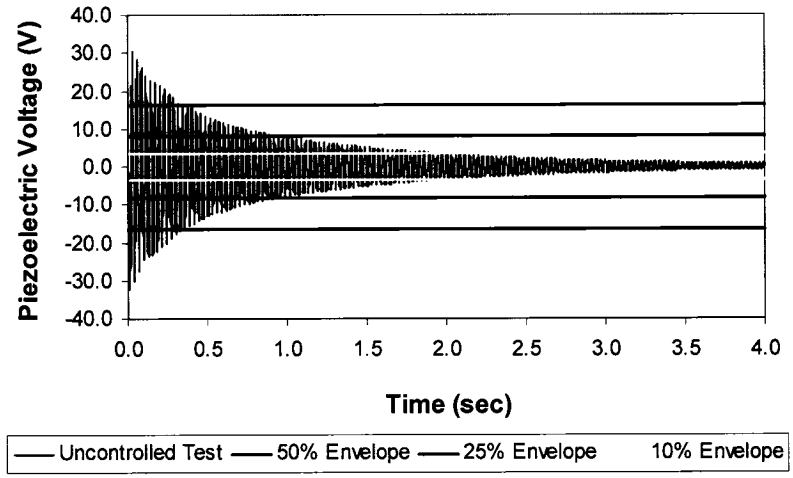

Figure 3-8: Schematic of Envelopes used in Determining the Efficiency of the Vibration Suppression Tests

3.5.7.1 Surface Bonded Piezoelectric Patch Control Results

In this experimental investigation tests were conducted with and without the use of an additional sensor. The additional sensor was an accelerometer that was placed near the free end of the plate as shown previously in Figure 3-7. For each of the tests in this investigation the different feedback gains used to determine the effects of the actuator voltage magnitude were 1.0, 1.3, 1.5, and 1.8. These values were selected such that the maximum feedback voltage would not exceed the maximum capacity of the piezoelectric patch supplied by the manufacturer, 100 V.

3.5.7.1.1 Series 1 Results: Initial Displacement Loading With No Accelerometer

A total of three tests were conducted for each of the gain levels as well as the non-controlled specimen. Figures 3-9 through 3-12 show the comparison of the varying feedback gains relative to the proceeding state, for a set of each of these tests. The

proceeding state is the non-controlled state for a feedback of 1.0, and is the previous level gain for larger gains (i.e. feedback gain of 1.0 vs. 1.3). It can be seen from these figures that the vibration amplitude could be effectively reduced with a feedback gain of 1.0, and the reduction continues as the gain increases.

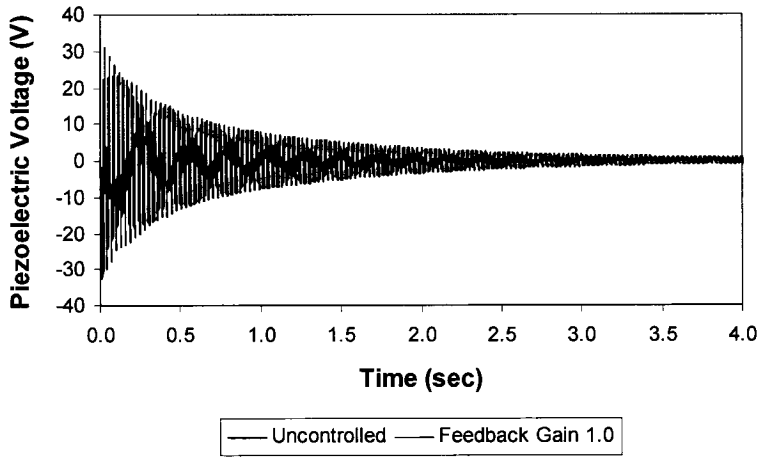

Figure 3-9: Piezoelectric Response for Non-controlled Specimen vs. Feedback Gain of 1.0 for Series 1 Tests

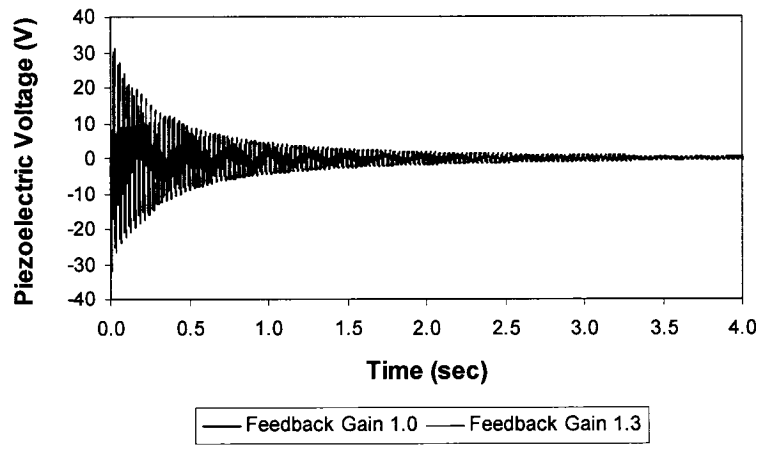

Figure 3-10: Piezoelectric Response for Feedback Gain of 1.0 vs. Feedback Gain of 1.3 for Series 1 Tests

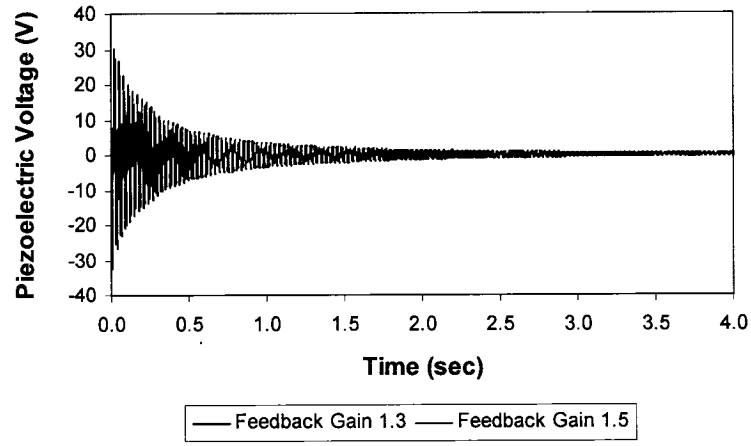

Figure 3-11: Piezoelectric Response for Feedback Gain of 1.3 vs. Feedback Gain of 1.5 for Series 1 Tests

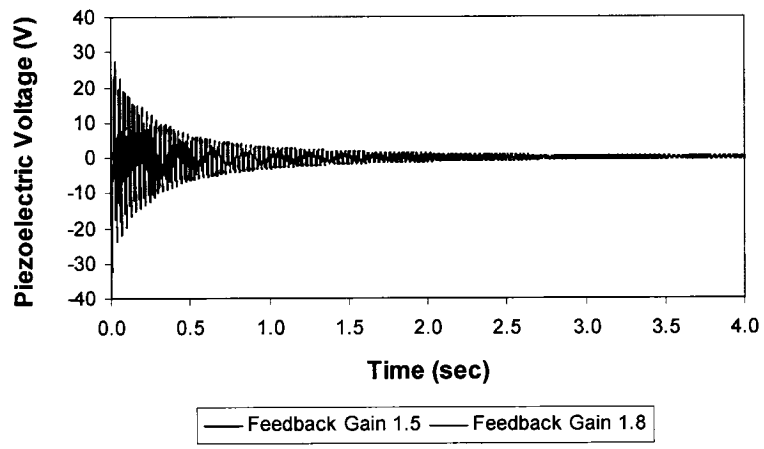

Figure 3-12: Piezoelectric Response for Feedback Gain of 1.5 vs. Feedback Gain of 1.8 for Series 1 Tests

To give a better indication of the actual percent reduction in the vibration amplitude, the average time required and percent reduction to reach the 50, 25, and 10 percent amplitude levels for each of the different gain levels for the series 1 experiments are shown in Table 3-3, where the average is for all the tests conducted. As these results show, the maximum percent reduction is generally seen at the 25% level, with the exception being a feedback gain of 1.5. These results also show the increase in suppression as the gain is increased.

Table 3-3: Average Time Required and Percent Reduction to Reach 50%, 25%, and 10% of Non-controlled Piezoelectric Sensor Response for Varying Feedback Gains for Series 1 Tests

Test Set-up	Time to reach 50% amplitude (sec) (% Reduction from Non-controlled)	Time to reach 25% amplitude (sec) (% Reduction from Non-controlled)	Time to reach 10% amplitude (sec) (% Reduction from Non-controlled)
No Control	0.3446	0.8965	1.966
Feedback Gain of 1.0	0.2478 (28.1)	0.5898 (34.2)	1.345 (31.6)
Feedback Gain of 1.3	0.1956 (43.2)	0.4756 (47.0)	1.072 (45.5)
Feedback Gain of 1.5	0.1460 (57.6)	0.3930 (56.2)	0.9564 (51.4)
Feedback Gain of 1.8	0.1260 (63.4)	0.3220 (64.1)	0.8293 (57.8)

3.5.7.1.2 Series 2: Initial Displacement Loading With Accelerometer

A total of three tests were conducted for each of the gain levels, 1.0, 1.3, 1.5, and 1.8, as well as the non-controlled specimen. Figures 3-13 through 3-16 show the comparison of the piezoelectric sensor voltage for varying feedback gains relative to the proceeding state, for each set of these tests.

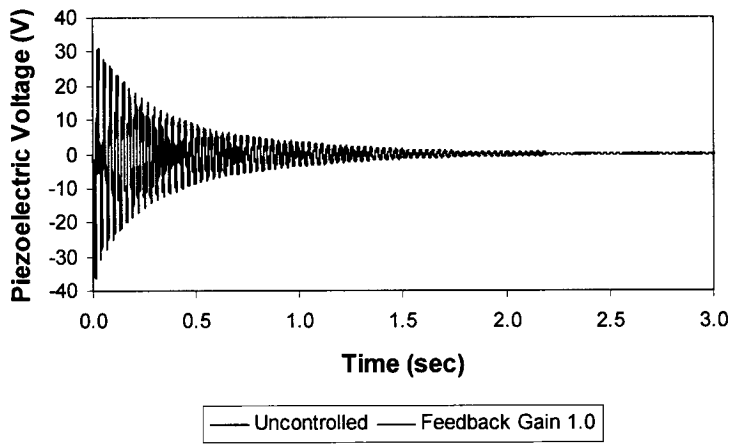

Figure 3-13: Piezoelectric Response for Non-controlled Test vs. Feedback Gain of 1.0 for Series 2 Tests

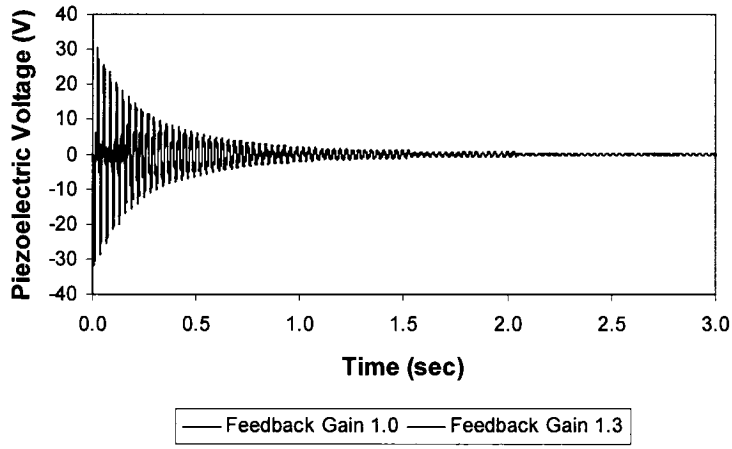

Figure 3-14: Piezoelectric Response for Feedback Gain of 1.0 vs. Feedback Gain of 1.3 for Series 2 Tests

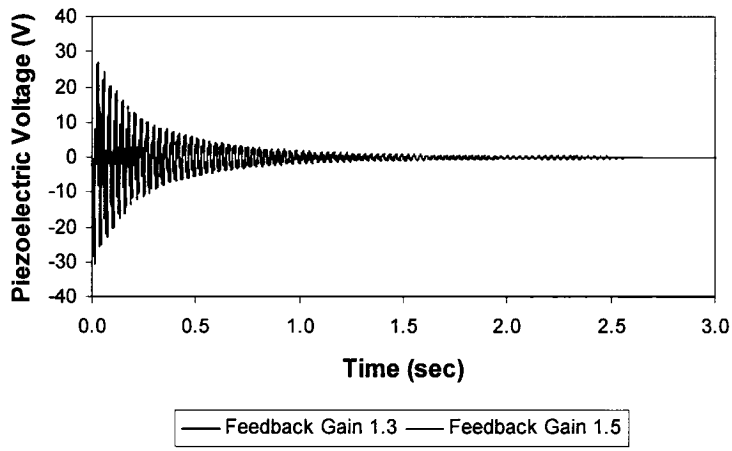

Figure 3-15: Piezoelectric Response for Feedback Gain of 1.3 vs. Feedback Gain of 1.5 for Series 2 Tests

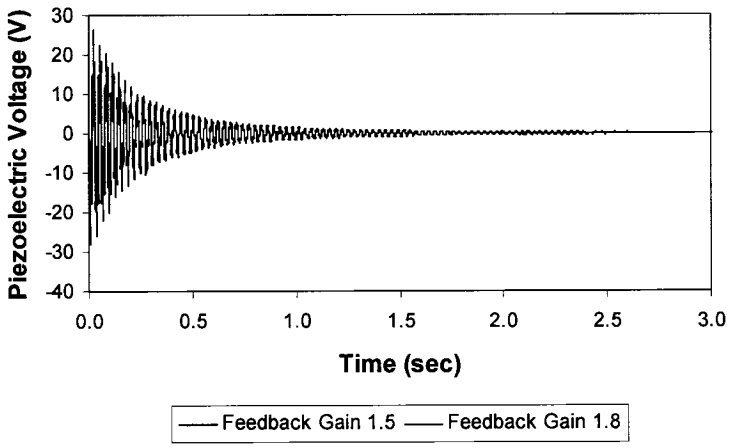

Figure 3-16: Piezoelectric Response for Feedback Gain of 1.5 vs. Feedback Gain of 1.8 for Series 2 Tests

To give a better indication of the actual percent reduction in the vibration amplitude, the average time required and percent reduction to reach the 50, 25, and 10 percent amplitude levels for each of the different gain levels for the series 2 tests are shown in Table 3-4.

Table 3-4: Average Time Required and Percent Reduction to Reach 50%, 25%, and 10% of Non-controlled Piezoelectric Sensor Response for Varying Feedback Gains for Series 2 Tests

Test Set-up	Time to reach 50% amplitude (sec) (% Reduction from Non-controlled)	Time to reach 25% amplitude (sec) (% Reduction from Non-controlled)	Time to reach 10% amplitude (sec) (% Reduction from Non-controlled)
No Control	0.2078	0.5053	1.026
Feedback Gain of 1.0	0.1477 (29.0)	0.3599 (28.8)	0.7316 (28.8)
Feedback Gain of 1.3	0.1170 (43.7)	0.2970 (41.2)	0.6450 (37.2)
Feedback Gain of 1.5	0.0888 (57.3)	0.2230 (55.9)	0.5360 (47.8)
Feedback Gain of 1.8	0.0690 (66.8)	0.1890 (62.6)	0.4760 (53.6)

One very noticeable difference seen in the series 1 and series 2 tests is the time difference to decay to the different levels. This is due somewhat to the added mass of the accelerometer, however the major influence is the coaxial cable used to connect the accelerometer, which is quite stiff. These two factors are the reason for the relatively large decrease in the decay times for the specimen with the accelerometers attached.

Figures 3-17 through 3-20 show the comparison of the accelerometer voltage response for the varying feedback gains relative to their proceeding state.

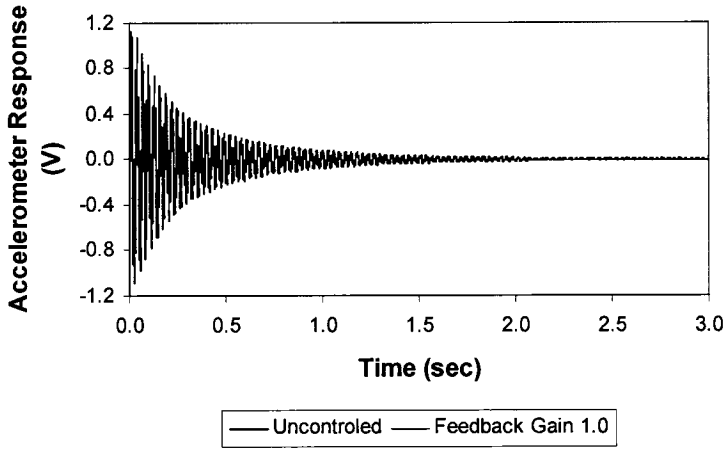

Figure 3-17: Accelerometer Response for Non-controlled Specimen vs. Feedback Gain of 1.0 for Series 2 Tests

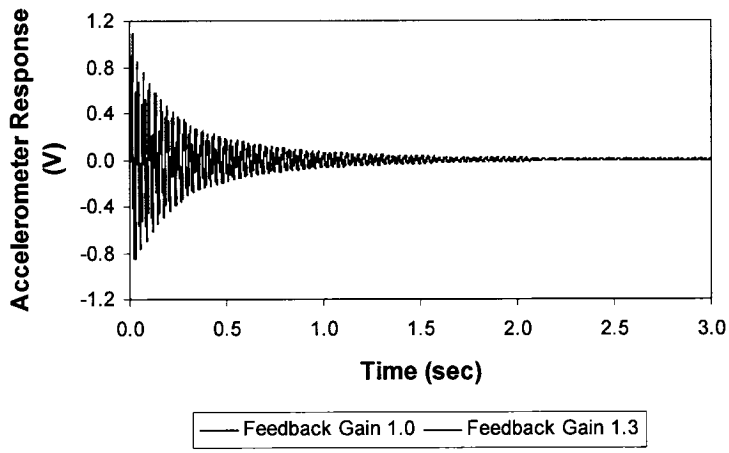

Figure 3-18: Accelerometer Response for Feedback Gain of 1.0 vs. Feedback Gain of 1.3 for Series 2 Tests

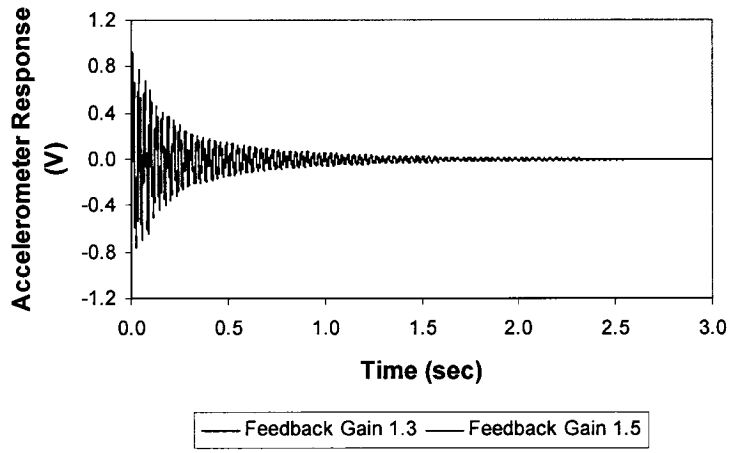

Figure 3-19: Accelerometer Response for Feedback Gain of 1.3 vs. Feedback Gain of 1.5 for Series 2 Tests

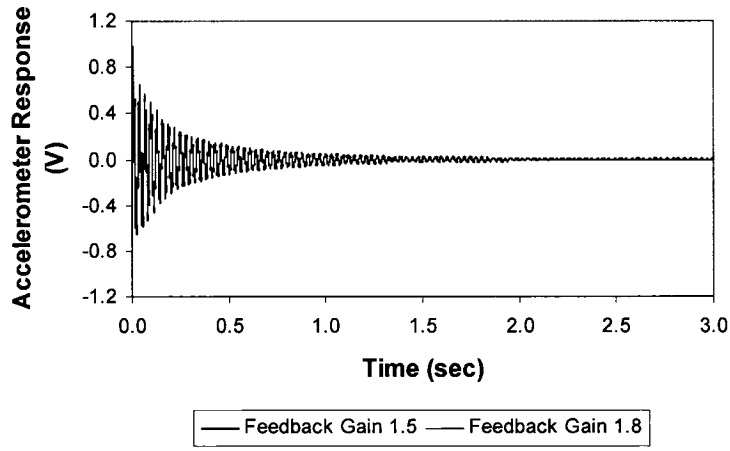

Figure 3-20: Accelerometer Response for Feedback Gain of 1.5 vs. Feedback Gain of 1.8 for Series 2 Tests

The average time required and percent reduction in the vibration amplitude for the accelerometer sensor to reach the 50, 25, and 10 percent amplitude levels for each of the different gain levels for the series 2 tests is shown in Table 3-5.

Table 3-5: Average Time Required and Percent Reduction to Reach 50%, 25%, and 10% of Non-controlled Accelerometer Response for Varying Feedback Gains for Series 2 Tests

Test Set-up	Time to reach 50% amplitude (sec) (% Reduction from Non-controlled)	Time to reach 25% amplitude (sec) (% Reduction from Non-controlled)	Time to reach 10% amplitude (sec) (% Reduction from Non-controlled)
No Control	0.1889	0.4018	0.7913
Feedback Gain of 1.0	0.1484 (21.4)	0.3277 (18.4)	0.7344 (7.2)
Feedback Gain of 1.3	0.1305 (30.9)	0.2948 (26.6)	0.7011 (11.4)
Feedback Gain of 1.5	0.1128 (40.3)	0.2506 (37.6)	0.6241 (21.1)
Feedback Gain of 1.8	0.0833 (55.9)	0.2030 (49.5)	0.4901 (38.1)

3.5.7.1.3 Series 3: Impulse Loading Results

In this investigation tests were conducted only with the use of the accelerometer attached near the free end of the plate. For this series of tests the three different feedback gain values used were 1.0, 1.5, and 1.8.

As can be seen from Figure 3-21 the accelerometer recorded erratic results due to its proximity to the location of the impulse load. Therefore, the accelerometer results were not used for comparison purposes.

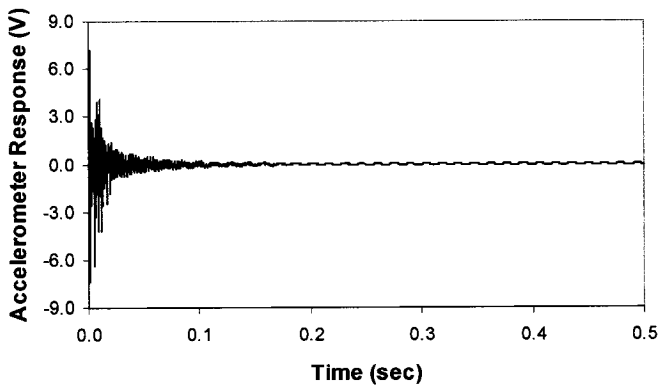

Figure 3-21: Accelerometer Response Under Impact Loading

Figure 3-22 shows a typical response of the impulse hammer for impact loading of the FRP plates, recorded through an instrumented hammer.

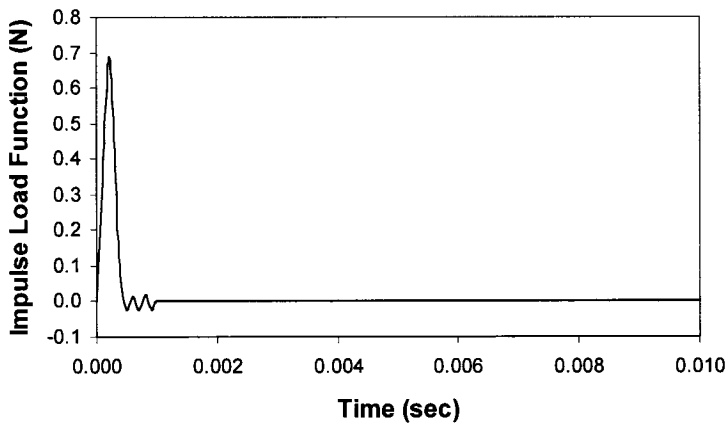

Figure 3-22: Typical Impulse Hammer Loading Function

Figures 3-23 through 3-25 show the comparison of the piezoelectric sensor voltage response for the varying feedback gains relative to their proceeding state for series 3 tests.

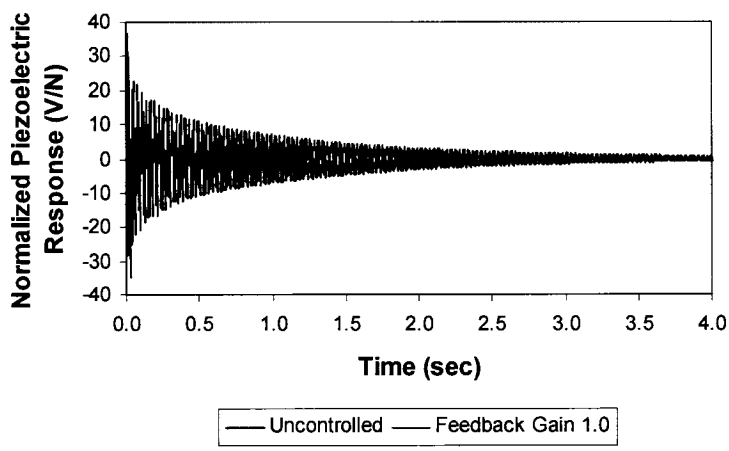

Figure 3-23: Piezoelectric Response for Non-controlled Specimen vs. Feedback Gain of 1.0 for Series 3 Tests

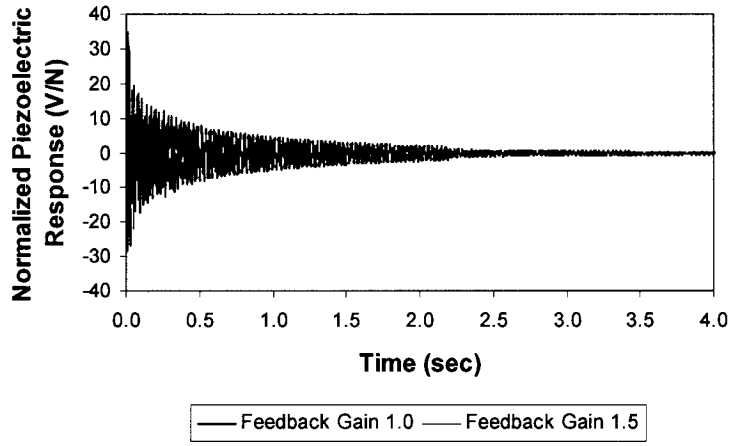

Figure 3-24: Piezoelectric Response for Feedback Gain of 1.0 vs. Feedback Gain of 1.5 for Series 3 Tests

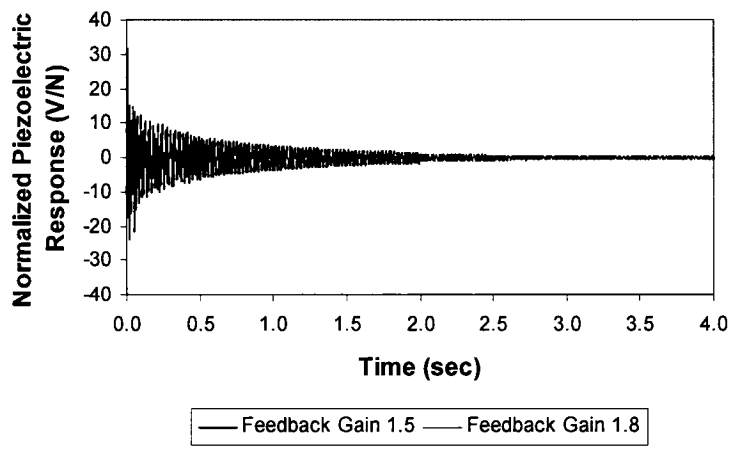

Figure 3-25: Piezoelectric Response for Feedback Gain of 1.5 vs. Feedback Gain of 1.8 for Series 3 Tests

The average time required and percent reduction to reach the 50, 25, and 10 percent amplitude levels for each of the different gain levels for the series 3 tests is shown in Table 3-6.

Table 3-6: Average Time Required and Percent Reduction to Reach 50%, 25%, and 10% of Non-controlled Piezoelectric Sensor Response for Varying Feedback Gains for Series 3 Tests

Test Set-up	Time to reach 50% amplitude (sec) (% Reduction from Non-controlled)	Time to reach 25% amplitude (sec) (% Reduction from Non-controlled)	Time to reach 10% amplitude (sec) (% Reduction from Non-controlled)
No Control	0.1209	0.6725	1.777
Feedback Gain of 1.0	0.0818 (32.4)	0.4558 (32.2)	1.362 (23.4)
Feedback Gain of 1.5	0.0554 (54.2)	0.3254 (51.6)	1.082 (39.1)
Feedback Gain of 1.8	0.0450 (62.8)	0.2620 (61.0)	0.7282 (59.0)

3.5.7.2 Vibration Suppression Results Implementing an Embedded Piezoelectric Patch

In this experimental investigation the same tests were carried out as for the surface bonded piezoelectric patch. The initial displacement loading was tested with feedback gains of 1.0, 1.3, 1.5, and 1.8. For the impact loading tests, feedback gains of 1.0, 1.5, and 1.8 were investigated. The initial displacement tests were performed with and without the use of an additional accelerometer, whereas the impact tests were only conducted with the use of the accelerometer.

3.5.7.2.1 Series 4: Initial Displacement Loading With No Accelerometer Attached

Figures 3-26 through 3-29 show the comparison of the varying feedback gains relative to the proceeding state, as was described previously.

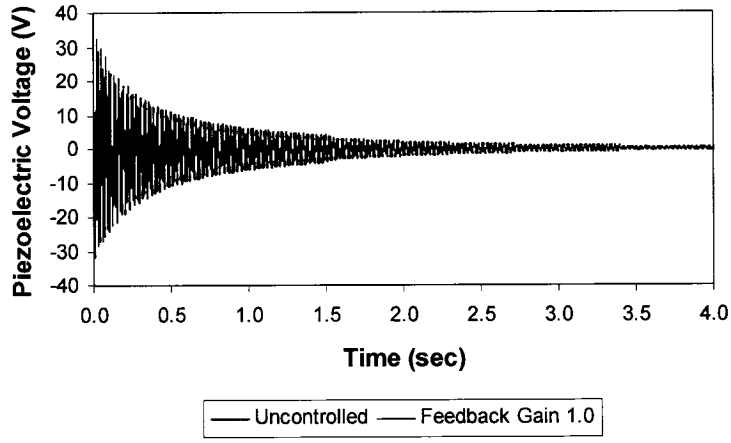

Figure 3-26: Piezoelectric Response for Non-controlled Specimen vs. Feedback Gain of 1.0 for Series 4 Tests

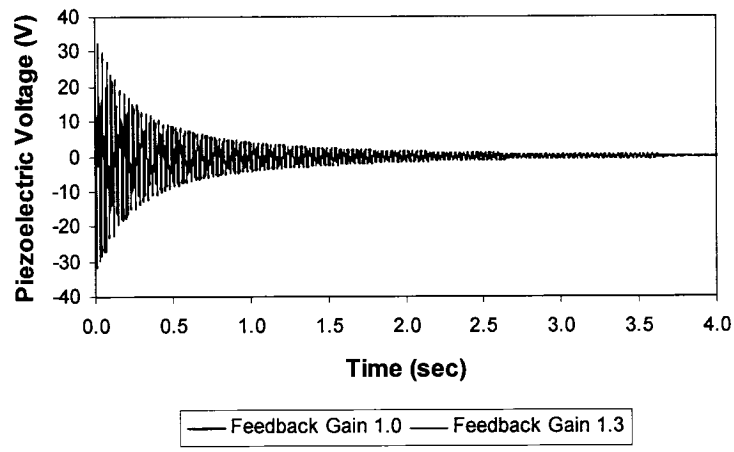

Figure 3-27: Piezoelectric Response for Feedback Gain of 1.0 vs. Feedback Gain of 1.3 for Series 4 Tests

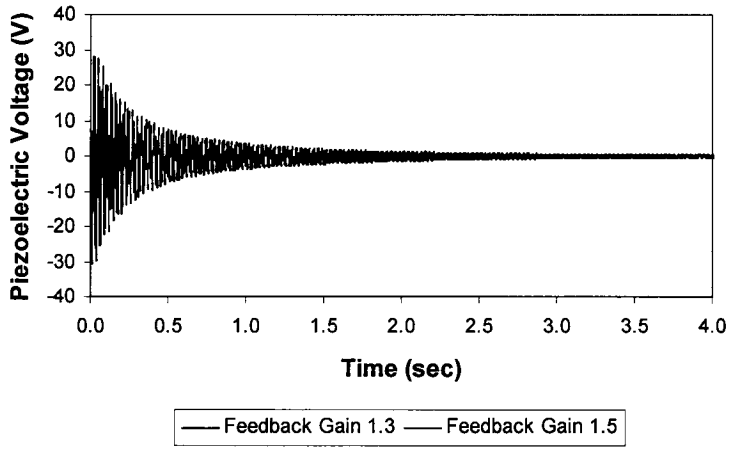

Figure 3-28: Piezoelectric Response for Feedback Gain of 1.3 vs. Feedback Gain of 1.5 for Series 4 Tests

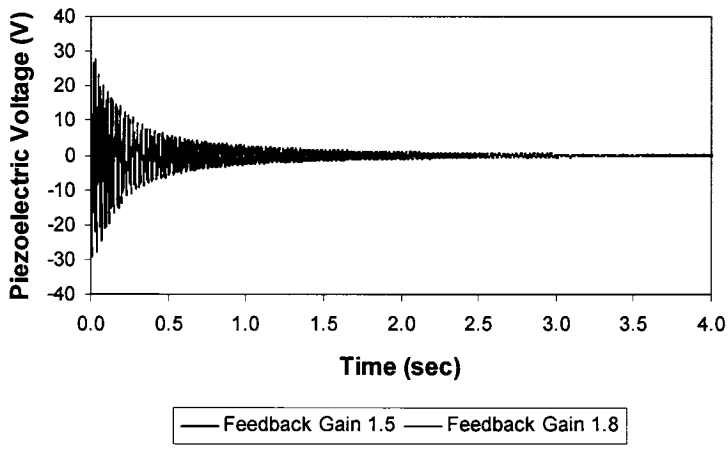

Figure 3-29: Piezoelectric Response for Feedback Gain of 1.5 vs. Feedback Gain of 1.8 for Series 4 Tests

To provide a better indication of the actual percent reduction in the vibration amplitude for the piezoelectric sensor, the average time required and percent reduction to reach the 50, 25, and 10 percent amplitude levels for each of the different gain levels for the series 4 tests are shown in Table 3-7.

Table 3-7: Average Time Required and Percent Reduction to Reach 50%, 25%, and 10% of Non-controlled Piezoelectric Sensor Response for Varying Feedback Gains for Series 4 Tests

Test Set-up	Time to reach 50% amplitude (sec) (% Reduction from Non-controlled)	Time to reach 25% amplitude (sec) (% Reduction from Non-controlled)	Time to reach 10% amplitude (sec) (% Reduction from Non-controlled)
No Control	0.2945	0.7830	1.523
Feedback Gain of 1.0	0.2407 (18.3)	0.6078 (22.4)	1.190 (21.9)
Feedback Gain of 1.3	0.2080 (29.4)	0.5378 (31.3)	1.078 (29.2)
Feedback Gain of 1.5	0.1810 (38.5)	0.4900 (37.4)	1.004 (34.1)
Feedback Gain of 1.8	0.1740 (40.9)	0.4440 (43.3)	0.9290 (39.0)

3.5.7.2.2 Series 5: Initial Displacement Loading With Accelerometer Attached

Figures 3-30 through 3-33 show the comparison of the piezoelectric sensor voltage response for the varying feedback gains relative to their proceeding state for series 5 tests.

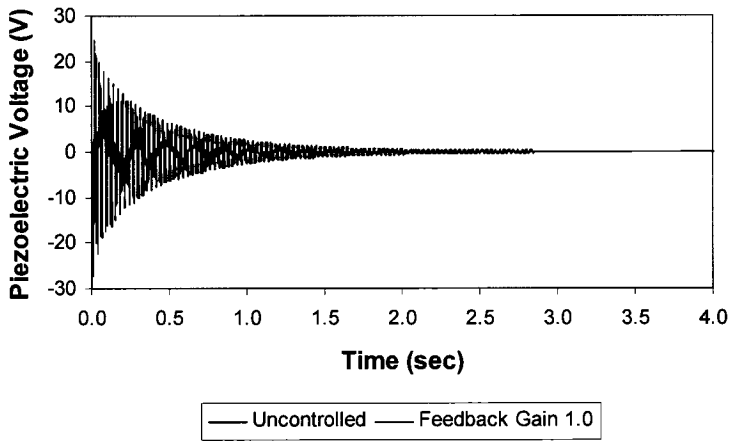

Figure 3-30: Piezoelectric Response for Non-controlled Specimen vs. Feedback Gain of 1.0 for Series 5 Tests

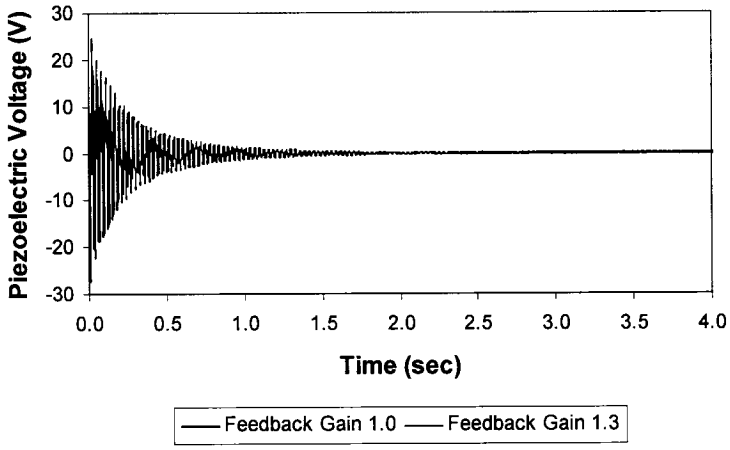

Figure 3-31: Piezoelectric Response for Feedback Gain of 1.0 vs. Feedback Gain of 1.3 for Series 5 Tests

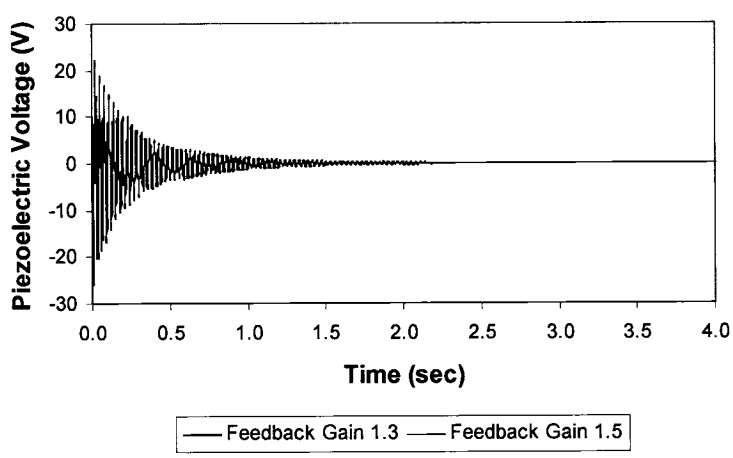

Figure 3-32: Piezoelectric Response for Feedback Gain of 1.3 vs. Feedback Gain of 1.5 for Series 5 Tests

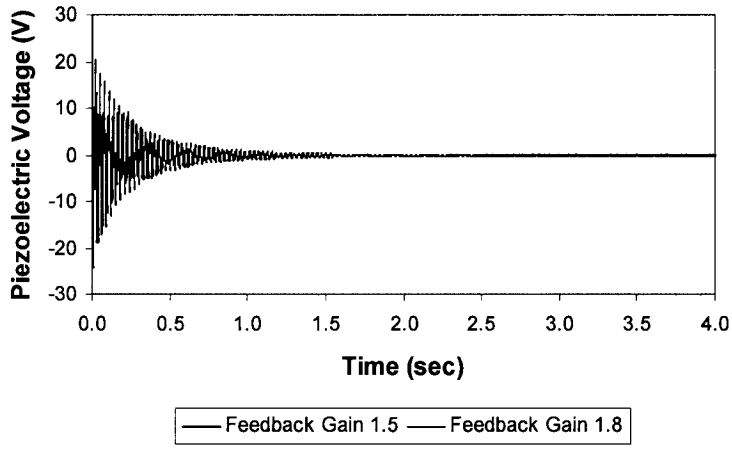

Figure 3-33: Piezoelectric Response for Feedback Gain of 1.5 vs. Feedback Gain of 1.8 for Series 5 Tests

The actual percent reduction in the vibration amplitude for the piezoelectric sensor, the average time required and percent reduction to reach the 50, 25, and 10 percent amplitude levels for each of the different gain levels for the series 5 tests are shown in Table 3-8.

Table 3-8: Average Time Required and Percent Reduction to Reach 50%, 25%, and 10% of Non-controlled Piezoelectric Sensor Response for Varying Feedback Gains for Series 5 Tests

Test Set-up	Time to reach 50% amplitude (sec) (% Reduction from Non-controlled)	Time to reach 25% amplitude (sec) (% Reduction from Non-controlled)	Time to reach 10% amplitude (sec) (% Reduction from Non-controlled)
No Control	0.2057	0.4935	1.007
Feedback Gain of 1.0	0.1679 (18.4)	0.3990 (19.1)	0.8080 (19.7)
Feedback Gain of 1.3	0.1410 (31.4)	0.3560 (27.9)	0.7560 (24.9)
Feedback Gain of 1.5	0.1300 (36.8)	0.3140 (36.4)	0.6822 (32.2)
Feedback Gain of 1.8	0.1140 (44.6)	0.2870 (41.8)	0.6520 (35.2)

Figures 3-34 through 3-37 show the comparison of the accelerometer voltage response for the varying feedback gains relative to their proceeding state for series 5 tests.

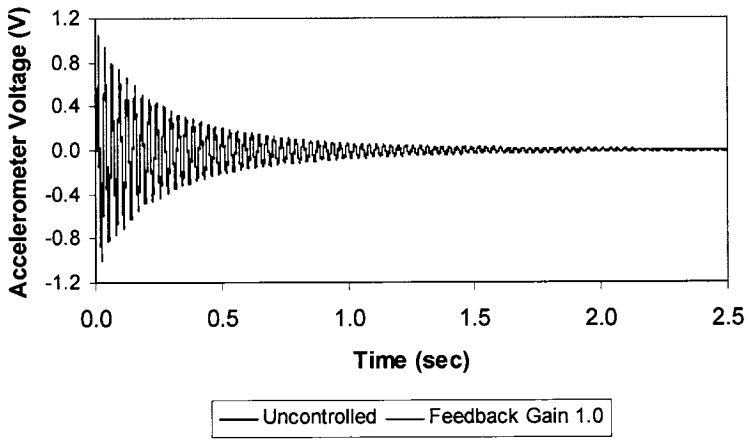

Figure 3-34: Accelerometer Response for Non-controlled Specimen vs. Feedback Gain of 1.0 for Series 5 Tests

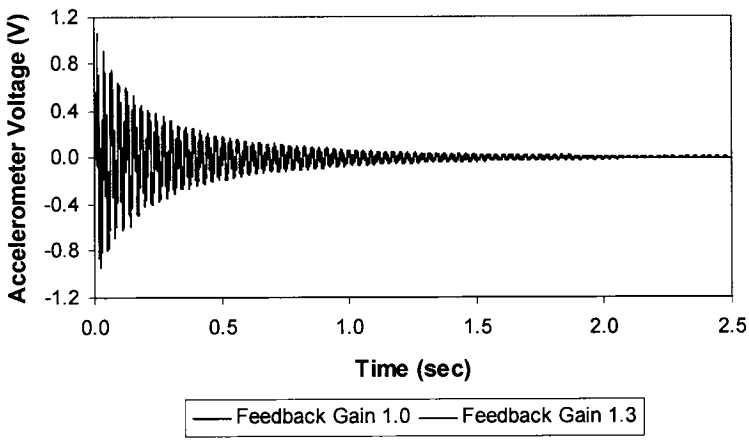

Figure 3-35: Accelerometer Response for Feedback Gain of 1.0 vs. Feedback Gain of 1.3 for Series 5 Tests

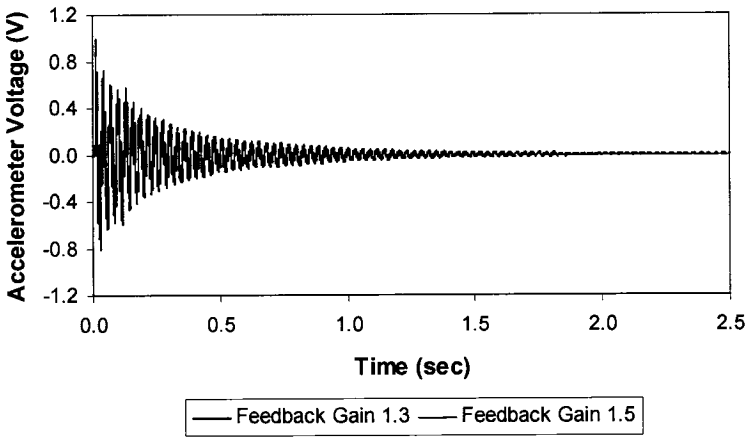

Figure 3-36: Accelerometer Response for Feedback Gain of 1.3 vs. Feedback Gain of 1.5 for Series 5 Tests

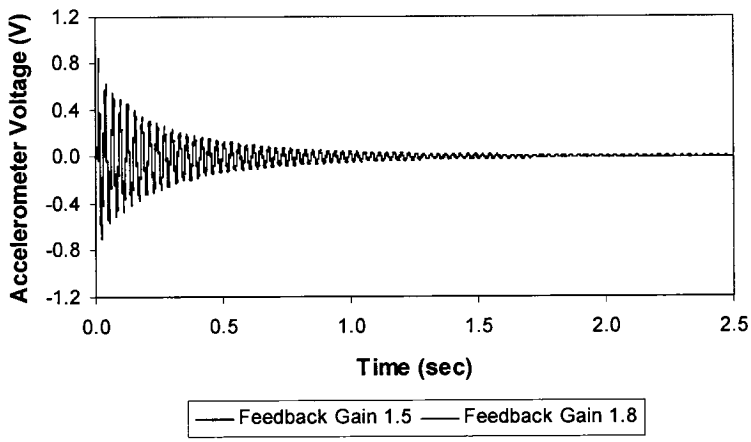

Figure 3-37: Accelerometer Response for Feedback Gain of 1.5 vs. Feedback Gain of 1.8 for Series 5 Tests

The average time required and percent reduction to reach the 50, 25, and 10 percent amplitude levels of the non-controlled specimens for each of the different gain levels for the series 5 tests are shown in Table 3-9.

Table 3-9: Average Time Required and Percent Reduction to Reach 50%, 25%, and 10% of Non-controlled Accelerometer Response for Varying Feedback Gains for Series 5 Tests

Test Set-up	Time to reach 50% amplitude (sec) (% Reduction from Non-controlled)	Time to reach 25% amplitude (sec) (% Reduction from Non-controlled)	Time to reach 10% amplitude (sec) (% Reduction from Non-controlled)
No Control	0.1714	0.4180	0.8102
Feedback Gain of 1.0	0.1465 (14.5)	0.3649 (12.7)	0.7717 (4.8)
Feedback Gain of 1.3	0.1356 (20.9)	0.3457 (17.3)	0.7488 (7.6)
Feedback Gain of 1.5	0.1272 (25.8)	0.3181 (23.9)	0.6943 (14.3)
Feedback Gain of 1.8	0.1124 (34.4)	0.2890 (30.9)	0.6098 (24.7)

3.5.7.2.3 Series 6: Impact Loading Results

Figures 3-38 through 3-40 show the comparison of the piezoelectric sensor voltage response for the varying feedback gains relative to their proceeding state for series 6 tests.

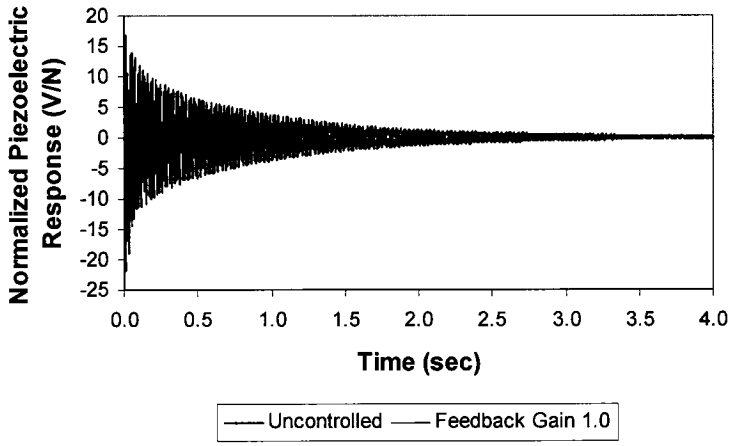

Figure 3-38: Piezoelectric Response for Non-controlled Specimen vs. Feedback Gain of 1.0 for Series 6 Tests

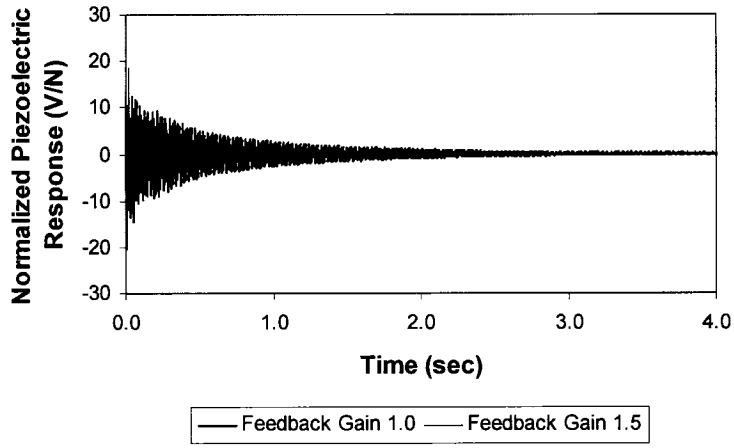

Figure 3-39: Piezoelectric Response for Feedback Gain of 1.0 vs. Feedback Gain of 1.5 for Series 6 Tests

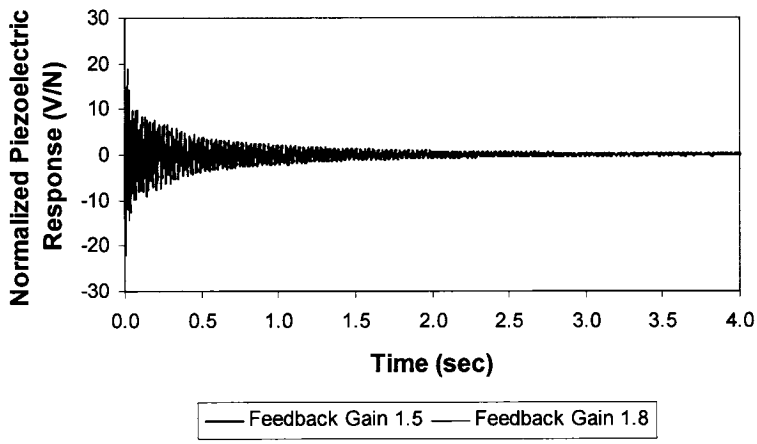

Figure 3-40: Piezoelectric Response for Feedback Gain of 1.5 vs. Feedback Gain of 1.8 for Series 6 Tests

The actual percent reduction in the vibration amplitude for the piezoelectric sensor, the average time required and percent reduction to reach the 50, 25, and 10 percent amplitude levels for each of the different gain levels for the series 6 tests are shown in Table 3-10.

Table 3-10: Average Time Required and Percent Reduction to Reach 50%, 25%, and 10% of Non-controlled Piezoelectric Sensor Response for Varying Feedback Gains for Series 6 Tests

Test Set-up	Time to reach 50% amplitude (sec) (% Reduction from Non-controlled)	Time to reach 25% amplitude (sec) (% Reduction from Non-controlled)	Time to reach 10% amplitude (sec) (% Reduction from Non-controlled)
No Control	0.1330	0.6525	1.509
Feedback Gain of 1.0	0.1038 (22.0)	0.5130 (21.4)	1.270 (15.8)
Feedback Gain of 1.5	0.0852 (35.9)	0.4362 (33.1)	1.109 (26.5)
Feedback Gain of 1.8	0.0770 (42.1)	0.3820 (41.5)	0.9200 (39.0)

3.5.7.3 Comparison of Surface Bonded vs. Embedded Piezoelectric Patch

Due to the linear behavior of both FRP and piezoelectric materials the vibration suppression achieved by an embedded actuator relative to a surface bonded actuator should be only a function of the embedding depth. In this investigation the embedded actuator was located at a depth of 1/3 the distance from the top surface of the plate. Therefore, the suppression achieved by the embedded sensor should be approximately 2/3 of that achieved by the surface bonded patch. The relative results for the percent reduction in the suppression achieved by the embedded piezoelectric patch relative to the surface bonded piezoelectric patch are shown in Tables 3-11 through 3-14.

Table 3-11: Percent Vibration Suppression in Piezoelectric Sensor for Series 4 Tests Relative to Series 1 Tests

Test Set-up	Embedded Suppression Relative to Surface Bonded Suppression (%)		
	Reduction to 50 %	Reduction to 25 %	Reduction to 10 %
Feedback Gain 1.0	65.0	65.4	69.3
Feedback Gain 1.3	67.9	66.7	64.2
Feedback Gain 1.5	66.9	66.6	66.4
Feedback Gain 1.8	64.5	67.6	67.5

Table 3-12: Percent Vibration Suppression in Piezoelectric Sensor for Series 5 Tests Relative to Series 2 Tests

	Percent Reduction to 50 %	Percent Reduction to 25 %	Percent Reduction to 10 %
Feedback Gain 1.0	63.4	66.5	68.6
Feedback Gain 1.3	71.9	67.6	67.0
Feedback Gain 1.5	64.2	65.1	67.4
Feedback Gain 1.8	66.7	66.8	65.7

Table 3-13: Percent Vibration Suppression in Accelerometer Sensor for Series 5 Tests Relative to Series 2 Tests

	Percent Reduction to 50 %	Percent Reduction to 25 %	Percent Reduction to 10 %
Feedback Gain 1.0	67.8	68.9	66.1
Feedback Gain 1.3	67.6	65.0	66.5
Feedback Gain 1.5	64.0	63.5	67.7
Feedback Gain 1.8	61.6	62.4	65.0

Table 3-14: Percent Vibration Suppression in Piezoelectric Sensor for Series 6 Tests Relative to Series 3 Tests

	Percent Reduction to 50 %	Percent Reduction to 25 %	Percent Reduction to 10 %
Feedback Gain 1.0	67.8	66.3	67.7
Feedback Gain 1.5	66.3	64.2	67.7
Feedback Gain 1.8	67.0	67.9	66.1

As the above results show, very good correlation between the suppression achieved by an embedded piezoelectric actuator and a surface bonded actuator based on the embedding depth was observed.

3.6 Vibration Suppression in PVC Pipe

This experimental investigation was conducted to determine the capabilities of the small PZT QuickPack actuators for vibration suppression in cylindrical shells. This was performed for different feedback gains applied to the sensor response.

3.6.1 Test Specimens

The PVC pipe that was chosen to perform this experimental investigation was a 6" APEX PVC sewer pipe, with the section properties as given in Table 3-15. The size of the pipe was selected such that the piezoelectric patches would not have to be significantly curved to contour to the surface.

Table 3-15: PVC Pipe Vibration Suppression Section Dimensions

Dimension	Size
Outside Diameter	159.1 mm
Inside Diameter	150.0 mm
Wall Thickness	4.55 mm

There were five piezoelectric patches bonded to the surface of the pipe with the use of West System's two-part epoxy system. The procedure used to surface bond the patches to the pipe surface was the same as that for the FRP plate. The patch locations and pipe dimensions are as shown in Figure 3-41, where sensor 1 is located nearest the fixed end through sensor 5 nearest the free end.

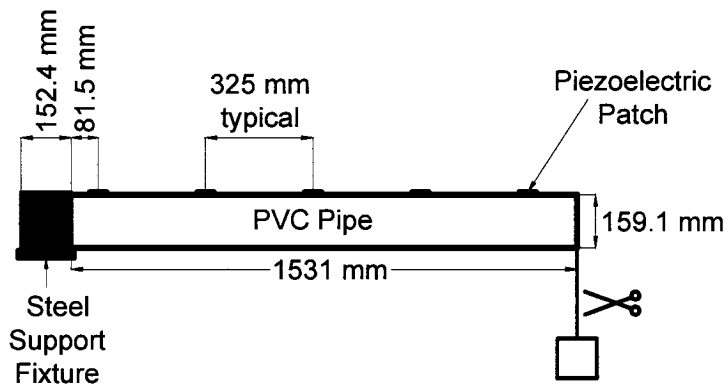

Figure 3-41: PVC Pipe Vibration Suppression Test Specimen

3.6.2 Testing Apparatus and Equipment

To investigate the vibration suppression capabilities of the PVC pipe, a cantilever beam set-up was used. In order to conduct the test as a cantilever beam, a steel pipe/plate

system was added to one end for added strength and stability in clamping, as shown above in Figure 3-41. This end was then pressed under 2.23 kN force using a 1957 kN capacity Tinus-Olsen Universal Testing machine.

The responses of the piezoelectric patches were simultaneously monitored with a differential channel set-up using a multi-purpose DT3010 data acquisition card manufactured by Data Translation (Marlboro, MA). This PCI board contains 32 single-ended/16 differential analog inputs along with 2 analog outputs, all at 12-bit resolution. The actuation signals were output from the computer using the DT331 analog output board, a 4 channel, 12-bit resolution analog output board with a throughput of 10 Ks/sec. Both board have a maximum operating range of ±10 volts.

It was found that visual based programs, such as LabVIEW and DT VEE Pro, were unable to perform the full control experiments due to the number of channels used. For this reason a C++ program was developed in-house to monitor and feedback the responses of the piezoelectric patches with a frequency of 1500 Hz. The program was developed to have inputs for the number of points to acquire from each channel as well as the feedback gain applied to each channel. The output of the program was a text file that contained all the sensor response values as well as the duration of the test.

With the addition of more actuators to the system, a three-channel power amplifier was assembled in-house, to be used in conjunction with the previously mentioned power amplifier. The reason for excluding one of the patches from the vibration suppression process will be described in the results section. The three-channel amplifier set-up is shown in Figure 3-42.

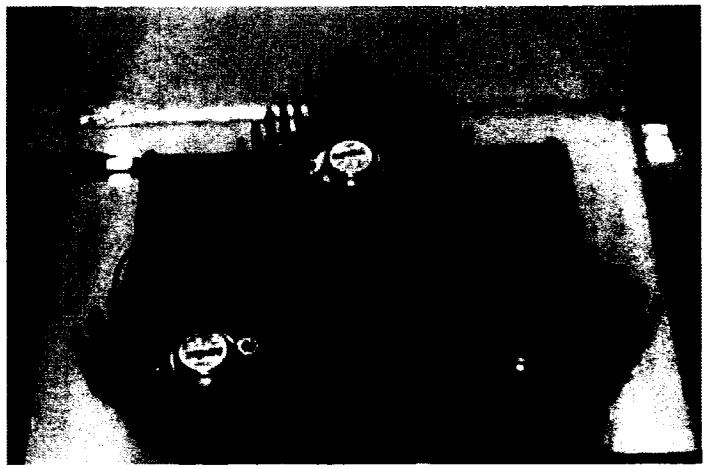

(a)

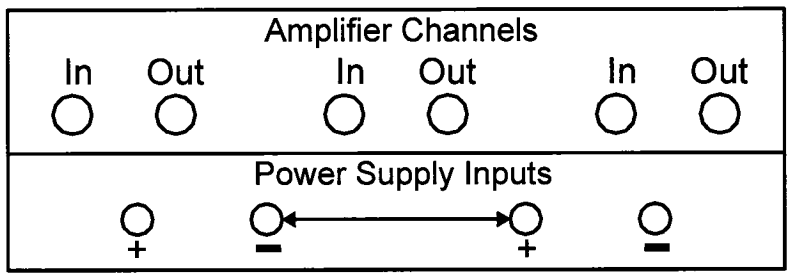

(b)

Figure 3-42: Front Panel Set-up for Three Channel Power Amplifier (a) Circuitry of Amplifier (b) Front Panel Connections

The three-channel power amplifier was assembled using three PA88 high voltage power amplifiers purchased from APEX Microtechnology (Tucson, AZ). With the use of appropriate capacitors and resistors, the gain of the amplifiers was determined. For our application the gains were set to 20 following the procedure outlined by the APEX. In order to produce a voltage output of ±V a dual supply would be required. Without the access to a dual supply, two single supplies were used by connecting the ground (-'ve) of one supply to the high (+'ve) of the other. With each of the two power supplies set to supply a voltage of V_s, the amplifiers could output a voltage range of $\pm(V_s\text{-}10)$ volts.

As previously mentioned, the sensor signals were reduced to 6.5% of their actual value using a resistor T-circuit, which protects the data acquisition board from overload damage.

3.6.3 Experimental Procedure

In order to conduct the experiments a known mass was hung, with the use of a strap, from the free end of the cantilevered pipe. The data acquisition program was started and then the strap holding the weight was cut, thus initiating a free vibration of the pipe. The signals from the PZT patches were monitored using single point value acquisition for all tests, to ensure consistent data acquisition between non-controlled and controlled tests. For control applications the value of the self-sensing elements were multiplied by a gain and sent to the piezoelectric patch, through the power amplifiers, as an actuation voltage.

3.6.4 Control Method

In order to actuate the piezoelectric patches the sensor voltage was fedback to the patches after the application of the appropriate gain. The control program was developed such that all sensor values were read; then, the actuation voltage was output. This method was found to be more efficient than reading one sensor at a time and actuating it. Due to the limitations of the computer systems and software a displacement based feedback control was used. This method involved applying a constant gain to the sensor voltage throughout the entire experiment.

3.6.5 Data Processing

The operations required to process the data included the correction any offset, removal of zero-state data, determination of the time for each point, verify the results, and writes the test period results to a file for further processing. These operations where performed by the MATLAB program pipevib.m, given in Appendix B.

The initial step in the data processing was to correct for any offset that was present. It was found that the last point in the data set was the value of the offset. Therefore this value was stored and subtracted from every point in the data set.

The removal of the zero state data included removing all the non-response data at the start and end of the test. The start of the test was determined by finding the position where the piezoelectric sensor response surpassed a set value, in these cases 0.08 volts. The test was then deemed to start 1 point before this value was surpassed, which was found by visually inspecting the results. The end of the test was determined by visually inspecting the free vibration of the pipe. It was found that the vibration amplitude of the pipe was fully decayed in less than four seconds, so four seconds was taken as the test completion time.

The point times were determined with the assumption that the data acquisition rate was consistent over the entire test period. With this assumption, the time between samples was determined by dividing the total test time by the number of samples acquired.

Due to unavailability of visual inspection capabilities in the data acquisition system for these tests, a checking procedure was required to verify that the full test was captured. This was achieved by plotting the time history of the results.

To make further data processing more efficient the reduced time history and the Fourier spectrum data were written to new text files.

3.6.6 PVC Pipe Vibration Suppression Results

In determining the efficiency of the control system for suppressing the vibration in the PVC pipe several different feedback gains were implemented. The maximum sensor voltage for the given loading determined the feedback gains, which were chosen as 10, 15, 20, 25, and 30. For the higher gains (20, 25, 30) the maximum capacity of the sensor

would be surpassed, however due to the very quick decay of the sensor signal the limit would only be surpassed for a maximum of five feedback values and only in sensor 1 for feedback gains of 20 and 25 and sensor 1 and 2 for a gain of 30. It was found that these limited overages caused by the higher gains did not damage the piezoelectric patches, so they were implemented.

For these experiments, two tests were conducted for each of the feedback gain levels. Along with these tests there were four tests conducted on the specimen without feedback gains. From visual inspection, the tests were compared visually to guarantee consistency. It was found that the results showed excellent consistency for both controlled and non-controlled experiments.

From the results, it was found that the sensor located in the proximity of the free end, sensor 5, produced erratic results as shown in Figure 3-43. Therefore, the results for this sensor were not used for comparison purposes in determining the effectiveness of suppression process.

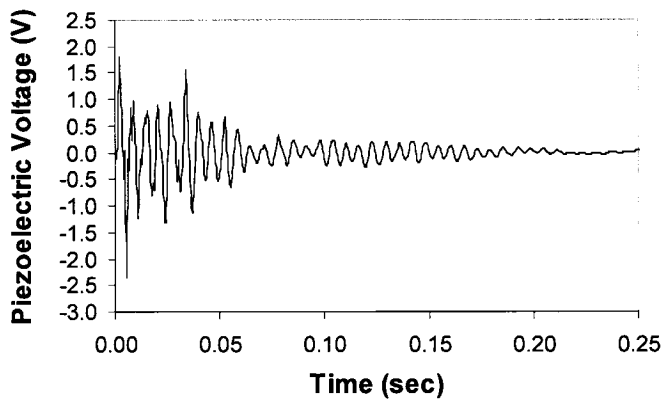

Figure 3-43: Typical Sensor 5 Response for Vibration Suppression of PVC Pipe

To determine the effectiveness of the controlled tests, the same comparison procedure as that used for the FRP plate was implemented, such that the time required to reach 50, 25, and 10 percent signal strength of the non-controlled specimens were determined.

Figures 3-44 through 3-48 show a visual comparison of the suppression achieved by the varying feedback gains relative to the proceeding state for sensor 1. From these figures it can be seen that some suppression in the vibration amplitude over the entire response history can be achieved it is however relatively small.

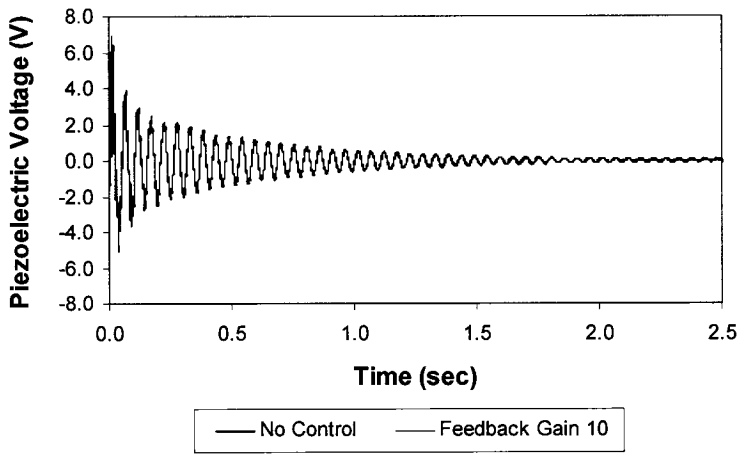

Figure 3-44: Piezoelectric Response of Sensor 1 for Non-controlled Specimen vs. Feedback Gain of 10 for PVC Pipe Suppression Tests

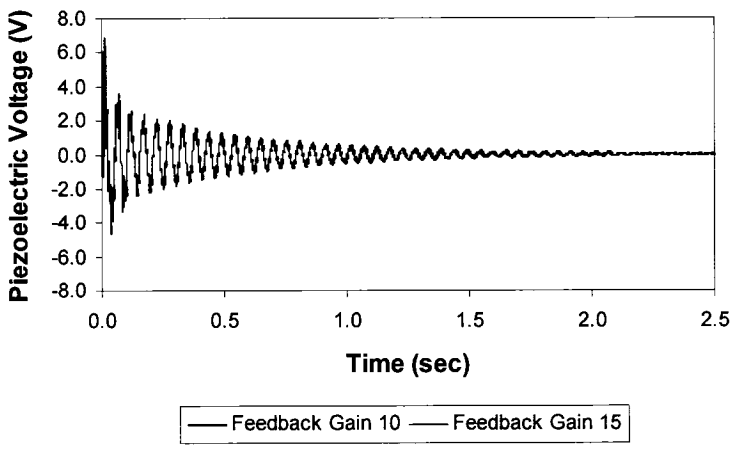

Figure 3-45: Piezoelectric Response of Sensor 1 for Feedback Gain of 10 vs. Feedback Gain of 15 for PVC Pipe Suppression Tests

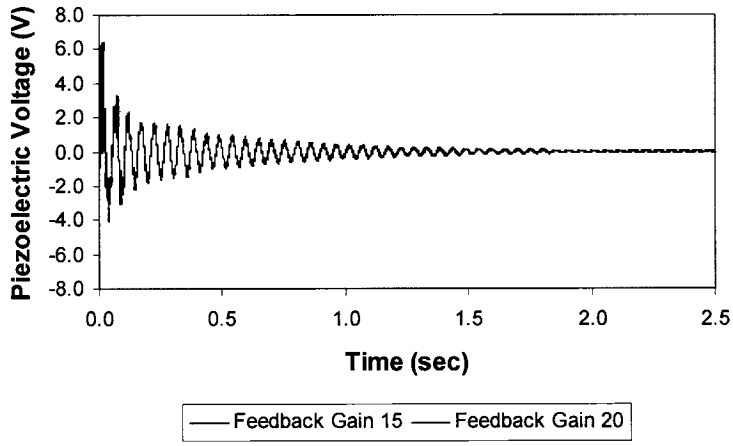

Figure 3-46: Piezoelectric Response of Sensor 1 for Feedback Gain of 15 vs. Feedback Gain of 20 for PVC Pipe Suppression Tests

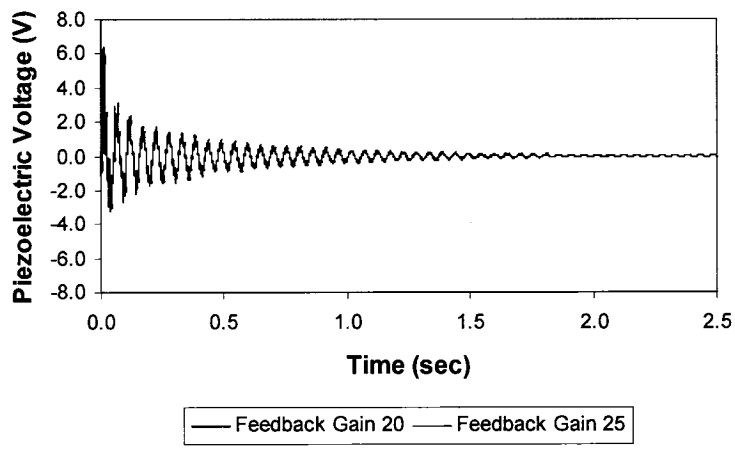

Figure 3-47: Piezoelectric Response of Sensor 1 for Feedback Gain of 20 vs. Feedback Gain of 25 for PVC Pipe Suppression Tests

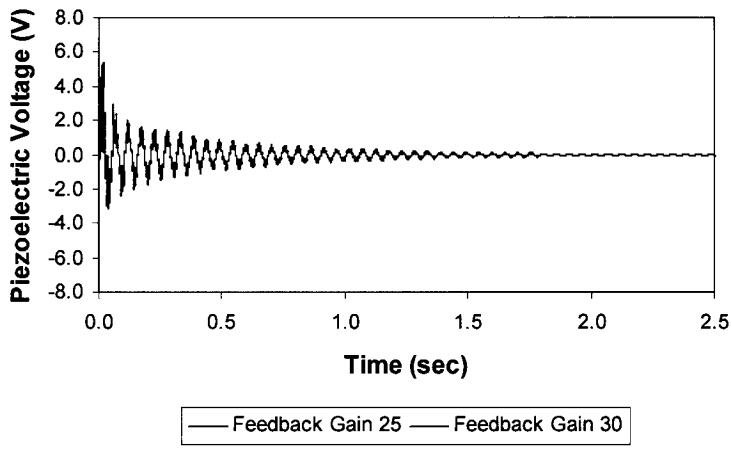

Figure 3-48: Piezoelectric Response of Sensor 1 for Feedback Gain of 25 vs. Feedback Gain of 30 for PVC Pipe Suppression Tests

The time required and percent reduction for the controlled responses to reach 50, 25, and 10 percent of the non-controlled specimens for all four sensors are shown in Table 3-16 through 3-18 respectively.

Table 3-16: Average Time Required and Percent Reduction to Reach 50% of the Non-controlled Piezoelectric Sensor Response for the PVC Pipe with Varying Feedback Gains

	Time to Reduced Signal Strength (sec) (Percent Reduction from Non-controlled Response (%))			
	Sensor 1	Sensor 2	Sensor 3	Sensor 4
Non-controlled	0.0942	0.0963	0.0970	0.0753
Feedback Gain 10	0.0851 (9.67)	0.0885 (8.05)	0.0896 (7.64)	0.0698 (7.25)
Feedback Gain 15	0.0785 (16.7)	0.0802 (16.7)	0.0815 (15.9)	0.0642 (14.7)
Feedback Gain 20	0.0717 (23.9)	0.0744 (22.7)	0.0741 (23.6)	0.0601 (20.1)
Feedback Gain 25	0.0618 (34.4)	0.0595 (38.2)	0.0574 (40.8)	0.0476 (36.8)
Feedback Gain 30	0.0397 (57.9)	0.0427 (55.6)	0.0386 (60.1)	0.0366 (51.3)

Table 3-17: Average Time Required to Reach 25% of the Non-controlled Piezoelectric Sensor Response for the PVC Pipe with Varying Feedback Gains

	Time to Reduced Signal Strength (sec) (Percent Reduction from Non-controlled (%))			
	Sensor 1	Sensor 2	Sensor 3	Sensor 4
Non-controlled	0.3885	0.3343	0.1736	0.1200
Feedback Gain 10	0.3575 (7.97)	0.3078 (7.91)	0.1587 (8.58)	0.1100 (8.35)
Feedback Gain 15	0.3299 (15.1)	0.2820 (15.6)	0.1495 (13.9)	0.1009 (15.9)
Feedback Gain 20	0.3051 (21.5)	0.2739 (18.1)	0.1400 (19.3)	0.0975 (18.7)
Feedback Gain 25	0.2790 (28.2)	0.2389 (28.5)	0.1199 (30.9)	0.0880 (26.7)
Feedback Gain 30	0.2001 (48.5)	0.1967 (41.2)	0.0970 (44.1)	0.0749 (37.6)

Table 3-18: Average Time Required to Reach 10% of the Non-controlled Piezoelectric Sensor Response for the PVC Pipe with Varying Feedback Gains

	Time to Reduced Signal Strength (sec) (Percent Reduction from Non-controlled (%))			
	Sensor 1	Sensor 2	Sensor 3	Sensor 4
Non-controlled	0.9160	0.8645	0.6516	0.3322
Feedback Gain 10	0.8632 (5.77)	0.8077 (6.57)	0.6180 (5.15)	0.3092 (6.94)
Feedback Gain 15	0.8352 (8.82)	0.7849 (9.20)	0.5953 (8.63)	0.3075 (7.44)
Feedback Gain 20	0.8114 (11.4)	0.7689 (11.0)	0.5681 (12.8)	0.2987 (10.1)
Feedback Gain 25	0.7169 (21.7)	0.7030 (18.7)	0.5107 (21.6)	0.2762 (16.8)
Feedback Gain 30	0.6609 (27.8)	0.6086 (29.6)	0.4374 (32.9)	0.2241 (32.5)

As can be seen from these results the degree of control for a given gain level decreases as the response decays. The major reasons for this are the method of control and the improper size of piezoelectric patches. As mentioned previously the feedback method used in this investigation was based on the displacement of the sensor with a consistent gain, which was limited by the ability of the computer acquisition system. In this type of system, as the sensor voltage decays, the actuation voltage eventually becomes too small to cause any reduction in the vibration characteristics of the pipe. Therefore as time progresses the vibration responses become closer together and no further suppression is observed. Moreover, the piezoelectric sensors were too small for the given set-up, and although they could produce suppression in the early stages of the response, this system failed to produce a practical response in the overall scope of the experiment.

Chapter 4

Damage Detection Methodology

4.1 Introduction

In the past there have been many investigations into damage detection or health monitoring in many civil engineering structures. This includes investigations into beams, trusses, plates, frames, bridges, offshore platforms, other large civil engineering structures, aerospace structures, and composite structures as reported by Doebling et al. (1996). Most of the current nondestructive evaluation techniques involve periodic inspections that involve ultrasonic equipment that is very time consuming and labor intensive. Therefore, it is of paramount importance to develop a damage detection system that does not require large amounts of labor, is inexpensive, and is systematically easy to implement. With the use of piezoelectric materials one can develop such a system to perform damage detection in real time, thus minimizing the need for periodic inspections. The following sections will explain the techniques involving smart materials for damage detection, including methods of signal monitoring, analysis, processing, and damage identification methods.

4.2 Response Measurements

There are mainly two methodologies in which piezoelectric patches can be implemented to monitor the state of damage in a structural system. These involve measuring the impedance of the sensor or the time response of the sensor. The following sections provide descriptions of these two methods.

4.2.1 Impedance Based Measurements

Several investigators have investigated works in this area; for example Liang et al (1993) described the coupling between the electrical and mechanical impedance of a piezoelectric transducer affixed to an elastic structure. Sun et al. (1995) used impedance measurements on a model space-truss to identify damage. Chaudhry et al. (1995a) studied local-area health monitoring on an aircraft tail-fuselage junction. Chaudhry, et al. (1995b) measured the structural integrity of a composite patch repair specimen. Ayres et al. (1998) investigated the health monitoring of a ¼-scale steel bridge junction.

In this method damage is detected through measuring the changes of impedance in the structure. The basis of this technique is that each part of the structure contributes to the overall impedance of structure to some extent. Any variation in the structural integrity would generally result in changes in the impedance. There are two groups of techniques in this domain, namely, the mechanical impedance and electrical impedance. Mechanical impedance techniques are based on the measurement of the impedance, Z, at a point of a structure. The impedance is defined as the ratio of the applied force input to the resultant velocity of the structure at the same point. Similar to the mechanical impedance, electrical impedance techniques measure change of electrical impedance, which is defined as the ratio of the applied voltage to the resulting current of the structure. The elastic admittance of the collocated sensor/actuator is assumed to be functionally equivalent to its mechanical impedance. This group of methods is capable of multi-location and real-time health monitoring. Impedance domain methods are particularly suitable for detecting planar defects such as delaminations in FRP. The inspection is reliable except when the system impedance becomes spring-controlled and then the impedance only decreases with stiffness, i.e. the case where the layer above the defect is thin and the base structure is relatively stiff.

This method is very accurate at monitoring local effects near the sensor because the impedance is not affected by far-field disturbances. However, this also means they are

very much localized in their damage detection capabilities and may not capture the full global damage of the system. With the impedance based measurement systems a high-resolution impedance analyzer attached to a data acquisition computer is required, thus being a relatively costly system.

4.2.2 Vibration Based Measurements

Work in this area has been carried out by Caccese et al. (2004) who investigated bolt load loss in hybrid composite-metal bolted connections using the time response of shear accelerometers and dynamic strain sensors. Mickens et al. (2003) studied damage detection capabilities in aircraft wings using a frequency response function (FRF) damage index, determined from the time response history of PZT patches. Sohn et al. (2004) used time history response method for damage detection in laminated composite plates. Lauwagie et al. (2002) and Kessler et al. (2002) used a laser vibrometer to monitor the time response for damage detection in composite plates.

The vibration based non-destructive evaluation, NDE, techniques bear resemblance to the impedance method since it uses vibrations to identify damage. Most vibrations-based NDE techniques rely on performing a system vibrations identification of the structure before and after damage. The presence of damage is inferred from subtle modification appearing either in the structural frequencies, or in the modal, stiffness, damping and mass, or in the structural modeshapes.

The time response method was found to be an effective tool to determine whether damage is present in a structure. There are many advantages to using a frequency response method in a SHM system such as the relatively low cost, they can be light and conformal, and they can provide good insight as to the global condition of the system.

4.3 Data Analysis Methods

There are many different methods available to analyze the response of sensors in structural health monitoring applications. These include modal analysis, frequency domain, time domain, and impedance domain.

4.3.1 Modal Analysis

These groups of methods utilize the information from all modal parameters like modal frequencies, mode shapes, and modal damping ratio or combinations of some of them to detect damage. The basic idea of these methods is that the above-mentioned modal parameters are functions of the physical properties of the structure, such as mass, damping, and stiffness. Therefore, changes in the physical properties caused by damage would result in changes to the modal properties. Usually, the presence of damage will decrease the mass and stiffness of the structure while increasing the local damping ratio. Among the three structural property parameters, mass is least sensitive to damage while damping is the most sensitive to damage. Because of its complex physical nature, proportional damping is often adapted in damage detection methods. According to their different detection techniques, the modal analysis methods can be divided into the following major categories, such as:

- Modal shape changes methods
- Modal shape curve methods
- Frequency response function method
- Combined modal parameters methods.

The majority of this group of methods uses the lower frequencies of the system and can best describe the global behavior of the structure. Therefore, they hold promise for global non-destructive inspection of a variety of structures, because surface measurements of a vibrating structure can provide information about the health of the

internal members without costly (or impossible) dismantling of the structure. Also, because of their global nature, these techniques allow the customization of measurement points. Another major advantage is that the modal information is relatively inexpensive to obtain and easy to extract.

However, there are many limitations to this group of methods. Firstly, some of the modal-based methods can only detect particular forms of damage in their diagnostic schemes. Secondly, the methods usually use the undamaged structural modal parameters as the baseline compared with the damage information. This will result in the need for a large data storage capacity for complex structures. But, a newly developed method, which tries to quantify damage without using a base line, may be a solution to this difficulty. Thirdly, they fail to detect small defects in global features.

4.3.2 Frequency Domain

Damage may also be detected by only using frequency response of the structure. The foundation of this group of methods is that damage produces a decrease in structural stiffness, which, in turn, produces decreases in the natural frequencies. The location of the defect can be estimated from the degree of change in natural frequency, which in turn, depends on the position of the defect for a particular mode of vibration. In other words, local or distributed changes in stiffness produce changes in natural frequencies, which affect each mode differently depending on the damage location. This is because the damage event is a local phenomenon in most cases. Salawu (1997) suggested that monitoring local high-frequency modes of local area provide a better indication of damage for small damage. It was also suggested by Salawu (1997) that resonant frequency is a better indicator of defects than frequencies, because it can change more significantly than frequencies do when properties change. Some of the other methods available in the frequency domain category include the damage index method suggested by Cawley and Adams (1979) and the sensitivity analysis method studied by Sanders et

al. (1992). As only frequency information is required, these approaches can provide cost effective structural assessment techniques.

However, natural frequency changes alone may not be sufficient for a unique identification of the location of structural damage. The current frequency domain methods are either using lower frequencies for providing global information of structures or using higher frequencies for providing local information of structures. None of these can provide sufficient information for the detection of both small and large defects.

4.3.3 Time Domain

Basically, all methods in this category are related because they use time history. These methods could be independent of modal information although they are usually combined with frequency domain methods. Damage is estimated using time histories of the input and vibration responses of the structure. Using time response over a long period while at the same time taking into account the information in several modes so that the damage evaluation is not dependent on any particular one could be sensitive to any modes. The big advantage of the methods in this group is that they can detect damage situations both globally and locally by changing the input frequencies.

4.4 Signal Processing Methods

Independent of the measured parameters used to determine the state of the structure the processing of the data can be performed in many ways. In damage detection applications a change in the stiffness, damping, or mass of a system, will result in a change of vibration characteristics in the system. Changes in natural frequencies, modal damping, and mode shapes, cannot be visualized or determined directly from the time history response of the system, thus a transformation to some kind of frequency domain must be completed. Some of these methods include the Fourier analysis, spectrograph, wavelet analysis, and the empirical mode decomposition to name a few. The following sections will provide a description of how these signal processing methods are implemented.

4.4.1 Fourier Analysis

The most commonly used and available algorithm associated with the frequency domain is the Fourier transform. The Discrete Fourier Transform (DFT) is used to produce frequency analysis of discrete non-periodic signals, and is given by the algorithm shown by equation [4.1].

$$F(k) = \sum_{n=0}^{N-1} x_n e^{-i2\pi nk/N} \qquad [4.1]$$

where:

F(k) = Fourier spectrum

x_n = time history response

$i = \sqrt{-1}$

k = 0,1,2,…,N-1

N = number of data points

Due to the large number of calculations involved with the DFT, ($O(N^2)$), due to the requirement of N multiplications for each of the N terms, the Fast Fourier Transform (FFT) is often implemented as an efficient method of achieving the same result, but with less overhead involved in the calculations. The only requirement of the FFT is that the data set is a factor of 2. The FFT is calculated by breaking the discrete Fourier into the sum of odd and even terms. This results in the equation [4.2] which reduces the number of calculation to O(N*log*N).

$$F(k) = \sum_{n=0}^{N/2-1} x_{2n} e^{-i2\pi(2n)k/N} + \sum_{n=0}^{N/2-1} x_{2n+1} e^{-i2\pi(2n+1)k/N} \qquad [4.2]$$

where:

x_{2n} = even terms

x_{2n-1} = odd terms

The Fourier transform determines the contribution of the individual natural frequencies of the system to the overall response, such that the largest contributing natural frequencies to the overall response will have the largest power. This method however is limited to systems that are linear and strictly periodic or stationary.

4.4.2 Spectrogram Analysis

The spectrogram is essentially a limited time window-width Fourier spectral analysis. By successively sliding the window along the time axis, one can get a time-frequency distribution. Since this method relies on the traditional Fourier spectral analysis, one has to assume the data to be piecewise stationary. This assumption is not always justified in non-stationary data. The window size must be chosen to make sure that the data over the chosen time scale is stationary. In order to localize an event in time, the window width must be narrow to get good time resolution while being wide enough to get the required frequency resolution. These conflicting requirements render this method of limited usage. It is, however, extremely easy to implement with the fast Fourier transform; thus, it has attracted a wide following.

4.4.3 The Wavelet Analysis Method

The wavelet approach is essentially an adjustable window Fourier spectral analysis with the general mathematical definition shown in equation [4.3]:

$$W(a,b,X,\psi) = |a|^{-1/2} \int_{-\infty}^{\infty} X(t)\psi^*\left(\frac{t-b}{a}\right)dt \qquad [4.3]$$

where:

W(a,b,X,ψ) = energy of the system

$\psi^*(.)$ = basic wavelet function

a = dilation factor

b = translation of the origin

X(t) = time history data

t = time

The requirements of the analysis is that the basic wavelet function, $\psi^*(.)$, must have a mean of zero, (i.e. the integral must be zero) and the function must have the possibility of time shifting. Although time and frequency do not appear explicitly in the transformed result, the variable, 1/a, gives the frequency scale and, b, the temporal location of an event.

An intuitive physical explanation of the wavelet equation is that $W(a,b,X,\psi)$ is the energy of the function X(t) with scale a, at time = b. For specific applications, the basic wavelet function, $\psi^*(.)$, can be modified according to special needs, but its form has to be chosen before the analysis. A few of the common forms chosen for the wavelet function include the Gaussian, Morlet, Daubechies, and Meyer. Continuous or discrete, the wavelet analysis is basically a linear analysis. A very appealing feature of the wavelet analysis is that it provides a uniform resolution for all the scales and also, local information is not lost as in the case of the FFT. Limited by the size of the basic wavelet function, the downside of the uniform resolution is uniformly poor resolution. Although wavelet analysis has been available only in the last ten years or so, it has become extremely popular, since it is very useful in analyzing data with gradual frequency changes. Most of its applications have been in edge detection and image compression.

Versatile as the wavelet analysis is, the problem with the most commonly used Morlet wavelet is its leakage generated by the limited length of the basic wavelet function. This makes the quantitative definition of the energy-frequency-time distribution difficult. Sometimes, the interpretation of the wavelet can also be counterintuitive. To define a change occurring locally, one must look for the result in the high-frequency range. The higher the frequency, the more localized the basic wavelet will be. If a local event occurs only in the low-frequency range, one will still be forced to look for its effects in the high-frequency range. Another difficulty of the wavelet analysis is its non-adaptive nature. Once the basic wavelet is selected, one will have to use it to analyze all the data. Since the most commonly used Morlet wavelet is Fourier based, it also suffers the many

shortcomings of the Fourier spectral analysis such as only giving physically meaningful interpretation to linear phenomena. However, it can resolve the interwave frequency modulation provided the frequency variation is gradual, but it cannot resolve the intrawave frequency modulation because the basic wavelet has a length of 5.5 waves.

4.4.4 Empirical Mode Decomposition (EMD)

The empirical mode decomposition is a method developed to deal with both non-stationary and nonlinear data by decomposing the signal, as shown by Huang et al. (1998). Contrary to almost all the other methods, EMD is intuitive, direct, a posteriori and adaptive, with the basis of the decomposition based on, and derived from, the data. The decomposition is based on the following assumptions:

- The signal has at least two extremes, one maximum and one minimum
- The characteristic time scale is defined by the time lapse between the extremes
- If the data were totally devoid of extremes but contained only inflection points, the data can be differentiated to reveal the extremes

The essence of the method is to identify the intrinsic oscillatory modes by their characteristic time scales in the data empirically, and then decompose the data accordingly. Drazin (1992) proposed the first step of the analysis is to visually examine the data. From this examination, one can immediately identify the different scales directly by either the time lapse between two successive alternations of local maxima and minima, or the time lapse between two successive zero crossings. For finer resolution of the oscillatory modes the time scale should be derived from the time lapse between successive extremes. This method also allows for the decomposition of data with non-zero mean, either all positive or all negative values, without zero crossings. A systematic way to extract the oscillatory modes of the response, designated as the sifting process, is described as follows.

By virtue of the intrinsic mode function (IMF) definition, the decomposition method can simply use the envelopes defined by the local maxima and minima separately. Where, an IMF is a function that satisfies the following conditions:

- The number of extremes and the number of zero crossings must either equal or differ at most by one in the whole data set
- At any point the mean value of the envelope defined by the local maxima and the envelope defined by the local minima is zero

The initial process in the EMD method is to identify the extremes of the signal. A cubic spline is then fit to the local maxima to form the upper envelope, and the local minima to form the lower envelope. The functions defining the upper and lower envelopes should contain all data between them. The mean of the envelope is designated as m_1, and the difference between the original data set, x(t), and the mean is the first component, h_1, of the decomposition given equation [4.4]:

$$x(t) - m_1 = h_1 \qquad [4.4]$$

where:

x(t) = time history data set

m_1 = mean of the envelope

h_1 = first component

A pictorial representation of this process is shown in Figure 4-1.

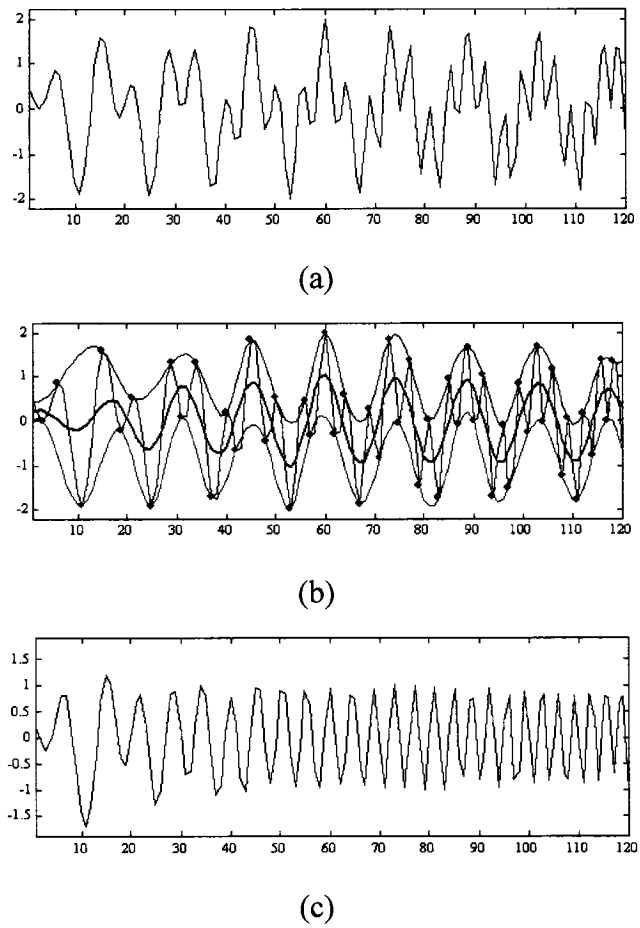

Figure 4-1: Procedure for Empirical Mode Decomposition (a) Original signal (b) Upper Boundary Defined by Blue Line, Lower Boundary Defined by Red Line, Mean of Boundaries (m_1) Defined by Pink Line (c) Resulting h_1, Difference Between Original Signal and m_1

The purpose of the sifting process is to eliminate riding waves and make the wave-profiles more symmetric. Therefore, the sifting process usually has to be carried out several times, until a well-defined signal is obtained. For the second sifting process, h_1 is treated as the data, and the above procedure is repeated. This process is continued until the resulting data set becomes an IMF. For k processes the resulting component, h_{1k} is given by equation [4.5]:

$$h_{1(k-1)} - m_{1k} = h_{1k} \qquad [4.5]$$

As mentioned above the sifting process is to eliminate riding waves, and to smooth uneven amplitudes. While the first condition is absolutely necessary for the instantaneous frequency to be meaningful, the second condition is also necessary in case the neighboring wave amplitudes have too large a disparity. Unfortunately, the second effect, when carried to the extreme, could obliterate the physically meaningful amplitude fluctuations. Therefore, the sifting process should be applied with care, for carrying the process to an extreme could make the resulting IMF a pure frequency modulated signal of constant amplitude. To guarantee that the IMF components retain enough physical sense of both amplitude and frequency modulations, we have to determine a criterion for the sifting process to stop. This can be accomplished by limiting the size of the standard deviation computed from two consecutive sifting results as shown in equation [4.6].

$$SD = \sum \left[\frac{\left| \left(h_{1(k-1)}(t) - h_{1k}(t) \right) \right|^2}{h_{1(k-1)}^2(t)} \right] \qquad [4.6]$$

where:

SD = standard deviation

A typical value for SD is usually set between 0.2 and 0.3.

Ideally, h_1, should be an IMF. However in reality, overshoots and undershoots are common, which can also generate new extremes and shift or exaggerate the existing ones. Even if the fitting is perfect, a gentle hump on a slope can be amplified to become a local extreme in changing the local zero from a rectangular to a curvilinear coordinate system. New extremes generated in this way actually recover the proper modes lost in the initial examination. In fact, the sifting process can recover low-amplitude riding waves with repeated siftings.

Another complication is that the envelope mean may be different from the true local mean for nonlinear data; consequently, some asymmetric wave forms can still exist no matter how many times the data are sifted.

Moreover serious problems of the spline fitting may occur near the ends, where the cubic spline fitting may have large swings. The end swings can eventually propagate inward and corrupt the whole data span especially in the low-frequency components.

Once the sifting process has resulted in an IMF, the resulting component is determined as shown in equation [4.7].

$$c_1 = h_{1k} \qquad [4.7]$$

where:

c_1 = the first component

Once the component is determined, the residual is calculated using equation [4.8].

$$x(t) - c_1 = r_1 \qquad [4.8]$$

where:

r_1 = the first residual

The residual is now considered the signal and the decomposition process is carried out until a second IMF is determined. The new residual, r_2, is then determined with r_1-$c_2 = r_2$, and so on until a predetermined condition is met. This can happen either when the component, c_n, or the residue, r_n, becomes so small that it is less than the predetermined value of substantial consequence, or when the residue, r_n, becomes a monotonic function from which no more IMF can be extracted. At this stage the residual will be either the mean trend or a constant.

By using equation [4.9] the signal original time history signal is represented by a set of n-empirical modes and a residual.

$$x^*(t) = \sum_{i=1}^{n} c_i + r_n \qquad [4.9]$$

where:

$x^*(t)$ = resulting decomposed response

n = number of components

c_i = individual components

r_n = last residual which is no longer an IMF

4.5 Damage Indices

Once the data processing method, such as Fourier transform, wavelet analysis, or EMD, has been chosen and performed the method of analyzing the data must be chosen, by selecting a suitable measure or comparison method to determine the presence of damage. In most cases this is done through the use of a damage index, however some early work in the area used simple modal analysis methods. These modal analysis methods included looking at natural frequency shifts, damping affects, and mode shape distortions. These methods were found to give some promising results but lacked the ability to determine the presence of small damages and damage in large structures due to small changes in modal properties.

For the reasons mentioned above a new method for measuring the state of damage had to be developed, which resulted in the use of damage indices. The damage index is a relative value that compares a current structural state, damaged or undamaged, to a baseline state, which is generally taken as the initially undamaged state. There are several ways in which a damage index can be computed but most are related to statistical approaches. Such methods include the root mean square deviation (RMSD), mean absolute percentage deviation (MAPD), covariance (Cov), correlation coefficient (CC),

sum of absolute differences (SAD), and sum square of differences (SSD) to name a few. The following sections will provide a description of how these methods are implemented.

4.5.1 Root Mean Square Deviation (RMSD)

Giurgiutiu and Rogers (1998) investigated the root mean square deviation (RMSD) between the responses of the two states as a measure of the damage. Later Bhalla (2000) determined the RMSD method was the most effective damage index for structural damage. The RMSD index has the form shown in equation [4.10] as presented by Giurgintiu and Rogers (1998).

$$RMSD(\%) = \sqrt{\frac{\sum_{i=1}^{N}(y_i - x_i)^2}{\sum_{i=1}^{N} x_i^{\,2}}} \times 100 \qquad [4.10]$$

where:

RMSD(%) = RMSD Damage Index (%)

x_i = signature of the baseline or undamaged measurement

y_i = signature of the subsequent measurement

i = 1,2,3,…,N

N = number of data points

4.5.2 Mean Absolute Percent Deviation (MAPD)

As defined by Tseng and Naidu (2002), the MAPD evaluates the average of the deviation between the two data sets at each individual data point and is given by equation [4.11]:

$$MAPD(\%) = \frac{100}{N}\sum_{i=1}^{N}\left|\frac{y_i - x_i}{x_i}\right| \qquad [4.11]$$

where:

MAPD(%) = MAPD damage index (%)

4.5.3 Correlation Coefficient (CC)

The correlation coefficient is a measure of the covariance of the two signatures divided by the product of their standard deviations and has the form shown in equation [4.12] as given by Mays and Tung (1992).

$$CC = \frac{Cov(x,y)}{\sigma_X \sigma_Y} \qquad [4.12]$$

where:

CC = correlation coefficient

σ_x = standard deviations of the baseline signature

σ_y = standard deviations of the subsequent signature

Cov = covariance of the baseline and damaged responses

and where:

$$Cov = \frac{1}{N}\sum_{i=1}^{N}(x_i - \bar{x})(y_i - \bar{y}) \qquad [4.13]$$

$\bar{x}$ = mean of the baseline signature

$\bar{y}$ = mean of the subsequent signature

4.5.4 Sum of Absolute Differences (SAD)

As defined by Sun and Chang (2002), the SAD damage index is a measure of the sum of the absolute difference in the damaged and subsequent signatures, and has the form shown in equation [4.14].

$$SAD = \sum_{i=1}^{m}|x_i - y_i| \qquad [4.14]$$

4.5.5 Sum of Square Differences (SSD)

Sun and Chang (2002) defined the sum of the squares of the difference in the damaged and undamaged signatures as the SSD index, which has the form shown in equation [4.15].

$$SSD = \sum_{i=1}^{m} (x_i - y_i)^2 \qquad [4.15]$$

Chapter 5

Damage Detection of Pipe Joints

5.1 Introduction

Most of the current nondestructive evaluation (NDE) techniques, such as acoustic or ultrasonic, magnetic field, radiographs, eddy-current, and thermal field involve periodic inspections that involve extensive equipment and are very time consuming. For these reasons a system that is self-sustaining is more desirable. With the growth in piezoelectric material applications and the potential reduction in the cost of these sensors, this is becoming a viable option.

As stated earlier the use of modal analysis techniques to determine damage in structural systems has been studied extensively over the past decade. These methods consider the changes in natural frequencies, damping, and mode shapes of the system to evaluate the presence of damage. In order to use a modal method the loading must be consistent throughout all tests, which is difficult to attain. Looking strictly at changes in the aforementioned parameters gives a good indication of the global conditions but it can be inaccurate in assessing the local conditions.

Most vibrations-based NDE techniques rely on performing a system vibrations identification of the structure, before and after the presence of damage. The presence of damage is inferred from subtle modification appearing either in the structural frequencies, or in the modal, stiffness, damping and mass, or in the structural modeshapes. Also mentioned earlier; another technique used in structural health monitoring (SHM) application is the use of impedance-based techniques. With the implementation of a vibration-based time history analysis, as used in this work, a low frequency response can be used in determining the presence of damage, which makes it inexpensive from the standpoint of the data acquisition requirements. With impedance-based methods an

impedance analyzer and more advanced data acquisition systems are required to capture the high frequency responses, which will increase the cost of the system.

There are several issues that make the system more desirable when monitoring the integrity of a structural system to determine its integrity, as noted in the list below.

- The complexity of the required equipment
- Location of the sensor relative to the damage should not affect the capabilities of the detection system
- Location of the damage, such as top or bottom of the joint
- Support conditions of the system
- Means of loading and loading location

In this work a vibration-based time history response method implementing the FRF was used to investigate the above issues. The FRF method compares the frequency spectrums of the response normalized by the input spectrum. This eliminates the requirement of an equal magnitude load; however, the position of the load should remain consistent. In this investigation three statistical damage indices, the RMSD, MAPD, and CC methods were used to compare the FRF for different degrees of damage.

As mentioned in the previous chapter, there are several means by which the data can be collected, analyzed, processed, and displayed to determine the presence of damage in any type of structure. This chapter will show the results for an extensive experimental investigation into an easily implemented and fairly inexpensive damage detection system for studying pipe joint load loss in adhesively bonded and mechanically fastened pipe joints.

5.2 Damage Detection in Adhesively Bonded Joints

Adhesive bonded joints are used to join various structural components in several fields such as pipelines, aircraft structures, and also in repairing components to name a few. In each of these cases it is very difficult to determine the presence or growth of a damage without using very expensive and labor-intensive NDE methodologies such as ultrasonic. The proposed system for NDE of adhesively bonded joints, here applied to pipe joints, can be implemented at a relatively inexpensive cost.

Adhesively bonded joints, as a primary structural connection method, can offer efficient and lightweight alternative to the traditionally used bolted connections. There are various advantages in using adhesively bonded joints over the conventional mechanically fastened ones. These include: fewer parts, full load transfer, better resilience to fatigue, full sealing of the joint, relatively stiffer and lighter weight joints, smoother contours, less susceptibility to corrosion, and the elimination of stress concentration due to drilled holes, and therefore better fatigue endurance. Nevertheless, the current state of bonding technology introduces some shortfalls. For instance, a bonded joint may degrade due to the environmental effects; the joint thickness would have limitations; only transfer of load through shear is permitted; the joint cannot be disassembled readily, and thermal residual stresses can be induced as a result of the curing cycle often associated with bonded joints. As a result, the bonding technology and the associated design processes are continually evolving. In particular, the surface preparation process must be considered quite carefully, as the surface preparation is the key to obtaining a quality adhesively bonded joint, since bonded joint inspection requires special equipment and skill. This aspect of bonding has created an "Achilles heel" in the unequivocal acceptance of adhesive bonding in the aviation industry.

In the past few years, however, the manufacturing processes have been refined to ensure joint quality. However, long-term joint integrity cannot be still satisfactorily guaranteed following a potential cause of concern for damage (i.e. impact or corrosion).

5.2.1 Test Specimens

There were three different test specimens that were used to determine the damage detection capabilities in PVC bonded pipe joints using the proposed approach. They were manufactured using an IPEX 6" PVC sewer pipe, with the section properties as given previously in Table 3-11. The procedure used to prepare the joints were as follows:

- The pipe sections were cut to the appropriate length using a band saw
- The surface was cleaned with isopropyl alcohol to remove dirt
- IPEX XIRTEC 7 primer was applied to the section of the joint to be bonded
- IPEX XIRTEC 11 PVC cement was then applied to the bonding section
- The two sections of pipe were slid together
    - For fully bonded pipe the pipe was rotated to ensure a full bond was achieved
    - For the debonded pipe joints the two sections were carefully inserted into one another to ensure the debonded section did not get bonded together
- The pipes were stood up vertically to cure, for a period of 2 hours, to ensure the cement did not run into the debond section

Using the above procedure, three test specimens containing different amounts of damage were manufactured, as shown in Table 5-1.

Table 5-1: Degree of Damage in Adhesively Bonded Pipe Joint

Test Specimen	Damage Present
1	No Damage
2	¼ Debonded
3	½ Debonded

The piezoelectric patches implemented in this investigation were QP15N PZT QuickPack strain sensors available from Mide Technology Corporation (Medford, MA). These patches were bonded to the surface of the joint using West System's two-part epoxy; the

rational for the positioning will be explained in the following preliminary investigation section. Once the patches were positioned, they were cured for approximately 12 hours under a vacuum at 20mm Hg pressure used to remove air voids and ensure a strong bond. On the test specimens containing damage, piezoelectric sensors were positioned at the center of the damaged section of the joint and 180^0 around the joint from that sensor. For the fully bonded pipe there was only one sensor bonded at the center of the joint.

5.2.2 Preliminary Investigation

Once the joint bond was set, a preliminary study was conducted to determine the optimal placement of the piezoelectric sensors. The preliminary study involved monitoring the pipe response with accelerometers for varying degrees of damage, including the above mentioned set-ups, as well as a joint with no adhesive applied. From these results the natural frequencies were determined and a quick modal analysis was performed. It was found that monitoring the pipe in the area neighboring the actual joint area produced very small changes in the natural frequencies, even for a pipe with no bond at all. However, with the sensors on the joint considerable differences could be seen in the second natural frequency (the first circumferential mode). Therefore, the joint was selected as the location for the sensors.

5.2.3 Experimental Apparatus and Equipment

To determine the damage in the adhesively bonded PVC pipe joints, the dynamic responses of the pipes were monitored at the joint using a simply supported beam set-up, as shown in Figure 5-1, where the excitation locations are labeled one through six and all measurements are in millimeters.

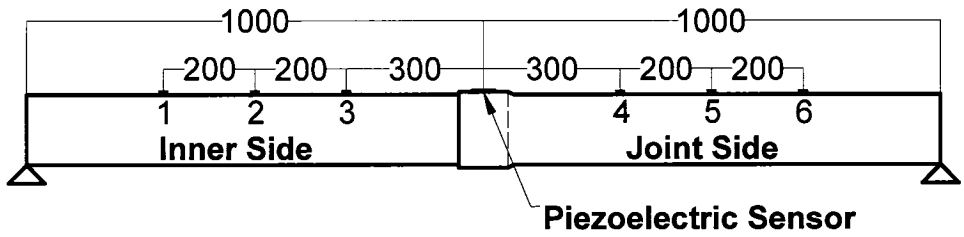

(a)

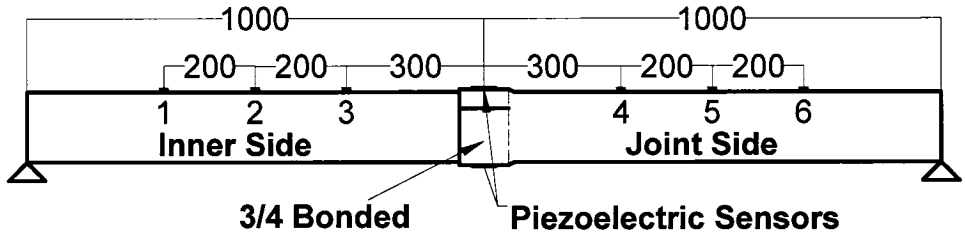

(b)

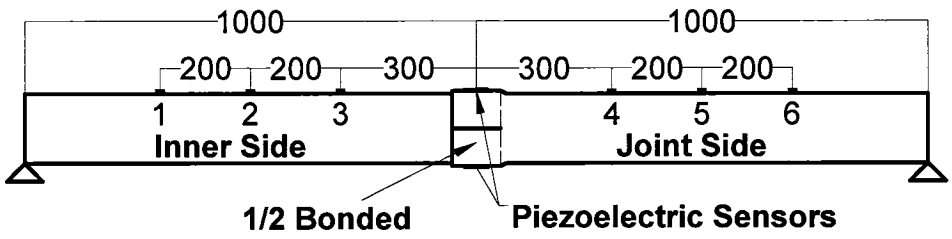

(c)

Figure 5-1: Experimental Test Set-up for Adhesively Bonded Pipe Joints (a) Fully Bonded Joint, (b) ¼-Debonded Joint, (c) ½-Debonded Joint

The supports of the pipe sections were made using 6" cast iron flanges that were fastened to a massive steel platform. In order to fit the pipe section to the supports, a larger IPEX 6" PVC Blue Brute water pipes were milled out to fit tightly over the ends of the IPEX sewer pipe. Once the Blue Brute piping was fitted to the ends of the beams, they were clamped into the flanges, as shown in Figure 5-2.

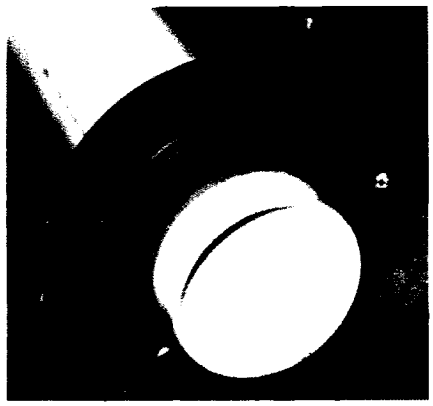

Figure 5-2: Support System for the Adhesively Bonded Pipe Joints

The responses of the piezoelectric sensors were continuously monitored with a multipurpose PCI DT3010 data acquisition card, manufactured by Data Translation (MA, USA), using a differential channel configuration. The data acquisition programs used to monitor the piezoelectric responses was developed in VEE Pro, which is a visual programming software. There was 40,000 data points monitored for each test at a rate of 10 kHz. Due to noise present in the lab, the computer was powered with the use of a power conditioner, which helps remove the noise from the system.

The loading of the specimens was performed with a PCB Piezotronics 086B01 impulse hammer. The impulse hammer response was monitored continuously using a DT-24EZ data acquisition card also manufactured by Data Translation (MA, USA), with a single ended channel configuration. The data acquisition programs used to monitor the impulse hammer response was developed in LabVIEW, with the use of DT-LV Link, which is a software that allows LabVIEW to communicate with Data Translation products. For each test there was 20,000 data points monitored at a rate of 10 kHz. Due to the response of the impulse hammer being of O(mV), the output was amplified with the use of a PCB Piezotronics Inc. series 790 power amplifier. The power amplifier also eliminated most of the noise from the impulse hammer response signal.

5.2.4 Experimental Procedure

Every experiment was conducted by starting the data acquisition systems then impacting the desired location with the impulse hammer. For each experimental set-up, three tests were performed to ensure consistency and reproducibility in the results. To increase the efficiency of the testing procedure all tests performed with the same set-up were saved to a single file. These results were then separated during the data processing procedure.

To ensure all test results were processed in the same time scale, the time lag between the time of impact and the piezoelectric response was measured. The method used to determine the time lag was to monitor both signals with a differential channel set-up, which was performed using a single data acquisition computer. Continuously monitoring the piezoelectric sensor and the impulse hammer responses allowed for the two signals to be monitored simultaneously. Therefore, the time between the initiations of the impulse hammer response and initiation of the piezoelectric sensor response would be the time for the loading to reach the sensors. It was determined with this set-up the magnitude of the impulse load would be acquired incorrectly, and as a result this method was not implemented in the full experimental investigation.

To determine the parametric effects of the system a total of 24 test set-ups were conducted on each specimen. The test parameters that were varied through the experiments included the load location, support tightness, and debond location. The influence of the loading location on the results were verified by loading six different spots on the pipe specimens, which included three locations on each side of the joint as shown in Table 5-2.

Table 5-2: Impulse Hammer Excitation Locations for the Adhesively Bonded Pipe Joints (The numbers are with reference to Figure 5-1)

Excitation Location Number	Side Impacted	Distance From Joint Center
1	Joint Side	300 mm
2	Joint Side	500 mm
3	Joint Side	700 mm
4	Inner Side	300 mm
5	Inner Side	500 mm
6	Inner Side	700 mm

The fixture tightness was adjusted by varying the torque of the bolts clamping the flange to the pipe section. The two torques used in tightening the supports are shown in Table 5-3.

Table 5-3: Support Fixture Tightness for the Adhesively Bonded Pipe Joints

Fixture Tightness Number	Fixture Bolt Torque
1	84 N.m
2	43.4 N.m

The debonded section of the damaged pipe or sensor on the fully bonded pipe was placed in two locations to determine if the location of the damage affected the damage index, as shown in Table 5-4.

Table 5-4: Sensor/Debond Locations for Adhesively Bonded Pipe Joints

Sensor/Debond Location Number	Position of Sensor/Debond
1	Top
2	Bottom

An overview of the various set-up configurations considered is shown in Table 5-5.

Table 5-5: Test Set-up Configurations for the Adhesively Bonded Pipe Joints (The Numbers are with reference to Tables 5-2 through 5-4)

Test Number	Parameters (Fixture Tightness, Sensor Location, Excitation Location)	Test Number	Parameters (Fixture Tightness, Sensor Location, Excitation Location)
1	1,1,1	13	1,2,1
2	1,1,2	14	1,2,2
3	1,1,3	15	1,2,3
4	1,1,4	16	1,2,4
5	1,1,5	17	1,2,5
6	1,1,6	18	1,2,6
7	2,1,1	19	2,2,1
8	2,1,2	20	2,2,2
9	2,1,3	21	2,2,3
10	2,1,4	22	2,2,4
11	2,1,5	23	2,2,5
12	2,1,6	24	2,2,6

5.2.5 Data Processing Methods

Once all tests were completed the results were processed. This was done with the use of several MATLAB codes that performed different operations on the data. All the MATLAB codes used in the data processing of the adhesive pipe joints are provided in Appendix C.

5.2.5.1 Removal of Non-Response Data

Due to the experimental procedure the data initially had to be separated and all non-response data removed. The MATLAB codes fullpiezo.m and dampiezo.m, were implemented to separate the tests as well as removing the non-response data of the piezoelectric sensors for the fully bonded joint and the damaged joints, respectively. The only difference in the files was the requirement for the extra sensor in the damaged pipe joints. The first step in removing the non-response data was to read the experimental response file into the MATLAB programs. The first value greater then the noise level was then located and a set number of data points prior to this value were kept, where the

number of points retained was dependent on the time lag. The rest of the data prior to this point was removed, which was the non-response points between the time of program initiation and the application of the impact load. The final step was to remove the non-response data at the end of the file, which was determined visually with knowledge of the free vibration time of the system.

5.2.5.2 Response of Piezoelectric Sensors for Fully Bonded Pipe

Due to the fully bonded pipe containing only a single piezoelectric sensor, tests were conducted with the sensor located on the top and bottom of the joint. This allowed for the full comparison of all test results since the damaged pipes had two piezoelectric sensors. To save on later computational efforts, the tests results for the fully bonded joint were merged according to similar set-up properties, such as load location and support tightness. This was performed by the MATLAB code merge.m, which stored the test results for test set-up 1 and 13, 2 and 14, etc. in the same variables. This stored the response files for the fully bonded pipe in the same format as the damaged pipes, which had the results for sensors on the top and bottom of the joint.

5.2.5.3 Impulse Hammer Response Processing

The impulse hammer responses were processed with the MATLAB code loadresponse.m. The removal of the zero state data included removing all the non-response data at the start and end of the test. The start of the test was determined by finding the position where the impulse hammer voltage surpassed a set value, in these cases 0.1 volts. The test was then deemed to have started 2 points before this value was surpassed, which was found by visually inspecting the results. The actual loading response of the impulse hammer was found to last for approximately 1.5 msec, with the vibration response lasting for approximately 20 msec.

5.2.5.4 Determination of Frequency Response Functions (FRF's)

In order to properly analyze the data, the frequency response functions for the individual tests are required. For this investigation the frequency response functions were the ratio of the piezoelectric sensors Fourier spectrum divided by the impulse hammer Fourier spectrum. The FRF were determined through the use of the MATLAB code normalize.m.

To reduce the number of lines in the main program several small programs were developed to perform most of the data processing. These programs include swap.m, filterdata.m, fastfourier.m, and frf.m.

For the fully bonded pipe joint the piezoelectric sensor responses were organized such that the top sensor signals were collected and written into the first three columns of the output file and the bottom sensor was written to columns four through six. However for the damaged pipe joint tests the piezoelectric sensor responses were organized such that the sensor on the debonded section of the joint was in the first three columns and the responses for the sensor on the bonded section was located in columns four through six. In order to perform proper comparisons of the results the program swap.m was utilized for tests 13 through 24. This program switches the order of the piezoelectric sensor responses such that the sensor on the top of the joint is in the first three columns and the sensor on the bottom is in columns four through six, as is the case with the fully bonded joint.

The program filterdata.m was a program developed to filter the piezoelectric sensor responses, using the Butterworth band pass filter. The program fastfourier.m was a program used to compute the 8192-point fast Fourier transform (FFT) of the piezoelectric sensors as well as the impulse load function.

The last call to process the signal was made to the frf.m program, which computed the FRF of the responses. This program normalized the piezoelectric FFT with respect to the impulse load FFT. This program was used for the damaged pipe joints, which contained only three loading functions for the six sensor responses. For the fully bonded joint, which contains six piezoelectric sensor responses, as well as six loading responses, line 8 of the code was removed.

5.2.5.5 Evaluation of Damage Indices

Once the FRF's for all the responses were found, the damage indices were computed. The MATLAB codes developed include RMSDindex.m, MAPDindex.m, CCindex.m, and preceding.m. The first three programs listed above computed the RMSD, MAPD, and CC damage indices relative to the zero damage states respectively. The program preceding.m computed all three damage indices for the half debonded joint relative to the quarter-debonded joint, where the preceding state for the quarter-debonded pipe is the undamaged state.

5.2.6 Experimental Results

The frequency response functions for all tests were determined using a Fourier spectrum analysis as described previously. For all cases the damage indices were evaluated relative to the undamaged state, as well as to the proceeding state. All damage index numerical results for the different set-ups, and specimens are shown in Appendix D.

5.2.6.1 Typical Responses

A typical time-history response and Fourier spectrum for a top surface bonded piezoelectric sensor are shown in Figures 5-3 and 5-4 respectively.

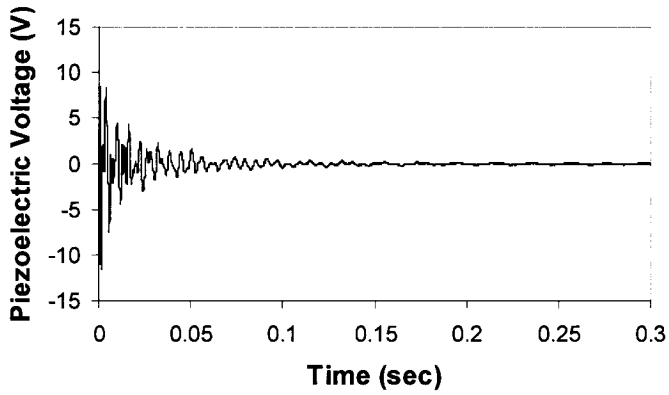

Figure 5-3: Typical Time History Response for the Top Surface Piezoelectric Sensor on the Adhesively Bonded Pipe Joints

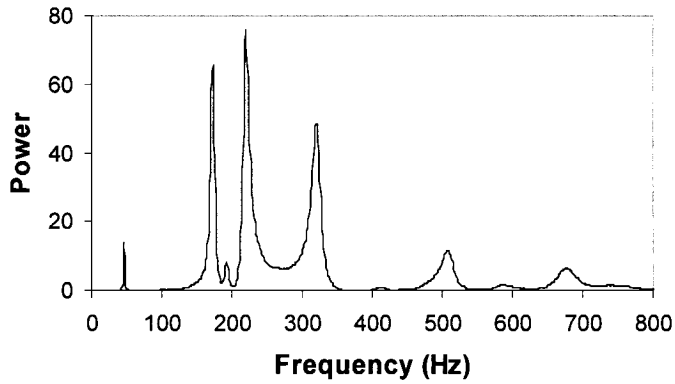

Figure 5-4: Typical Fourier Spectrum of the Top Surface Piezoelectric Sensor on the Adhesively Bonded Pipe Joints

Figure 5-5 shows a typical frequency response function for the three different degrees of damage.

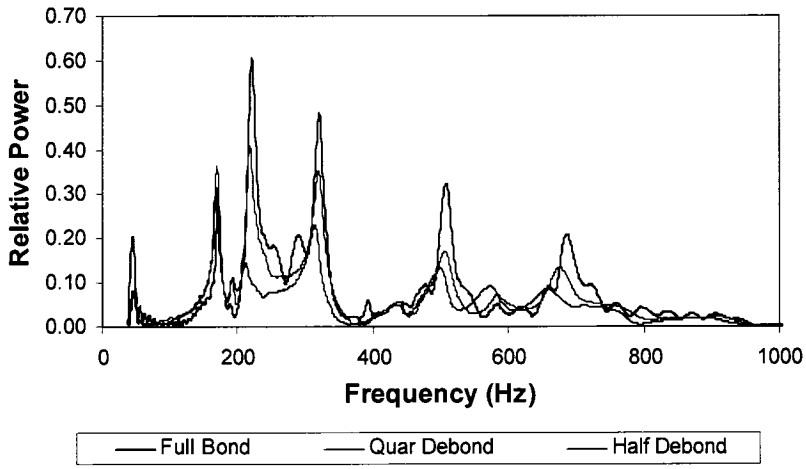

Figure 5-5: Typical Frequency Response Function for Varying Degrees of Damage in Top Sensor for the Adhesively Bonded PVC Pipe Joint

From Figure 5-5 it can be seen from a visual inspection that damage is present in the quarter and half debonded joint from the significant frequency shifts in most natural frequencies. This however would not give any indication of the degree of damage within the system.

5.2.6.2 Effect of Sensor Location

The first requirements of an efficient SHM system are to minimize the requirements for complicated and expensive equipment. It would be more desirable to have a robust system that would use as few sensors as possible. It would be most desirable if only one sensor could detect the presence of a damage. The best system would then be the one that would use only one sensor, and not necessarily having the sensor located at the damage region. The RMSD, MAPD, and CC damage indices are shown in Figure 5-6 for the two sensors on the ¼-debonded pipe joint for test set-ups one through six, respectively. Where, sensor 1 is located on the debonded section of the joint, and sensor 2 on the bonded section of the joint.

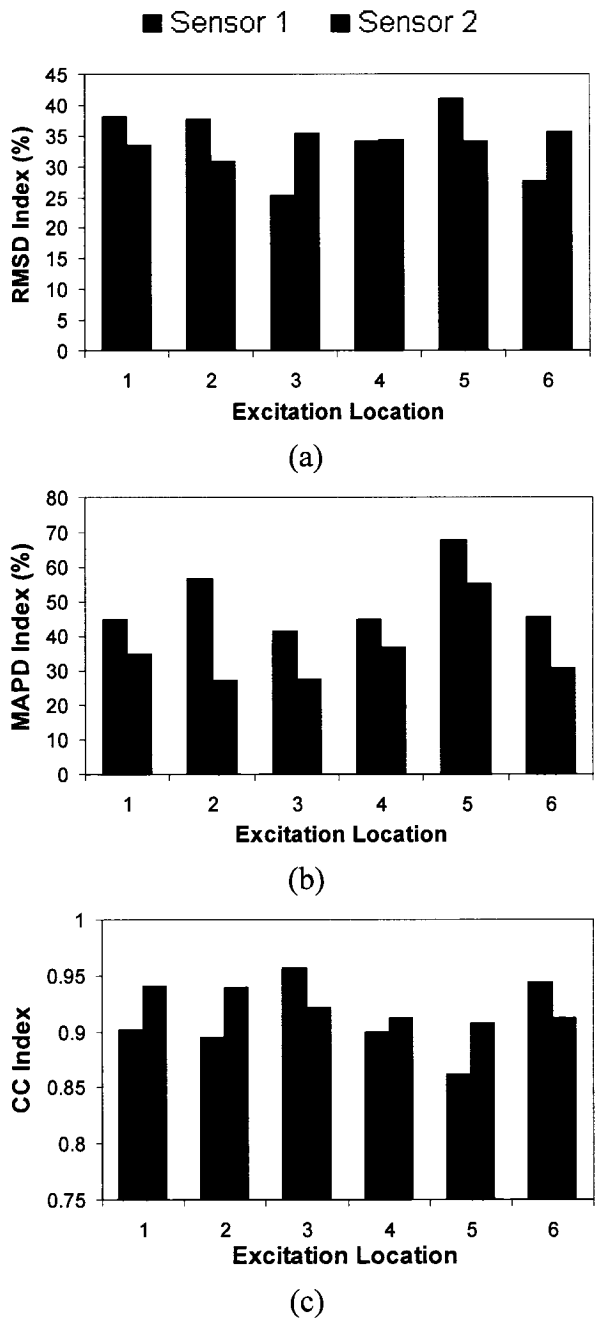

Figure 5-6: Comparison of Damage Indices for Sensors 1 and 2 of the ¼-Debonded Joint (a) RMSD Index, (b) MAPD Index, and (c) CC Index

As can be seen from Figure 5-6, the sensor position relative to the damage does not significantly affect the capability of the system to detect the damage. However, depending on the location of the excitation, varying index magnitudes are observed, as

will be discussed in a later section. Also of note is the consistency of the results for the individual sensors. In general, sensor 2 produces more consistent index values for an individual set-up, as well as experiments with the excitation on a single side of the joint. This is also evident by the coefficient of variation (COV) for the individual test set-ups, which are shown for all experiments in Appendix D.

5.2.6.3 Location of Damage

In order to determine the effect of the location of the damage relative to the orientation of the set-up, tests were conducted with the debonded section of the joint on the top and bottom of the section. Figure 5-7 shows the damage indices for sensor 1 comparing the results for the damage located on the top and bottom of the section for the ¼-debonded joint.

As Figure 5-7 shows, the ability of the system to detect damage for a given set-up is not compromised by the location of the damage. Another point to note is the damage index is in general more consistent for the damage located on the bottom of the joint. However, the maximum index value does not depend on the location of the damage, as it fluctuates for the different impact locations. Also as was seen previously, the location of the excitation does influence the magnitude of the indices.

5.2.6.4 Effect of Excitation Force Location

Due to limitations in accessing many piping systems in practical applications, it is beneficial to have the capabilities and the choice of exciting the system at any location. For this reason, experiments were conducted to determine the influence of the location of the excitation force on the damage detection system. The damage indices for loadings at varying distances from the joint for sensors 1 and 2 of the ¼-debonded pipe are shown in Figure 5-8.

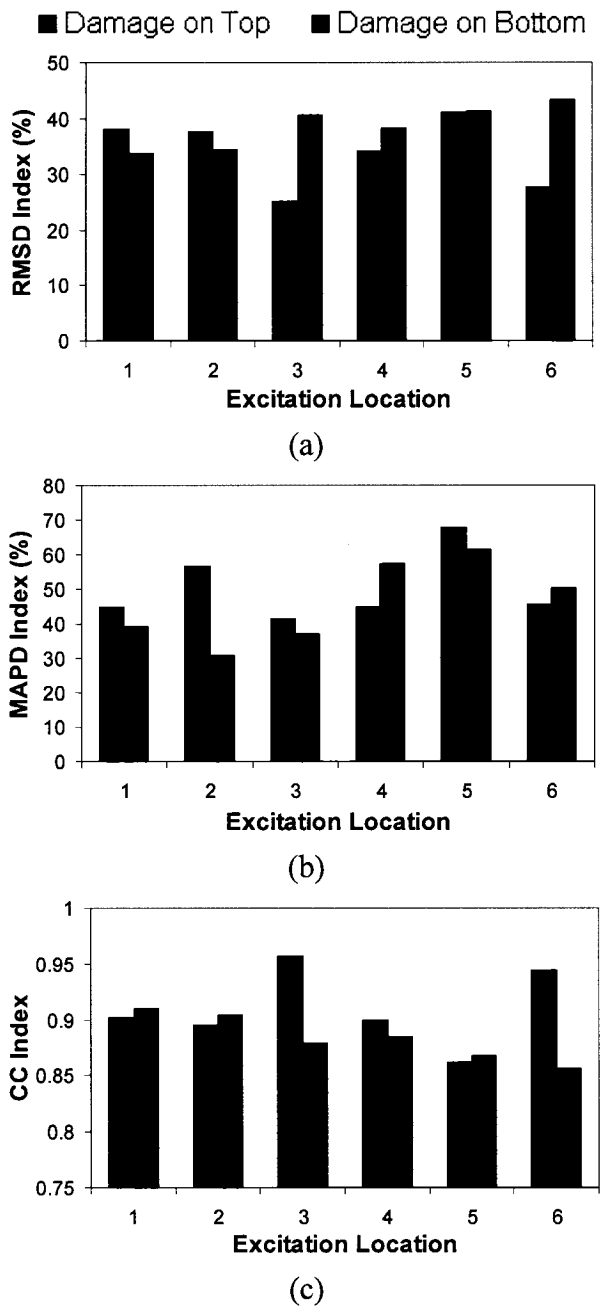

Figure 5-7: Comparison of the Damage Indices for Sensor 1 of the ¼-Debonded Joint for Damage Located on the Top and Bottom of the Section (a) RMSD Index, (b) MAPD Index, and (c) CC Index

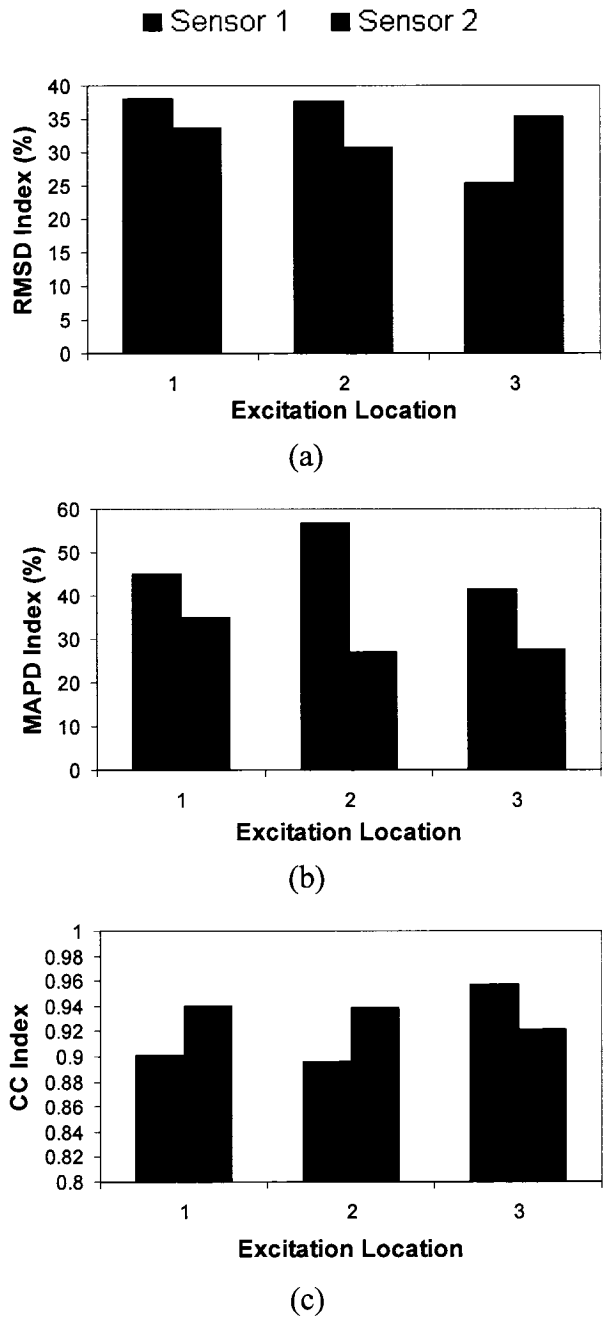

Figure 5-8: Comparison of the Damage Indices for Sensor 1 and 2 of the ¼-Debonded Joint for Excitation at Varying Distances From the Joint (a) RMSD Index, (b) MAPD Index, and (c) CC Index (The excitation location numbers are reference from Table 5-2)

From Figure 5-8 it can be seen that the location of the excitation load indeed influences the magnitude of the damage index, however the capability of the system to determine the presence of damage is not diminished by these fluctuations. It should be noted that the choice of damage index influences the optimal position for excitation. For the RMSD and CC indices, the optimal position of excitation is close to the supports, whereas, the optimal RMSD index is observed with excitation at the center of the spans. However, the proposed method demonstrates that the presence of damage can be determined by exciting the system virtually at any location.

In adhesively bonded joints, the two sections making up the joint are distinctly different, where one is on the inner side of the joint the other on the outer. Figure 5-9 shows how the two sides of the pipe joint are distinguished, and Figure 5-10 displays the results by comparing the damage indices of the ¼-debonded joint for loading of each side, where hit locations one through three for the outer side correspond to excitation locations four through six, respectively.

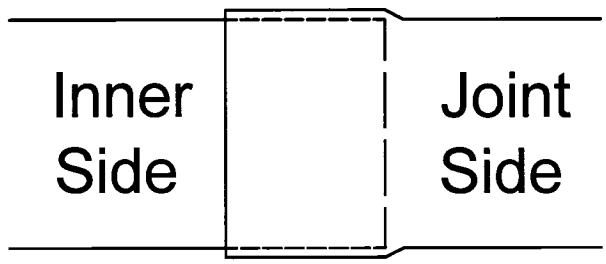

Figure 5-9: Adhesively Bonded Pipe Joint Side Description

As can be seen from Figure 5-10 the side of the joint that was excited had an insignificant affect on the resulting indices, although exciting the inner joint side in general produces better results. The figure also indicates that exciting the pipe section at the mid-span of either sides of the piping system produced more distinguishable results, as was seen previously in Figure 5-8.

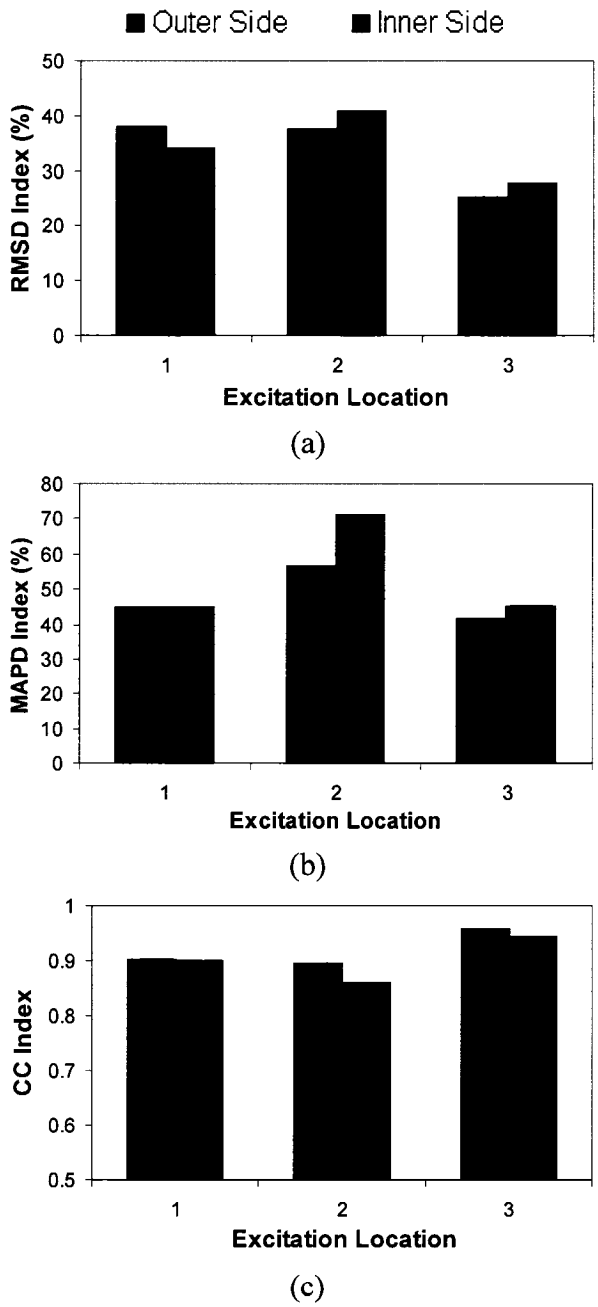

Figure 5-10: Comparison of the Damage Indices for Sensor 1 of the ¼-Debonded Joint for Varying Loading Locations: Side of Joint Impacted (a) RMSD Index, (b) MAPD Index, and (c) CC Index

5.2.6.5 Effect of Support Condition

In real world applications the boundary conditions of the system change throughout the life of the component. Therefore, it is of great importance to determine the effects of the boundary conditions on the capabilities of the damage detection system. To determine this influence, two different clamping pressures were applied to the supports as reported earlier in Table 5-3. Figure 5-11 shows the results for sensor 1 of the quarter-debonded joint for the two different support conditions considered in this investigation.

As the results in Figure 5-11 indicate, the support condition has very little influence on the resulting damage indices and further illustrates the robustness of the proposed damage detection system. It should be noted that the stiffer support condition does produce more pronounced damage indices, however, the pattern observed for both support conditions is the same.

5.2.6.6 Degree of Damage

In general, in adhesively bonded joints, the presence of damage will become more likely as the system ages. Therefore, it is of paramount importance not only having the capability to determine the presence of damage, but also be able to monitor its growth. In order to determine the capabilities of the proposed method, specimens with varying levels of damage were tested and compared. Figures 5-12 through 5-14 show the results of the three damage indices for varying degrees of damage, relative to the zero state damage.

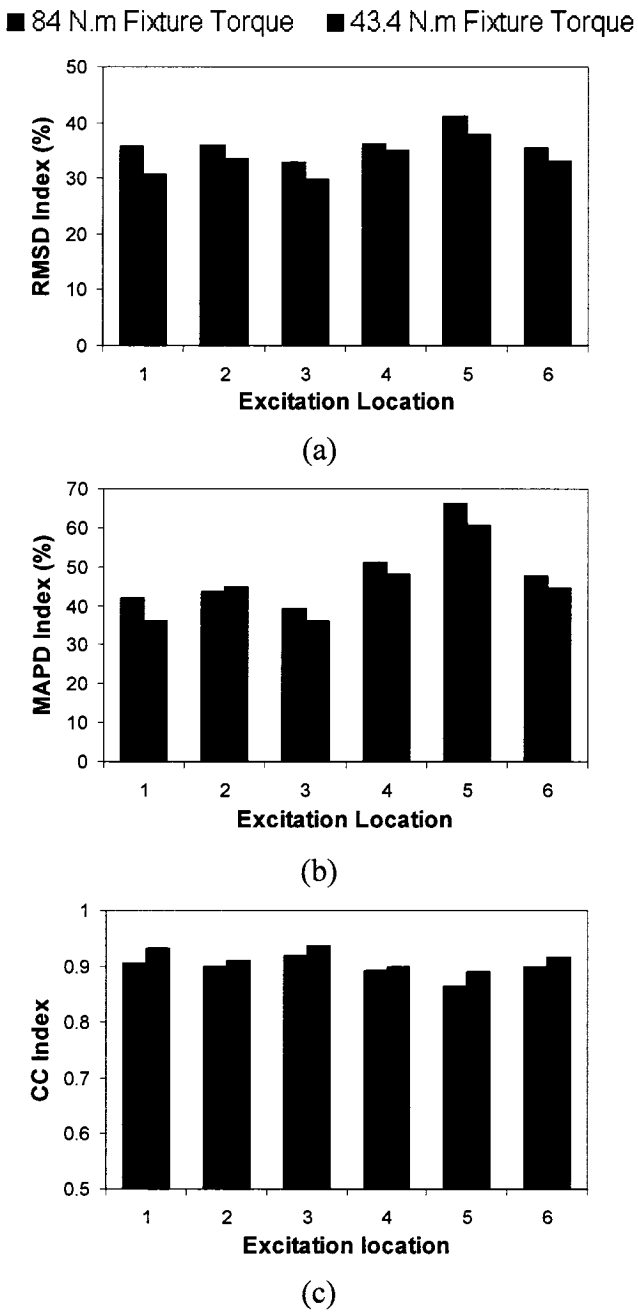

Figure 5-11: Comparison of the Damage Indices for Sensor 1 of the ¼-Debonded Joint for Varying Support Tightness (a) RMSD Index, (b) MAPD index, and (c) CC Index

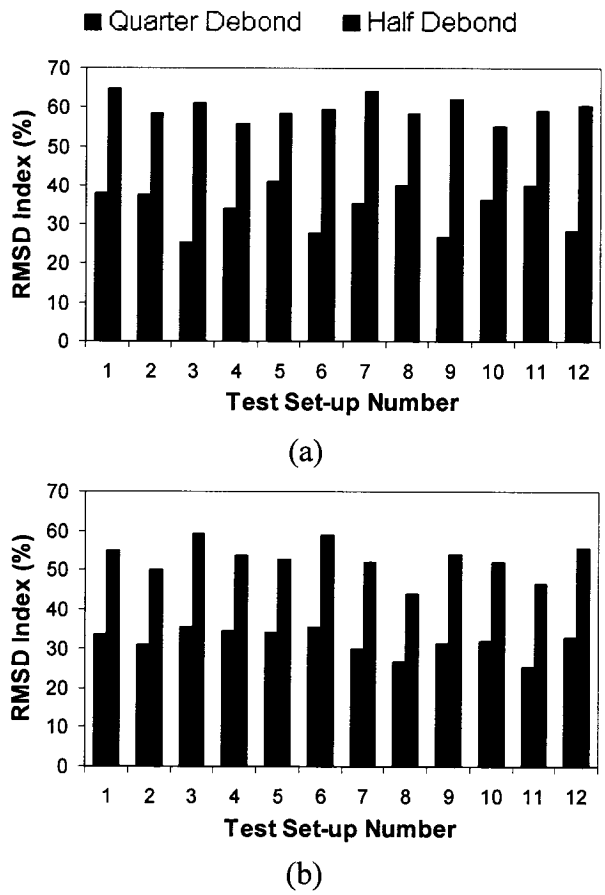

Figure 5-12: RMSD Damage Index for Varying Degrees of Damage Relative to the Undamaged State (a) Sensor 1, and (b) Sensor 2 (Test set-up number is referenced from Table 5-5)

As the results in Figure 5-12 show, there is a very noticeable difference in the damage indices of the ¼-debonded pipe and ½-debonded pipe relative to the undamaged state. To compare the consistency of the results for all impact locations, the average growth ratio along with the coefficient of variation of the RMSD indices of the ½-debonded pipe relative to the undamaged state divided by the RMSD indices of the quarter-debonded pipe are shown in Table 5-6.

Table 5-6: Average RMSD Growth Ratio of the ½-Debonded Pipe relative to the ¼-Debonded Pipe for all Excitation Locations

Sensor Number	Average RMSD Ratio	COV (%)
1	1.745	0.179
2	1.641	0.059

As the results in Table 5-6 show, the growth ratio in the RMSD index is larger for sensor 1; however, sensor 2 produces more consistent results as observed from the coefficient of variation.

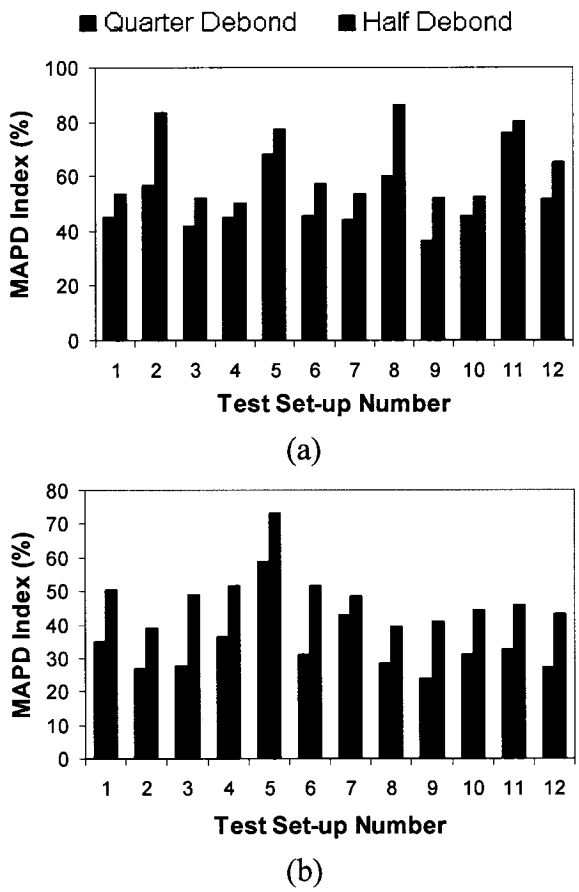

Figure 5-13: MAPD Damage Index for Varying Degrees of Damage Relative to the Undamaged State (a) Sensor 1, and (b) Sensor 2

As was observed with the RMSD index, significant differences are observed in the MAPD index of the ¼-debonded and ½-debonded pipe joints. To evaluate the

consistency of the results for all excitation locations, the average growth rate and coefficient of variation in the MAPD indices are shown in Table 5-7.

As can be seen from the results in Table 5-7, sensor 2 produces results with better consistency as well as a larger average growth rate.

Table 5-7: Average MAPD Growth Ratio of the Half-Debonded Pipe relative to the ¼-Debonded Pipe for all Excitation Locations

Sensor Number	Average RMSD Ratio	COV (%)
1	1.239	0.142
2	1.493	0.129

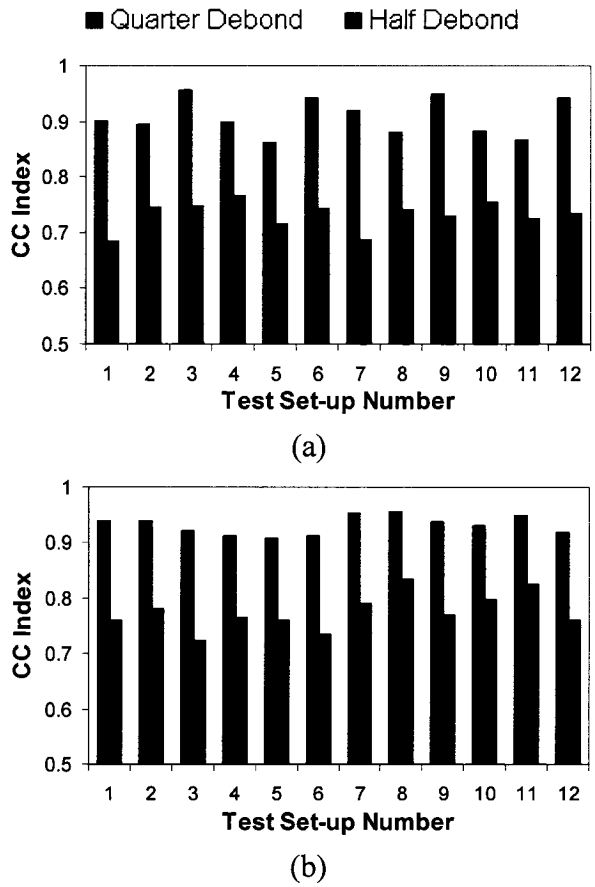

Figure 5-14: CC Damage Index for Varying Degrees of Damage Relative to the Undamaged State (a) Sensor 1, and (b) Sensor 2

As observed with the previous two indices, the CC index provides a very good quantitative measure of the severity of damage. To evaluate the consistency of the results for the different excitation locations, the average reduction rate and coefficient of variation in the MAPD indices are shown in Table 5-8.

Table 5-8: Average Reduction Ratio in the CC Damage Index of the ½-Debonded Pipe Relative to the ¼-Debonded Pipe for all Excitation Locations

Sensor Number	Average CC Ratio	COV (%)
1	0.817	0.039
2	0.833	0.037

As was observed with the RMSD index, sensor 1 produces results with larger index changes, while sensor 2 produces more consistent results for the CC index.

As the above results showed, the proposed damage detection method displays great versatility in determining the presence of damage when compared to an undamaged state. However, if a system were to be monitored over an extended period it would be beneficial to only require the latest set of data rather than storing all data to that point. Therefore, a more suitable measure would be the relative state damage index, which compares one state of damage to the preceding state of damage. The relative state indices would give a better description of the actual progression of the damage as well as reduce the required data storage. Figures 5-15 through 5-17 show the results of the two piezoelectric sensors for varying amounts of damage relative to the proceeding state, for the RMSD, MAPD, and CC indices, respectively.

As can be seen from Figure 5-15, the relative RMSD index produces results that provide a relatively good quantitative measure of the degree of damage. As was observed with the RMSD index relative to the undamaged state, sensor 2 produces results that are more consistent over the entire excitation range.

The average relative RMSD index values for test set-ups 1 through 12, for the two relative states of damage, are tabulated in Table 5-9. From these results it can be seen that sensor 2 not only produces more consistent results over the full excitation range, but also provides a better quantitative measure of the severity of damage.

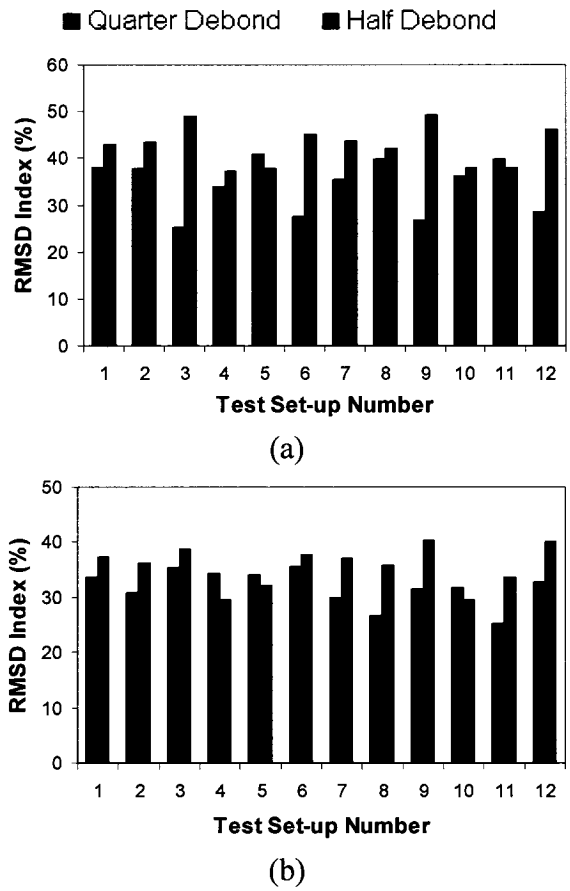

Figure 5-15: RMSD Damage Index for Varying Degrees of Damage Relative to the Preceding State of Damage (a) Sensor 1, and (b) Sensor 2

Table 5-9: Average Relative RMSD Damage Index for Test Set-ups 1-12 of the Adhesively Bonded Pipe Joint

Damage State	Sensor Number	Average Relative RMSD Index (%)	COV of Relative RMSD Index (%)
Quarter-Debonded	1	34.22	16.5
	2	31.81	10.7
Half-Debonded	1	42.76	10.1
	2	35.70	9.62

As can be seen from Figure 5-16, the relative MAPD index provide a quantitative measure of the severity of damage, however, it is fairly inconsistent between excitation locations.

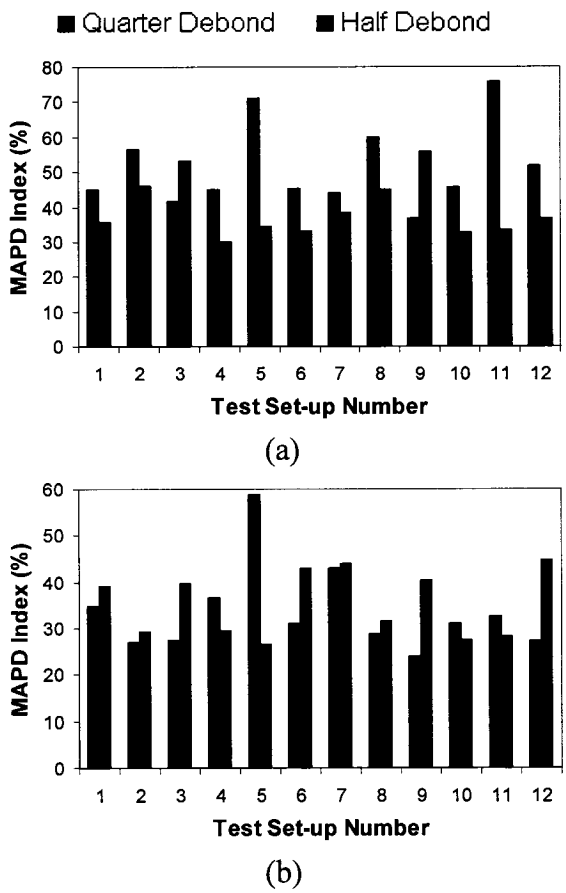

Figure 5-16: MAPD Damage Index for Varying Degrees of Damage Relative to the Preceding State of Damage (a) Sensor 1, and (b) Sensor 2

The average relative MAPD index values for test set-ups 1 through 12, for the two relative states of damage, are tabulated in Table 5-10. From these results it can be seen that sensor 2 provides a better quantitative measure of the severity of damage, however, as the large coefficients of variation show the results are not very consistent.

Table 5-10: Average Relative MAPD Damage Index for Test Set-ups 1-12 of the Adhesively Bonded Pipe Joint

Damage State	Sensor Number	Average Relative MAPD Index (%)	COV of Relative MAPD Index (%)
Quarter-Debonded	1	51.58	23.4
	2	33.50	21.4
Half-Debonded	1	39.50	26.4
	2	35.29	20.2

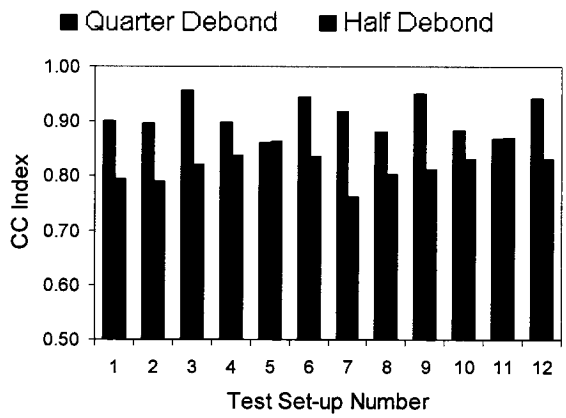

(a)

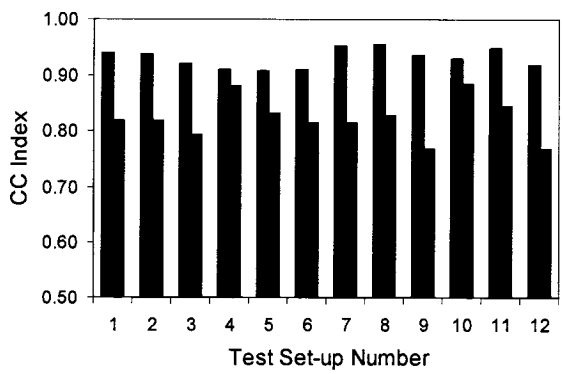

(b)

Figure 5-17: CC Damage Index for Varying Degrees of Damage Relative to the Preceding State of Damage (a) Sensor 1, and (b) Sensor 2

As can be seen from Figure 5-17, the relative CC index provides a relatively good quantitative measure of the severity of damage. However, the CC index consistently shows that the severity of damage between the quarter-debonded and undamaged joint is less than the damage between the half-debonded and quarter-debonded joint.

Table 5-11 provides the average relative CC index values for test set-ups 1 through 12, for the two relative states of damage. Unlike the other two indices used in this study, it can be seen from Table 5-11 that for the CC index sensor 1 provides a better quantitative measure of the severity of damage as well as more consistent results over the all loading locations.

Table 5-11: Average Relative CC Damage Index for Test Set-ups 1-12 of the Adhesively Bonded Pipe Joint

Damage State	Sensor Number	Average Relative CC Index (%)	COV of Relative CC Index (%)
Quarter-Debonded	1	0.908	3.68
	2	0.931	4.65
Half-Debonded	1	0.821	3.78
	2	0.823	5.96

5.3 Damage Detection in Mechanically Fastened Pipe Joints

Mechanically fastened pipe joints are used in various fields of fluid transportation such as the oil and gas industry as well as water distribution systems. The degradation of the joint over time is generally linked to bolt loosening. This can occur due to side sliding of the bolt or nut, bending of the joint, thermal gradients, and joint shifting to name a few. In these cases it is generally difficult to determine the degradation of the joint without periodic checks or a failure in the system. In previous work on mechanically fastened pipe joints, performed by Park et al. (2001), the sensors were positioned directly on the joint. When joint repair is required these sensors will be located in regions of extensive work, which could easily result in their damage. The proposed system developed for detecting the degradation in a mechanically fastened pipe joints has the sensors located away from the joint, which would make them less susceptible to damage during repairs. Also, the proposed system can be implemented at a relatively inexpensive cost and can monitor the system in real time.

5.3.1 Test Specimens

There were four different test specimens that were developed for the proposed system to detect the degradation of mechanically fastened pipe joints. Due to the different piping systems used for varying applications, such as in the oil and gas industry as well as water distribution systems, two different materials were studied. The materials used to develop the joint systems were an IPEX 6" PVC Blue Brute water pipe and a 6" cast iron, cement lined water pipe, with the section properties as shown in Table 5-12.

Table 5-12: Section Properties of Pipes Used in Damage Detection of Mechanically Fastened Joint

Pipe Section	Outside Diameter	Inside Diameter	Thickness	Cement Lining Thickness
PVC	176 mm	154.5 mm	10.75 mm	N/A
Cast Iron	176 mm	154.5 mm	7.75 mm*	3.0 mm

* Thickness of the Cast Iron Material

For each of these materials two pipe set-ups were developed, such that the two set-ups for each material were the same. The first set-up consisted of two pipe sections of equal length and the other with two pipe sections with a side ratio of 3:1. The dimensions of the experimental

The piezoelectric patches implemented in this investigation were QP15N PZT QuickPack strain sensors available from Mide Technology Corporation. These patches were bonded to the surface of the joint using West System's two-part epoxy; the rational for the positioning will be explained in the following preliminary investigation section. Once the patches were positioned, they were cured for approximately 12 hours under a vacuum at 20mm Hg pressure to remove air voids, and promote consolidation to ensure a strong bond. On the test specimens containing damage, piezoelectric sensors were positioned at the center of the damaged section of the joint and 180^0 around the joint from that sensor. For the fully bonded pipe there was only one sensor bonded at the center of the joint.

5.3.2 Experimental Apparatus and Equipment

To determine the damage in the mechanically fastened pipe joints, the dynamic responses of the pipes were monitored with two piezoelectric sensors, one located on each side of the joint. The pipes were tested with a simply supported beam set-up, as shown in Figure 5-18.

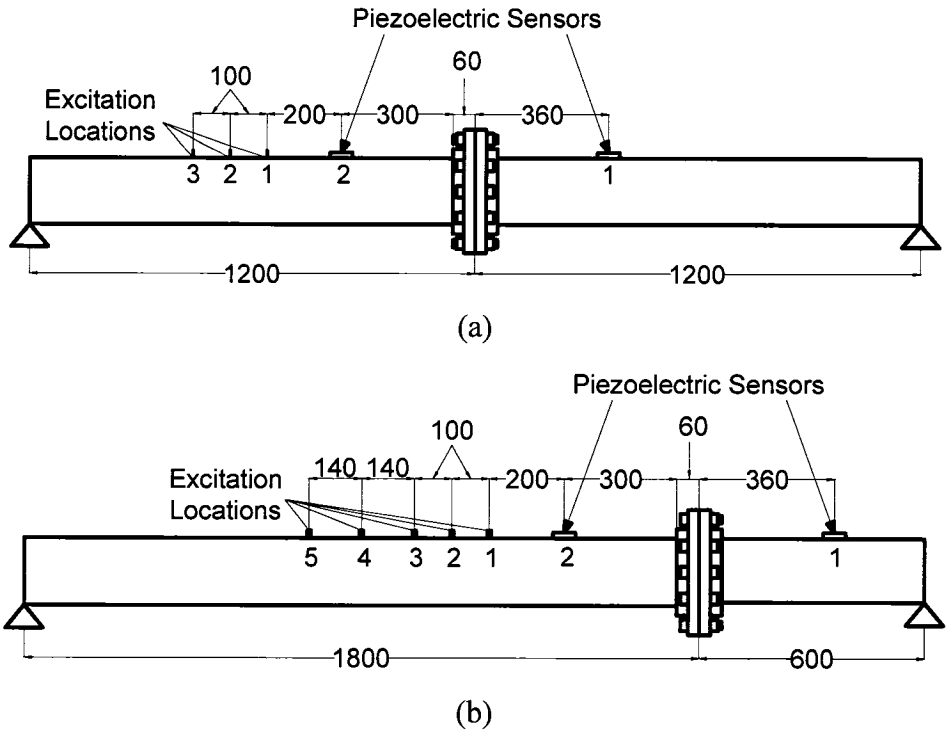

Figure 5-18: Experimental Test Set-up for Mechanically Fastened Pipe Joints (a) Span Ratio of 1:1 (b) Span Ratio of 3:1

The flanges used to connect the two sections of pipe together were standard 6-inch flanges that are fastened using 8-¾" bolts as shown in Figure 5-19.

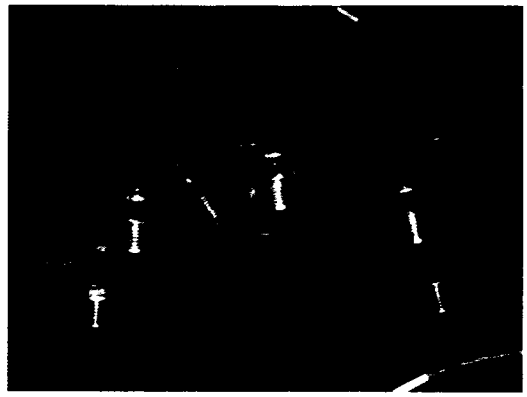

Figure 5-19: Flange used to Connect Pipe Sections

The standards used in determining the initial undamaged state of the joint were taken from Section 1510, Waterline Installation, of the North Carolina Department Of Transportation Standard Specifications For Roads And Structures, which gave the range shown in Table 5-13.

Table 5-13: Torque Specifications for the Bolted Joint

Pipe Size (mm)	Bolt Size (mm)	Range of Torque (N-m)
101.6-609.6	19.05	101.7-122

From these values an initial torque of 108.5 N-m was selected. The bolts connecting the pipe sections together were tightened using a torque wrench with the following procedure:

- Bolts were tightened using a crisscross pattern, such that bolts at 180^0 were tightened sequentially as shown in Figure 5-20
- The bolts were tightened in increments of 20% of the final bolt torque until 80% of the final value was reached
- The bolts were tightened sequentially clockwise around the flange to the final torque value

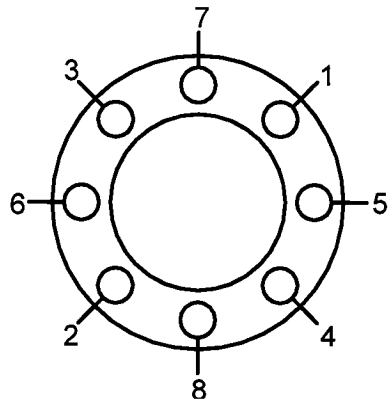

Figure 5-20: Order of Bolt Tightening for the Mechanically Fastened Pipe Joint

The supports of the pipe sections were made using 6" cast iron flanges that were fastened to a massive steel platform. The pipe sections were clamped into the flanges, as shown in Figure 5-21.

Figure 5-21: Support System for the Mechanically Fastened Pipe Joints

The responses of the piezoelectric sensors were continuously monitored with a multi-purpose PCI DT3010 data acquisition card, manufactured by Data Translation (MA, USA), using a differential channel configuration. The data acquisition programs used to monitor the piezoelectric responses was developed in VEE Pro, which is a visual programming software. 40,000 data points monitored for each test at a rate of 10 kHz. Due to noise present in the lab, the computer was powered with the use of a power conditioner, which helps remove the noise from the system.

The loading of the specimens was performed with a PCB Piezotronics 086B01 impulse hammer. The impulse hammer response was monitored continuously using a DT-24EZ data acquisition card, also manufactured by Data Translation, with a single ended channel configuration. The data acquisition programs used to monitor the impulse hammer response was developed in LabVIEW, with the use of DT-LV Link, which is a software that allows LabVIEW to communicate with Data Translation products. For each test there was 10,000 data points monitored at a rate of 10 kHz. Due to the response of the impulse hammer being of order mV, the output was amplified with the use of a PCB Piezotronics Inc. series 790 power amplifier. The power amplifier also eliminated most of the noise from the impulse hammer response signal.

5.3.3 Experimental Procedure

Every experiment was conducted by starting the data acquisition systems then impacting the desired location with the impulse hammer. For each experimental set-up, four tests were performed to ensure consistency and reproducibility in the results. To increase the efficiency of the testing procedure all tests performed with the same set-up were saved to a single file. These results were then separated during the data processing procedure. Due to the available facilities for testing only one side of the pipe sections were impacted. If both sides were to be loaded the set-up would have to be moved, which would effect the set-up parameters, such as set-up alignment as well as joint tightness.

To ensure all test results were processed in the same time scale, the time lag between the time of impact and the piezoelectric response was measured. The method used to determine the time lag was the same as that implemented in the adhesively bonded joints described earlier in this chapter.

5.3.3.1 Pipe Set-up With Span Ratios of 1:1

The test parameters that were varied through the experiments included the load location and joint tightness. The fixture tightness was kept consistent for all experiments at a value of 80 ft-lb.

The influence of the loading location was determined by loading three different locations on a single side of the pipe joint. The values were selected based on one being at the mid-span of the pipe section and the others being equidistant on either side of the mid-span. The locations chosen for applying the impact load are shown in Table 5-14.

Table 5-14: Impulse Hammer Impact Locations for the Pipe Sections with a 1:1 Span Ratio

Excitation Location Number	Distance to the Outer Joint Edge
1	500 mm
2	600 mm
3	700 mm

There were a total of seven different flange set-ups used to simulate the degradation in the mechanical joint. The initial joint had all bolts tightened to a torque of 80 ft-lb. This set-up was tested for all load locations, and then a single bolt was loosened to 40 ft-lb. Once these tests were complete a second bolt was loosened to 40 ft-lb, once these tests were complete a third bolt was loosened to 40 ft-lb. For the last three degrees of damage the three bolts were sequentially removed from the joint. Table 5-15 shows the procedure used to simulate joint damage, and Figure 5-22 shows the numbering of the bolts.

Table 5-15: Bolt Loosening Method Used to Simulate Damage in the Mechanically Fastened Joint

Damage Level	Bolt Torques
0	All Bolts 108.5 N-m

1	Bolt 1 loosened to 54.25 N-m
2	Bolt 2 loosened to 54.25 N-m
3	Bolt 8 loosened to 54.25 N-m
4	Bolt 1 Removed
5	Bolt 2 Removed
6	Bolt 8 Removed

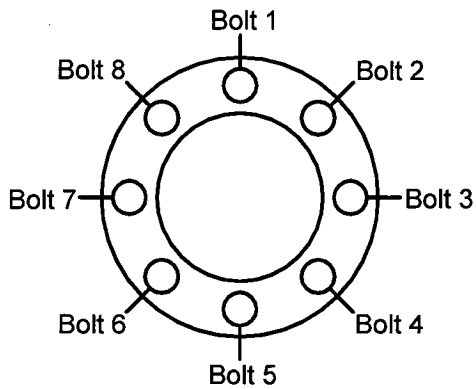

Figure 5-22: Bolt Numbering System for Simulating Damage in the Mechanically Fastened Joint

The test configurations used for the equal span joint tests are shown in Table 5-16.

Table 5-16: Test Configurations for the Mechanically Fastened Pipe Joint with a 1:1 Span Ratio

Test Number	Parameters (Excitation Location, Damage Level)	Test Number	Parameters (Excitation Location, Damage Level)
1	1,0	12	3,3
2	2,0	13	1,4
3	3,0	14	2,4
4	1,1	15	3,4
5	2,1	16	1,5
6	3,1	17	2,5
7	1,2	18	3,5
8	2,2	29	1,6
9	3,2	20	2,6
10	1,3	21	3,6
11	2,3		

5.3.3.2 Pipe Set-up With Span Ratios of 3:1

The test parameters that were varied through the experiments included the load location and joint tightness. The fixture tightness was kept consistent for all experiments at a value of 108.5 N-m.

The influence of the loading location was determined by loading five different locations on a single span of the pipe joint, which in this case was the longer span. The values were selected based on using the same distances from the joint as the equal span pipe set-up, as well as one at mid-span and another at equidistance from the mid-span as the closest point. The locations chosen for applying the impact load are shown in Table 5-17.

Table 5-17: Impulse Hammer Impact Locations for Pipe Sections with a 3:1 Span Ratio

Excitation Location Number	Distance to the Outer Joint Edge
1	500 mm
2	600 mm
3	700 mm
4	840 mm
5	980 mm

The same method used to simulate the degradation of the joint in the equal span pipe set-up was used in this set-up.

The test configurations used for this damage detection investigation for a 3:1 span ratio are shown in Table 5-18.

Table 5-18: Test Configurations for Mechanically Fastened Pipe Joint with a 3:1 Span Ratio

Test Number	Parameters (Excitation Location, Damage Level)	Test Number	Parameters (Excitation Location, Damage Level)
1	1, 0	19	4, 3
2	2, 0	20	5, 3
3	3, 0	21	1, 4
4	4, 0	22	2, 4
5	5, 0	23	3, 4
6	1, 1	24	4, 4
7	2, 1	25	5, 4
8	3, 1	26	1, 5
9	4, 1	27	2, 5
10	5, 1	28	3, 5
11	1, 2	29	4, 5
12	2, 2	30	5, 5
13	3, 2	31	1, 6
14	4, 2	32	2, 6
15	5, 2	33	3, 6
16	1, 3	34	4, 6
17	2, 3	35	5, 6
18	3, 3		

5.3.4 Data Processing Methods

The data processing was performed with the use of several MATLAB codes. For these series of tests the processing method was the same as that used for the adhesively bonded pipe joint, so it will not be explained in detail. The MATLAB codes used for processing the data are provided in Appendix E.

5.3.5 Experimental Results

The frequency response functions for all tests were determined using the Fourier spectrum. For all cases the damage indices were evaluated relative to the undamaged state, as well as to the proceeding state. All damage index numerical results for the

different set-ups, and specimens are shown in Appendix F through I for the 1.2x1.2 m cast iron pipe, 1.8x0.6 m cast iron pipe, 1.2x1.2 m PVC pipe, 1.8x0.6 m PVC pipe sections respectively.

5.3.5.1 Cast Iron Pipe Section With a Span Ratio of 1:1

A typical time-history response and Fourier spectrum for the piezoelectric sensors are shown in Figures 5-23 and 5-24 respectively.

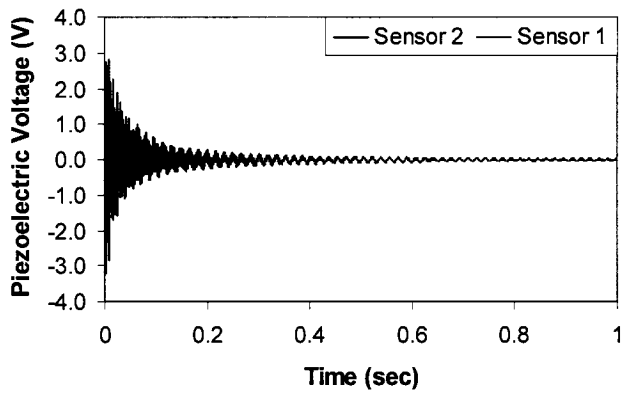

Figure 5-23: Typical Time History Response of the Piezoelectric Sensors for the Cast Iron Mechanically Fastened Pipe Joint with a Span Ratio of 1:1

As can be seen from Figure 5-24, the Fourier spectrum of the two sensors is very different. For the sensor located across the joint from the excitations, sensor 1, approximately 10 different vibration modes make a significant contribution to the spectrum. For the sensor located on the excitation side of the joint, sensor 2, there are only 3 vibration modes that contribute significantly to the spectrum. This is due to the relatively large magnitude of the fundamental frequency at around 700 Hz. With this, sensor 1 would be able to determine the presence of smaller damages as well provide a better indication (larger damage indices) of the presence of damage.

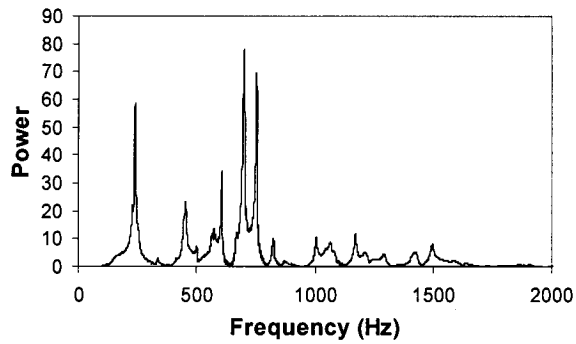

(a)

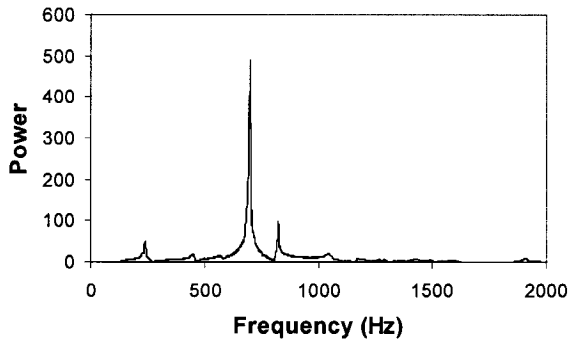

(b)

Figure 5-24: Typical Fourier Spectrum of the Piezoelectric Sensors for the Cast Iron Mechanically Fastened Pipe Joint with a Span Ratio of 1:1 (a) Sensor 1 (b) Sensor 2

5.3.5.1.1 Effect of Sensor Location on Damage Index

To determine the most appropriate location for the piezoelectric sensor in the proposed damage detection system the damage indices for the two sensors are compared in Figure 5-25 for the average RMSD, MAPD, and CC indices, respectively.

■ Sensor 1 ■ Sensor 2

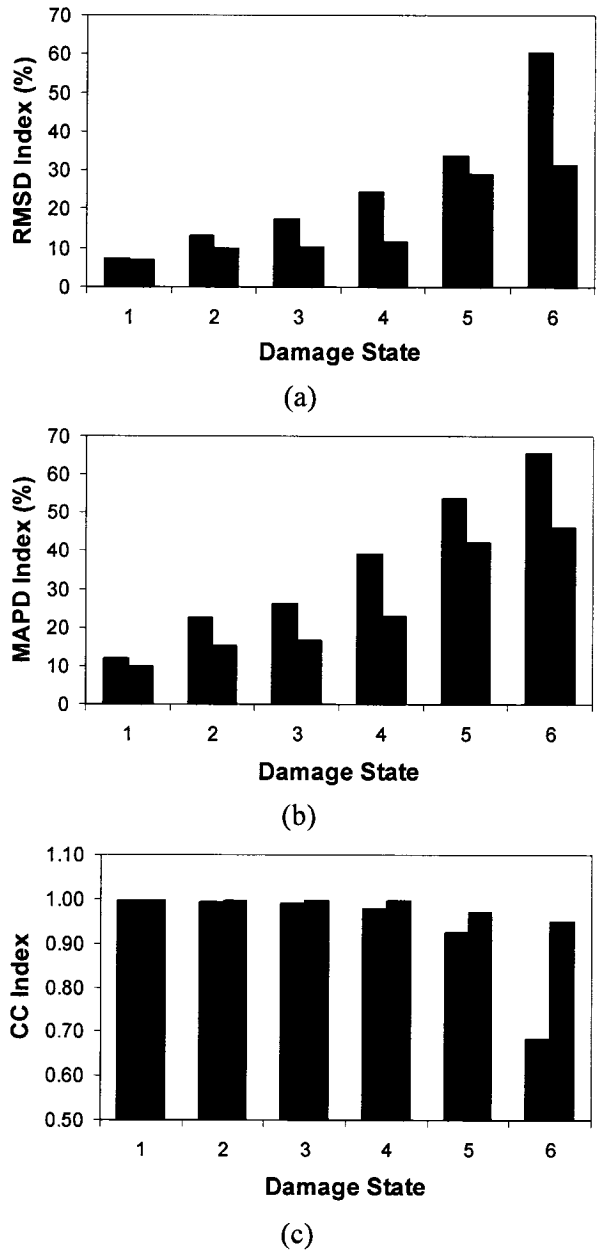

Figure 5-25: Average Damage Indices of the 1.2x1.2m Cast Iron Pipe Section for Excitation Location 1 (a) RMSD Index, (b) MAPD Index, and (c) CC Index

From the above results, it can be clearly seen that the sensor located across the joint from the location of the impact can produce better data for damage detection than the sensor on the loading side. This would be expected since the sensor on the far side of the joint monitors a stimulus that progresses through the joint. As the joint degrades, the intensity

of the vibration wave that progresses through the joint would decrease and a more progressive damage index is seen. For the sensor on the excited side of the joint, a contribution to the response is detected before the wave progresses to the joint. For this sensor, a part of the response is observed without the contribution of the damage. Therefore, in the case of the sensor on the excitation side of the joint, the damage index is seen to progress as the damage progresses, however, the results do not show as much damage growth as the sensor across the joint. Looking at the indices for sensor 1, the RMSD index produces results with the most consistent growth through the progression of the damage. Due to the small values of the CC index, it does not show the progression of the damage until damage state 4. The MAPD index produces results that are consistent with those seen in the RMSD index, with the exception of damage state 2, which was observed to have a relatively large value when compared to damage states 1 and 3.

5.3.5.1.2 Effect of Loading Location on Damage Index

To determine the most effects of the loading location in the proposed damage detection system the damage indices for different loading locations for sensor 1 are compared in Figure 5-26 for the average RMSD, MAPD, and CC indices respectively.

From the results in Figure 5-26, it can be seen that the optimal impact location for this set-up is nearest the joint. In most cases, loading the specimen at this location shows the largest degree of damage but also produces results with the most consistent growth through the progression of the damage.

■ Excitation Location 1 ■ Excitation Location 2 □ Excitation Location 3

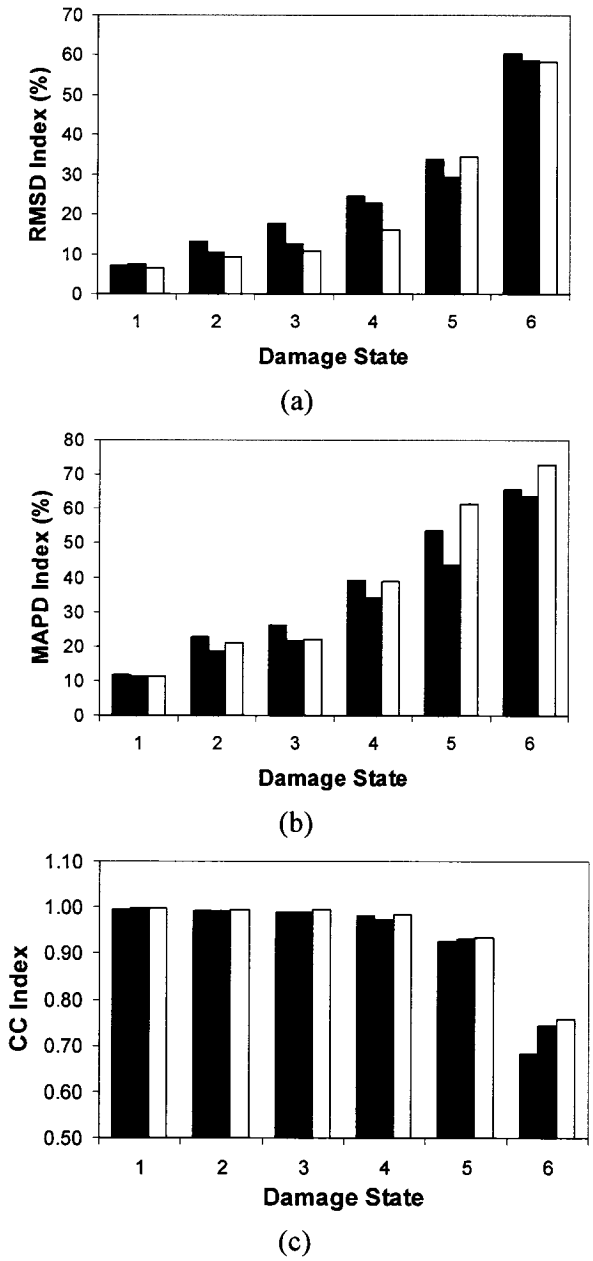

Figure 5-26: Average Damage Indices of Sensor 1 for the 1.2x1.2m Cast Iron Pipe Section with Varying Excitation Locations (a) RMSD Index, (b) MAPD Index, and (c) CC Index

5.3.5.1.3 Relative Damage Index Results

The average RMSD, MAPD, and CC damage indices relative to the preceding state of damage for loading location 1 are shown in Figure 5-27.

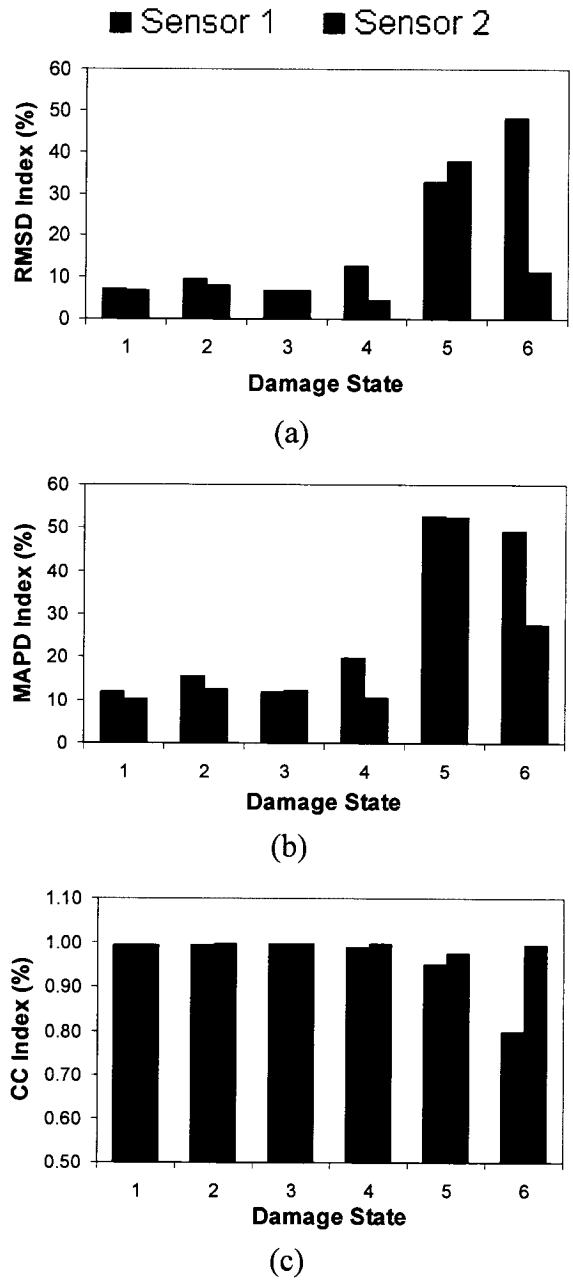

Figure 5-27: Average Damage Indices of the 1.2x1.2m Cast Iron Pipe Section Relative to the Preceding State of Damage (a) RMSD Index, (b) MAPD Index, and (c) CC Index

As can be seen from Figure 5-27, the first 4 damage states produce index values that are fairly consistent when compared to the proceeding state. For the final two degrees of damage, the relative index shows the progression of damage as being much larger. It

should also be noted that sensor 2 produces damage indices that do not reflect as large of a damage, however the values are generally more consistent.

5.3.5.2 Cast Iron Pipe Section With a Span Ratio of 3:1

A typical time-history response and Fourier spectrum for the piezoelectric sensors are shown in Figures 5-28 and 5-29 respectively.

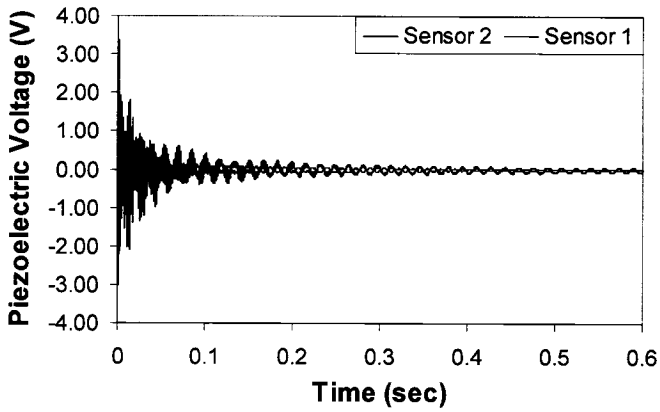

Figure 5-28: Typical Time History Response of the Piezoelectric Sensors for the Cast Iron Mechanically Fastened Pipe Joint with a Span Ratio of 3:1

Similar to the equal spanned cast iron pipe, there is a significant difference in the Fourier spectrum of the two sensors, as seen in Figure 5-29. Sensor 1 has approximately 10 different vibration modes that contribute significantly to the spectrum, whereas, sensor 2 has approximately 6 significant modal contributions.

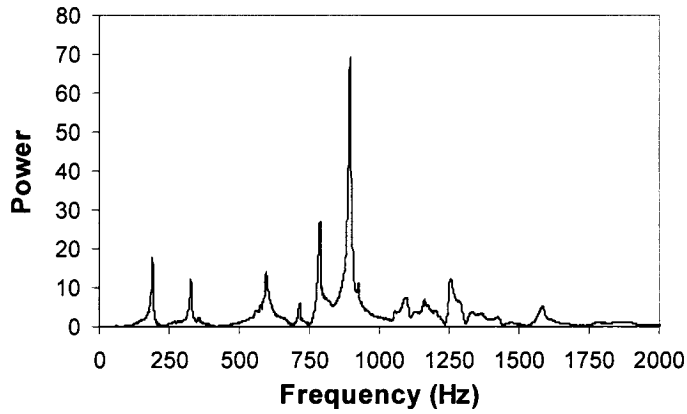

(a)

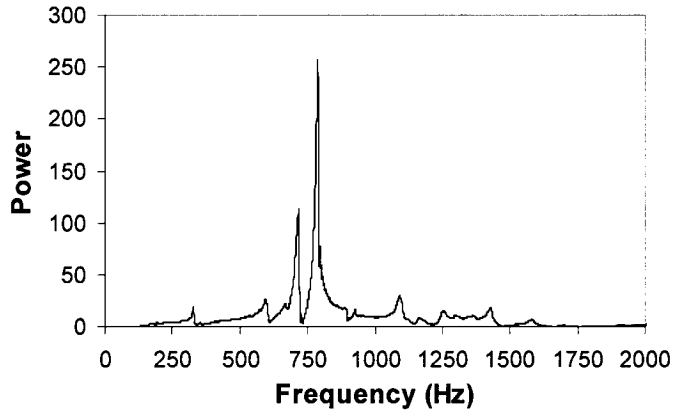

(b)

Figure 5-29: Typical Fourier Spectrum of the Piezoelectric Sensors for the Cast Iron Mechanically Fastened Pipe Joint with a Span Ratio of 3:1 (a) Sensor 1 (b) Sensor 2

5.3.5.2.1 Effect of Sensor Location on Damage Index

To determine the most appropriate location for the piezoelectric sensor in the proposed damage detection system the damage indices for the two sensors are compared in Figure 5-30 for the average RMSD, MAPD, and CC indices respectively.

As was observed in the cast iron section with equal spans, the sensor located across the joint from the impact can produce better data for damage detection than the sensor on the loaded span. As explained previously, this was as expected.

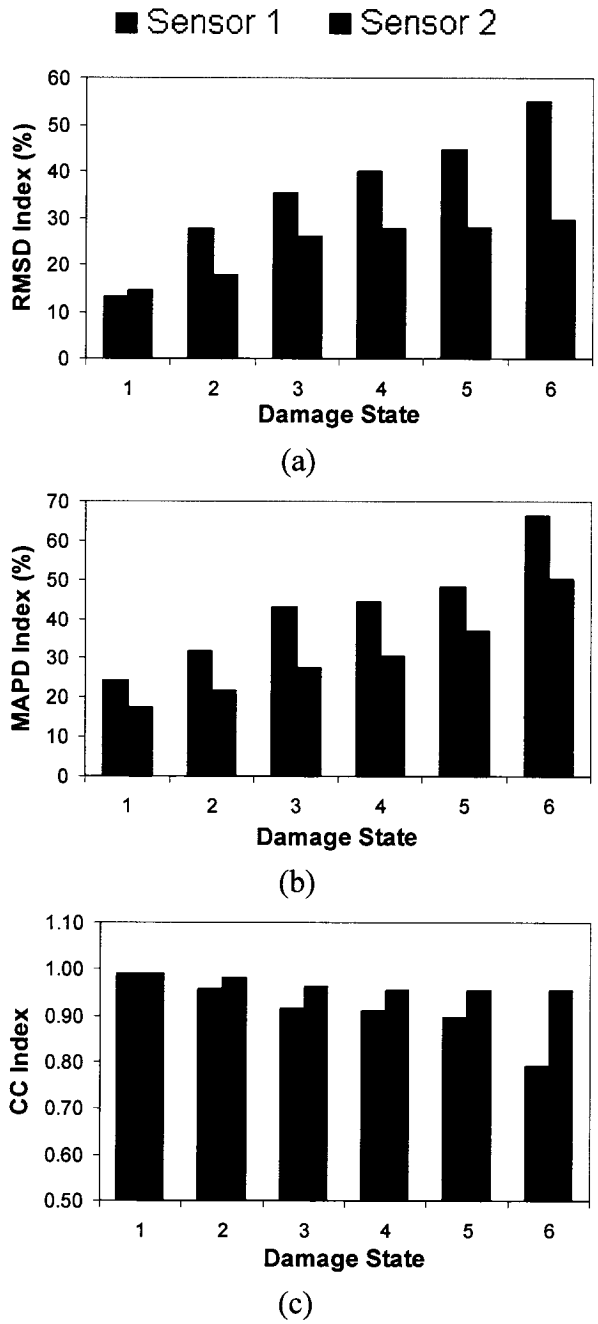

Figure 5-30: Average Damage Indices of the 1.8x0.6m Cast Iron Pipe Section for Excitation Location 1 (a) RMSD Index, (b) MAPD Index, and (c) CC Index

Looking at the indices for sensor 1 in Figure 5-30, it can be seen that the RMSD index produces the most consistent results, where a noticeable increase in the damage index is observed as the damage progresses.

5.3.5.2.2 Effect of Loading Location on Damage Index

The damage indices for different loading locations for sensor 1 are compared in Figure 5-31 for the average RMSD, MAPD, and CC indices, respectively.

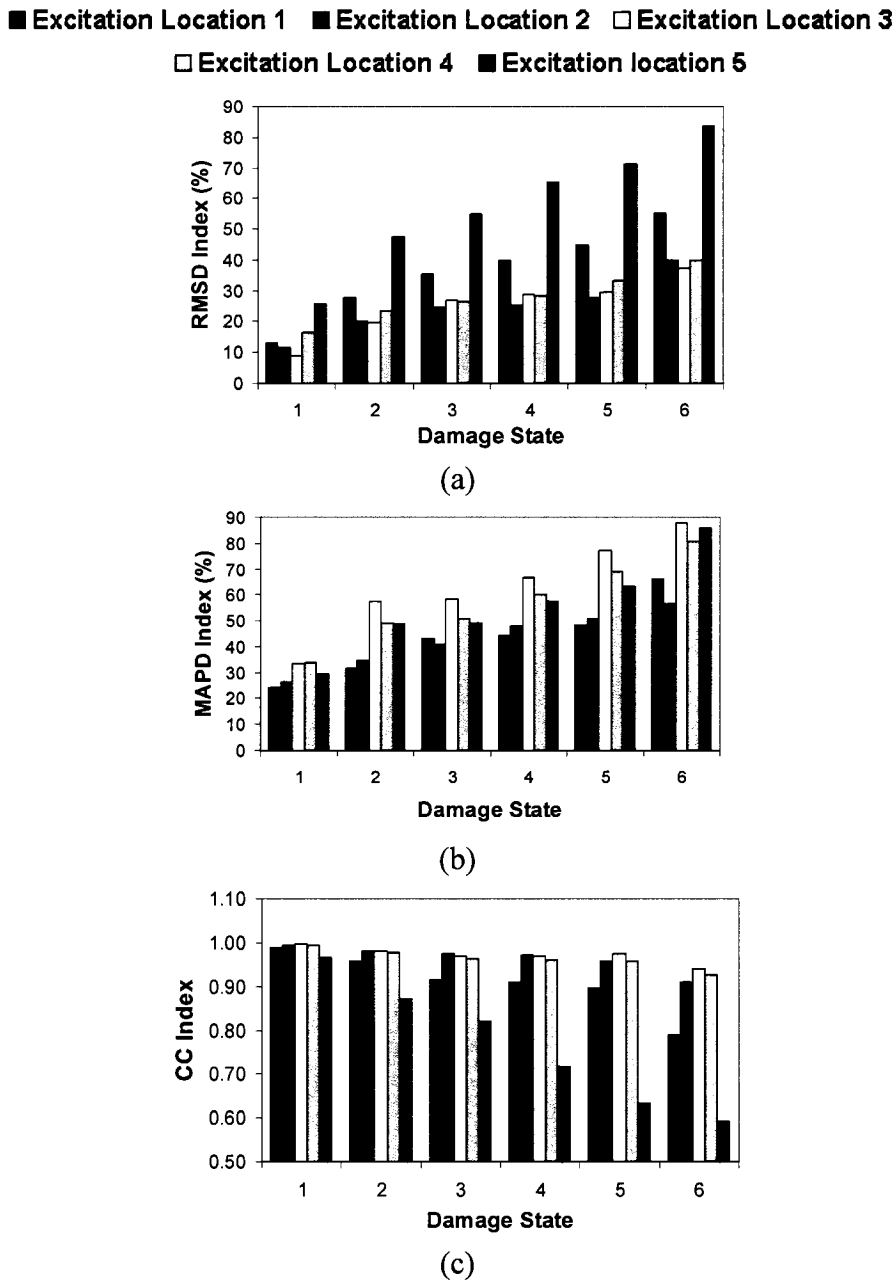

Figure 5-31: Average Damage Indices of Sensor 1 for the 1.8x0.6m Cast Iron Pipe Section with Varying Excitation Locations (a) RMSD Index, (b) MAPD Index, and (c) CC Index

From the above results, it can be seen that the optimal impact location varies with the damage indices implemented. In the case of the RMSD and CC indices, exciting the section away from the sensor, impact location 1 and 5, tends to produce index values that give a better indication of the damage growth. For the MAPD index, all results show a growth in value as the damage progresses, with impact location two producing results with a gradually consistent growth. Also to note is that this index does not produce results as consistent as those observed with the RMSD and CC indices.

5.3.5.2.3 Relative Damage Index Results

The average RMSD, MAPD, and CC damage indices relative to the preceding state of damage for loading location 1 are shown in Figure 5-32.

As can be seen from Figure 5-32, the RMSD and MAPD indices produce relative damage values that vary throughout the progression of the damage. As was observed for the equal span cast iron section, the CC index remains relatively consistent for the first four damage states; with the last two producing index values that show a larger progression in damage.

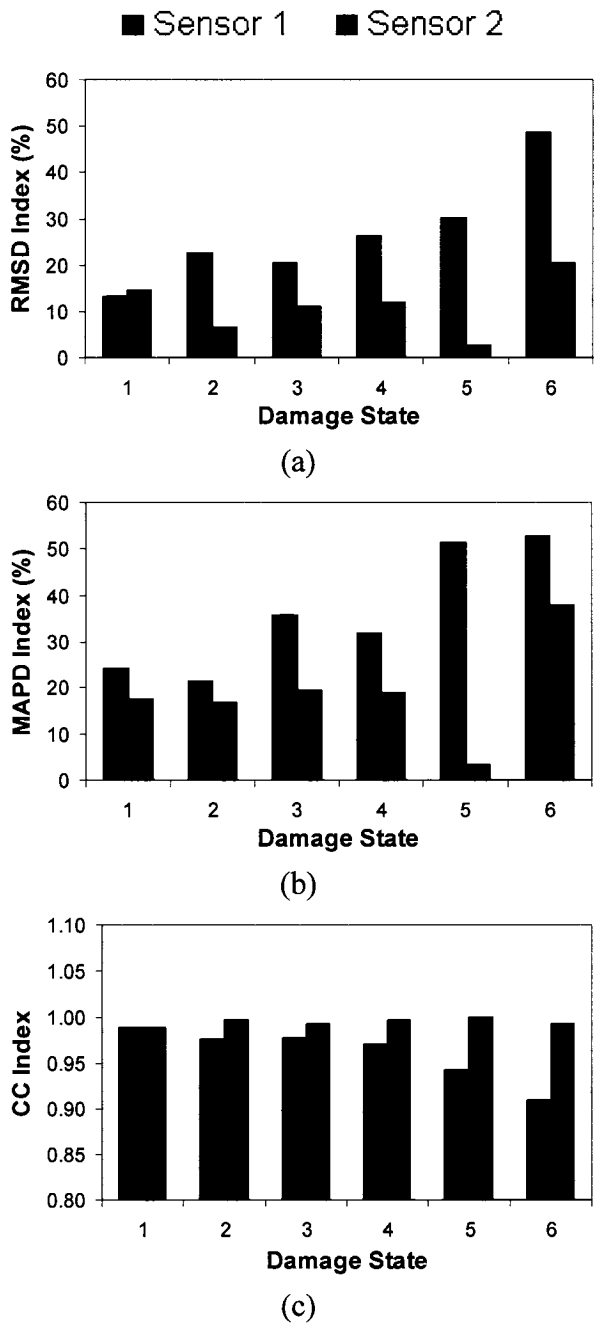

Figure 5-32: Average Damage Indices Relative to the Preceding State of Damage for the 1.8x0.6m Cast Iron Pipe Section (a) RMSD Index, (b) MAPD Index, and (c) CC Index

5.3.5.3 PVC Pipe Section With a Span Ratio of 1:1

A typical time-history response and the Fourier spectrum for the piezoelectric sensors are shown in Figures 5-33 and 5-34, respectively.

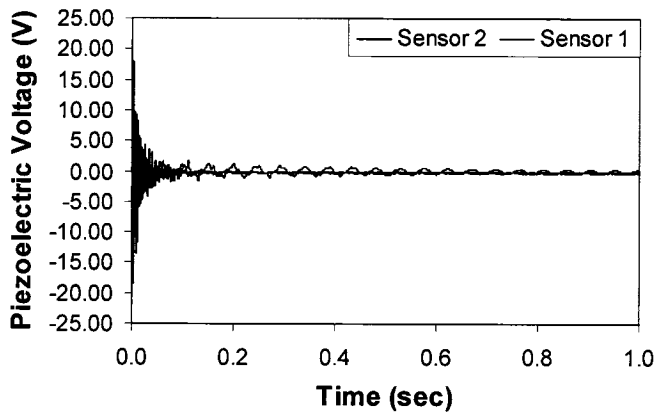

Figure 5-33: Typical Time History Response of the Piezoelectric Sensors for the PVC Mechanically Fastened Pipe Joint with a Span Ratio of 1:1

Similar to the cast iron pipe sections, there is a significant difference in the Fourier spectrum of the two sensors, as seen in Figure 5-34. A major difference in the two spectrums is observed in the position of the dominant frequencies. Sensor 1 had major contributions from frequencies in the range of 100-200 Hz, along with significant contributions in the range of 300-500 Hz. The dominant frequencies in the response of Sensor 2 were observed in the frequency range of 300-500 Hz, with a significant contribution between 800-900 Hz, and a smaller contribution in the lower frequency range of 100-200 Hz. Also it was observed that sensor 1 has approximately 9 different vibration modes that contribute to the spectrum, whereas, sensor 2 has approximately 5 significant modal contributions.

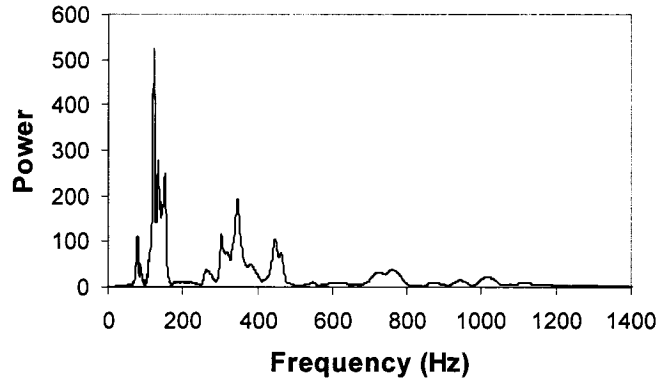

(a)

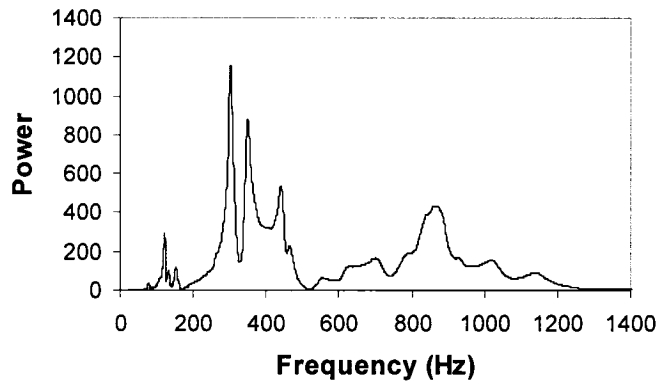

(b)

Figure 5-34: Typical Fourier Spectrum of the Piezoelectric Sensors for the PVC Mechanically Fastened Pipe Joint with a Span Ratio of 1:1 (a) Sensor 1 (b) Sensor 2

5.3.5.3.1 Effect of Sensor Location on Damage Index

To determine the most appropriate location for the piezoelectric sensor in the proposed damage detection system the damage indices for the two sensors are compared in Figure 5-35 for the average RMSD, MAPD, and CC indices, respectively.

As was observed with both span ratios in the cast iron sections the sensor located across the joint from the impact produces a better indication of the degree of damage then the sensor on the excitation side.

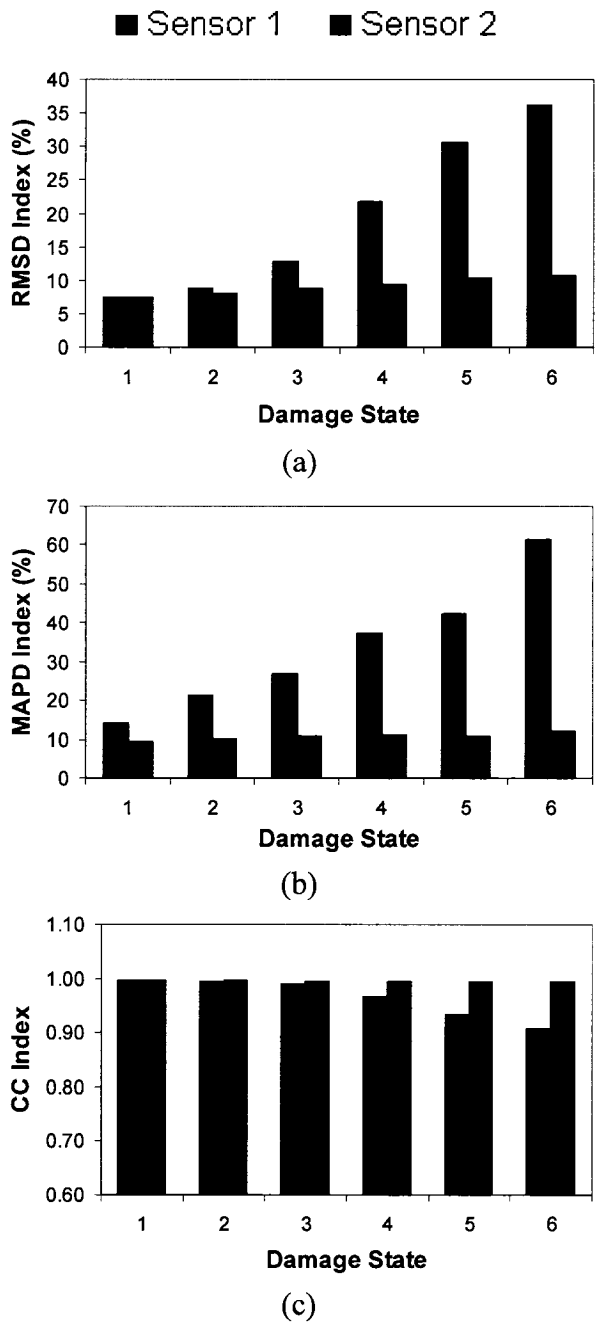

Figure 5-35: Average Damage Indices for the 1.2x1.2m PVC Pipe Section for Excitation Location 1 (a) RMSD Index (b) MAPD Index (c) CC Index

5.3.5.3.2 Effect of Loading Location on Damage Index

To determine the most effects of the loading location in the proposed damage detection system the damage indices for different loading locations for sensor 1 are compared in Figure 5-36 for the average RMSD, MAPD, and CC indices respectively.

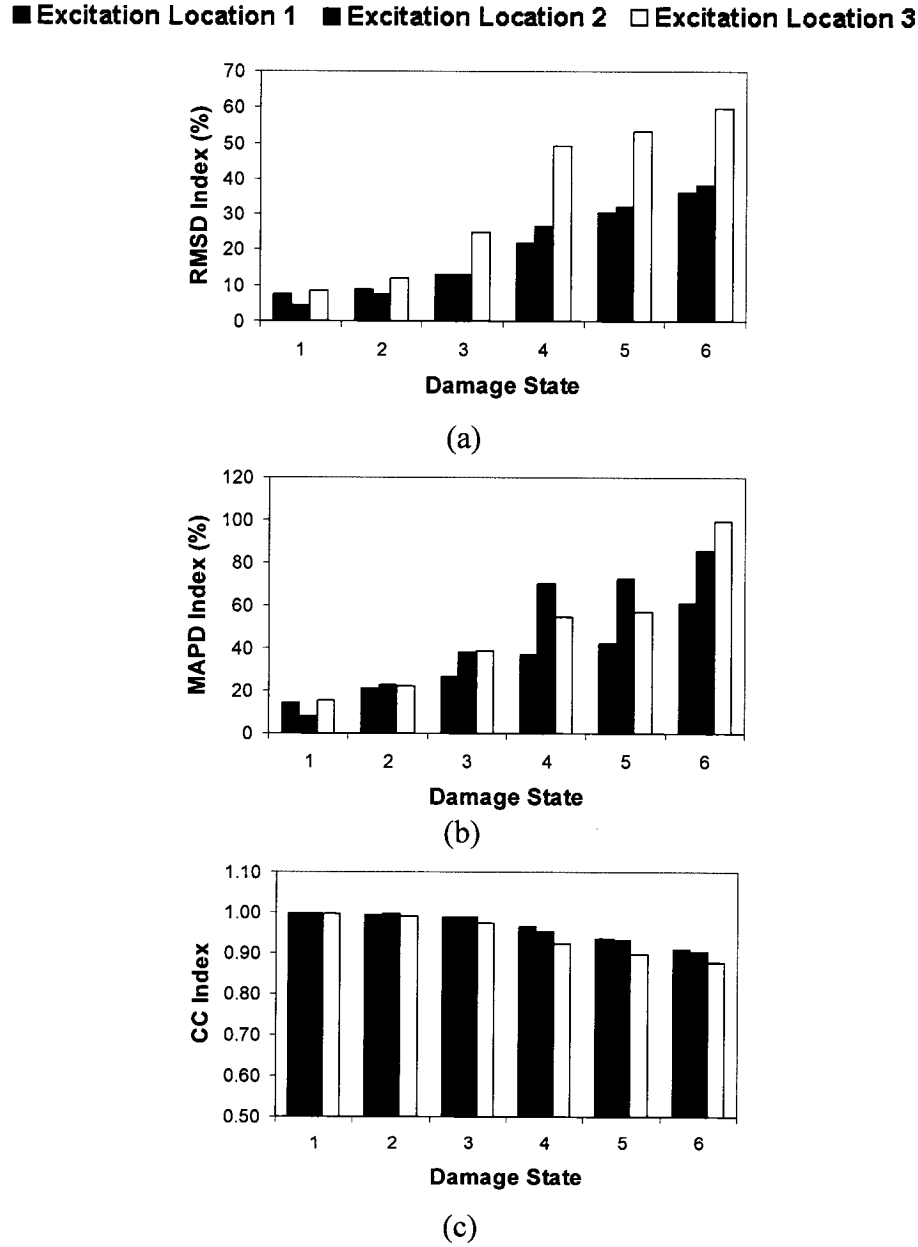

Figure 5-36: Average Damage Indices of Sensor 1 for the 1.2x1.2m PVC Pipe Section with Varying Excitation Locations (a) RMSD Index, (b) MAPD Index, and (c) CC Index

In general, from the above results it can be seen that excitation location three produces the most pronounced damage index level. However, in the case of the RMSD and MAPD indices, exciting the section at location one produces results with more consistent growth throughout the progression of the damage. The CC index produces consistent results for all excitation locations, with location three producing results indicating the largest damage growth.

5.3.5.3.3 Relative Damage Index Results

The average RMSD, MAPD, and CC damage indices relative to the preceding state of damage for loading location 1 is shown in Figure 5-37.

Unlike the relative damage indices that were observed with the cast iron section, the RMSD and MAPD indices produce values that are relatively inconsistent throughout the progression of damage. When evaluating the damage growth implementing the relative CC index, very consistent results were observed. However, as was reported earlier the CC index produces results that seem much less sensitive to the damage progression. This can be observed in Figure 5-36, where only a 10% change in the index value is observed in damage state 6 relative to the undamaged state. Therefore, a more consistent relative measure would be expected using the CC index, as was seen in the cast iron sections.

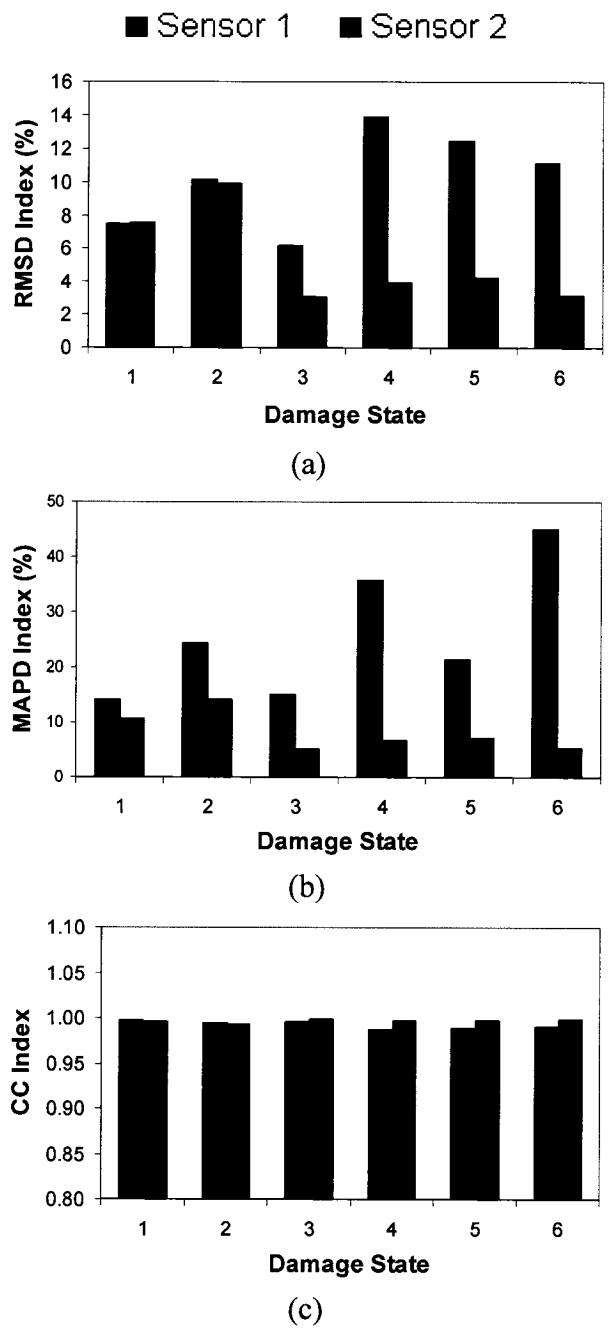

Figure 5-37: Average Damage Indices Relative to the Preceding State of Damage for the 1.2x1.2m PVC Pipe Section (a) RMSD Index, (b) MAPD Index, and (c) CC Index

5.3.5.4 PVC Pipe Section With a Span Ratio of 3:1

A typical time-history response and Fourier spectrum for the piezoelectric sensors are shown in Figures 5-38 and 5-39, respectively.

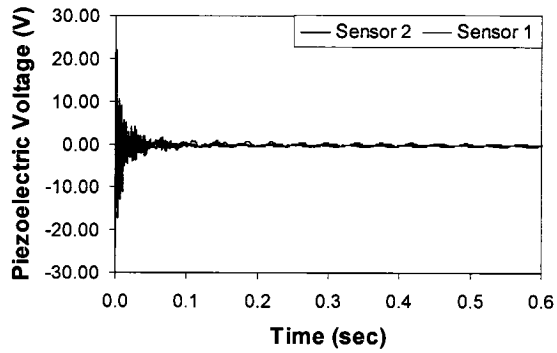

Figure 5-38: Typical Time History Response of the Piezoelectric Sensors for the PVC Mechanically Fastened Pipe Joint with a Span Ratio of 3:1

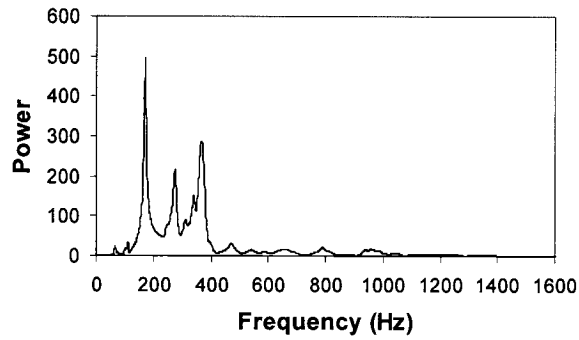

(a)

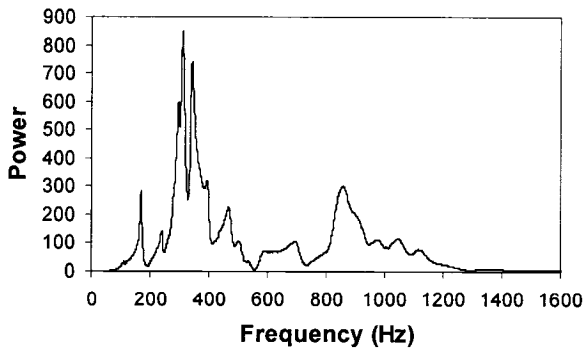

(b)

Figure 5-39: Typical Fourier Spectrum of the Piezoelectric Sensors for the PVC Mechanically Fastened Pipe Joint with a Span Ratio of 3:1 (a) Sensor 1 (b) Sensor 2

Unlike all other tests configurations, for this set-up, it was observed that sensor 1 contains fewer frequency contributions to its Fourier spectrum then observed for sensor 2, as shown above in Figure 5-39. With the PVC pipe having a 3:1 span ratio, the weight of the flange has a more pronounced mass effect on the response then with the stiffer cast iron and equal span PVC sections. This would reduce the number of frequency components observed by a sensor on the non-impacted side of the joint, where there is only three major contributions. It should be noted, that sensor 2 still contains a similar number of significant frequency contributions as was observed in the other sections with six. The extra contributions observed in sensor 2 are the higher modes, circumferential and higher bending modes, that would be caused by the proximity of the impact.

5.3.5.4.1 Effect of Sensor Location on Damage Index

To determine the most appropriate location for the piezoelectric sensor in the proposed damage detection system, the damage indices for the two sensors are compared in Figure 5-40 for the average RMSD, MAPD, and CC indices, respectively.

As was observed in all cases, the optimal location for the piezoelectric sensor is across the joint from the excitation as was explained earlier.

5.3.5.4.2 Effect of Loading Location on Damage Index

To determine the most effects of the loading location in the proposed damage detection system the damage indices for different loading locations for sensor 1 are compared in Figure 5-41 for the average RMSD, MAPD, and CC indices, respectively.

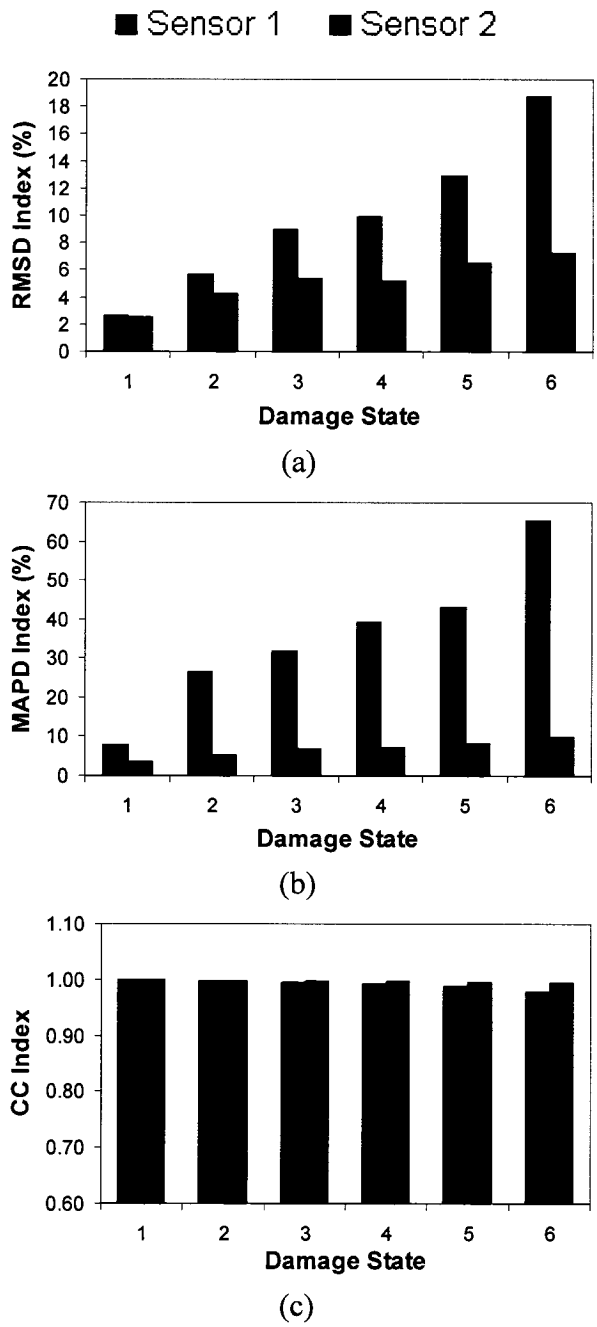

Figure 5-40: Average Damage Indices for 1.8x0.6m PVC Pipe Section for Excitation Location 1 (a) RMSD Index, (b) MAPD Index, and (c) CC Index

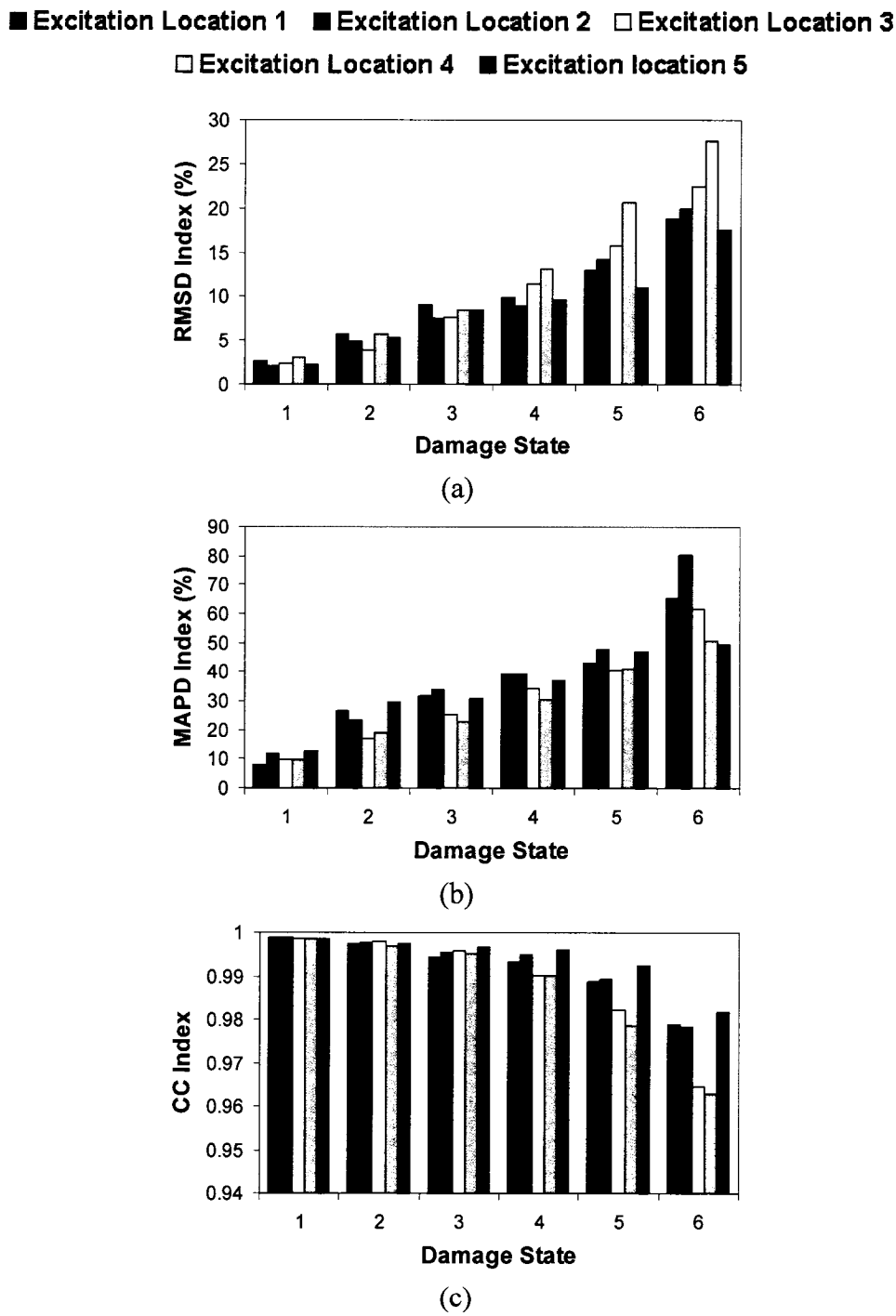

Figure 5-41: Average Damage Indices of Sensor 1 for the 1.8x0.6m PVC Pipe Section with Varying Excitation Locations (a) RMSD Index, (b) MAPD Index, and (c) CC Index

Unlike the other pipe sections studied in this investigation, the optimal excitation location is in the vicinity of center span. For this section, the results for excitation locations three and four produce results with the most consistent growth, and for the RMSD and CC indices indicate the largest presence of damage. This is thought to be due to the decreased number of modes exhibited in the response of sensor 2. For sensor 2, the major frequency contributions are the lower bending modes, which are excited more easily by impacting the pipe near its mid-span. Therefore, more significant changes in the Fourier spectrum are observed with excitation near the mid-span of the section.

5.3.5.4.3 Relative Damage Index Results

The average RMSD, MAPD, and CC damage indices relative to the preceding state of damage for loading location 1 is shown in Figure 5-42.

As was seen with the equal span PVC section, the relative RMSD and MAPD damage indices for sensor 1, are not consistent throughout the progression of the damage. Also as was observed with the equal span PVC pipe, the relative CC index is consistent over the progression of the damage, for the same reasoning as described earlier.

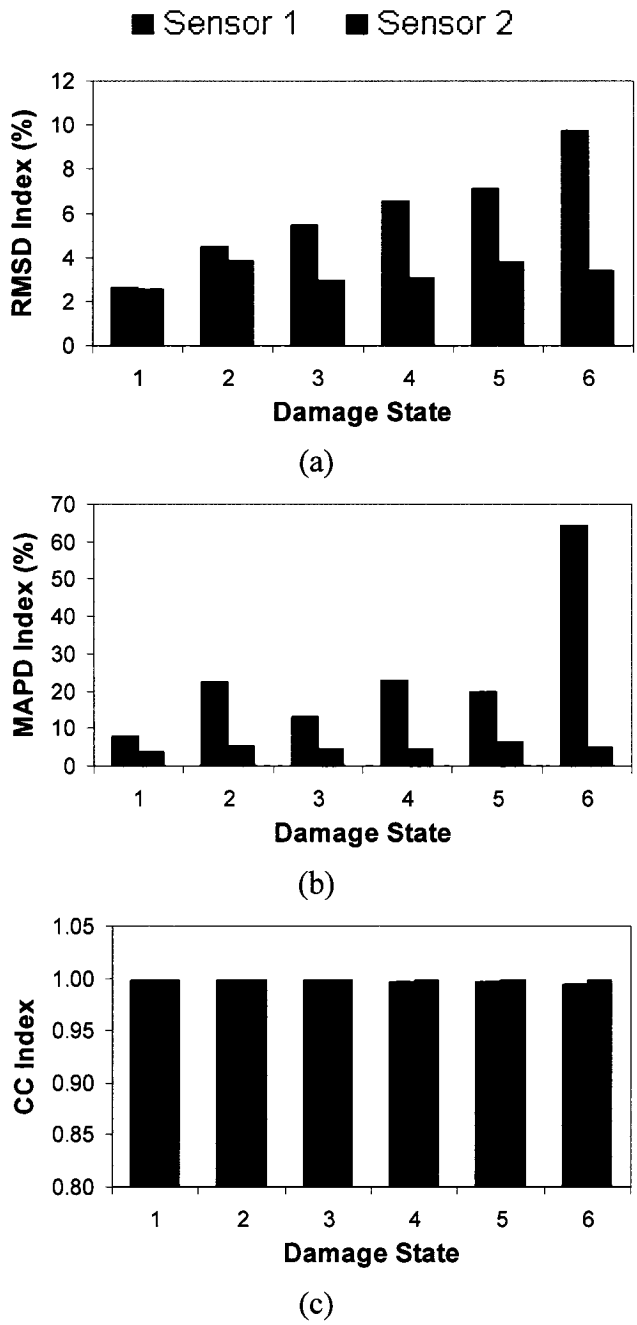

Figure 5-42: Average Damage Indices Relative to the Preceding State of Damage for the 1.8x0.6m PVC Pipe Section (a) RMSD Index, (b) MAPD Index, and (c) CC Index

Chapter 6

Behavior of Piezoelectric Laminate Plates

6.1 Introduction

Compared to conventional engineering materials, composites can be designed to produce exceptional strength and stiffness with minimum weight. A measure of these attributes are the so-called "specific properties" in which the either strength or stiffness are divided by material's density. For the reasons mentioned above the applications of composite materials have been expanding at an extraordinary rate over the past decades. Along with composite materials, the field of smart materials, such as piezoelectrics, shape memory alloys, magnetostrictives, and newer materials like magnetic shape memory alloys have been rapidly expanding. One of the major reasons for this is the ease of application due to the tailor ability of the lighter weight composite materials. Applications such as vibration control, shape control, and damage detection have been investigated in varying levels with most smart materials. In vibration suppression and damage detection applications, piezoelectric materials have been leading the way. Some of the reasons for this include a full range of sizes available, ease of implementation, relatively lower expense, and the linear elastic behavior to name a few. With the increase in applications of both smart materials and laminated composites a full understanding of their capabilities and limitations must be explored.

6.2 Fiber Reinforced Polymer (FRP) Composites

Composite materials are used increasingly in high-performance applications that require high specific strength and/or stiffness, low electrical conductivity, transparency to radio emissions, resistance to corrosion, etc. In such applications, these composites represent highly engineered materials with properties carefully tailored to the application. Understanding the mechanical response issues surrounding these materials requires an understanding of material science, manufacturing methods, failure mechanisms,

environmental effects, fractography, composite design, maintenance, inspection, and the effects of impact and environmental damage. The most common fiber materials used in polymeric composites are glass, carbon, and aramid.

Glass is the most common material used for commercial fiber reinforced polymer composites, and comes in several different grades. E-Glass is the most inexpensive and commonly used fiber. The "E" designation stands for "electrical" because of its superior insulative properties. E-Glass has high fiber strength relative to both carbon and aramid (~3.5 GPa) and relatively low fiber modulus (~72 GPa). S-Glass is an aerospace type of glass, which is stronger (~4 GPa) and higher modulus (~86 GPa). The "S" designation is for "strength," and is a trade name of Owens-Corning Inc (Toledo, OH). C-Glass is a corrosion resistant type of glass, and is usually used as a surfacing veil cloth on outer surfaces of laminates, or against tool surfaces to protect the laminate from corrosion. Typical density for a glass/epoxy composite with 60% fiber volume is ~2000 kg/m^3. Often combined with a polyester or epoxy, this combination is relatively inexpensive when compared to other composite materials. Product examples include: boat hulls and marine structures, automotive panels, pressure vessels, military ordinance, and oil field pipe to name a few.

Aramid fibers offer exceptional tensile properties but are very poor in compressive applications. The most widely used aramid fibers are "Kevlar®," which is a Dupont Inc. tradename. Kevlar® has a high fiber modulus (~186 GPa) relative to glass. Kevlar is made in two types: Kevlar 29, and Kevlar 49. These fibers have a modulus of 70 GPa and 112 GPa respectively, and both have a strength of ~3.5 GPa. Kevlar is an extremely tough fiber used for ballistic armor and damage tolerance in laminates. Kevlar is hygroscopic, susceptible to creep, and extremely tough to machine. Typical properties of a Kevlar 49 unidirectional laminate with 60% fiber volume: modulus: 83 GPa, strength: ~2.2 GPa, and density: ~1400 kg/m^3. Product examples of aramid include pressure vessels, armor, and cordage.

Carbon fibers offer exceptional strength and stiffness and are most commonly combined with an epoxy or phenolic matrix. Carbon (graphite) fibers possess both high fiber modulus (<230 to 827+ GPa), and high fiber strength (<1.4 to 6.9 GPa). Typical properties of a unidirectional carbon/epoxy unidirectional laminate with 60% fiber volume are a modulus of <100 GPa to 413+ GPa, strength: 1.4 GPa to 4.1 GPa and density of ~1550 kg/m^3. Product examples with carbon fibers include aircraft and aerospace components, military ordinance, drive shafts, pressure vessels, and recreational products such as golf shafts and bicycles to name a few.

6.2.1 Classical Laminate Plate Theory

The classical lamination plate theory (CLPT) is almost identical to the classical plate theory (CPT) with the only difference being the constituent material properties (stress-strain relations). The CPT usually assumes that the material is isotropic, while a fiber reinforced composite laminate with multiple layers may have more complicated stress-strain relations. The four cornerstones of the lamination theory are the kinematic, constitutive, force resultant, and equilibrium equations are shown in equations [6.1] through [6.4] respectively.

$$\begin{Bmatrix} \varepsilon_x \\ \varepsilon_y \\ \gamma_s \end{Bmatrix} = \begin{Bmatrix} \varepsilon_x^O \\ \varepsilon_y^O \\ \gamma_s^O \end{Bmatrix} + z\begin{Bmatrix} \kappa_x \\ \kappa_y \\ \kappa_s \end{Bmatrix} = \begin{Bmatrix} \dfrac{\partial u_o}{\partial x} \\ \dfrac{\partial v_o}{\partial y} \\ \dfrac{\partial u_o}{\partial y} + \dfrac{\partial v_o}{\partial x} \end{Bmatrix} + z\begin{Bmatrix} \dfrac{\partial^2 w}{\partial x^2} \\ \dfrac{\partial^2 w}{\partial y^2} \\ -\dfrac{2\partial^2 w}{\partial x \partial y} \end{Bmatrix} \qquad [6.1]$$

where:

ε_x, ε_y = the strain in the x and y direction respectively (m/m)

γ_s = shear strain in the xy plane (m/m)

ε^o = strain components at the neutral axis (m/m)

κ = curvature (m^{-1})

z = distance to layer from the neutral axis (m)

$$\begin{Bmatrix} \sigma_x \\ \sigma_y \\ \tau_s \end{Bmatrix}_k = \begin{bmatrix} Q_{xx} & Q_{xy} & Q_{xs} \\ Q_{yx} & Q_{yy} & Q_{ys} \\ Q_{sx} & Q_{sy} & Q_{ss} \end{bmatrix}_k \begin{Bmatrix} \varepsilon_x \\ \varepsilon_y \\ \gamma_s \end{Bmatrix}_k \qquad [6.2]$$

where:

σ_x and σ_y = stress in x and y direction respectively (Pa)

τ_s = shear stress in xy plane (Pa)

Q_{ij} = stiffness matrix components (Pa)

i, j = x, y, or shear, s, directions

$$\begin{bmatrix} N_x \\ N_y \\ N_s \end{bmatrix} = \sum_{k=1}^{n} \int_{h_{k-1}}^{h_k} \begin{Bmatrix} \sigma_x \\ \sigma_y \\ \tau_s \end{Bmatrix}_k dz$$

$$\begin{bmatrix} M_x \\ M_y \\ M_s \end{bmatrix} = \sum_{k=1}^{n} \int_{h_{k-1}}^{h_k} \begin{Bmatrix} \sigma_x \\ \sigma_y \\ \tau_s \end{Bmatrix}_k z dz \qquad [6.3]$$

where:

N_x and N_y = normal forces per unit length in the x and y directions, respectively (N/m)

N_s = shear force per unit length in xy plane (N/m)

M_x and M_y = bending moments per unit length in x and y directions, respectively (N.m/m)

M_s = twisting moment per unit length (N.m/m)

$$\frac{\partial N_x}{\partial x}+\frac{\partial N_{yx}}{\partial y}=-p_x$$
$$\frac{\partial N_{xy}}{\partial x}+\frac{\partial N_y}{\partial y}=-p_y \qquad [6.4]$$
$$\frac{\partial^2 M_x}{\partial x^2}+2\frac{\partial^2 M_{xy}}{\partial x \partial y}+\frac{\partial^2 M_y}{\partial y^2}=-p_z$$

where:

p_x, p_y, and p_z = distributed external loads applied in the x, y, and z directions respectively (Pa)

The plate is constructed by a homogeneous, but not necessarily isotropic material, and subjected to both transverse and in-plane loadings. The goal is to develop the relations between the external loadings and the displacements. However, the relations between the resultant forces, N and M, and the strains, e and k are of most interest in practice. Therefore by substituting for the stresses in the force resultant equations we get the following expressions for the force-deformation and moment-deformation equations.

$$\begin{bmatrix} N \\ M \end{bmatrix}=\begin{bmatrix} A & B \\ B & D \end{bmatrix}\begin{bmatrix} \varepsilon^O \\ \kappa \end{bmatrix} \qquad [6.5]$$

where:

A = extensional stiffness relating in-plane loads to in-plane strain (Pa)

B = coupling stiffness relating in-plane loads to curvatures and moments to in-plane strains (Pa.m)

D = bending stiffness relating moments to curvatures ($Pa.m^2$)

These stiffness matrices are found using the following expressions.

$$A_{ij} = \sum_{k=1}^{n} Q_{ij}^{k}\left(h_k - h_{k-1}\right)$$
$$B_{ij} = \frac{1}{2}\sum_{k=1}^{n} Q_{ij}^{k}\left(h_k^2 - h_{k-1}^2\right) \qquad [6.6]$$
$$D_{ij} = \frac{1}{3}\sum_{k=1}^{n} Q_{ij}^{k}\left(h_k^3 - h_{k-1}^3\right)$$

where:

h_k and h_{k-1} = z-coordinates of the upper and lower surfaces of layer k (m)

i, j = x, y, s.

6.2.2 Interlaminar Stresses and Delamination in Laminated Composites

As was discussed in the previous section, the CLPT assumes plane stress conditions, inferring that the out-of-plane stress, σ_z, τ_{yz}, and τ_{xz} are negligible. In locations that do not include discontinuities this assumption is justified, however near discontinuities or defects, such as free edges and voids, this condition would not hold. In regions near these discontinuities or defects, out-of-plane stresses, also known in laminates as interlaminar stresses as well as out-of-plane normal stresses, are generated. Due to the presence of such stresses, laminates are susceptible to delaminations, constituting one of the most common failure modes in laminated composites. The existence of delaminations will lead to a decrease in stiffness and considerable degradation in the strength and service life of the laminate component. The following sections give a brief description of the causes of interlaminar stresses.

6.2.2.1 Material Discontinuities

The most investigated and documented type of discontinuity in laminated composites is the free edge effect. This may be at the actual edge of the laminated component or a manufactured discontinuity such as a bolthole. The stress distribution across the width of a $[\pm\theta]_s$ laminate take the form shown in Figure 6-1, along with the effect of ply angle on the interlaminar shear stress.

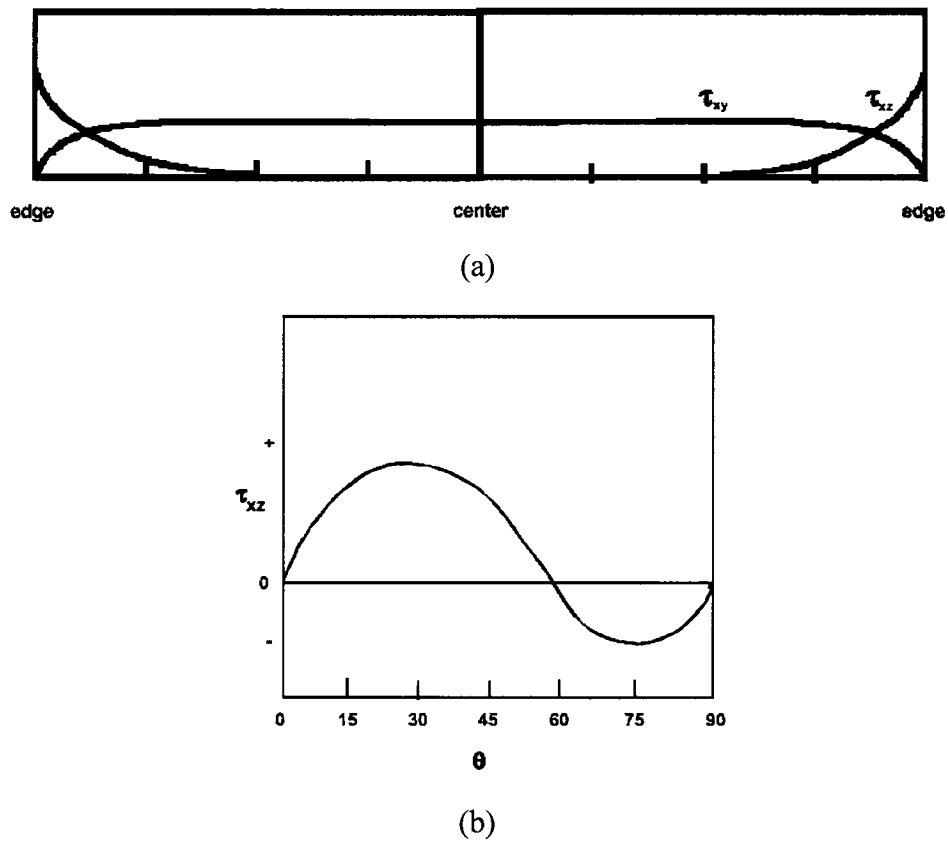

Figure 6-1: (a) Distribution of Shear Stresses τ_{xy} and τ_{xz} Across the Width of a Laminate (b) Effect of Fiber Angle on the Interlaminar Shear Stress τ_{xz}

In order to balance the forces at the free edge of the laminated composite an out-of-plane stress, σ_z, must be developed to counter act the interlaminar shear stresses. This non-zero stress, σ_z, tends to peel the plies apart, when it is a tensile stress, while the non-zero stresses, τ_{yz} and τ_{xz}, tend to slide the plies over one another, thus causing them to delaminate.

6.2.2.2 Manufacturing Defects

When laminated composites are manufactured there is always the possibility of impurities in the component such as voids, resin rich regions or matrix cracks. These defects will result in stress concentrations at the point of the defect leading to larger

interlaminar stresses. With the increase in interlaminar stress the growth of the defects is probable. If the defects are located within the same region of the laminate they will join to develop a larger defect, which could cause a decrease in stiffness, strength and eventually premature failure.

6.2.3 Piezoelectric Laminate Plate Behavior

From the expressions derived in the past sections a model of an integrated piezoelectric plate can now be developed. The following assumptions are made about the piezoelectric patch(s) or layer(s) in the development of the expressions:

- Plane stress is assumed (i.e. thickness << other dimensions)
- The Kirchhoff assumptions holds (i.e. A fiber normal to the mid plane remains normal to the mid plane after deformation. Ignore transverse shear)
- Uniform electric field and displacement through the thickness
- Linear piezoelectric behavior
- No contribution from the sensor to in-plane shear stresses ($e_{36} = 0$)

With the above assumptions the piezoelectric constitutive relationship can be reduced to the form shown in equation [6.7].

$$\begin{Bmatrix} T_{11} \\ T_{22} \\ T_{12} \end{Bmatrix} = \left[c^{E}\right] \begin{Bmatrix} S_{11} \\ S_{22} \\ 2S_{12} \end{Bmatrix} - \begin{Bmatrix} e_{31} \\ e_{32} \\ 0 \end{Bmatrix} E \qquad [6.7]$$

where:

T_{11} and T_{22} = stress in the x and y direction respectively (Pa)

T_{12} = shear stress in xy plane (Pa)

$[c^E]$ = piezoelectric stiffness matrix (Pa)

S_{11} and S_{22} = strain in the x and y direction, respectively (m/m)

S_{12} = shear strain in xy plane (m/m)

e_{31} and e_{32} = piezoelectric charge coefficients at constant electric field (C/m^2)

E = electric field (V/m)

$$D = \{e_{31} \quad e_{32} \quad 0\}\{S\} + \varepsilon^S E \qquad [6.8]$$

where:

D = electric displacement (C/m^2)

ε^s = permittivity at constant strain (F/m)

A laminate is created by bonding several layers, can be at different fiber orientations, such that it acts as one material. It is assumed that the bond between layers is perfect, which ensures continuous displacement across the layer boundaries. From this the constitutive relations can be written in the following form for the k^{th} layer in the piezoelectric laminate.

$$\{T\} = [\overline{Q}]_k \{S\}_k - [R_T]_k^{-1} \begin{Bmatrix} e_{31} \\ e_{32} \\ 0 \end{Bmatrix}_k E_k \qquad [6.9]$$

where:

$[\overline{Q}]_k$ = stiffness matrix of layer k

$[R_T]$ = rotation matrix relating the stress in piezoelectric material directions to the global axis directions

$$D = \{e_{31} \quad e_{32} \quad 0\}_k [R_S]_k \{S\}_k + \varepsilon_k E_k \qquad [6.10]$$

where:

$[R_S]$ = rotation matrix relating the strain in piezoelectric material directions to the global axis directions

Equation [6.11] relates the stiffness of the layer in the global coordinate system, $[\overline{Q}]_k$, to the stiffness matrix $[c^E]$.

$$\left[\overline{Q}\right]_k = \left[R_T\right]_k^{-1}\left[c^E\right]_k\left[R_S\right]_k \qquad [6.11]$$

As mentioned previously the assumption of a constant electric field across the thickness, t_k, of the piezoelectric layer, the electric field of an individual piezoelectric layer can be represented by equation [6.12].

$$E_k = -\phi_k / t_k \qquad [6.12]$$

where:

ϕ_k = the electric potential across the piezoelectric layer (V)

t_k = thickness of piezoelectric layer (m)

The constitutive equation of the laminate relating the in-plane forces, N, and bending moments, M, can be determined by integrating equation [6.9] over the thickness of the laminate, which results in equation [6.13].

$$\begin{Bmatrix} N \\ M \end{Bmatrix} = \begin{bmatrix} A & B \\ B & D \end{bmatrix}\begin{Bmatrix} \varepsilon^O \\ \kappa \end{Bmatrix} + \sum_{k=1}^{n}\begin{bmatrix} I_{3x3} \\ z_{mk} I_{3x3} \end{bmatrix}\left[R_T\right]_k^{-1}\begin{Bmatrix} \varepsilon_{11} \\ \varepsilon_{12} \\ 0 \end{Bmatrix}_k \phi_k dz \qquad [6.13]$$

where:

I_{3x3} = 3x3 identity matrix

and where:

$$z_{mk} = \frac{z_{k-1} + z_k}{2} \qquad [6.14]$$

z_{mk} = distance from the center of the k^{th} layer to the mid-plane of the laminate (m)

Similarly, by integrating the electric displacement, given in equation [6.10], over the thickness of the piezoelectric layer, with the assumptions as previously stated, gives the electric displacement for the k[th] layer.

$$D_k = \{\varepsilon_{31} \quad \varepsilon_{32} \quad 0\}[R_S]_k [I_{3x3} \quad z_{mk} I_{3x3}] \begin{Bmatrix} S^O \\ \kappa \end{Bmatrix} - \frac{\varepsilon_k}{h_k}\phi_k \qquad [6.15]$$

From the above expressions it can be seen that the first matrix on the right hand side of equation [6.13] is the stiffness matrix of a composite laminate using the CPT, as shown previously. Where matrices of the extensional stiffness, **A**, coupling stiffness, **B**, and bending stiffness, **D**, are as given earlier in equation [6.6]. The second term on the right hand side of equation [6.13] is the expression accounting for piezoelectric loading.

6.2.3.1 Piezoelectric Actuation

When a voltage, ϕ, is applied across the thickness of the piezoelectric element, in-plane loads would be developed. It is assumed that the piezoelectric material is isotropic within the plane, (xy), of the element, as is the case with most piezoelectric materials, the piezoelectric properties e_{31} and e_{32} will be equal. Using the second term on the right hand side of equation [6.13], the forces, N, and moments, M, generated by the actuation of the piezoelectric element can be reduced to the following expression.

$$\begin{Bmatrix} N_x \\ N_y \\ N_{xy} \end{Bmatrix} = -e_{31}\phi \begin{Bmatrix} 1 \\ 1 \\ 0 \end{Bmatrix} \qquad [6.16]$$

$$\begin{Bmatrix} M_x \\ M_y \\ M_{xy} \end{Bmatrix} = -e_{31} z_m \phi \begin{Bmatrix} 1 \\ 1 \\ 0 \end{Bmatrix} \qquad [6.17]$$

From equations [6.16] and [6.17] it can be seen that the in-plane loads generated by the actuator are uniform and independent of the surface orientation.

6.2.3.2 Piezoelectric Sensing

If the piezoelectric electrodes are connected to a charge amplifier, the output voltage of the sensor will be of the form shown in equation [6.18].

$$\phi = \frac{Q}{C_s} = \frac{1}{C_s}\int_{\Omega} D_{3k}\, d\Omega = -\frac{e_{31}}{C_s}\left[\int_{\Omega}\left(S_x^O + S_y^O\right)d\Omega + z_m \int_{\Omega}\left(\kappa_x + \kappa_y\right)d\Omega\right] \qquad [6.18]$$

where:

C_s = capacitance of the charge amplifier (F)

Q = Electric charge (C)

Ω = Domain of the piezoelectric sensor

The first integral on the right side of the equation shows the contribution of the average strains over the electrodes, where the second term shows the contribution of the average bending moment.

6.3 Effects of Embedding Piezoelectric Patches into FRP Plates

6.3.1 Currently Used Embedding Methods

Currently, the different methods used to embed piezoelectric patches in laminated composites include the cutout method, overlay method, and interlaced method. The cutout method involves cutting out an area in the fibers equal to that of the piezoelectric patch and inserting the patch at this location. In the overlay method, the piezoelectric patch is placed in the desired location and the fibers are continuously run over the patch. The interlaced embedding approach is a hybrid between the cutout and overlay methods. In the interlaced method some of the layers adjacent to the piezoelectric patch are cutout while others are overlaid above and below the piezoelectric patch. The following figure

shows different patch embedding techniques such as overlay, cutout, and several interlaced approaches.

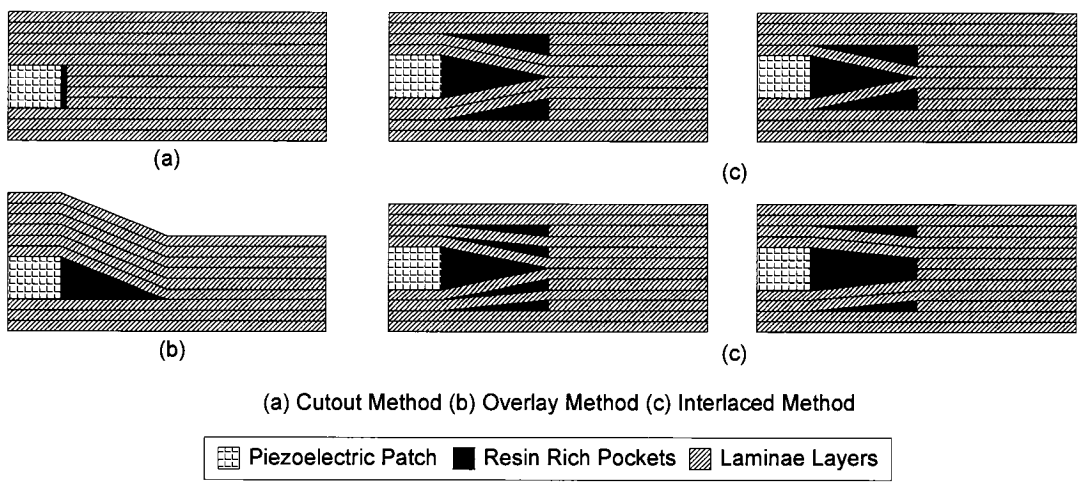

Figure 6-2: Different Embedding Techniques of Piezoelectric Patches

If a foreign material is embedded into a laminated composite, issues such as material discontinuities and/or resin rich regions are unavoidable, regardless of the embedding technique. With the embedding of these foreign materials, large interlaminar stresses around the discontinuities can be introduced, which can lead to premature failure.

Due to the increase in these stresses an investigation into the effects of embedding piezoelectric materials into a host graphite/epoxy laminate has been investigated. In the past there have been very few investigations into the effects of embedding piezoelectric materials on the induced stresses and strength of the laminated composite. The following paragraphs outline the work to date on the effects of embedding piezoelectric patches on the structural integrity of the host laminated composite material.

6.3.2 Finite Element Modeling Procedure

The present work in this thesis examines the influence of embedded piezoelectric patches into FRP plates that are subjected to uniform pressure bending. The modeling was performed with the use of the commercially available software package NISA.

6.3.2.1 Modeling Considerations

The considerations that were addressed within this investigation include the lay-up orientation of the laminate layers, embedding interface of the patch, piezoelectric patch size, and plate bending curvature (i.e. one-way and two-way bending). In a previous investigation by Singh and Vizzini (1993), it was found that the presence of the embedded piezoelectric patch caused the major increase in interlaminar stresses and the actuation of the piezoelectric patch resulted in minor changes. Therefore, the influence of actuation was not examined within this investigation.

6.3.2.2 Embedding Technique

The overlay method described earlier was chosen as the type of embedding technique due to its ease of implementation in practical situations, since it is less laborious. With this modeling procedure a resin rich pocket will be developed around the piezoelectric patch. The resin area was modeled such that the width of the resin coming out from the patch was equal to the thickness of the patch. The case with a patch thickness of 1mm is shown in Figure 6-3.

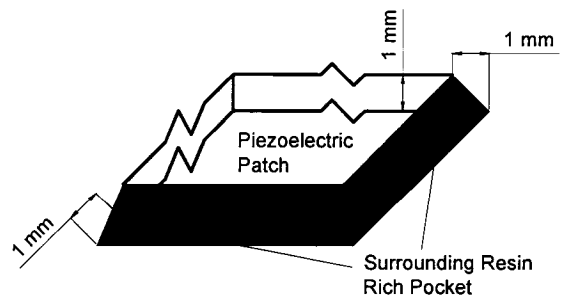

Figure 6-3: Modeling Method for Resin Rich Area Surrounding Piezoelectric Patch

6.3.2.3 Laminate Lay-up Sequence and Embedding Interface

There were five different lay-ups considered in the investigation of the two-way plate, which included $(0/90)_{8s}$, and four combinations of quasi-isotropic lay-ups implementing the fiber angles of $(0/90/\pm45)_{4s}$. For the one-way plate only two of these lay-ups were used. The lay-ups were chosen based on their practicality and to determine the influence of having the patch embedded at different interfaces.

The embedding interfaces were chosen such that the piezoelectric patch would be embedded at each interface, and it was deemed impractical to embed the patch under a single layer of the laminate. The lay-ups and their corresponding embedding interfaces for the two-way plate are shown in Table 6-1.

Table 6-1: Lay-up Sequences and Corresponding Embedding Interfaces for Two-way Plate Bending

Lay-up Number	Lay-up Configuration	Embedding Interfaces with Respect to the Top Layer
1	$(0/90)_{8S}$	Between layers 2&3, and 3&4
2	$(0/45/-45/90)_{4S}$	Between Layers 2&3 through Layers 5&6
3	$(90/45/-45/0)_{4S}$	Between Layers 2&3 through Layers 5&6
4	$(45/0/90/-45)_{4S}$	Between Layers 2&3 through Layers 5&6
5	$(90/45/0/-45)_{4S}$	Between Layers 2&3 through Layers 5&6

6.3.2.4 Material Properties

The material properties used in this investigation were chosen such that they were in the generally accepted ranges. The material properties used to model the FRP are shown in Table 6-2, followed by the material properties of the piezoelectric patch in Table 6-3. The properties used in modeling the piezoelectric patch for the one-way plate is the first column in Table 6-3.

Table 6-2: Laminate Material Properties

Property	Value
Elastic Modulus in Fiber Direction E_1	140 GPa
Elastic Modulus in Transverse Direction E_2	9.10 GPa
Shear Moduli G_{12} and G_{13}	7.10 GPa
Shear Modulus G_{23}	6.31 GPa
Poisson's Ratio ν_{xy} and ν_{xz}	0.35
Poisson's Ratio ν_{yz}	0.3
Density	1600 Kg/m^3

Table 6-3: Piezoelectric Patch Properties

Property	Material 1	Material 2	Material 3
Elastic Modulus E_{xx} and E_{yy}	67 GPa	58 GPa	90 GPa
Elastic Modulus E_{zz}	54 GPa	45 GPa	72 GPa
Shear Modulus G_{xy}	25.8 GPa	22.3 GPa	34.6 GPa
Shear Moduli G_{xz} and G_{yz}	20.7 GPa	17.3 GPa	27.7 GPa
Poisson's Ratio	0.3	0.3	0.3
Density	7850 Kg/m^3	7850 Kg/m^3	7850 Kg/m^3

6.3.2.5 Plate Dimension

The plate dimensions for this investigation were chosen such that one would be under two-way bending and the other under one-way bending. The dimensions used for these plates are shown in Table 6-4. The two-way plate was used as the standard specimen such that all investigations were carried out with this set-up.

Table 6-4: Plate Dimensions Used in FEM Analysis for Piezoelectric Patch Embedding Effects

Dimension	Two-way Plate	One-way Plate
Length (0° fiber direction)	508 mm	508 mm
Width (90° fiber direction)	508 mm	127 mm
Thickness	32 Layers @ 0.25 mm	32 Layers @ 0.25 mm

6.3.2.6 Piezoelectric Patch Dimensions

With the different piezoelectric patches that are currently available, which vary in size and material properties, a range of patch dimensions were used to determine the influence of the patch size on the stress concentrations due to embedding. The dimensions of the piezoelectric patch used in the models are shown in Table 6-5, where the first column contains the standard dimensions that were used in modeling the one-way and all two-way plate systems.

Table 6-5: Dimensions used to Model the Embedded Piezoelectric Patch

Dimension	Model 1	Model 2	Model 3
Length (mm)	76.2	50.8	101.6
Width (mm)	25.4	50.8	76.2
Thickness (mm)	0.5	0.25	1.0

6.3.2.7 Element Types

In developing the models of the laminate plate with an embedded piezoelectric patch two types of elements were used. A 3-D layered solid element was used to model the laminate plate and a general 3-D solid element was used to model the piezoelectric patch and surrounding resin rich area.

6.3.2.8 Full Plate Model

Initially full plate models were developed to inspect the increase in stresses due to embedded piezoelectric patches. Figure 6-4 shows the plate orientations and relative location of piezoelectric patch for the full models.

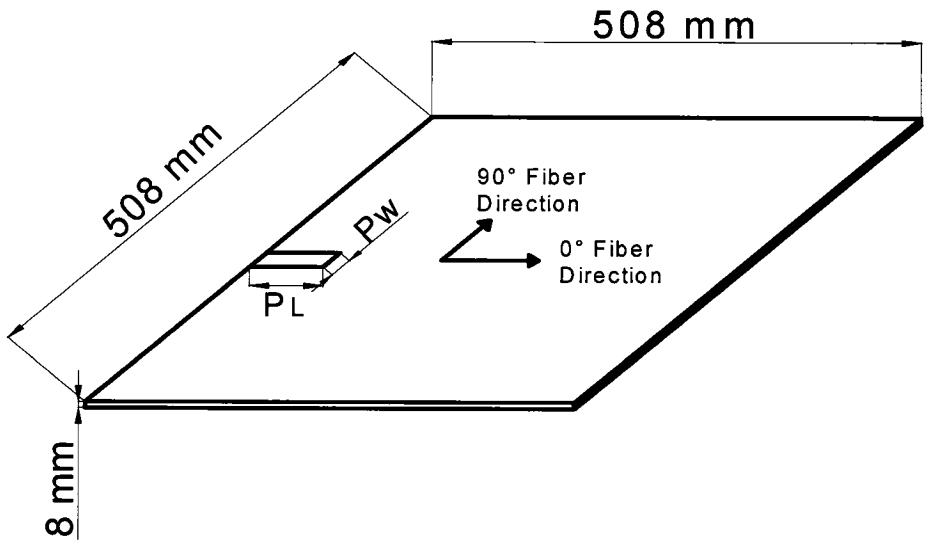

(a)

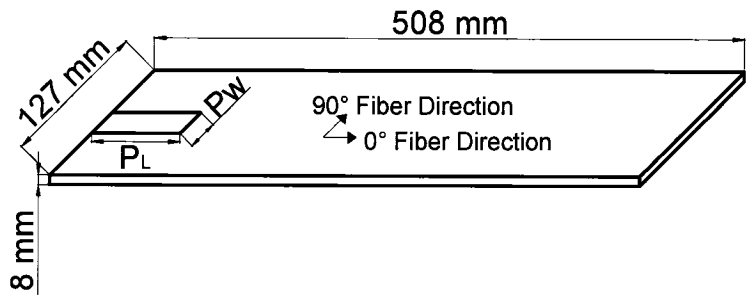

(b)

Figure 6-4: Plate Orientations used for Investigation of Embedding Effects

In these models a very coarse mesh was used to determine the positions of stress concentrations resulting from the embedded patch. The highest stress concentrations were found to exist above the resin pockets that were formed around the piezoelectric patch. The existence of this stress concentration can be seen in Figure 6-5, which is an example contour plot of the S_{xz} stress.

Figure 6-5: Example Contour Plot of S_{xz} Stress for Full Two-way Plate

From these results it was determined that only modeling of the portion of the plate around the piezoelectric patch was required. Therefore, a submodel was developed for the portion of the plate shown in Figure 6-5.

6.3.2.9 Submodeling Procedure

The major advantage associated with submodeling, also known as substructuring, is the reduction in computation time of the analysis. Submodeling involves modeling only the portion of the problem that is of major interest or importance. The mesh is generally refined in the selected area and the boundary conditions for the submodel is the displacement results from the full model. A submodeling routine is available in NISA and is outlined in the following steps.

1) Conduct the analysis of the full plate with a coarse mesh.
2) Load the database file, which contains the geometry and mesh data of the model, and the post processing file, which contains the results from the full analysis, into the NISA's preprocessor (the display module).
3) Delete all geometry data from the file, such as the areas or volumes (depending on the element type used). This removal does not include the elements in the model.

This allows the preprocessor to renumber the geometric entities beginning from one in the submodel.

4) Select the region of the model to be submodeled. Selecting the elements that are present in the region to be submodeled does this.
5) Create the proper geometric entities on the full model elements. This will create one geometric entity, such as a hyperpatch for solid elements, for each element from the full model. At this point the user is asked if the old model data should be deleted; select yes. This deletes all the full model mesh data, such as nodes and elements, from the current database. Without selecting yes, all elements from the full model will be present in the submodel, thus creating errors.
6) Remesh the geometric entities with the required elements. This is done in the same manner as meshing any model in NISA, with the exception of the meshing commands being under the submodeling menu.
7) Once the full mesh is created on all geometries, the boundary conditions must be applied to the outside boundary of the submodel. These values are the resulting displacements from the full model at the location of the nodes. For the new nodes on the boundary that did not exist in the full model (i.e. resulting from the refined mesh) NISA will linearly interpolate to determine their displacements. The automatic option in the "transfer b.c." menu applies displacements to every node in the model, which does not yield the correct results. Therefore, the user should manually select the new boundary nodes of the submodel. At this juncture the user is prompted to merge the nodes and, therefore, must select "yes", or the model will not be properly connected.
8) The final step in the submodeling procedure is to apply any external loading onto the submodel. Only external load that is present on the submodel portion in the full model should be applied to the submodeled portion.
9) The new models are then saved and run in the same manner as any usual NISA analysis.

To determine the limitations in the aforementioned submodeling procedure a small study was performed on a simple steel plate. It was found that elements in the submodel located within a distance of ¾ a full model element of the boundary could yield fictitious results. This is due to the fictitious strains that occur at the boundary conditions of a model. When a submodel is developed, boundary conditions are applied to all external nodes, leading to the fictitious strains in the elements near the cut boundaries. However, these errors can be accounted for by modeling one extra element on the cut boundary lines.

6.3.2.10 Submodels Developed

Using the described procedure several submodel of the area surrounding the piezoelectric patch was developed. The elements used for the initial submodel of the full plate are shown in Figure 6-6.

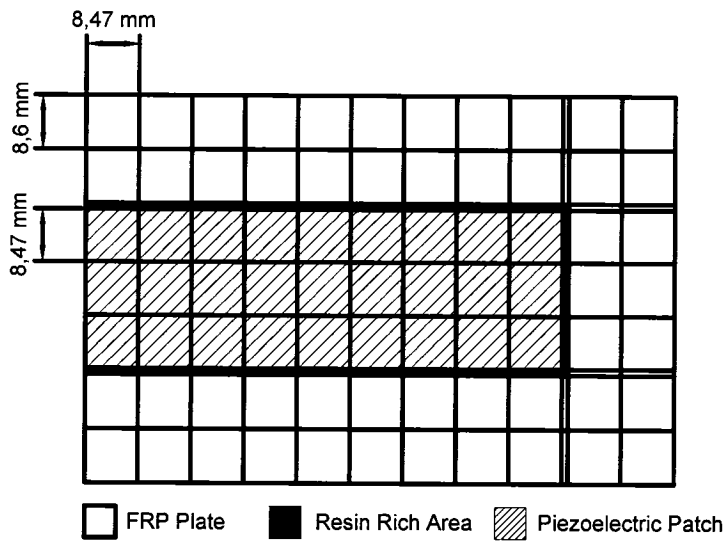

Figure 6-6: Elements used for the Initial Submodeling Procedure

The mesh was refined in this area such that the FRP plate and piezoelectric patch elements were increased to 400, with a 20x20 mesh, and the resin rich area was initially

remeshed with 80 elements, consisting of a 20x4 mesh. The contour plot for the out-of-plane shear stress, S_{xz}, for a 20x4 mesh in the resin rich area is shown in Figure 6-7.

Figure 6-7: Example Contour Plot of S_{xz} Stress for First Submodel of the Two-way Plate

As can be seen from the above result, the maximum stress concentration is located in the FRP above the resin rich area. It was also found to be symmetric about the centerline of the piezoelectric patch. Knowing the region of the stress concentration and due to the large computation time for one of these submodels, a further refined submodel was developed.

The elements used from the initial submodel, in the refined submodel are shown in Figure 6-8.

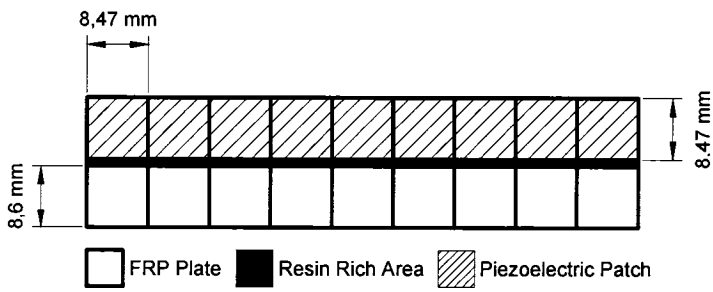

Figure 6-8: Elements used for Refined Submodeling Procedure

With the reduced size of this submodel, a convergence study was carried out to determine the required number of elements in the vicinity of the resin rich area. It was found that the 20x20 mesh in the FRP plate and piezoelectric patch areas, implemented in the previous submodel, were sufficient, however more elements were required in the width of the elements in the vicinity of the resin rich area. It was found that the out of plane stresses in the FRP above the resin rich area did not converge with the mesh 20x4 mesh used in the initial submodel, so it was further refined. It was found that the out-of-plane stresses converged with a 20x8 mesh in the resin rich area, along with the FRP above and below it. A typical NISA input file for the three different models are provided in Appendix J.

6.4 Results and Discussion

The procedure used in the parametric investigation to determine the influence of embedding the piezoelectric patch into a host laminate composite plate was as follows:

- Modeled the two-way plate with all lay-ups and embedding interfaces as noted in Section 6.3.2.3
- Modeled the one-way plate with two of the five lay-ups, such that the 90^0 laminae were placed at the outer surfaces
- Modeled lay-up five, varying the material properties of the piezoelectric sensor, with all embedding interfaces used as noted in Section 6.3.2.4
- Modeled lay-up two, varying the dimensions of the piezoelectric sensor, with one embedding interface as noted in Section 6.3.2.6

Due to the area of interest being in the vicinity of the piezoelectric patch, only the layer stresses at this location were recorded.

6.4.1 Influence of Laminate Lay-up and Embedding Interface on Laminate Layer Stresses

The initial step in determining the influence of embedding the piezoelectric patch into the host FRP plate was to examine the effects of the layer stresses in all layers above the piezoelectric patch, as well as the two layers directly below the patch. It was found that the in-plane stresses changed marginally in most layers, even when the layer was located above the piezoelectric patch. Table 6-6 shows the average stress increase factors for the five lay-ups used in this investigation and Table 6-7 tabulates the average layer stresses without the inclusion of the piezoelectric patch. Where the average was taken for the five different lay-ups, without the inclusion of the piezoelectric patch.

Table 6-6: Average Stress Increase Factors of the In-plane Stresses for Layers Above the Piezoelectric Sensor for the Two-way Plate Models

Lay-up Number	Stress Component	Fiber Orientation			
		0^0	90^0	45^0	-45^0
1	S_{xx}	1.17	4.2	N/A	N/A
	S_{yy}	1.528	1.28	N/A	N/A
	S_{xy}	3.5	3	N/A	N/A
2	S_{xx}	1.17	3.27	1.50	1.45
	S_{yy}	1.73	1.35	1.52	1.45
	S_{xy}	4.00	4.00	1.50	1.52
3	S_{xx}	1.18	3.34	1.53	1.46
	S_{yy}	1.48	1.36	1.54	1.47
	S_{xy}	4.00	4.00	1.58	1.51
4	S_{xx}	1.27	4.14	1.48	1.38
	S_{yy}	1.71	1.30	1.40	1.44
	S_{xy}	5.00	5.00	1.48	1.46
5	S_{xx}	1.23	3.20	1.51	1.38
	S_{yy}	1.53	1.40	1.56	1.41
	S_{xy}	3.60	4.00	1.55	1.47

As the results of Tables 6-6 and 6-7 show, the largest increase factors are seen in the layers that possess the smallest magnitude of stress, and that the resulting increase would not be of concern. It should also be noted that the increase in the in-plane stresses are

fairly consistent for the different lay-ups used in this study. Although the in-plane stresses show minor changes in magnitude, the out-of-plane stresses show dramatic increases when the layer is positioned above the piezoelectric patch. When the layers were positioned below the piezoelectric sensor all stresses showed very small changes and in some cases decreases were observed.

Table 6-7: Average In-plane Stress Components In the Layers with No Piezoelectric Patch Embedded

Stress Component	Fiber Orientation			
	0^0	90^0	45^0	-45^0
S_{xx}	243.6	5.47	126.5	120.9
S_{yy}	5.93	14.67	11.38	11.23
S_{xy}	1.35	1.34	13.34	12.16

Table 6-8 shows the resulting average increase factors for the out-of-plane stresses for the five different lay-ups and Table 6-9 shows the average layer stresses without the inclusion of the piezoelectric patch.

Table 6-8: Average Stress Increase Factors of the Out-of-plane Stresses for the Two-way Plate Models

Lay-up Number	Stress Component	Fiber Orientation			
		0^0	90^0	45^0	-45^0
1	S_{zz}	10.5	3.7	N/A	N/A
	S_{yz}	17	1.07	N/A	N/A
	S_{xz}	1.04	14.75	N/A	N/A
2	S_{zz}	26	17.9	69.5	87.1
	S_{yz}	24.2	1.09	3.01	3.45
	S_{xz}	1.13	20.1	3.6	2.79
3	S_{zz}	15.24	17.69	98.7	104.1
	S_{yz}	28.72	1.02	3.78	4.8
	S_{xz}	0.99	26.4	4.58	4.04
4	S_{zz}	20.9	17.3	135.7	137.6
	S_{yz}	18.4	1.03	3.8	4.2
	S_{xz}	1.09	20.9	4.79	3.85
5	S_{zz}	11.5	16.94	116.2	101.9
	S_{yz}	29.4	1.02	3.09	4.03
	S_{xz}	1.23	22.3	4.01	3.56

As can be seen from Table 6-8, the out-of-plane stresses show dramatic increases with the embedding of the piezoelectric patch with the exception of the shear stress, S_{xz}, in the 0^0 layers, or the shear stress, S_{yz}, in the 90^0 layers. However, the factors that shows increases of greater than 20 times are somewhat misleading. This is due to the existence of very small stress components in the model with no piezoelectric patch (i.e. dividing by a very small number). This is shown in Table 6-9. These factors are the peel stresses, S_{zz}, in the 45^0 orientation layers, as well as the shear stresses, S_{yz} and S_{xz}, in the 0^0 layers and 90^0 layers respectively. Also the increase factors for the $\pm 45^0$ layers are very similar but are such that the S_{xz} shear stress factor for the 45^0 layer is similar to the S_{yz} factor for the -45^0 layer, and vice versa. Nonetheless, with the large magnitude of these factors the increases in out-of-plane stress components are substantial. Also, unlike with the in-plane stresses, the increase factors of the out-of-plane stresses are more dependent on the lay-up orientation.

Table 6-9: Average Out-of-plane Stress Components for Two-way Plate Bending with No Piezoelectric Patch Embedded

Stress Component	Fiber Orientation			
	0^0	90^0	45^0	-45^0
S_{zz}	1.32	1.40	0.22	0.19
S_{yz}	0.61	3.62	2.74	2.80
S_{xz}	3.62	0.61	2.80	2.74

It can be seen from Table 6-9 that the maximum through thickness stresses occur in the 0^0 and 90^0 layers, which on average are very close in magnitude. The maximum shear stress, S_{xz}, and minimum shear stress, S_{yz}, occur in the 0^0 layer while the maximum shear stress, S_{yz}, and minimum shear stress, S_{xz} occur in the 90^0 layer. Also for all out-of-plane stresses the $\pm 45^0$ layers show very similar stress results. From these observations, the maximum interlaminar peel stress was observed at an interface with the two plies separated by 45^0, and the maximum interlaminar shear stresses were observed at the (0/90) interface.

Due to the large increases seen in the out-of-plane stresses the interlaminar stresses were determined for all lay-ups. These were calculated by taking the difference in the out-of-plane stresses in adjacent layers. The following sections will examine the influences of embedding the piezoelectric patch into the FRP plate on the interlaminar stresses. Due to the layers stresses below the embedding interface remaining practically unchanged by the presence of the piezoelectric patch, the only interlaminar stresses recorded for the models with the embedded piezoelectric sensor were those in the interfaces above the patch and the first interface below the patch. As well, due to the interlaminar peel stress only being of concern when the two plies are being pulled apart, only the maximum tensile effects of through thickness stress, S_{zz}, were recorded. Throughout the following sections a positive S_{zz} value indicates a stress that tends to separate the adjacent plies, where a negative value indicates the plies are being squeezed together. Also only the maximum out-of-plane shear stresses, S_{xz} and S_{yz}, were recorded, due to those areas producing the largest interlaminar shear stresses. The location of these maximums was observed at the edge of the resin rich region along the side of the piezoelectric patch.

6.4.1.1 Interlaminar Stresses in Lay-up 1 Subjected to Two-way Plate Bending

The interlaminar stresses between the top five layers of lay-up 1 without the inclusion of the piezoelectric patch are shown in Table 6-10.

Table 6-10: Interlaminar Stresses in Two-way Plate Bending With No Piezoelectric Patch Embedded for Lay-up 1

	Interlaminar Stress Values (MPa)		
Interface	S_{zz}	S_{yz}	S_{xz}
Layers 1 and 2	-0.213	3.021	3.021
Layers 2 and 3	0.363	3.021	3.021
Layers 3 and 4	-0.181	3.021	3.021
Layers 4 and 5	0.331	3.021	3.021

As can be seen from Table 6-10 the interlaminar shear stresses are the same throughout the thickness of the plate. Whereas, the interlaminar peel stress depends on the depth

through the plate, as well the orientation of the ply on top of the interface. This is due to the out-of-plane stress, S_{zz}, being larger in the 90^0 layers then in the 0^0 layers, as well as a gradual decrease in this stress as the layers get closer to the neutral axis. Therefore, when the 90^0 layer is on the top of the interface, the interlaminar peel stress between the layers would be positive and tend to pull the layers apart. When the 0^0 layers is on top of the interface, the resulting interlaminar peel stress is compressive (negative), and the plies are squeezed together.

The interlaminar stresses for the plate with the inclusion of the piezoelectric patch embedded at interfaces two and three are shown in Table 6-11.

Table 6-11: Interlaminar Stresses in Two-way Plate Bending With Piezoelectric Patch Embedded at Interfaces 2 and 3 for Lay-up 1

Embedding Interface	Interface	Interlaminar Stress Values (MPa)		
		S_{zz}	S_{yz}	S_{xz}
Layers 2 and 3	Layers 1 and 2	3.743	1.618	3.072
	Layers 2 and 3	4.424	3.146	2.372
	Layers 3 and 4	1.661	3.114	2.814
Layers 3 and 4	Layers 1 and 2	5.721	3.283	1.627
	Layers 2 and 3	-5.841	3.312	1.621
	Layers 3 and 4	10.96	2.806	2.698
	Layers 4 and 5	-0.514	3.254	3.201

One can observe several trends in the data tabulated in Table 6-11. The most notable is that the largest interlaminar peel stress occurs at the embedding interface, and shows large stress increase factors of up to approximately 60 times. However, with the $(0/90)_{8s}$ lay-up the maximum interlaminar shear stresses do not show noticeable changes. Considering the interlaminar shear stress, S_{xz}, its maximum value is only 10% higher then that without the piezoelectric sensor embedded. This is caused by two factors. The first is that the stress in the 0^0 shows very minor changes and stays constant. The second is due to the layer stress in the 90^0 layer being initially very small and increasing to a value that is approximately twice the 0^0 layer stress. The reverse is also the case with the, S_{yz}, interlaminar shear stress where the 90^0 layer stays fairly constant, and the 0^0 layer

increasing to approximately twice its value. Therefore, with this lay-up orientation the maximum interlaminar shear stresses are not largely influenced.

6.4.1.2 Interlaminar Stresses in Lay-up 2 Subjected to Two-way Plate Bending

The interlaminar stresses between the top seven layers of lay-up 2 in the laminate without the inclusion of the piezoelectric patch are shown in Table 6-12.

Table 6-12: Interlaminar Stresses in Two-way Plate Bending With No Piezoelectric Patch Embedded for Lay-up 2

Interface	Interlaminar Stress Values (MPa)		
	S_{zz}	S_{yz}	S_{xz}
Layers 1 and 2	0.881	2.338	0.923
Layers 2 and 3	0.019	0.037	0.037
Layers 3 and 4	-1.084	0.923	2.338
Layers 4 and 5	0.494	3.298	3.298
Layers 5 and 6	0.631	2.338	0.923
Layers 6 and 7	0.019	0.037	0.037

Unlike the case with the cross-ply FRP plate, the interlaminar stresses in this quasi-isotropic lay-up are dependent on the lay-up orientation as seen above in Table 6-12. From this table it can be seen that without the inclusion of the piezoelectric sensor, the maximum peel stress, S_{zz}, occurs at the (-45/90) interface and the maximum interlaminar shear stresses, S_{xz} and S_{yz}, occur at the (90/0) interface. This is expected as was noted in section 6.4.1.

The interlaminar stresses for the same plate with the inclusion of the piezoelectric patch embedded at interfaces two through five are shown in Table 6-13.

Again; there are several trends present in Table 6-13. The most notable one is that the largest interlaminar peel stress, S_{zz}, occurs at the embedding interface, and that the maximum value increases as the piezoelectric sensor is embedded further into the plate.

With lay-up two, the position of the maximum interlaminar shear stresses varies depending on the embedding interface.

With the piezoelectric sensor embedded between layers two and three, interface 2, the interlaminar shear stresses at all interfaces above the piezoelectric patch show substantial increases, with the maximum occurring at the embedding interface. The maximum at interface two is due to the large increase in the shear stresses of the 45^0 layer, and relatively no change in the -45^0 layer. The increase in interlaminar stresses, S_{zz} and S_{yz}, at interface one is due to larger increase in the S_{zz} and S_{yz} layer stresses of the 0^0 layer, compared to the 45^0 layer. The increase in the interlaminar shear stress, S_{xz}, is due to the very minor change in the 0^0 layer stress and a large change in the 45^0 layer stress.

Table 6-13: Interlaminar Stresses in Two-way Plate Bending With Piezoelectric Patch Embedded at Interfaces 2, 3, 4 and 5 for Lay-up 2

Embedding Interface	Interface	Interlaminar Stress Values (MPa)		
		S_{zz}	S_{yz}	S_{xz}
Layers 2 and 3	Layers 1 and 2	6.780	6.004	6.381
	Layers 2 and 3	8.343	8.116	8.628
	Layers 3 and 4	0.357	1.064	0.779
Layers 3 and 4	Layers 1 and 2	5.790	7.041	6.444
	Layers 2 and 3	-1.170	2.261	1.120
	Layers 3 and 4	16.22	6.896	6.052
	Layers 4 and 5	-1.728	2.543	0.286
Layers 4 and 5	Layers 1 and 2	5.780	7.614	6.455
	Layers 2 and 3	-1.060	2.874	2.938
	Layers 3 and 4	-1.440	6.392	7.328
	Layers 4 and 5	22.51	3.040	9.436
	Layers 5 and 6	0.861	4.036	0.612
Layers 5 and 6	Layers 1 and 2	4.340	7.551	5.429
	Layers 2 and 3	1.040	2.037	2.686
	Layers 3 and 4	0.900	5.121	4.762
	Layers 4 and 5	-5.150	10.40	7.518
	Layers 5 and 6	24.02	8.237	1.888
	Layers 6 and 7	-0.030	0.582	0.026

With the piezoelectric sensor embedded between layers three and four, interface 3, the interlaminar shear stresses at all interfaces above the piezoelectric patch show increases, with the maximum occurring at the first interface. It should be noted that the interlaminar shear stresses at embedding interface are very close to those of interface one. The reasons for occurring at interface one are as follows:

- The stress changes in the $\pm 45^0$ layers above the piezoelectric sensor are very similar resulting in the smallest interlaminar shear stresses
- For the shear stress S_{xz} the change in the 0^0 layer is very minor, where the change in the 45^0 layer is larger than that of the -45^0 layer
- For the shear stress S_{yz} the change in the 0^0 layer is very large while the 45^0 layer shows a smaller increase then the -45^0 layer. This results in the interlaminar stress being larger at the (0/45) interface then the (-45/90) interface by only 2%.

With the piezoelectric sensor embedded between layers four and five, interface 4, the interlaminar shear stresses at all interfaces above the piezoelectric patch show increases, with the maximum interlaminar S_{yz} stress occurring at the (0/45) interface, and the maximum S_{xz} occurring at the (90/0) interface. The y-z interlaminar shear at the interface actually shows a minor decrease of 6%. This is due to the change in the 0^0 layer stress, located directly under the piezoelectric patch. This change is slightly larger than the change in stress of the 90^0 layer located directly above the piezoelectric patch. The maximum interlaminar x-z shear stress is observed at the (90/0) interface as is expected. This is because the 90^0 layer possesses the largest S_{xz} stress, while the 0^0 layer shows minor changes in its S_{xz} stress when located below the embedding interface.

With the piezoelectric sensor embedded between layers five and six, interface 5, the maximum interlaminar shear stresses should be observed at the same interface as the results with no piezoelectric patch embedded. This is because all possible interfaces in

the laminate are located above the embedded patch. This was found to be the case with the maximum interlaminar shear stresses observed at the (90/0) interface.

Looking at all embedding interfaces, the worst case is seen when the piezoelectric patch is embedded at interface five. When the piezoelectric patch is embedded at this interface, the maximum peel stress is developed at the (0/45) interface. Due to a laminate possessing the same strength for both interlaminar shear stresses, the worst case will be when the maximum of either occurs. When the piezoelectric patch is embedded at interface 5, the maximum interlaminar shear stress is observed in the y-z plane at the (0/90) interface.

6.4.1.3 Interlaminar Stresses in Lay-up 3 Subjected to Two-way Plate Bending

The interlaminar stresses between the top seven layers of lay-up 3, without the inclusion of the piezoelectric patch are shown in Table 6-14.

Table 6-14: Interlaminar Stresses in the Two-way Plate Bending With No Piezoelectric Patch Embedded for Lay-up 3

Interface	Interlaminar Stress Values (MPa)		
	S_{zz}	S_{yz}	S_{xz}
Layers 1 and 2	1.211	0.871	2.054
Layers 2 and 3	-0.015	0.056	0.056
Layers 3 and 4	-1.233	2.054	0.871
Layers 4 and 5	0.386	2.869	2.869
Layers 5 and 6	0.919	0.871	2.054
Layers 6 and 7	-0.006	0.056	0.056

From Table 6-14 it can be seen that without the inclusion of the piezoelectric sensor the maximum peel stress, S_{zz}, occurs at the (-45/0) interface, or interface 3. Whereas the maximum interlaminar shear stresses, S_{xz} and S_{yz}, occur at interface 4, or the (0/90) interface.

The interlaminar stresses for the plate with the inclusion of the piezoelectric patch embedded at interfaces two through five are shown in Table 6-15.

From Table 6-15 there are several trends that can be observed in the data. The most notable is that the largest interlaminar peel stress, S_{zz}, occurs at the embedding interface, and that the maximum value increases as the piezoelectric sensor is embedded further into the plate. With this lay-up orientation, the position of the maximum interlaminar shear stresses varies depending on the embedding interface.

Table 6-15: Interlaminar Stresses in Two-way Plate Bending With the Piezoelectric Patch Embedded at Interfaces 2, 3, 4 and 5 for Lay-up 3

Embedding Interface	Interface	Interlaminar Stress Values (MPa)		
		S_{zz}	S_{yz}	S_{xz}
Layers 2 and 3	Layers 1 and 2	1.270	4.043	4.969
	Layers 2 and 3	10.72	4.401	9.225
	Layers 3 and 4	-1.175	2.532	0.470
Layers 3 and 4	Layers 1 and 2	1.220	8.101	4.990
	Layers 2 and 3	0.200	2.510	1.170
	Layers 3 and 4	14.17	11.71	7.756
	Layers 4 and 5	2.013	2.543	2.729
Layers 4 and 5	Layers 1 and 2	2.800	6.376	6.810
	Layers 2 and 3	1.200	0.980	0.980
	Layers 3 and 4	-1.590	5.520	6.413
	Layers 4 and 5	19.49	12.54	0.002
	Layers 5 and 6	-0.929	0.787	1.072
Layers 5 and 6	Layers 1 and 2	2.260	6.917	6.080
	Layers 2 and 3	1.890	0.942	1.535
	Layers 3 and 4	-1.200	3.560	6.612
	Layers 4 and 5	0.550	11.41	13.71
	Layers 5 and 6	19.92	3.431	10.54
	Layers 6 and 7	-0.017	0.547	0.018

With the piezoelectric sensor embedded between layers two and three, interface 2, the interlaminar shear stresses at all interfaces above the piezoelectric patch show increases, with the maximums occurring at the embedding interface. The maximum at interface two is due to the large increase in the shear stresses of the 45^0 layer, and relatively no change

in the -45^0 layer directly below the piezoelectric patch. There is a very minor increase in the peel stress at interface one, which was observed as a large increase with the 0^0 layer being at the outer surface as in lay-up one. The increase in interlaminar stresses, S_{xz} and S_{yz}, at interface one is for similar reasons as lay-up one. The increase in the interlaminar shear stress, S_{yz}, is due to the very minor change in the 90^0 layer stress and a large change in the 45^0 layer stress, while the shear stress, S_{xz}, in the 90^0 layer shows a larger increase when compared to the 45^0 layer.

With the piezoelectric sensor embedded between layers three and four, at interface 3, the interlaminar shear stresses at all interfaces above the piezoelectric patch show increases, with the maximum occurring at the embedding interface. The maximum occur due to the large changes in the -45^0 layer, with very minor changes in the stresses of the 0^0 layer.

With the piezoelectric sensor embedded between layers four and five, at interface 4, the maximum interlaminar shear stress, S_{yz}, occurs at the (0/90) interface, and the maximum interlaminar shear stress, S_{xz}, occurs at the (90/45) interface. The y-z interlaminar shear at the interface actually shows a major decrease to approximately zero. This is due to the change in the 0^0 stress directly above the piezoelectric patch being slightly larger than the change in the 90^0 layer below the piezoelectric patch, resulting in almost identical layer stresses. The maximum interlaminar y-z shear stress is observed at the (90/0) interface as is expected. Since the 0^0 layer possesses the largest change in the S_{yz} shear stress and the 90^0 layer shows minor changes below the embedding interface. The maximum interlaminar x-z shear stress is observed at interface 1 due to the very large increase of the 90^0 layer stress.

With the piezoelectric sensor embedded at interface 5, between layers five and six, the maximum interlaminar shear stresses should be observed at the same interface as the results with no piezoelectric patch embedded. This is due to all interfaces being observed

above the embedded patch. This is the case with the maximum interlaminar shear stresses being observed at the (0/90) interface.

Looking at all embedding interfaces the worst case is seen when the piezoelectric patch is embedded at interface five. When the piezoelectric patch is embedded at this interface the maximum peel stress is developed at the (90/45) interface. Also with the piezoelectric patch embedded at interface 5 the maximum interlaminar shear stress is developed in the x-z plane at the (0/90) interface.

6.4.1.4 Interlaminar Stresses in Lay-up 4 Subjected to Two-way Plate Bending

The interlaminar stresses between the top seven layers of lay-up 4 without the inclusion of the piezoelectric patch are shown in Table 6-16.

Table 6-16: Interlaminar Stresses in Two-way Plate Bending With No Piezoelectric Patch Embedded for Lay-up 4

Interface	Interlaminar Stress Values (MPa)		
	S_{zz}	S_{yz}	S_{xz}
Layers 1 and 2	-1.120	1.957	0.881
Layers 2 and 3	-0.077	2.978	2.978
Layers 3 and 4	1.309	0.881	1.957
Layers 4 and 5	0.061	0.140	0.140
Layers 5 and 6	-0.922	1.957	0.881
Layers 6 and 7	-0.046	2.978	2.978

From Table 6-16 it can be seen that without the inclusion of the piezoelectric sensor the maximum peel stress, S_{zz}, occurs at the (90/-45) interface, or interface 3. Whereas the maximum interlaminar shear stresses, S_{xz} and S_{yz}, occur at interface 2, or the (0/90) interface.

The interlaminar stresses for the plate with the inclusion of the piezoelectric patch embedded at interfaces two through five are shown in Table 6-17.

From Table 6-17 it can be seen that the largest interlaminar peel stress, S_{zz}, occurs at the embedding interface, however unlike lay-ups two and three the maximum value is observed with the piezoelectric patch embedded near the surface of the plate, with the value decreasing as the embedding depth increases.

Table 6-17: Interlaminar Stresses in Two-way Plate Bending With the Piezoelectric Patch Embedded at Interfaces 2, 3, 4 and 5 for Lay-up 4

Embedding Interface	Interface	Interlaminar Stress Values (MPa)		
		S_{zz}	S_{yz}	S_{xz}
Layers 2 and 3	Layers 1 and 2	1.170	7.636	10.79
	Layers 2 and 3	28.51	10.12	0.085
	Layers 3 and 4	-1.071	0.147	0.106
Layers 3 and 4	Layers 1 and 2	1.290	4.856	8.088
	Layers 2 and 3	0.940	8.419	12.26
	Layers 3 and 4	26.43	2.893	8.683
	Layers 4 and 5	-0.024	0.039	0.676
Layers 4 and 5	Layers 1 and 2	3.220	3.430	8.132
	Layers 2 and 3	3.120	9.847	10.53
	Layers 3 and 4	-3.840	7.027	3.520
	Layers 4 and 5	24.29	3.980	4.451
	Layers 5 and 6	-0.855	1.370	0.698
Layers 5 and 6	Layers 1 and 2	2.650	2.460	9.527
	Layers 2 and 3	4.210	9.309	11.17
	Layers 3 and 4	-1.670	8.679	5.252
	Layers 4 and 5	-2.480	0.420	3.852
	Layers 5 and 6	22.61	7.066	9.113
	Layers 6 and 7	1.540	0.507	0.135

With the piezoelectric patch embedded at interface 2 the maximum x-z interlaminar shear stress is developed at the first interface. This is due to the large change in the layer stress of the 45^0 layer with a small increase in the 0^0 layer stress. For this embedding interface the maximum interlaminar y-z shear stress is observed at the (0/90) interface due to the large change in the 0^0 layer stress and minor changes in the 90^0 layer stress.

As was stated previously, the maximum interlaminar shear stress, without the presence of a piezoelectric patch, is always developed at the (0/90) interface for this type of loading.

With a lay-up orientation of $(45/0/90/-45)_{4s}$, the (0/90) interface is located above the piezoelectric patch for all embedding depths with the exception of the first interface. Therefore, as expected, the maximum interlaminar shear stresses are observed at this interface for the piezoelectric patch embedded at interfaces three through five. The maximum interlaminar shear stress observed is in the x-z plane with the piezoelectric patch embedded at interface three.

6.4.1.5 Interlaminar Stresses in Lay-up 5 Subjected to Two-way plate Bending

The interlaminar stresses between the top seven layers of lay-up 5 without the inclusion of the piezoelectric patch are shown in Table 6-18.

Table 6-18: Interlaminar Stresses in Two-way Plate Bending With No Piezoelectric Patch Embedded for Lay-up 5

Interface	Interlaminar Stress Values (MPa)		
	S_{zz}	S_{yz}	S_{xz}
Layers 1 and 2	1.313	0.943	2.027
Layers 2 and 3	-1.347	1.929	0.845
Layers 3 and 4	1.318	2.027	0.943
Layers 4 and 5	-0.927	0.845	1.929
Layers 5 and 6	0.991	0.943	2.027
Layers 6 and 7	-0.943	1.929	0.845

From Table 6-18 it can be seen that without the inclusion of the piezoelectric sensor the maximum peel stress, S_{zz}, occurs at the (45/0) interface, however the interlaminar stress at the first three interfaces are relatively similar. As stated previously, the smallest magnitudes in the x-z and y-z shear stresses for a layer are observed in the 90^0 and 0^0 layers respectively. Therefore, as expected the maximum interlaminar x-z shear stress is observed at the (90/45) interface, and the maximum y-z stress is observed at the (0/-45) interface.

The interlaminar stresses for the plate with the inclusion of the piezoelectric patch embedded at interfaces two through five are shown in Table 6-19.

Table 6-19: Interlaminar Stresses in Two-way Plate Bending With the Piezoelectric Patch Embedded at Interfaces 2, 3, 4 and 5 for Lay-up 5

Embedding Interface	Interface	Interlaminar Stress Values (MPa)		
		S_{zz}	S_{yz}	S_{xz}
Layers 2 and 3	Layers 1 and 2	0.050	3.415	1.170
	Layers 2 and 3	8.692	7.106	8.850
	Layers 3 and 4	1.278	1.920	1.100
Layers 3 and 4	Layers 1 and 2	3.090	2.384	2.430
	Layers 2 and 3	-0.410	6.157	6.352
	Layers 3 and 4	12.76	8.104	0.434
	Layers 4 and 5	0.950	0.384	1.882
Layers 4 and 5	Layers 1 and 2	2.730	6.041	4.620
	Layers 2 and 3	-0.670	4.841	7.964
	Layers 3 and 4	1.450	2.790	7.124
	Layers 4 and 5	12.74	6.184	7.163
	Layers 5 and 6	-0.350	0.805	1.231
Layers 5 and 6	Layers 1 and 2	3.140	4.737	5.770
	Layers 2 and 3	0.750	4.243	6.864
	Layers 3 and 4	0.990	2.420	5.288
	Layers 4 and 5	-0.820	6.714	6.636
	Layers 5 and 6	16.87	2.738	9.314
	Layers 6 and 7	-0.795	1.462	1.839

As was the case for all lay-up orientations the maximum peel stress is observed at the interface with the embedded piezoelectric patch. For this lay-up, $(45/0/-45/90)_{4s}$, the maximum peel stress is observed with the piezoelectric patch embedded at interface 5.

Unlike the other quasi-isotropic lay-up orientations used in this investigation, the $(45/0/-45/90)_{4s}$ lay-up is the only one without a (0/90) interface. Therefore the pattern of the maximums will not be consistent with the other lay-ups used. For embedding interfaces two, three, and four the maximum y-z interlaminar shear stress is observed at the embedding interface. This is due to the stress increase of the layer directly above the piezoelectric patch and very little change in the layer stress directly below the embedded patch. The maximum x-z interlaminar stress is governed by the very minor change in the

0^0 layer stress in the presence of the piezoelectric patch. In this case the maximum occurs at interface two for embedding interface two, three, and four.

For embedding interface five the opposite occurs. The maximum y-z interlaminar shear is governed by the very minor change in the 90^0 layer directly above the piezoelectric patch. In this case, with the small change in the 90^0 layer stress with the large increase of the layer stress in the -45^0 ply the maximum y-z interlaminar stress is observed at interface four. With this embedding interface the maximum x-z interlaminar stress is observed at the embedding interface, due to the stress increase of the layer directly above the piezoelectric patch and very little change in the layer stress directly below the embedded patch.

With this lay-up orientation it was observed that the worst interface for embedding the piezoelectric patch is at the (-45/90) interface, or interface five. With the piezoelectric patch embedded at this interface the maximum peel stress is observed along with the maximum interlaminar shear in the x-z plane.

6.4.2 Influence of Plate Curvature on Interlaminar Stress Distribution

For this study two lay-ups, $(90/\pm45/0)_{4s}$ and $(90/45/0/-45)_{4s}$, were considered under one-way bending. These lay-ups were chosen since in these plates the 90^0 layers are stacked at the outer surfaces, giving maximum plate stiffness.

From the stress results, similar increases for the in-plane stresses were observed in the plate subjected to one-way bending, as those observed in the plate subjected to two-way bending. Also like the plates subjected to two-way bending, the out-of-plane stresses in the plates subjected to one-way bending displayed dramatic increases with the embedding of the piezoelectric sensor. One issue to note from the out-of-plane stresses in the plates subjected to one-way bending is that larger increases in the out-of-plane layer stresses in the layers above the embedded piezoelectric sensor were noticed, then those observed in

the two-way plate. Therefore, only the effects of the out-of-plane stresses resulting from embedding the piezoelectric sensor into the host FRP plate are examined further.

6.4.2.1 Interlaminar Stresses in Lay-up 3 Subjected to One-way Plate Bending

The interlaminar stresses between the top seven layers of lay-up 3 without the inclusion of the piezoelectric patch are shown in Table 6-20.

From Table 6-20 it can be seen that without the inclusion of the piezoelectric sensor the maximum peel stress, S_{zz}, occurs at the (90/45) interface, or interface 1. This is a different interface than that observed for the plate subjected to two-way bending, where the maximum stress occurred at interface 3. Note that however both maxima occurred at interfaces where the adjacent layers were separated by 45^0. The maximum interlaminar shear stresses, S_{xz} and S_{yz}, were observed at the (0/90) interface, which is consistent with the same plate subjected to two-way bending.

Table 6-20: Interlaminar Stresses in Plate Subjected to One-way Bending With No Piezoelectric Patch Embedded for Lay-up 3

Interface	Interlaminar Stress Values (MPa)		
	S_{zz}	S_{yz}	S_{xz}
Layers 1 and 2	0.657	2.290	0.362
Layers 2 and 3	-0.009	0.085	0.085
Layers 3 and 4	-0.059	0.362	2.290
Layers 4 and 5	-0.366	2.567	2.567
Layers 5 and 6	0.527	2.290	0.362
Layers 6 and 7	0.001	0.085	0.085

The interlaminar stresses for the plate with the inclusion of the piezoelectric patch embedded at interfaces two through five are shown in Table 6-21.

As was the case with the plate subjected to two-way bending the maximum interlaminar peel stress is developed at the embedding interface. Also, as was the case with the plate subjected to two-way bending, the maximum peel stress is developed when the

piezoelectric sensor is embedded at interface five, between the 90^0 and 45^0 layers. However, unlike the two-way plate where the peel stress increased as the embedding depth increased, the peel stress stayed fairly consistent for all embedding interfaces.

Table 6-21: Interlaminar Stresses in One-way Plate Bending With Piezoelectric Patch Embedded at Interfaces 2, 3, 4 and 5 for Lay-up 3

Embedding Interface	Interface	Interlaminar Stress Values (MPa)		
		S_{zz}	S_{yz}	S_{xz}
Layers 2 and 3	Layers 1 and 2	0.290	10.05	4.930
	Layers 2 and 3	36.26	10.20	14.13
	Layers 3 and 4	0.438	2.774	1.992
Layers 3 and 4	Layers 1 and 2	0.870	12.44	7.050
	Layers 2 and 3	-0.630	0.770	1.150
	Layers 3 and 4	35.21	13.35	9.774
	Layers 4 and 5	-0.624	4.568	4.568
Layers 4 and 5	Layers 1 and 2	0.740	10.20	6.140
	Layers 2 and 3	-0.210	1.340	1.310
	Layers 3 and 4	-0.060	6.160	9.216
	Layers 4 and 5	34.57	11.81	1.324
	Layers 5 and 6	0.392	1.455	2.795
Layers 5 and 6	Layers 1 and 2	0.450	12.80	7.750
	Layers 2 and 3	-0.100	0.890	0.720
	Layers 3 and 4	0.120	7.660	12.71
	Layers 4 and 5	-0.230	19.54	18.45
	Layers 5 and 6	36.50	1.483	17.60
	Layers 6 and 7	-0.174	0.040	0.544

With the piezoelectric sensor embedded at interfaces two, three, and five of the plates subject to one-way bending, the locations of the maximum interlaminar shear stresses are consistent with that observed in the two-way plate. For the sensor embedded at interface four, the maximum S_{yz} stress occurred at the embedding interface, which is also consistent with that observed in the two-way plate. However, the S_{xz} stress becomes maximum at interface three, the (-45/0) interface, and not at interface one, the (90/45) interface, as was the case with the two-way plate bending. In the plate subjected to two-way bending, the larger increase in the 90^0 layer stress compared to that of the 45^0 layer stress governed the interface of the maximum S_{xz} stress. In the case of one-way bending,

the maximum S_{xz} stress is governed by the minor change of the S_{xz} stress of the 0^0 layer and the large increase of the S_{xz} stress in the -45^0 layer.

6.4.2.2 Interlaminar Stresses of Lay-up 5 Subjected to One-way Plate Bending

The interlaminar stresses between the top seven layers of lay-up 5 without the inclusion of the piezoelectric patch are shown in Table 6-22.

From Table 6-22 it can be seen that without the inclusion of the piezoelectric sensor the maximum peel stress, S_{zz}, occurs at the (90/45) interface (interface 1). As was the case with lay-up three, this is a different interface than that observed for the plate subjected to two-way bending, however both occurred at interfaces where the adjacent layers were separated by 45^0. As observed with the plate subjected to two-way bending, the smallest magnitudes in the x-z and y-z shear stresses for a layer were observed in the 90^0 and 0^0 layers, respectively. Therefore, in the plate subjected to one-way bending, the locations of the maximum interlaminar shear stresses without the inclusion of the piezoelectric sensor are the same as the plate subjected to two-way bending. These maximums were observed at the (90/45) and (0/-45) interfaces for the x-z and y-z interlaminar shear stresses, respectively.

Table 6-22: Interlaminar Stresses in Two-way Plate Bending With No Piezoelectric Patch Embedded for Lay-up 5

Interface	Interlaminar Stress Values (MPa)		
	S_{zz}	S_{yz}	S_{xz}
Layers 1 and 2	0.675	0.161	1.750
Layers 2 and 3	-0.086	1.727	0.184
Layers 3 and 4	0.074	1.750	0.161
Layers 4 and 5	-0.436	0.184	1.714
Layers 5 and 6	0.511	0.161	1.750
Layers 6 and 7	0.129	1.727	0.184

The interlaminar stresses for the plate with the inclusion of the piezoelectric patch embedded at interfaces two through five are shown in Table 6-23.

From Table 6-23 it can be seen that the maximum peel stress is observed at the interface with the embedded piezoelectric patch. For this case the maximum peel stress is observed with the piezoelectric sensor embedded at interface 5, which is the same as that observed with the plate subjected to two-way bending. However, as was the case with lay-up three under one-way bending, the peel stress is relatively consistent for all embedding interfaces.

Table 6-23: Interlaminar Stresses in One-way Plate Bending With Piezoelectric Patch Embedded at Interfaces 2, 3, 4 and 5 for Lay-up 5

Embedding Interface	Interface	Interlaminar Stress Values (MPa)		
		S_{zz}	S_{yz}	S_{xz}
Layers 2 and 3	Layers 1 and 2	0.310	12.01	5.090
	Layers 2 and 3	35.61	13.28	12.50
	Layers 3 and 4	-0.476	2.763	2.039
Layers 3 and 4	Layers 1 and 2	0.750	8.795	4.880
	Layers 2 and 3	-0.350	6.500	10.50
	Layers 3 and 4	34.27	14.07	1.467
	Layers 4 and 5	-0.164	1.700	3.099
Layers 4 and 5	Layers 1 and 2	0.770	9.737	6.060
	Layers 2 and 3	0.100	4.860	8.708
	Layers 3 and 4	-0.570	5.840	9.858
	Layers 4 and 5	31.39	6.009	10.72
	Layers 5 and 6	0.420	1.836	2.778
Layers 5 and 6	Layers 1 and 2	0.480	13.30	7.850
	Layers 2 and 3	0.130	6.950	12.65
	Layers 3 and 4	-0.240	7.670	13.30
	Layers 4 and 5	-0.060	12.16	7.160
	Layers 5 and 6	35.90	1.564	18.96
	Layers 6 and 7	0.081	4.020	1.963

With the piezoelectric sensor embedded at interfaces two and three, the locations of the maximum interlaminar shear stresses are consistent with those observed in the two-way plate. With the plate subjected to one-way bending, the maximum interlaminar shear stresses have the same pattern as when the sensor was embedded at interface four and five. In these two cases, the maximum S_{yz} stress occurs at interface one, and the

maximum S_{xz} at the embedding interface. The reason for the location of the maximum S_{yz} is due to the minor increase in the 90^0 layer stress along with a major increase of the stress in the 45^0 layer. The governing factor in the location of the maximum S_{xz} stress is the very large increases of the stress in the layer directly above the piezoelectric sensor, along with small stress changes in the layer directly below the piezoelectric sensor.

From this investigation, it was found that the stress concentrations developed by embedding a piezoelectric sensor into a host laminate plate were more pronounced when the plate was subjected to one-way bending then two-way bending. One reason for this could be the shear stress distribution of the full plate model. In both sets of plate model the maximum in-plane shear stress, S_{xy}, of the $\pm 45^0$ layers occurs at the free edges of the plates, while the maximum in-plane shear in the 0^0 and 90^0 layers occurs in the vicinity of the plate corners. An example of the distribution pattern of the in-plane shear stresses, S_{xy}, for the $\pm 45^0$ layers and the 0^0 and 90^0 layers is shown in Figure 6-9 for lay-up 2 subjected to two-way plate bending.

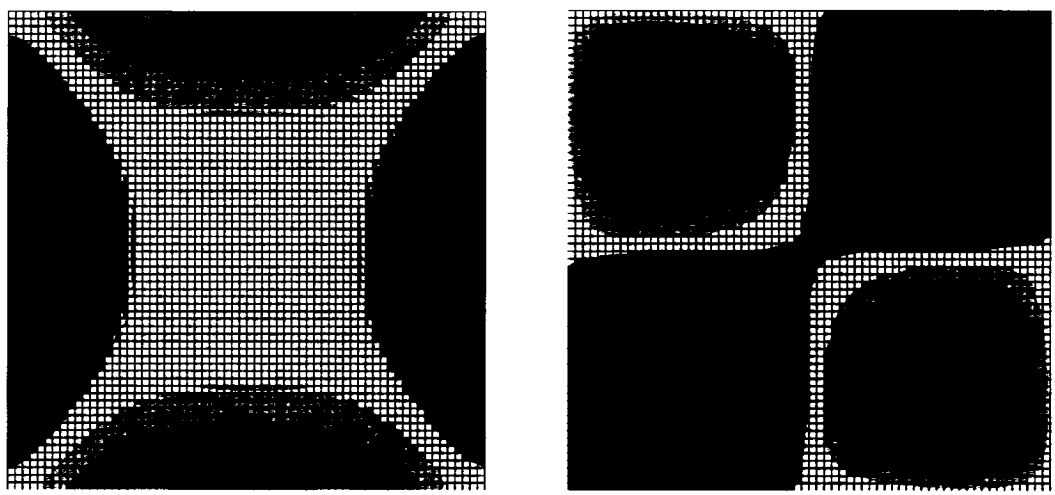

(a) (b)

Figure 6-9: In-plane Shear Stress Distribution for Lay-up 2 Subjected too Two-way Bending (a) $\pm 45^0$ layers (b) 0^0 and 90^0 layers

With the stress distributions as shown in Figure 6-9(a), it can be seen that with a piezoelectric patch embedded near the edge of the plate, it will be in a region of high in-plane shear stresses in the 45^0 layers. However, if a plate is manufactured to be square, or under two-way bending, a piezoelectric patch can be located at regions of relatively low shear stresses in the 0^0 and 90^0 layers, as shown in Figure 6-9(b). With narrow plates, plates under one-way bending, the distribution of the shear stresses is similar, however, the distance from the plate center to the region of high shear stress in the 0^0 and 90^0 layers would be very small. Therefore, in narrow plates, a piezoelectric patch embedded near the edge would be located in regions of high shear stress in all layers. This will result in higher out-of-plane stress concentrations as was seen in the comparison of the two-way and one-way plates in this section.

6.4.3 Effect of Piezoelectric Material Properties on Interlaminar Stress Distribution

In determining the effect of the piezoelectric material properties, a plate subjected to two-way bending, with a quasi-isotropic lay-up of $(90/45/0/-45)_{4s}$, was modeled with three different piezoelectric material property sets. The values of the piezoelectric material properties were as given previously in Table 6-3, where material #3 is the stiffest and material #2 the least stiff. In these models the standard piezoelectric patch size was used, 76.2x25.4x0.5 mm, with it being embedded at interfaces two through five.

From these results, the same distribution of maximum interlaminar stress was observed as that for material #1. Therefore, for comparison purposes only the maximum interlaminar stresses were compared for the four embedding interfaces, as shown in Tables 6-24 and 6-25. The factors shown in these Tables 6-24 and 6-25 are the resulting interlaminar stresses for piezoelectric materials #2 and #3 normalized with respect to the results of #1.

From the factors in Tables 6-24 and 6-25 it can be easily seen that the stiffer the piezoelectric material, the greater the interlaminar stress developed. However, the effects of the piezoelectric material properties are very minor.

Table 6-24: Resulting Interlaminar Stress Factors for Piezoelectric Material #2 Normalized With Respect to Material #1

Embedding Interface of Piezoelectric Patch	Resulting Stress Factor		
	S_{zz}	S_{yz}	S_{xz}
2	0.970	0.970	0.974
3	0.989	0.987	0.983
4	0.986	0.960	0.998
5	0.997	0.999	0.989

Table 6-25: Resulting Interlaminar Stress Factors for Piezoelectric Material #3 Normalized With Respect to Material #1

Embedding Interface of Piezoelectric Patch	Resulting Stress Factor		
	S_{zz}	S_{yz}	S_{xz}
2	1.079	1.030	1.017
3	1.036	1.039	1.037
4	1.053	1.099	1.029
5	1.002	1.043	1.015

6.4.4 Influence of Piezoelectric Patch Size on Interlaminar Stress Distribution

To determine the influence of sensor size on the resulting stress concentrations, the different dimensions given earlier in Table 6-5, were used to model the embedded piezoelectric sensor. In order to determine the influence of an individual dimension, a single dimension of the patch was varied, while the other two were kept at the standard dimensions used for all other models. The lay-up used in determining the effects of patch size on the stress concentrations, was lay-up 2 with a lay-up orientation of $(0/\pm45/90)_{4s}$. In this study, a single embedding interface was used, interface 5, which was selected based on it being the worst-case scenario for this lay-up. For each dimensional investigation, two different sizes were implemented in conjunction with the standard dimensions used in the previous study. This resulted in a total of six different models with the piezoelectric sensor dimensions for each model as given in Table 6-26.

Table 6-26: Piezoelectric Patch Dimensions Used to Determine the Influence of Patch Dimensions on Stress Concentration Levels for Embedded Piezoelectric Sensors

Model Number	Piezoelectric Sensor Dimensions (mm) (length x width x thickness)
Standard Model	76.2 x 25.4 x 0.5
1	50.8 x 25.4 x 0.5
2	101.6 x 25.4 x 0.5
3	76.2 x 50.8 x 0.5
4	76.2 x 76.2 x 0.5
5	76.2 x 25.4 x 0.25
6	76.2 x 25.4 x 1.0

As was the case with varying the material properties of the piezoelectric patch, the distributions of the interlaminar stresses (i.e. position of the maximums) were consistent for all dimensional studies. Therefore, for comparison purposes only the maximum interlaminar stresses were compared for the different sensor sizes. The maximum interlaminar stresses for the varying piezoelectric sensor sizes, comparing the length, width, and thickness effects, are shown in Tables 6-27 through 6-29, respectively.

Table 6-27: Resulting Maximum Interlaminar Stress Values for Varying Piezoelectric Sensor Lengths (Piezoelectric Sensor Width = 25.4 mm, Thickness = 0.5 mm)

Piezoelectric Sensor Length (mm)	Resulting Maximum Interlaminar Stresses (MPa)		
	S_{zz}	S_{yz}	S_{xz}
76.2	24.02	10.40	7.518
50.8	24.17	10.62	7.674
101.6	23.95	9.994	7.438

From Table 6-27 it can be seen that the resulting interlaminar stresses due to changes in the length of the piezoelectric sensor are very small. This would be expected since the dimensional change is not introducing it to regions of high stress gradients.

Table 6-28: Resulting Maximum Interlaminar Stress Values for Varying Piezoelectric Sensor Widths (Piezoelectric Sensor Length = 76.2 mm, Thickness = 0.5 mm)

Piezoelectric Sensor Width (mm)	Resulting Maximum Interlaminar Stresses (MPa)		
	S_{zz}	S_{yz}	S_{xz}
25.4	24.02	10.40	7.518
50.8	23.90	10.54	8.233
76.2	23.89	10.93	8.578

From Table 6-28 it can be seen that increasing the width of the piezoelectric sensor results in very small changes, less than 1%, in the interlaminar peel stress. However, with the increasing width the piezoelectric patch is being introduced to the regions of high in-plane shear stress in the 0^0 and 90^0 layers, as was observed in the plates subjected to one-way bending in a previous section. This results in higher changes to the interlaminar shear stresses, which increase by a maximum of 5.1% and 14% for the y-z and x-z interlaminar shears respectively.

Table 6-29: Resulting Maximum Interlaminar Stress Values for Varying Piezoelectric Sensor Thickness (Piezoelectric Sensor Length = 76.2 mm, Width = 25.4 mm)

Piezoelectric Sensor Thickness (mm)	Resulting Maximum Interlaminar Stresses (MPa)		
	S_{zz}	S_{yz}	S_{xz}
0.50	24.02	10.40	7.518
0.25	22.142	7.670	5.370
1.00	26.44	12.31	10.13

From Table 6-29 it can be seen that the thickness of the piezoelectric does produce significant differences in the resulting interlaminar stress concentrations. By increasing the thickness of the piezoelectric patch to twice the standard thickness used in this study, increases of 10, 18, and 35 percent were seen in the interlaminar peel, y-z shear, and x-z shear stresses respectively. Decreases of 7.8, 26, and 29 percent were seen in the interlaminar peel, y-z shear, and x-z shear stresses for a piezoelectric sensor half the thickness of the standard sensor used in this study.

Chapter 7

Conclusions and Recommendations

7.1 Summary

In the first two chapters of this report the field of smart materials and systems were explored. This included outlining the different levels of smart systems as well as the materials that could be implemented within these systems. Along with the different smart materials available, the advantages and disadvantages associated with each material were discussed. From investigating the different smart materials available, piezoelectric materials were selected due to their ease of implementation, dual capabilities (sensing and actuation), and minimal equipment requirements. In the final sections of Chapter 2, some of the notable works previously conducted to investigate the multiple uses of piezoelectric materials were briefly discussed. This included the capability piezoelectrics for vibration suppression, damage detection, as well as their influences on the integrity of the host materials. It is hoped that these chapters provide the reader with all the information required to fully appreciate the available smart materials, and their full capabilities.

In Chapter 3 the capabilities of small piezoelectric patches for vibration suppression of FRP plates, as well as PVC piping was investigated through an extensive experimental investigation. The approach used to suppress the vibrations consisted of a feedback gain system that was based on the piezoelectric sensor voltage. In order to implement the sensor voltage directly as the feedback value, a self-sensing piezoelectric patch set-up was used. This was achieved by placing the piezoelectric patch as a capacitor element in an RC bridge circuit. An advantage to using a self-sensing piezoelectric sensor/actuator is to reduce the number of required piezoelectric patches, and therefore the cost of the system. It was found that dramatic vibration suppression was achievable in the FRP

plates with the use of this simple control system using a single piezoelectric self-sensing patch. The experimental results for a surface bonded, as well as an embedded piezoelectric patch, exhibited dramatic decreases in the vibration time of the FRP plate. Unfortunately, this was not the case with the larger PVC pipe system, which was too large and stiff for the proposed method of suppression.

Chapter 4 in this report provided details of the current damage detection methodologies that are based on implementing piezoelectric materials. Within this chapter, methods of data measurement, signal processing, data analysis, and damage evaluation methods were detailed. In brief, there are currently two methods used in monitoring the piezoelectric response, (i) is by monitoring the voltage time-history and (ii) by monitoring the impedance of the piezoelectric sensor. Signal processing methods include the Fourier analysis, spectrograph analysis, wavelet analysis, and the empirical mode decomposition. Each of these methods possess advantages and also have shortfalls that are based on the ease of implementation, system applicability, as well as their abilities to determine the presence and/or location of the damage. With each of the above mentioned data processing methods, an appropriate analysis method of the data could be implemented for determining the presence of damage. The data analysis methods include comparing the modal, frequency, time-history, or impedance properties of the system. In conjunction with the data analysis method, an appropriate damage evaluation method must also be implemented, which is generally involved with the use of damage indices. With the information provided within this chapter, it is hoped that the reader is fully informed on the different methods available for an efficient damage detection system.

Chapter 5 outlines details of an extensive experimental investigation into the capabilities of damage detection in pipe joints with the use of piezoelectric sensors. For this study, the goal was to develop a strategy to satisfy several criteria that would make an efficient and economical damage detection system. These criteria include minimizing the required equipment, along with making the outcome of the system independent of the sensor,

damage, and loading location as well as the support conditions. To perform these tasks the investigation was broken down into two sections. The first was an investigation into damage detection capabilities in adhesively bonded pipe joints, using the commercially available APEX 6" PVC sewer pipe. In this study the influences of sensor, damage, and loading locations were explored along with the influence of support conditions.

The second portion of this study involved studying the damage detection capabilities of the proposed methodology for mechanically fastened pipe systems. This study used two different test set-ups for both the PVC and cast iron utility pipe systems. This investigation determined the effects of sensor and loading locations as well as the ability to determine the degradation of the joint.

Chapter 6 gives the results for a finite element investigation into the influences of embedding piezoelectric patches into the host FRP plates. The issues that were addressed in this study included the influence of the laminate lay-up orientation, embedding interface of the piezoelectric patch, plate curvature, piezoelectric material properties, and the size of the piezoelectric patch, mainly on the out-of-plane the stresses.

7.2 Conclusions

From the findings of this report, the following conclusions are made:

1) Due to their ease of use, relatively minimal equipment requirement, relatively inexpensive cost, and multi-functionality, piezoelectric materials are leading the way in the field of smart materials.

2) For vibration control applications, piezoelectric materials are a very feasible option as long as the system is specifically developed for the desired application. The method used for this study was a very simplistic and easily implementable system, that showed some promise as well as some limitations. The promise of the proposed

system was observed in the vibration suppression of the FRP plates, where excellent results were seen for both the surface bonded and embedded piezoelectric sensor/actuator. Also, a direct correlation between the efficiency of the embedded piezoelectric patch to the surface bonded patch could be seen from the linear theory based on the embedding depth of the piezoelectric sensor/actuator. The limitation of the proposed method was observed when the system was applied for the vibration suppression of the PVC pipe. In this case, the simple method implemented earlier fell short of effectively suppressing the vibration. Although initial suppression capabilities were observed, in the full time response of the pipe the suppression was found to be insufficient. The above shortfall is attributed to the following reasons:

- With the acquisition system available, the experiments were limited to a single gain value for all sensor readings. Therefore, as the sensor voltage response decayed, the actuation voltage applied to the piezoelectric patches was also reduced. This led to insufficient actuation forces and therefore, no suppression in the time history response could be attained. With a computer algorithm capable of applying optimal control methodology, the set-up used in this investigation may have been sufficient.
- The piezoelectric patches were undersized. With larger piezoelectric actuators, the larger force required to suppress the vibration of the pipe could be achieved.

3) The proposed approach to damage detection monitored the time history response of the piezoelectric sensors, implemented the Fourier analysis, and easily implemental damage indices schemes to identify the degradation of both an adhesively bonded and mechanically fastened pipe joints. This approach for damage detection in pipe joints resulted in a system that is very economical, efficient, and user-friendly, and exhibited excellent results.

4) In the adhesively bonded pipe joints, the optimal location for the piezoelectric sensor was found to be situated directly on the joint. From the results, the capability of the damage detection system to determine the presence of damage, as well as provide a quantitative measure of the damage severity was well established. It was found with this method that the sensor could be located anywhere on the joint to produce excellent results. Also, the overall ability of this method to determine the presence of damage was not influenced by the location of the excitation force, sensor location, damage location, or the support conditions. However, it was found that for the given set-up a more pronounced damage index was found when the following conditions hold:

- Different loading locations
- More rigid support conditions
- Having the sensor located in the vicinity of the damage. This would however be impractical in real applications

5) In the case of mechanically fastened pipe joints, previous works involved bonding the piezoelectric sensor directly on the joint. In this configuration, however, the sensor located on the joint could be potentially damaged when general maintenance is applied. In the proposed system, however, the sensors were located away from the joint, yet produced very promising results. It was found that for these experiments the optimal location for the sensor would be across the joint from the loading, as would be expected due to the reduced signal progressing through the weaker joint. In the experiments conducted, all damage indices could clearly detect the degradation of the joint.

6) The mean absolute percent deviation (MAPD) index produced indices with distinctly large magnitudes, which were good for determining the presence of damage; the consistency however was not as good as those obtained through the root mean square deviation (RMSD) index. The correlation coefficient (CC) index produced very consistent results; however, the change in magnitude as the damage grows is relatively

small, which influences the capabilities of the system to identify damage growth. The RMSD index produced indices with large magnitudes as well as relatively good consistency. This consistency was clearly seen from the data of the two sensors processed through the RMSD, in the adhesively bonded joint. For the mechanically fastened joint, the RMSD produced results that showed a steady increase with damage. Therefore, the RMSD index was found to perform the best due to its consistently pronounced results.

7) With the proposed damage detection method, it was found that only a single sensor would be all that is required to produce practical results. In the case of the adhesively bonded joint, a single sensor could be located on the joint to produce good results even though it may not be located directly on the damaged section. For the mechanically fastened pipe joint, the single sensor only needs to be placed across the joint from the loading. In output only systems the determination of the presence of damage would be much more complicated. In order for this system to work, the exact input would not have to be known, however the loading conditions for comparing sets of outputs would have to be similar. An example of this would be if fluid flow were used as the input stimuli. In this case, it would have to be known that the fluid is flowing, or should be flowing, at a set rate. In this situation, if a leak is present at a joint, the vibration response of the system would fluctuate and the damage could be observed. It would not be sufficient to compare the response of the sensors if the measurements were for known flows at different levels.

8) The following observations were found from the investigation on the embedding effects of piezoelectric sensors:

- Among the lay-up sequences investigated, the cross-ply lay-up of $(0/90)_{8s}$ provided the best case (lowest through thickness stresses) for embedding the

piezoelectric sensor. However, this lay-up may not provide the required properties for general use due to limited shear resistance due to lack of the 45^0 plies.

- For the quasi-isotropic lay-ups, it is beneficial to eliminate the (0/90) interfaces. An increased interlaminar shear stress would be present in such interfaces. The lowest interlaminar shear stresses in the laminate were present in the quasi-isotropic lay-up of $(90/45/0/-45)_{4s}$. This laminate does not possess the (0/90) interface. This lay-up also produced the least interlaminar peel stress concentration.
- A simply supported plate that undergoes one-way bending produced much larger concentrations of interlaminar stresses than when it was subjected to two-way bending. This was due to the edges of the piezoelectric sensor being in the locations of higher stress gradients then that of the two-way plate.
- Stiffer piezoelectric materials produce larger interlaminar shear stresses. However, the maximum difference in interlaminar stresses between the most stiff and least stiff piezoelectric material was only 10%.
- The thickness of the piezoelectric sensor was found to be the most influential dimension in causing higher stresses. Major increases in the interlaminar stresses were observed when the thickness of the piezoelectric sensor was increased.
- Increasing the width of the piezoelectric patch produced moderate increases in the interlaminar stress concentrations. This is believed to be due to the edges of the piezoelectric patch entering areas of higher stress gradients.
- Varying the length of the piezoelectric patch produced insignificant differences in the interlaminar stress concentrations.

7.3 Recommendations for Future Work

The work performed in this thesis was to get a full understanding of the feasibility of implementing piezoelectric sensors and actuators for varying applications. The growth in the field of smart materials and systems over the past decade, and even through the period of time elapsed during the present investigation has been substantial. Currently, the works that have been performed on vibration suppression in many structural systems

have been widely documented; therefore, no specific recommendations would be made for such applications. However, through the other works performed in our investigation, the following recommendations for further studies are suggested.

1) The damage detection method that was implemented for this thesis showed excellent results for the set-ups used. However, this method was limited to pipes that are currently exposed (i.e. no buried pipes were investigated). Therefore, the following test set-ups are proposed for further experimental studies:
   - Conduct the experiments with the pipes full of fluid to simulate the real world situations
   - Bury the joint section of the pipe in various media (i.e. vary the stiffness of the surrounding material). This will determine whether the proposed system would be as effective in detecting the damage with the joint encased in various media.
   - Determine if the proposed damage detection approach works on pipes that are also loaded axially.
   - Determine if the vibrations caused by the fluid running through the pipe (or by changing the velocity of the fluid in the pipe, say, by shutting of the valves) could be directly used as the required exciting load. This will allow for a more efficient and continuous real time damage evaluation.

2) Conduct further finite element analyses to determine the influence of embedding piezoelectric patches on the interlaminar stresses when embedded into laminated structures. The further studies should investigate the following issues:
   - Modeling of the influence of piezoelectric sensor on different systems, such as repair patches or structures with curved surfaces.
   - Further study the influence of plate dimensions. This will allow for the development of a procedure to determine the optimal piezoelectric patch size relative to the plate width.

- Study the influence of laminate layer thickness along with piezoelectric patch thickness, where both generally vary with each lay-up.
- Further investigate the influence of piezoelectric material property for establishing a practical relationship between, for instance, the stiffness of the piezoelectric patch and the resulting stress concentrations.

References

Ayres, J.W., Lalande, F., Chaudhry, Z., and Rogers, C.A., (1998), Qualitative Impedance-Based Health Monitoring of Civil Infrastructures, Smart Material Structures, 7(5), 599-605.

Bhalla S., (2000), Smart system based automated health monitoring of structures, Unpublished Master's Thesis, Nanyang Technological University, Singapore.

Caccese V., Mewer R., and Vel S.S., (2004), Detection of Bolt Load Loss in Hybrid Composite /Metal Bolted Connections, Engineering Structures, 26(7), 895-906.

Cawley P., and Adams R.D., (1979), The Location of Defects in Structure from Measurements of Natural Frequencies, Journal of Strain Analysis, 14(2), 49-57.

Chandrashekhara K., and Varadarajan S., (1997), Adaptive Shape Control of Composite Beams with Piezoelectric Actuators, Journal of Intelligent Material Systems and Structures, 8(2), 112-124.

Chaudhry Z., Joseph T., Sun F.P., and Rogers C.A., (1995), Local-area health monitoring of aircraft via piezoelectric actuator/sensor patches, Proceedings of the Smart Structures and Materials 1995: Smart Structures and Integrated Systems, Feb 27-Mar 3, San Diego, CA, USA. Society of Photo-Optical Instrumentation Engineers, Bellingham, WA, USA.

Chaudhry Z., Lalande F., Ganino A., Rogers C.A., and Chung J., (1995), Monitoring the integrity of composite patch structural repair via piezoelectric actuators/sensors, Proceedings of the Proceedings of the 36th AIAA/ASME/ASCE/AHS/ASC Structures, Structural Dynamics, and Materials Conference and AIAA/ASME Adaptive Structures Forum. Part 4 (of 5), Apr 10-13 1995, New Orleans, LA, USA. AIAA, New York, NY, USA.

Chiu W.K., Galea S.C., Koss L.L., and Rajic N., (2000), Damage Detection in Bonded Repairs using Piezoceramics, Smart Material Structures, 9(4), 466-475.

Clark R.L., Saunders W.R., and Gibbs G.P., (1998), Adaptive Structures: Dynamics and Control, New York, Toronto, Wiley.

Doebling S.W., Farrar C.R., Prime M.B., and Shevitz, D.W., (1996), Damage Identification and Health Monitoring of Structural and Mechanical Systems from Changes in Their Vibration Characteristics: A Literature Review, Los Alamos National Laboratory Technical Paper LA-13070-MS.

Drazin P.G., (1992), Nonlinear systems, Cambridge, Cambridge University Press.

Future Fibers Technologies Pty. Ltd., (2001), Science of Fiber Optic Sensors, http://fft.com.au/backgrnd.html, Accesses 04/20.

Grewal A., Zimcik D.G., Hurtubise L., and Leigh B, (2000), Active Cabin Noise and Vibration Control for Turboprop Aircraft using Multiple Piezoelectric Actuators, J Intell Mater Syst Struct, 11(6), 438-447.

Giurgiutiu V., Reynolds A., Rogers C.A., Chao Y.J., and Sutton M.A., (1998), E/M Impedance Health Monitoring of Spot-Welded Structural Joints, ASME Adaptive Structures And Material Systems Symposium Nov. 15-20, Anaheim, CA, USA.

Giurgiutiu V., and Rogers C.A., (1998), Recent Advancements in the Electro-Mechanical (E/M) Impedance Method for Structural Health Monitoring and NDE, SPIE's 5th Annual International Symposium on Smart Structures and Materials, 1-5 March, Catamaran Resort Hotel, CA, USA.

Han J., and Lee I., (1998), Analysis of Composite Plates with Piezoelectric Actuators for Vibration Control using Layerwise Displacement Theory, Composites Part B:Eng, 29(5), 621-632.

Han J., Rew K., and Lee I., (1997), Experimental Study of Active Vibration Control of Composite Structures with a Piezo-Ceramic Actuator and a Piezo-Film Sensor, Smart Mater Struct., 6(5), 549-558.

Hwang W., Park H.C., and Hwang W., (1993), Vibration Control of a Laminated Plate with Piezoelectric Sensor/ Actuator: Finite Element Formulation and Modal Analysis, J Intell Mater Syst Struct, 4(3), 317-329.

Introduction to Products, (2001), http://www.txre.net/eng/chanpin.htm, Accessed 04/20.

Kessler S.S., Atalla M.J., Cesnik C.E.S., Soutis C., and Mark Spearing S, (2002), Damage Detection in Composite Materials using Frequency Response Methods. Composites Part B:Eng, 33(1), 87-95.

Kang Y.K., Park H.C., Hwang W., and Han K.S., (1996), Optimum Placement of Piezoelectric Sensor/Actuator for Vibration Control of Laminate Beams, AIAA Journal, 34(9), 1921-1926.

Koko T.S., Orisamolu I.R., Smith M., and Akpan U.O., (1997), Finite-element-based design tool for smart composite structures. Proceedings of the Smart Structures and Materials 1997: Mathematics and Control in Smart Structures, Mar 3-6, San Diego, CA, USA, Society of Photo-Optical Instrumentation Engineers, Bellingham, WA, USA.

Lauwagie T., Sol H., and Dascotte E., (2002), Damage identification in beams using inverse methods. Proceedings of the Proceedings of the 2002 International Conference on Noise and Vibration Engineering, ISMA, Sep 16-18 2002, Leuven, Belgium. Katholieke Universiteit Leuven, Heverlee, B-3001, Belgium.

Liang C., Sun F.P., and Rogers C.A., (1993), Impedance method for dynamic analysis of active material systems. Proceedings of the 34th AIAA/ASME/ASCE/AHS/ASC Structures, Structural Dynamics, and Materials Conference, Apr 19-22 1993, La Jolla, CA, USA. Publ by AIAA, Washington, DC, USA.

Lim Y.H., Varadan V.V., and Varadan V.K., (1997), Closed-loop finite element modeling of active/passive damping in structural vibration control. Proceedings of the Smart Structures and Materials 1997: Mathematics and Control in Smart Structures, Mar 3-6 97, San Diego, CA, USA. Society of Photo-Optical Instrumentation Engineers, Bellingham, WA, USA.

Mall S., (2002), Integrity of graphite/epoxy Laminate Embedded with Piezoelectric sensor/actuator Under Monotonic and Fatigue Loads, Smart Mater Struct., 11(4), 527-533.

Mays L.W., and Tung Y.K., (1992), Uncertainty and reliability analysis of hydrosystems Hydrosystems Engineering and Management, New York, McGraw-Hill.

Mechanism of ER Effect, (2001), http://www.shokubai.co.jp/english/main/kaihatsu/tx_er /txer2.htm, Accessed 04/20.

Mickens T., Schulz M., Sundaresan M., Ghoshal A., Naser A.S., and Reichmeider R., Structural Health Monitoring of an Air Craft Joint. Mechanical Systems and Signal Processing, 17(2), 285-303.

Oshima K., Takigami T., and Hayakawa Y., (1997), Robust Vibration Control of a Cantilever Beam using Self-Sensing Actuator, JSME Int J Ser C, 40(4), 681-687.

Pardo de Vera C, Guemes JA. Embedded Self-Sensing Piezoelectric for Damage Detection. J Intell Mater Syst Struct. 1999; 9(11):876-882.

Park G, Muntges DE, Inman DJ. Self-Monitoring and Self-Healing Jointed Structures. Key Eng Mat. 2001; 204-205:75-84.

Piezo System Inc., Generator Transducer Relationships, (2001), http://www.piezo.com /genera.htm, Accessed 04/20.

Piezo System Inc., Motor Transducer Relationships, (2001), http://www.piezo.com /motor.htm, Accessed 04/20.

PolyTech PI Ceramics, (2001), http://www.polytecpi.com/pic.htm, Accessed 04/20.

Qiu J., and Tani J., (1996), Vibration Suppression of a Cylindrical Shell using a Hybrid Control Method, J Intell Mater Syst Struct, 7(3), 278-285.

Redmond J., and Barney P., (1997), Vibration Control of Stiff Beams and Plates using Structurally Integrated PZT Stack Actuators, J. Intell. Mater Syst. Struct., 8(6), 525-535.

Ritdumrongkul S., Abe M., Fujino Y., and Miyashita T., (2003), Quantitative health monitoring of bolted joints using piezoceramic actuator-sensor. Proceedings of the Smart Structures and Materials 2003: Smart Systems and Nondestructive Evaluation for Civil Infrastructures, Mar 3-6 2003, San Diego, CA, United States. The International Society for Optical Engineering.

Salawu O.S., (1997), Detection of Structural Damage through Changes in Frequency: A Review, Eng. Struct., 19(9), 718-723.

Sanders D.R., Kim Y.I., and Stubbs N., (1992), Nondestructive Evaluation of Damage in Composite Structures using Modal Parameters, Exp Mech., 32(3), 240-251.

Saravanan C., Ganesan N., and Ramamurti V., (2000), Analysis of Active Damping in Composite Laminate Cylindrical Shells of Revolution with Skewed PVDF sensors/actuators, Composite Structures, 48(4), 305-318.

Shah D.K., Chan W.S., Joshi S.P., and Subramanian S., (1990), Analysis of laminates with embedded piezoelectric layers. Proceedings of the Winter Annual Meeting of the American Society of Mechanical Engineers, Nov 25-30 1990, Dallas, TX, USA. Publ by ASME, New York, NY, USA.

Shukla D.R., and Vizzini A.J. Interlacing for Improved Performance of Laminates with Embedded Devices, Smart Mater Struct., 5(2), 225-229.

Singh D.A., and Vizzini A.J., (1994), Structural Integrity of Composite Laminates with Interlaces Actuators, Smart Mater Struct., 3(1), 71-79.

Soares, C.M.M., Soares, C.A.M., and Correia, V.M.F, (1999), Optimal Design of Piezolaminated Structures, Composite Structures, 1999, 47, 625-634.

Soh C.K., Tseng K.K., Bhalla S., and Gupta A., (2000), Performance of Smart Piezoceramic Patches in Health Monitoring of a RC Bridge, Smart Mater Struct., 9(4), 533-542.

Sohn H., Park G., Wait J.R., Limback N.P., and Farrar C.R., (2004), Wavelet-Based Active Sensing for Delamination Detection in Composite Structures, Smart Mater Struct., 13(1):153-160.

Smith M.J., Koko T.S., and Orisamolu I.R., (1998), Comparative Assessment of Optimal Control Methods with Integrated Performeance Constraints, Proceedings of ASME Annual Meeting, Anaheim, California.

Squire P., (1999), Magnetostrictive Materials for Sensors and Actuators, Ferroelectrics, 228(1-4), 305-319.

Sun D., and Tong L., (2001), Modal Control of Smart Shells by Optimized Discretely Distributed Piezoelectric Transducers, Int J Solids Structures., 38(18), 3281-3299.

Sun F.P., Chaudhry Z.A., Rogers C.A., Mujmundar M., and Liang, C., (1995), Automated real-time structure health monitoring via signature pattern recognition. Proceedings of the Smart Structures and Materials 1995: Smart Structures and Integrated Systems, Feb 27-Mar 3 95, San Diego, CA, USA. Society of Photo-Optical Instrumentation Engineers, Bellingham, WA, USA.

Sun Z., and Chang C.C., (2002), Structural Damage Assessment Based on Wavelet Packet Transform, Journal of Structural Engineering, 128(10), 1354-1361

Tani J., Qiu J., and Miura H., (1994), Vibration Control of a Cylindrical Shell System using Piezoelectric Film. Nippon Kikai Gakkai Ronbunshu, C Hen/Transactions of the Japan Society of Mechanical Engineers: Part C., 60(570), 443-449.

Tani J., Qiu J., and Miura H., (1995), Vibration Control of a Cylindrical Shell using Piezoelectric Actuators, J Intell Mater Syst Struct., 6(3), 380-388.

Tseng K.K., and Naidu A.S.K., (2002), Non-Parametric Damage Detection and Characterization using Smart Piezoceramic Material, Smart Mater Struct., 11(3), 317-329.

Wada B.K., Fanson J.I., and Crawley E.F., (1990), Adaptive Structures, Mech Eng., 112(11), 41-46.

Wang C., and Vaicaitis R., (1998), Active Control of Vibrations and Noise of Double Wall Cylindrical Shells, J Sound Vibrat., 216(5), 865-888.

Yang S.M., and Bian J.J., (1996), Vibration Suppression Experiments on Composite Laminated Plates using an Embedded Piezoelectric Sensor and Actuator, Smart Mater Struct., 5(4), 501-507.

Yang S., Gu L., and Gibson R.F., (2001), Nondestructive Detection of Weak Joints in Adhesively Bonded Composite Structures, Composite Structures, 51(1), 63-71.

Appendix A MATLAB Codes Developed for Processing the Plate Vibration Suppression Results

piezosensor.m

```
% THIS PROGRAM REMOVES THE NON-RESPONSE DATA FROM THE
PIEZOELECTRIC SENSOR RESPONSE
% IT ALSO CALCULATES THE INDIVIDUAL POINT TIMES FOR THE
EXPERIMENT

format long

clear;

% Import test results into variable test
test(:,1) = importdata('c:\directory\filename');

% Determines the number of data points in the entire file
[z,y]=size(test);
% The variable 'n' will hold the number of data points for each parameter
n=(z/2);

% The following seperates the time and piezoelectric voltage from the file
% The piezoelectric sensor voltage is stored in the variable 'volt'
% The time recordings from the experiment file are stored in variable 't'
volt = test(1:n,1);
t = test(n+1:z,1);

% Loop corrects for any offset in the sensor response
for i = 1:n
   volt(i,1) = volt(i,1)-volt(n,1);
end

% Determines the test start position and stores it in variable 'start'
s=find(abs(test) > 0.5);
start=s(1)-3;

% The following command removes the initial nonresponse data from the variable 'volt'
volt(1:start,1) = [];

% The following loop determines the magnitude of the time jump and stores it in the
variable 'jump'
% The magnitude of the jump will be stored in the position the jump occurs
for i=2:n
   jump(1)=1;
   if t(i)-t(i-1) == 0
      jump(i)=0;
   else
```

```
      jump(i)=tm(i)-tm(i-1);
   end
end

% The following command determine the position of each time jumps and stores it in the
variable 'q'
q = find(jump > 0);

% Determines the number of time jumps and stores it in the variable 'w'
[w,b] = size(transpose(q));

% The following loop determines the deltatime for each interval in the data set
for i = 2:w;
   l = q(i)-q(i-1);       % 'l' will hold the number of points in the current interval
   g = q(i);              % 'g' will hold the global position of the jump in the time reading
   f = jump(g);           % 'f' will hold the time change during the interval
   for j = g-l+1:g
      deltatime(j) = f/l; % 'deltatime' will store the deltatime for each point up to the last
jump
   end
end

[d,e]=size(transpose(deltatime));

% The following sets the deltatime of the last few data points
for i = 1:n-d;
   deltatime(d+i) = deltatime(d);
end

% The following loop computes the full time vector for the test
% Variable 'time_holder' stores the full time vector
for i=2:n;
   time_holder(1,1) = 0;
   time_holder(i,1) = time_holder(i-1,1)+deltatime(i);
end

% The following command removes the initial nonresponse data and reinitializes the time
to zero
% The final time scale for each data point is stored in the variable 'time'
time_start = time_holder(start,1);          % 'time_start' stores the response start time
time_holder(1:start,1) = [];                % Removes initial nonresponse times

% Reinitializes the starting time to zero
```

```
for i = 1:n-start
   time(i,1) = time_holder(i,1)-time_start;
end

% Variable 'end_time" will store the location of points past 4 seconds
% 'end_time(1,1)' will be the last point in the data
end_time = find(time > 4.0);

% The following commands remove the data in 'time' and 'volt' past the 4 second point
volt(end_time(1,1)+1:n-start,1) = [];
time(end_time(1,1)+1:n-start,1) = [];

% The time and sensor voltage are stored as columns in the variable 'results'
results = [time volt];

% Plots the piezoelectric voltage vs. time
plot(results(:,1),results(:,2))

% The variable 'results' is written to a file named 'experiment.txt'
save experiment.txt results -ASCII
```

hammer.m

```
% THIS PROGRAM PROCESSES THE IMPULSE HAMMER TEST RESULTS TO
REMOVE NON-RESPONSE DATA

format long

clear;

% The hammer result file is read into the variable 'hammer'
hammer(:,1) = importdata('c:\directory\filename.txt');

% The variable 'rate' is the acquisition rate of the hammer
rate = 10000;

% 'a' will hold the number of points in the data set
[a,b] = size(accel);

% The following loop corrects for any offset that may be present
for i = 2:a
   hammer(i,1) = hammer(i,1) - hammer(1,1);
end

% The following commands determine the actual starting point of the experiment
% The location of the start is stored in the variable 'start'
s = find(hammer(:,1) > 0.01);
start = s(1) - 2;

% The following loop stores the hammer voltage and time in a single variable 'results'
% Initializes the starting point to zero
results(a-start,1:2) = 0.0;
for i = start:0.5*rate
   results(i-start+1,1) = results(i-start,1)+1/rate; % Determines the time column
   results(i-start+1,2) = hammer(i,1);              % Determines the hammer voltage column
end

% Plots the hammer voltage vs. time
plot(results(:,1),results(:,2))

% The variable 'results' is written to a TEXT file named 'experiment.txt'
save experiment.txt results –ASCII
```

accelerometer.m

```
% THIS PROGRAM PROCESSES THE ACCELEROMETER TEST RESULTS TO
REMOVE NON-RESPONSE DATA

format long

clear;

% The accelerometer result file is read into the variable 'accel'
accel(:,1) = importdata('c:\directory\filename.txt');

% The variable 'rate' is the acquisition rate of the accelerometer
rate = 10000;

% 'a' will hold the number of points in the data set
[a,b] = size(accel);

% The following loop corrects for any offset that may be present
for i = 2:a
   accel(i,1) = accel(i,1) - accel(1,1);
end

% Initializes the first data point
accel(1,1) = 0.0;

% The following commands determine the actual starting point of the experiment
% The location of the start is stored in the variable 'start'
s = find(accel(:,1) > 0.01);
start = s(1) - 2;

% The following loop stores the accelerometer voltage and time in a single variable
'results'
results(a-start,1:2) = 0.0;  % Initializes the starting point to zero
for i = start:4*rate
   results(i-start+1,1) = results(i-start,1)+1/rate; % Determines the time column
   results(i-start+1,2) = accel(i,1);              % Determines the accelerometer voltage
end

% Plots the accelerometer voltage vs. time
plot(results(:,1),results(:,2))

% The variable 'results' is written to a file named 'experiment.txt'
save experiment.txt results -ASCII
```

Appendix B MATLAB Codes Developed for Processing the PVC Pipe Vibration Suppression Results

pipevib.m

```
% OPERATIONS PERFORMED IN THIS CODE ARE AS FOLLOWS
% 1) REMOVES NON-RESPONSE DATA FROM THE PIEZOELECTRIC SENSORS
% 2) DETERMINES THE FAST FOURIER TRANSFORM OF THE TEST DATA
% 3) PRODUCES PLOTS TO CHECK FOR INCONSISTENCIES BEFORE
PROCESSING RESULTS

clear;

format long;

% The following commands allow the used to input
% The required test data on the main MATLAB screen

% Baseline test properties
a = input('Enter baseline file name: ')              % Filename
b = input('Enter baseline test time: ')              % Total time for test
c = input('Enter number of samples in baseline test: ') % Number of data points monitored

%Control test properties
d = input('Enter control file name: ')               % Filename
e = input('Enter control test time: ')               % Total time for test
f = input('Enter number of samples in control test: ')  % Number of data points monitored

% Number of sensors used in the test
num_sensors = input('Enter number of sensors in the test: ')

% Controls the plots to be shown 'y' for yes, 'n' for no
plot_voltage = input('Plot voltage vs. time: ');
plot_fourier = input('Plot fourier spectrum: ');

% Loads the baseline file into variable 'base'
base = load(a);
% Loads the control file into variable 'control'
control = load(d);

% Loop determines if any offset exists in each sensor response
for i = 1:num_sensors
   base_offset(i,1) = base(c,i);
   control_offset(i,1) = control(f,i);
end

% Following loops correct for any offset that exists
for i = 1:c
```

```
   base(i,:) = base(i,:)-base_offset;
end
for i = 1:f
   control(i,:) = control(i,:)-control_offset;
end

% Determines the start of the test based on the sensor closest to the free end
base_start = find(abs(base(:,num_sensors))>0.08);
control_start = find(abs(control(:,num_sensors))>0.08);

% Removes the non-response data from the start of the test
base(1:base_start-1,:) = [];
control(1:control_start-1,:) = [];

% Determine the delta time between the data points
delt_a = b/c;   % Baseline delta time stored in 'delt_a'
delt_b = e/f;   % Control delta time stored in 'delt_b'

% Initialization for entering a time column
base(:,6) = 0.0;
control(:,6) = 0.0;

% Determines the new size of the data sets after removal of initial non-response data
[z,zz] = size(base);
[w,ww] = size(control);

% Following loops determine the time column for the data sets
for i = 2:z
   base(i,6) = base(i-1,6) + delt_a;
end
for i = 2:w
   control(i,6) = control(i-1,6) + delt_b;
end

% Determines at which point the data is past 4 seconds for the end of test
% 'base_end(1,1)' will be the first point beyond 4 seconds in the baseline file
base_end = find(base(:,6) > 4.0);
% 'control_end(1,1)' will be the first point beyond 4 seconds in the control file
control_end = find(control(:,6) > 4.0);

% Removes the non-response data from the end of the tests
base(base_end(1,1)+1:z,:) = [];
control(control_end(1,1)+1:w,:) = [];
```

```
% the following loop computes the Fourier spectrum of the results
for i = 1:num_sensors
   baseY(:,i) = fft(base(:,i),4096);
   basePYY(:,i) = baseY(:,i).* conj(baseY(:,i))/4096;
   controlY(:,i) = fft(control(:,i),4096);
   controlPYY(:,i) = controlY(:,i).* conj(controlY(:,i))/4096;
end

% Determines the rate of acquisition for the experiments
del_a_inv = inv(delt_a);   % Baseline acquisition rate is stored in 'del_a_inv'
del_b_inv = inv(delt_b);   %Control acquisition rate is stored in 'del_b_inv,

% Determines frequency scale for Fourier plots
fa = del_a_inv*(0:2048)/4096;
fb = del_b_inv*(0:2048)/4096;

% The following loops produces the plots
% Plots the voltage response for the baseline, control, and comparison
if plot_voltage == 'y'
   for i = 1:num_sensors
     figure(1); subplot(5,1,i); plot(base(:,6),base(:,i));
     legend('Baseline Specimen');
     figure(2); subplot(5,1,i); plot(control(:,6),control(:,i));
     legend('Control Specimen');
     figure(2+i); plot(base(:,6),base(:,i));...
              hold on;...
              plot(control(:,6),control(:,i),'-r');
     legend('Baseline Specimen','Control Specimen');
     xlabel('Time (sec)');
     ylabel('Voltage (V)');
     if i == 1
       title('Piezoelectric Sensor 1 Voltage');
     elseif i == 2
       title('Piezoelectric Sensor 2 Voltage');
     elseif i == 3
       title('Piezoelectric Sensor 3 Voltage');
     elseif i == 4
       title('Piezoelectric Sensor 4 Voltage');
     else
       title('Piezoelectric Sensor 5 Voltage');
     end
  end
  figure (1); subplot(5,1,1); title('Piezoelectric Sensor Voltage for the Baesline
Specimen');
```

```
            subplot(5,1,5); xlabel('Time (sec)');
            subplot(5,1,3); ylabel('Sensor Voltage (V)');
  figure (2); subplot(5,1,1); title('Piezoelectric Sensor Voltage for the Controlled
Specimen');
            subplot(5,1,5); xlabel('Time (sec)');
            subplot(5,1,3); ylabel('Sensor Voltage (V)');
end


% Plots the Fourier spectrum for the baseline, control, and comparison
if plot_fourier == 'y'
  for i = 1:num_sensors
     figure(8); subplot(5,1,i); plot(fa,basePYY(1:2049,i));
     legend('Baseline Specimen');
     figure(9); subplot(5,1,i); plot(fb,controlPYY(1:2049,i));
     legend('Control Specimen');
     figure(9+i); plot(fa,basePYY(1:2049,i));...
        hold on;...
        plot(fb,controlPYY(1:2049,i),'-r');
     legend('Baseline Specimen','Control Specimen');
     xlabel('Frequency (Hz)');
     ylabel('Power');
     if i == 1
        title('Fourier Power Spectrum for Sensor 1');
     elseif i == 2
        title('Fourier Power Spectrum for Sensor 2');
     elseif i == 3
        title('Fourier Power Spectrum for Sensor 3');
     elseif i == 4
        title('Fourier Power Spectrum for Sensor 4');
     else
        title('Fourier Power Spectrum for Sensor 5');
     end
  end
  figure (8); subplot(5,1,1); title('Fourier Power Spectrum for the Baesline Specimen');
            subplot(5,1,5); xlabel('Frequency (Hz)');
            subplot(5,1,3); ylabel('Power');
  figure (9); subplot(5,1,1); title('Fourier Power Spectrum for the Controlled Specimen');
            subplot(5,1,5); xlabel('Frequency (Hz)');
            subplot(5,1,3); ylabel('Power');
end


% Saves results to text files
```

```
% Saves time history files
save nocontrol.txt base -ASCII  % No control file
save control.txt control -ASCII % Control file
% Saves fourier spectrum files
save noconfourier.txt basePYY -ASCII    % No control file
save confourier.txt controlPYY -ASCII   % Control file
```

Appendix C MATLAB Codes Developed for Processing the Adhesively Bonded Pipe Joint Experimental Results

fullpiezo.m

```
% THIS CODE REMOVES ANY NON-RESPONSE DATA AND ANY OFFSET

clear;

format long;

% Command for entering the result file which is entered on the main MATLAB prompt
a = input('Enter baseline file name: ');

% 'points' is the number of data points acquired
points = 20000;
% 'rate' is the data acquisition rate
rate = 10000;

% Loads piezoelectric sensor file into variable 'base_holder'
base_holder = load(a);

[a,aa] = size(base_holder);

% Determines the number of tests performed
number_tests = a/(points);

% Seperates the results of the different tests into different columns in variable 'base'
for j = 1:number_tests
   for i = 1:points
      base(i,j) = base_holder(i+(j-1)*points,1);
   end
end

base_holder = [];

% Following loop corrects for any offset in the data
for i = 1:number_tests
   for j = 1:points
      base(j,i) = base(j,i) - base(points,i)
   end
end

% Puts voltage into proper scale, measured value was 6.5% of actual
test1 = base(:,1)/0.065;    % Test 1
test2 = base(:,2)/0.065;    % Test 2
test3 = base(:,3)/0.065;    % Test 3
```

```
base = [];

% Determines when the voltage is greater than 1 volt to determine test start point
st1 = find(abs(test1) > 1); % Test 1
st2 = find(abs(test2) > 1); % Test 2
st3 = find(abs(test3) > 1); % Test 3

% Determines start point of test, 200 chosen to eliminate any possibility of initial offsets
start1 = find(st1 > 200);   % Test 1
start2 = find(st2 > 200);   % Test 2
start3 = find(st3 > 200);   % Test 3

% Removes all non-response data before the start of the test
test1(1:st1(start1(1,1),:)-5,:) = [];   % Test 1
test2(1:st2(start2(1,1),:)-5,:) = [];   % Test 2
test3(1:st3(start3(1,1),:)-5,:) = [];   % Test 3

% Eliminates results past 1 second, non-response data
test1 = test1(1:10000,1);   % Test 1
test2 = test2(1:10000,1);   % Test 2
test3 = test3(1:10000,1);   % Test 3

% Initializes the time to zero
time(1,1) = 0.0;

% Loop computed the time vector for the data
for i = 2:10000
   time(i,1) = time(i-1,1) + 1/rate;
end

% Plots the sensor responses for the three tests on one plot
figure(1); plot(time, test1(:,1),time, test2(:,1),'-r',time, test3(:,1),'-g' );

% Stores all three tests in one variable 'result'
result(:,1) = test1(:,1);   % Test 1
result(:,2) = test2(:,1);   % Test 2
result(:,3) = test3(:,1);   % Test 3

% Saves the variable 'result' to a text file 'filename.txt'
save filename.txt result –ASCII
```

dampiezo.m

```
% THIS CODE REMOVES ANY NON-RESPONSE DATA AND ANY OFFSET

clear;
format long;

% Command for entering the result file which is entered on the main MATLAB prompt
a = input('Enter baseline file name: ');

% 'points' is the number of data points acquired
points = 20000;
% 'rate' is the data acquisition rate
rate = 10000;

% Loads piezoelectric sensor file into variable 'base_holder'
base_holder = load(a);

[a,aa] = size(base_holder);

% Determines the number of tests performed
number_tests = a/(2*points);

% Seperates the results of the different tests into different columns in variable 'base'
for j = 1:2*number_tests
   for i = 1:points
      base(i,j) = base_holder(i+(j-1)*points,1);
   end
end

base_holder = [];

% Following loop corrects for any offset in the data
for i = 1:2*number_tests
   for j = 1:points
      base(j,i) = base(j,i) - base(points,i)
   end
end

% Seperates the test results and puts voltage into proper scale, measured value was 6.5%
of actual
test1 = base(:,1:2)/0.065;    % Test 1, sensor 1 & 2
test2 = base(:,3:4)/0.065;    % Test 2, sensor 1 & 2
test3 = base(:,5:6)/0.065;    % Test 3, sensor 1 & 2
```

```
base = [];

% Determines when the voltage is greater than 1 volt to determine test start point
st1 = find(abs(test1) > 1); % Test 1
st2 = find(abs(test2) > 1); % Test 2
st3 = find(abs(test3) > 1); % Test 3

% Determines start point of test, 200 chosen to eliminate any possibility of initial offsets
start1 = find(st1 > 200);   % Test 1
start2 = find(st2 > 200);   % Test 2
start3 = find(st3 > 200);   % Test 3

% Removes all non-response data before the start of the test
test1(1:st1(start1(1,1),:)-5,:) = [];   % Test 1
test2(1:st2(start2(1,1),:)-5,:) = [];   % Test 2
test3(1:st3(start3(1,1),:)-5,:) = [];   % Test 3

% Eliminates results past 1 second, non-response data
test1 = test1(1:10000,1:2);   % Test 1
test2 = test2(1:10000,1:2);   % Test 2
test3 = test3(1:10000,1:2);   % Test 3

% Initializes the time to zero
time(1,1) = 0.0;

% Loop computed the time vector for the data
for i = 2:10000
   time(i,1) = time(i-1,1) + 1/rate;
end

% Plots the sensor responses for the three tests on one plot
figure(1); plot(time, test1(:,1),time, test2(:,1),'-r',time, test3(:,1),'-g' ); % Sensor 1
figure(2); plot(time, test1(:,2),time, test2(:,2),'-r',time, test3(:,2),'-g' ); % Sensor 2

% Stores all three tests in one variable 'result'
result(:,1) = test1(:,1);   % Test 1, sensor 1
result(:,4) = test1(:,2);   % Test 1, sensor 2
result(:,2) = test2(:,1);   % Test 2, sensor 1
result(:,5) = test2(:,2);   % Test 2, sensor 2
result(:,3) = test3(:,1);   % Test 3, sensor 1
result(:,6) = test3(:,2);   % Test 3, sensor 2

% Saves the variable 'result' to a text file 'filename.txt'
save filename.txt result –ASCII
```

merge.m

```
% This program merges the forces for tests 1&13, 2&14, etc. for the full bond joint
% This is done because only one sensor is used so it merges the results so the full
% bonded pipe has the equivalent of two sensors

clear;
format long;

% File inputs, to be entered on the main MATLAB prompt
% Call for piezoelectric sensor files for corresponding tests
a = input('Enter the first sensor file name: ');
b = input('Enter the second sensor file name: ');
% Calls for loading files for corresponding tests
c = input('Enter the first load file name: ');
d = input('Enter the second load file name: ');

% Loads the files into variables
% Piezoelectric sensor data stored to variables piezo1 for first test, piezo2 for second test
piezo1 = load(a);
piezo2 = load(b);
% Loading data stored to variables force1 for first test, force2 for second test
force1 = load(c);
force2 = load(d);

% Merges the two tests into one variable
% 'piezo' contains the two sets of sensor results
piezo(:,1:3) = piezo1;
piezo(:,4:6) = piezo2;
% 'force' contains the two sets of loading results
force(:,1:3) = force1;
force(:,4:6) = force2;

% Saves the variables to text files
% Piezoelectric sensor results to 'piezofile.txt'
save piezofile.txt piezo -ASCII
% Loading function results to 'forcefile.txt'
save forcefile.txt force –ASCII
```

loadresponse.m

```
% THIS PROGRAM SORTS THE LOADING FILES FOR A GIVEN TEST SETUP BY
REMOVING NON-RESPONSE DATA

clear;

format long;

% Input for load file, the name is entered on the main MATLAB prompt
b = input('Enter baseline file name: ');

% Test data
points = 20000; % Number of data points
rate = 10000;   % Rate of data acquisition

% Loads the load file into variable 'base_holder'
base_holder = load(b);

% Determines the total number of points in the file and stores it in 'a'
[a,aa] = size(base_holder);

number_tests = a/points;        % Determines number of tests
col_in_data = number_tests+1;   % Determines the number of columns required for the
output file

% Loop seperates the tests into their own column and stores it in variable 'base'
for j = 1:number_tests
   for i = 1:points
      base(i,j) = base_holder(i+(j-1)*points,1);
   end
end

% Following commands determine the points greater than 0.09 volts for the start of the
test
st1 = find(base(:,1) > 0.10);   % Test 1
st2 = find(base(:,2) > 0.10);   % Test 2
st3 = find(base(:,3) > 0.10);   % Test 3

% Converts the voltage to load (Newtons), and stores it in the variables 'load#'
load1 = base(:,1)*1000/9.96;    % Loading for test 1
load2 = base(:,2)*1000/9.96;    % Loading for test 2
load3 = base(:,3)*1000/9.96;    % Loading for test 3
```

```
% Variable 's#(1,1)' contains the start point of the test
% Comparison to 50 due to offset at very start of test in hammer voltage
s1 = find(st1 > 50);      % Test 1
s2 = find(st2 > 50);      % Test 2
s3 = find(st3 > 50);      % Test 3

% Removes data more than 1 second after first value greater than 0.9 volts
load1(st1(s1(1,1),1)+999:points,:) = [];  % Test 1
load2(st2(s2(1,1),1)+999:points,:) = [];  % Test 2
load3(st3(s3(1,1),1)+999:points,:) = [];  % Test 3

% Removes non-response data before loading applied
load1(1:st1(s1(1,1),1)-2,:) = [];  % 'load1' contatins 1 second worth of data for test 1
load2(1:st2(s2(1,1),1)-2,:) = [];  % 'load2' contatins 1 second worth of data for test 2
load3(1:st3(s3(1,1),1)-2,:) = [];  % 'load3' contatins 1 second worth of data for test 3

% Initialize the start time to zero
time(1,1) = 0.0;

% Loop computes the time vector for the loading history
for i = 2:1000
   time(i,1) = time(i-1,1) + 1/rate;
end

% Following commands plot the time history of the loading
figure(1); plot(time,load1);
figure(2); plot(time,load2);
figure(3); plot(time,load3);

% Following stores all load results into one variable 'force'
force(:,1) = load1;
force(:,2) = load2;
force(:,3) = load3;

% 'actual_loading' will hold only the loading portion of the hammer, not the full dynamic
response
actual_loading = force;
actual_loading(11:1000,:) = [];

% Saves the variable 'actual_loading' to a text file 'filename.txt'
save filename.txt actual_loading –ASCII
```

normalize.m

```
% THIS PROGRAM NORMALIZES THE FOURIER SPECTRUMS FOR THE
DAMAGED ADHESIVELY BONDED PIPE JOINTS

clear;

format long;

% File inputs to be entered on MATLAB main prompt
a = input('Enter the piezo file name: ');   % Piezoelectric response file
b = input('Enter the load file name: ');    % Load file

% Data acquisition rate
rate = 10000;

% Plot Controls, 'y' means plots, 'n' is do not plot
plot_fourier = 'y';
% Filter requirements, 'y' mean filter, 'n' means no filter required
filter_required = 'y';

% Loads the test files
p = load(a);    % Piezoelectric response stored in 'p'
force = load(b);    % load file stored in 'force'

% Function call to 'swap' which changes the order of the sensors
% Only used for test results from tests 13 through 24
piezo = swap(p, force);

[pr,pc] = size(piezo);
[fr,fc] = size(force);

%Following filters the data through function 'fullfilter'
if filter_required = 'y'
   filt_piezo = filterdata(piezo,pc);
else
   filt_piezo = piezo;
end

%Following performs the Fast Fourier transform through function 'fastfourier'
piezo_pow = fastfourier(filt_piezo);
force_pow = fastfourier(force);

%Following normalizes the piezoelectric response wrt the load results through function
'normalize'
```

```
norm = frf(piezo_pow,force_pow);

% Determines frequency scale for fourier plots
f = rate*(0:4096)/8192;

% Following loop plots the normalized Fourier spectrums
% Range of plot can be changed by changing the limits in the variable 'f' & 'norm'
if plot_fourier == 'y'
% Plots all three tests seperately on one subplot
   for i = 1:pc/2
      figure(1); subplot(pc/2,1,i); plot(f(1,33:1000),norm(33:1000,i));      % Sensor 1
      legend('First Sensor');
      figure(2); subplot(pc/2,1,i); plot(f(1,33:1000),norm(33:1000,i+pc/2)); % Sensor 2
      legend('Second Sensor');
   end
% Plots all three test on a single plot, 'j' determines sensor
% 'j = 1' plots sensor 1 for all tests on a single plot
% 'j = 2' plots sensor 2 for all tests on a single plot
   for j = 1:2
     figure(3+j); plot(f(1,33:1000),norm(33:1000,j+2*(j-1)));...        % Test 1
                  hold on;...
                  plot(f(1,33:1000),norm(33:1000,j*2+(j-1)),'-r');...   % Test 2
                  hold on;...
                  plot(f(1,33:1000),norm(33:1000,j*3),'-g');            % Test 3
   end
end

% 'fourier' holds the desired Fourier range for damage index evaluation
% The range can be changed to norrow or enlarge evaluation window by changing the
row limits
fourier = norm(55:2154,:);

% Outputs the variable 'fourier' to the text file 'filename.txt'
save filename.txt fourier -ASCII
```

swap.m

```
% THIS FUNCTION SWITCHES THE ORDER OF THE PIEZOELECTRIC SENSORS

function zero = zer(base)

% Commands to switch sensor 1 to columns 4-6, and sensor 2 to columns 1-3
p = base;
piezo(:,1:3) = p(:,4:6);
piezo(:,4:6) = p(:,1:3);

% 'zero' is variable returned to main program
zero=piezo;
```

filterdata.m

```
% THIS FUNCTION FILTES THE PIEZOELECTRIC RESPONSE

function filtered = testfilter(base,number)

rate = 10000;

% Selects filter: Butterworth bandpass filter
[c,d] = butter(filter order,[low cutoff frequency,high cutoff frequency]);

% Loop filters the data of all sensors
for i = 1:number
   base(:,i) = filter(c,d,base(:,i));
end

% 'filtered' passed back to main program with filtered responses
filtered = base;
```

fastfourier.m

```
% THE FUNCTION COMPUTES THE 8192 POINT FFT OF THE INPUT DATA

function fourier = fastfourier(base)

baseY = fft(base,8192);

% 'fourier' is variable passed back to main program with fft of data
fourier = baseY;
```

frf.m

```
% THIS FUNCTION COMPUTES THE FRF OF THE RESPONSE DATA

function normal = normalize(piezo,force)

[a,b] = size(piezo);
[c,d] = size(force);

for i = 1:d
   hold(:,i) = (piezo(:,i)./(force(:,i)));
   hold(:,i+d) = (piezo(:,i+d)./(force(:,i)));
end

normal = hold;
```

RMSDindex.m

```
% DETERMINES THE RMSD DAMAGE INDEX FOR THE QUARTER AND HALF
DEBOND RELATIVE TO FULL BOND STATE

clear;

format long;

% File inputs, to be entered on the main MATLAB prompt
% Input for the undamaged fourier spectrum
a = input('Enter the filename of the undamaged specimen: ');
% Inputs for the damaged fourier spectrums for the different tests
b = input('Enter the first filename of the quarter debonded pipe: ');
c = input('Enter the first filename of the half debonded pipe: ');
d = input('Enter the second filename of the quarter debonded pipe: ');
e = input('Enter the second filename of the half debonded pipe: ');

% Following commands load the data into the proper variables
base_four_his = load(a);
dam_four_his(:,1:6) = load(b);
dam_four_his(:,7:12) = load(c);
dam_four_his(:,13:18) = load(d);
dam_four_his(:,19:24) = load(e);

% 'num_comp' is the number of comparison files to enter, number of damaged files input
num_comp = 4;
```

```
% Computes the square of the individual points in the undamaged data: xi^2 in RMSD
equation
sq_four_base = (base_four_his).^2;

% Computes the sum of the squares of the individual points in the undamaged data:
sum(xi^2) in RMSD equation
for i =1:6
   sums_four(1,i) = sum(sq_four_base(:,i));
end

% Following loop calculates the difference in the individual points of the
% undamaged and damaged Fourier spectrums: (yi-xi) in the RMSD equation
for i = 1:num_comp
   for j = 1:6
      diff_four(:,j+6*(i-1)) = dam_four_his(:,j+6*(i-1))-base_four_his(:,j);
   end
end

% Determines the square of the differences found above: (yi-xi)^2 in RMSD equation
sq_four_diff = (diff_four).^2;

% Determines the sum of the squares found above: sum((yi-xi)^2) in RMSD equation
for i = 1:num_comp
   for j = 1:6
      sum_four_diff(1,j+6*(i-1)) = sum(sq_four_diff(:,j+6*(i-1)));
   end
end

% Computes the RMSD damage index for each of the tests
for i = 1:num_comp
   for j = 1:6
      RMDS_four(i,j) = sqrt(sum_four_diff(1,j+6*(i-1))./sums_four(1,j))*100;
   end
end

% Saves the RMSD damage indices to the text file 'filename.txt'
save filename.txt RMDS_four -ASCII
```

MAPDindex.m

```
% DETERMINES THE MAPD DAMAGE INDEX FOR THE QUARTER AND HALF
DEBOND RELATIVE TO FULL BOND STATE

clear;

format long;

% File inputs, to be entered on the main MATLAB prompt
% Input for the undamaged fourier spectrum
a = input('Enter the filename of the undamaged specimen: ');
% Inputs for the damaged fourier spectrums for the different tests
b = input('Enter the first filename of the quarter debonded pipe: ');
c = input('Enter the first filename of the half debonded pipe: ');
d = input('Enter the second filename of the quarter debonded pipe: ');
e = input('Enter the second filename of the half debonded pipe: ');

% Following commands load the data into the proper variables
base_four_his = load(a);
dam_four_his(:,1:6) = load(b);
dam_four_his(:,7:12) = load(c);
dam_four_his(:,13:18) = load(d);
dam_four_his(:,19:24) = load(e);

% 'num_comp' is the number of comparison files to enter, number of damaged files input
num_comp = 4;

% Following loop calculates the difference in the individual points of the
% undamaged and damaged Fourier spectrums: (yi-xi) in the MAPD equation
for i = 1:num_comp
   for j = 1:6
      diff_four(:,j+6*(i-1)) = dam_four_his(:,j+6*(i-1))-base_four_his(:,j);
   end
end

% 'N_four' will hold the number of data points in the Fourier spectrums: N in MAPD
equation
[N_four,p] = size(diff_four);

% Loop calculates the division of the difference in Fourier spectrums by the
% value of the undamaged spectrum: (yi-xi)/xi in MAPD equation
for i = 1:num_comp
   for j = 1:6
```

```
      div_diff_four(:,j+6*(i-1)) = diff_four(:,j+6*(i-1))./base_four_his(:,j);
   end
end

% Command takes the absolute value of the previous step
% absolute value of ((yi-xi)/xi) in MAPD equation
div_diff_four = abs(div_diff_four);

% Determines the sum of the above step for each test
% sum(absolute value of ((yi-xi)/xi)) in MAPD equation
for i = 1:num_comp
   for j = 1:6
      sum_four_diff(1,j+6*(i-1)) = sum(div_diff_four(:,j+6*(i-1)));
   end
end

% Computes the MAPD damage index
for i = 1:num_comp
   for j = 1:6
      MAPD_four(i,j) = sum_four_diff(1,j+6*(i-1))*100/N_four;
   end
end

% Saves the MAPD damage indices to the text file 'filename.txt'
save filename.txt MAPD_four -ASCII
```

CCindex.m

```
% DETERMINES THE CC DAMAGE INDEX FOR THE QUARTER AND HALF
DEBOND RELATIVE TO FULL BOND STATE
clear;

format long;

% File inputs, to be entered on the main MATLAB prompt
% Input for the undamaged fourier spectrum
a = input('Enter the filename of the undamaged specimen: ');
% Inputs for the damaged fourier spectrums for the different tests
b = input('Enter the first filename of the quarter debonded pipe: ');
c = input('Enter the first filename of the half debonded pipe: ');
d = input('Enter the second filename of the quarter debonded pipe: ');
e = input('Enter the second filename of the half debonded pipe: ');

% Following commands load the data into the proper variables
base_his = load(a);
dam_his(:,1:6) = load(b);
dam_his(:,7:12) = load(c);
dam_his(:,13:18) = load(d);
dam_his(:,19:24) = load(e);

% 'num_comp' is the number of comparison files to enter, number of damaged files input
num_comp = 4;

% computes the standard deviation of the undamaged and damaged data
std_base = std(base_his);
std_dam = std(dam_his);

% computes the mean of the undamaged and damaged data
mean_base = mean(base_his);
mean_dam = mean(dam_his);

% Determines the size of the data matrices
[N,n] = size(base_his);
[P,p] = size(dam_his);

% Following loops determine the difference between the individual points and the mean
% 'diff_base' is the difference for the undamaged data: (xi-x) in covariance equation
for i = 1:n
   diff_base(:,i) = base_his(:,i) - mean_base(1,i);
end
```

```
% 'diff_dam' is the difference for the damaged data: (yi-y) in covariance equation
for i = 1:p
   diff_dam(:,i) = dam_his(:,i) - mean_dam(1,i);
end

% Following loop computes the multiplication of the difference between the individual
data points and the overall
% mean for the individual points of the undamaged and damaged specimens: (xi-x)(yi-y)
in covariance equation
for i = 1:num_comp
   for j = 1:6
      multi_diff(:,j+6*(i-1)) = diff_dam(:,j+6*(i-1)).*diff_base(:,j);
   end
end

% Computes the sum of the differences found above for the individual tests: sum((xi-
x)(yi-y)) in covariance equation
for i = 1:num_comp
   for j = 1:6
      sum_multi_diff(1,j+6*(i-1)) = sum(multi_diff(:,j+6*(i-1)));
   end
end

% Computes the covariance in the data sets
Cov = sum_multi_diff/N;

% Following loop calculates the CC damage index for each test
for i = 1:num_comp
   for j = 1:6
      CC(i,j) = Cov(1,j+6*(i-1))/(std_base(1,j)*std_dam(1,j+6*(i-1)));
   end
end

% Saves the CC damage indices to the text file 'filename.txt'
save filename.txt CC -ASCII
```

preceeding.m

```
% PRECEEDING STATE DAMAGE INDEX EVALUATION
% This program computes the damage state of the half debond relative to the quarter
debond

clear;

format long;

% File inputs, to be entered on the main MATLAB prompt
% Inputs for the first stage of damage
a = input('Enter the first filename of the quarter debonded pipe: ');
b = input('Enter the second filename of the quarter debonded pipe: ');
% Inputs for the second stage of damage
c = input('Enter the first filename of the half debonded pipe: ');
d = input('Enter the second filename of the half debonded pipe: ');

% Stores the data to the proper variables
base_his(:,1:6) = load(a);
base_his(:,7:12) = load(b);
dam_his(:,1:6) = load(c);
dam_his(:,7:12) = load(d);

% 'num_comp' is the number of comparison files, half the number of damaged files input
num_comp = 1;

% **********SECTION 1 COMPUTES THE RELATIVE CC DAMAGE
INDEX**********

% Computes the standard deviation of the baseline and damaged data for each test: Used
in CC index
std_base = std(base_his);
std_dam = std(dam_his);

% Computes the mean of the undamaged and damaged data: Used in CC index
mean_base = mean(base_his);
mean_dam = mean(dam_his);

% Determines the size of the data sets, capital letter is number
% of data points, small letter is number of test sets
[N,n] = size(base_his);
[P,p] = size(dam_his);
```

```
% Following loops determine the difference between the individual points and the mean
% 'diff_base' is the difference for the undamaged data: (xi-x) in covariance equation
for i = 1:n
   diff_base(:,i) = base_his(:,i) - mean_base(1,i);
end
% 'diff_dam' is the difference for the damaged data: (yi-y) in covariance equation
for i = 1:p
   diff_dam(:,i) = dam_his(:,i) - mean_dam(1,i);
end

% Following loop computes the multiplication of the difference between the individual
data points and the overall
% mean for the individual points of the undamaged and damaged specimens: (xi-x)(yi-y)
in covariance equation
for i = 1:num_comp
   for j = 1:12
      multi_diff(:,j+6*(i-1)) = diff_dam(:,j+6*(i-1)).*diff_base(:,j);
   end
end

% Computes the sum of the differences found above for the individual tests: sum((xi-
x)(yi-y)) in covariance equation
for i = 1:num_comp
   for j = 1:12
      sum_multi_diff(1,j+6*(i-1)) = sum(multi_diff(:,j+6*(i-1)));
   end
end

% Computes the covariance in the data sets
Cov = sum_multi_diff/N;

% Following loop calculates the CC damage index for each test
for i = 1:num_comp
   for j = 1:12
      CC(i,j) = Cov(1,j+6*(i-1))/(std_base(1,j)*std_dam(1,j+6*(i-1)));
   end
end

% ********** END OF SECTION 1 **********
```

```
% ********** SECTION 2 COMPUTES THE RELATIVE MAPD DAMAGE INDEX **********

% Following loop calculates the difference in the individual points of the
% undamaged and damaged Fourier spectrums: (yi-xi) in the MAPD equation
for i = 1:num_comp
   for j = 1:12
      diff_four(:,j+6*(i-1)) = dam_his(:,j+6*(i-1))-base_his(:,j);
   end
end

% 'N_four' will hold the number of data points in the Fourier spectrums: N in MAPD
equation
[N_four,p] = size(diff_four);

% Loop calculates the division of the difference in Fourier spectrums by the
% value of the undamaged spectrum: (yi-xi)/xi in MAPD equation
for i = 1:num_comp
   for j = 1:12
      div_diff_four(:,j+6*(i-1)) = diff_four(:,j+6*(i-1))./base_his(:,j);
   end
end

% Command takes the absolute value of the previous step
% absolute value of ((yi-xi)/xi) in MAPD equation
div_diff_four = abs(div_diff_four);

% Determines the sum of the above step for each test
% sum(absolute value of ((yi-xi)/xi)) in MAPD equation
for i = 1:num_comp
   for j = 1:12
      sum_four_diff(1,j+6*(i-1)) = sum(div_diff_four(:,j+6*(i-1)));
   end
end

% Computes the MAPD damage index
for i = 1:num_comp
   for j = 1:12
      MAPD_four(i,j) = sum_four_diff(1,j+6*(i-1))*100/N_four;
   end
end

% ********** END OF SECTION 2 **********
```

```
% ********** SECTION 3 COMPUTES THE RELATIVE RMSD DAMAGE INDEX **********

% Computes the square of the individual points in the undamaged data: xi^2 in RMSD equation
sq_four_base = (base_his).^2;

% Computes the sum of the squares of the individual points in the undamaged data: sum(xi^2) in RMSD equation
for i =1:12
   sums_four(1,i) = sum(sq_four_base(:,i));
end

% Following loop calculates the difference in the individual points of the
% undamaged and damaged Fourier spectrums: (yi-xi) in the RMSD equation
for i = 1:num_comp
   for j = 1:12
      diff_four(:,j) = dam_his(:,j)-base_his(:,j);
   end
end

% Determines the square of the differences found above: (yi-xi)^2 in RMSD equation
sq_four_diff = (diff_four).^2;

% Determines the sum of the squares found above: sum((yi-xi)^2) in RMSD equation
for i = 1:num_comp
   for j = 1:12
      sum_four_diff(1,j) = sum(sq_four_diff(:,j));
   end
end

% Computes the RMSD damage index for each of the tests
for i = 1:num_comp
   for j = 1:12
      RMDS_four(i,j) = sqrt(sum_four_diff(1,j)./sums_four(1,j))*100;
   end
end

% ********** END OF SECTION 3 **********

% Following commands save the resulting relative damage indexes to text files
save CCpre.txt CC -ASCII          % Relative CC index to 'CCpre.txt'
save MAPDpre.txt MAPD_four -ASCII  % Relative MAPD index to 'MAPDpre.txt'
save RMDSpre.txt RMDS_four -ASCII  % Relative RMSD index to 'RMSDpre.txt'
```

Appendix D Damage Indices and Plots for All Adhesively Bonded Pipe Joints

Table D-1: RMSD Damage Index Relative to Zero Damage State for Adhesively Bonded Pipe Joint with ¼-Debond for Tests 1-12

Test Set-up	Sensor 1 RMSD Index (%)					Sensor 2 RMSD Index (%)				
	Test 1	Test 2	Test 3	Average	COV (%)	Test 1	Test 2	Test 3	Average	COV (%)
1	35.07	42.04	37.11	38.08	9.41	33.15	33.98	33.54	33.56	1.24
2	35.54	38.53	39.06	37.71	5.04	30.98	31.23	30.22	30.81	1.71
3	25.00	25.47	25.48	25.32	1.08	35.71	34.93	35.71	35.45	1.27
4	34.87	34.12	33.25	34.08	2.38	34.26	33.58	35.28	34.37	2.49
5	42.03	40.63	40.17	40.94	2.37	33.67	32.73	35.84	34.08	4.68
6	28.91	27.48	26.70	27.70	4.04	35.25	35.67	35.79	35.57	0.80
7	34.88	35.70	35.80	35.46	1.42	28.41	30.06	31.39	29.95	4.98
8	39.65	41.67	38.12	39.81	4.47	27.04	26.35	26.63	26.67	1.30
9	26.71	27.20	26.41	26.77	1.49	31.11	31.87	31.22	31.40	1.31
10	33.85	38.24	36.97	36.36	6.22	32.44	32.61	30.27	31.77	4.11
11	38.92	41.90	38.99	39.94	4.25	25.02	24.72	26.08	25.27	2.84
12	26.97	28.36	30.27	28.53	5.81	33.29	32.40	32.59	32.76	1.44

Table D-2: RMSD Damage Index Relative to Zero Damage State for Adhesively Bonded Pipe Joint with ¼-Debond for Tests 13-24

Test Set-up	Sensor 1 RMSD Index (%)					Sensor 2 RMSD Index (%)				
	Test 1	Test 2	Test 3	Average	COV (%)	Test 1	Test 2	Test 3	Average	COV (%)
13	36.78	42.58	37.04	38.80	8.45	34.45	33.87	32.54	33.62	2.91
14	27.46	31.72	28.75	29.31	7.45	34.40	34.51	34.28	34.40	0.33
15	32.86	33.30	33.63	33.26	1.16	40.75	40.78	40.54	40.69	0.32
16	34.33	31.80	31.34	32.49	4.95	39.54	37.96	37.25	38.25	3.06
17	33.88	29.39	30.58	31.28	7.43	41.27	40.74	42.09	41.37	1.65
18	34.25	33.93	33.33	33.84	1.38	42.87	44.25	43.01	43.38	1.74
19	36.08	38.12	36.55	36.92	2.90	25.70	25.91	25.86	25.82	0.42
20	31.22	33.99	30.54	31.92	5.73	27.24	27.02	27.86	27.37	1.60
21	32.48	32.93	33.55	32.99	1.63	32.34	32.47	33.49	32.77	1.91
22	31.16	32.25	33.21	32.21	3.19	33.41	32.78	34.78	33.65	3.03
23	31.41	36.17	30.96	32.85	8.79	34.85	35.60	37.08	35.84	3.16
24	30.02	28.93	38.07	32.34	15.43	36.17	37.58	39.22	37.66	4.05

Table D-3: MAPD Damage Index Relative to Zero Damage State for Adhesively Bonded Pipe Joint with ¼-Debond for Tests 1-12

Test Set-up	Sensor 1 MAPD Index (%)					Sensor 2 MAPD Index (%)				
	Test 1	Test 2	Test 3	Average	COV (%)	Test 1	Test 2	Test 3	Average	COV (%)
1	43.74	44.80	46.29	44.94	2.85	30.64	41.24	32.73	34.87	16.11
2	52.80	56.31	60.76	56.62	7.04	27.33	27.32	26.45	27.03	1.87
3	42.02	42.58	40.13	41.58	3.09	28.17	28.42	26.04	27.55	4.75
4	46.88	43.79	44.23	44.97	3.72	41.86	35.13	32.57	36.52	13.14
5	69.28	77.86	66.48	71.21	8.33	57.38	52.67	66.50	58.85	11.95
6	45.45	45.99	44.86	45.43	1.25	31.83	31.39	29.53	30.92	3.94
7	44.21	43.61	44.12	43.98	0.73	45.12	41.07	42.89	43.03	4.72
8	59.53	62.15	58.45	60.05	3.17	28.38	27.81	29.61	28.60	3.22
9	37.15	35.98	37.37	36.83	2.02	24.36	23.60	24.04	24.00	1.59
10	42.92	47.53	46.21	45.55	5.22	34.23	29.07	29.46	30.92	9.30
11	73.03	76.52	78.23	75.92	3.49	32.43	31.06	33.92	32.47	4.40
12	55.22	56.55	43.69	51.82	13.65	31.37	25.21	25.03	27.20	13.28

Table D-4: MAPD Damage Index Relative to Zero Damage State for Adhesively Bonded Pipe Joint with ¼-Debond for Tests 13-24

Test Set-up	Sensor 1 MAPD Index (%)					Sensor 2 MAPD Index (%)				
	Test 1	Test 2	Test 3	Average	COV (%)	Test 1	Test 2	Test 3	Average	COV (%)
13	33.73	34.87	33.24	33.95	2.48	43.10	42.65	32.17	39.31	15.73
14	35.91	37.97	36.22	36.70	3.02	32.74	29.26	30.10	30.70	5.91
15	31.26	30.30	34.49	32.02	6.85	37.92	35.91	37.72	37.18	2.98
16	32.05	31.24	31.76	31.68	1.29	65.25	58.14	48.45	57.28	14.72
17	51.42	51.46	48.82	50.56	2.99	59.45	61.29	63.17	61.31	3.04
18	45.10	43.54	47.14	45.26	3.99	49.05	52.00	49.61	50.22	3.12
19	28.34	30.69	28.67	29.23	4.35	31.65	25.54	27.11	28.10	11.29
20	39.84	38.75	37.59	38.73	2.91	30.44	28.59	29.92	29.65	3.22
21	33.48	32.61	44.70	36.93	18.26	35.38	35.30	34.83	35.17	0.85
22	31.61	31.93	33.37	32.31	2.90	48.88	47.35	55.18	50.47	8.23
23	46.10	48.78	47.79	47.56	2.85	43.71	45.12	47.36	45.40	4.06
24	45.31	47.73	48.44	47.16	3.48	33.02	36.95	42.14	37.37	12.25

Table D-5: CC Damage Index Relative to Zero Damage State for Adhesively Bonded Pipe Joint with ¼-Debond for Tests 1-12

Test Set-up	Sensor 1 CC Index					Sensor 2 CC Index				
	Test 1	Test 2	Test 3	Average	COV (%)	Test 1	Test 2	Test 3	Average	COV (%)
1	0.9263	0.8739	0.9042	0.9015	2.92	0.9398	0.9433	0.9374	0.9402	0.32
2	0.9068	0.8916	0.8881	0.8955	1.11	0.9403	0.9403	0.9364	0.9390	0.24
3	0.9570	0.9582	0.9563	0.9572	0.10	0.9200	0.9245	0.9197	0.9214	0.29
4	0.8956	0.8983	0.9036	0.8992	0.45	0.9116	0.9143	0.9094	0.9118	0.27
5	0.8538	0.8643	0.8660	0.8614	0.76	0.9093	0.9167	0.8982	0.9081	1.03
6	0.9391	0.9445	0.9472	0.9436	0.44	0.9106	0.9107	0.9133	0.9116	0.17
7	0.9171	0.9221	0.9167	0.9186	0.33	0.9554	0.9563	0.9498	0.9538	0.37
8	0.8796	0.8713	0.8896	0.8802	1.04	0.9547	0.9605	0.9530	0.9561	0.41
9	0.9503	0.9488	0.9528	0.9506	0.21	0.9377	0.9368	0.9372	0.9372	0.05
10	0.8982	0.8711	0.8791	0.8828	1.57	0.9321	0.9226	0.9382	0.9309	0.84
11	0.8734	0.8545	0.8750	0.8676	1.32	0.9510	0.9516	0.9452	0.9492	0.37
12	0.9470	0.9492	0.9315	0.9426	1.02	0.9166	0.9201	0.9191	0.9186	0.19

Table D-6: CC Damage Index Relative to Zero Damage State for Adhesively Bonded Pipe Joint with ¼-Debond for Tests 13-24

Test Set-up	Sensor 1 CC Index					Sensor 2 CC Index				
	Test 1	Test 2	Test 3	Average	COV (%)	Test 1	Test 2	Test 3	Average	COV (%)
13	0.9440	0.8930	0.9297	0.9222	2.85	0.9030	0.9111	0.9153	0.9098	0.69
14	0.9622	0.9433	0.9614	0.9556	1.12	0.9046	0.9023	0.9055	0.9041	0.18
15	0.9472	0.9479	0.9462	0.9471	0.09	0.8785	0.8783	0.8793	0.8787	0.06
16	0.9210	0.9330	0.9377	0.9306	0.92	0.8786	0.8874	0.8875	0.8845	0.58
17	0.9162	0.9503	0.9408	0.9358	1.88	0.8705	0.8679	0.8633	0.8672	0.42
18	0.9373	0.9391	0.9421	0.9395	0.26	0.8596	0.8501	0.8586	0.8561	0.61
19	0.9427	0.9422	0.9399	0.9416	0.16	0.9455	0.9477	0.9462	0.9465	0.12
20	0.9433	0.9409	0.9504	0.9448	0.52	0.9405	0.9410	0.9381	0.9399	0.16
21	0.9421	0.9437	0.9393	0.9417	0.23	0.9228	0.9230	0.9178	0.9212	0.32
22	0.9261	0.9181	0.9112	0.9185	0.81	0.9134	0.9180	0.9114	0.9143	0.37
23	0.9444	0.9129	0.9401	0.9325	1.83	0.9181	0.9150	0.9096	0.9142	0.47
24	0.9560	0.9463	0.9171	0.9398	2.15	0.8998	0.8919	0.8858	0.8925	0.79

Table D-7: RMSD Damage Index Relative to Zero Damage State for Adhesively Bonded Pipe Joint with ½-Debond for Tests 1-12

Test Set-up	Sensor 1 RMSD Index (%)					Sensor 2 RMSD Index (%)				
	Test 1	Test 2	Test 3	Average	COV (%)	Test 1	Test 2	Test 3	Average	COV (%)
1	64.14	67.27	62.58	64.67	3.70	54.95	54.80	55.08	54.95	0.25
2	57.79	58.59	58.53	58.30	0.77	50.13	50.12	50.65	50.30	0.60
3	61.25	60.68	61.30	61.08	0.56	59.30	58.63	59.52	59.15	0.78
4	56.93	54.91	55.53	55.79	1.85	53.32	53.65	54.44	53.80	1.07
5	59.92	57.95	57.86	58.58	1.98	54.03	52.08	51.83	52.65	2.28
6	59.05	59.57	59.69	59.44	0.57	57.94	59.14	59.42	58.83	1.33
7	63.48	64.75	64.36	64.20	1.02	51.18	52.29	52.58	52.01	1.42
8	58.73	60.98	56.08	58.60	4.19	44.87	44.40	42.41	43.90	2.97
9	61.18	62.59	62.43	62.06	1.24	53.57	54.69	54.23	54.16	1.03
10	54.04	55.13	56.46	55.21	2.19	53.11	51.90	51.56	52.19	1.56
11	59.02	61.94	56.03	59.00	5.01	46.56	47.10	46.22	46.63	0.96
12	59.41	59.61	62.39	60.47	2.75	55.54	56.23	55.56	55.78	0.70

Table D-8: RMSD Damage Index Relative to Zero Damage State for Adhesively Bonded Pipe Joint with ½-Debond for Tests 13-24

Test Set-up	Sensor 1 RMSD Index (%)					Sensor 2 RMSD Index (%)				
	Test 1	Test 2	Test 3	Average	COV (%)	Test 1	Test 2	Test 3	Average	COV (%)
13	57.56	61.73	56.48	58.59	4.73	59.73	61.51	60.78	60.67	1.47
14	50.21	50.41	50.06	50.23	0.36	57.46	56.65	56.80	56.97	0.76
15	56.19	57.76	57.70	57.22	1.56	65.19	65.84	65.62	65.55	0.50
16	51.48	49.63	50.76	50.62	1.84	57.74	57.66	58.72	58.04	1.02
17	48.60	47.79	48.26	48.22	0.84	57.21	57.93	57.91	57.69	0.71
18	54.29	54.73	53.37	54.13	1.28	63.06	64.04	62.93	63.34	0.96
19	58.36	59.04	60.10	59.17	1.48	57.66	58.53	60.84	59.01	2.79
20	51.59	51.63	50.54	51.25	1.20	54.35	52.90	54.19	53.82	1.49
21	59.75	60.31	60.74	60.27	0.82	63.30	63.56	63.84	63.57	0.42
22	48.31	50.35	49.05	49.24	2.10	56.78	55.58	55.69	56.02	1.18
23	48.36	50.50	45.24	48.03	5.51	49.63	49.96	50.70	50.10	1.09
24	55.25	54.51	57.11	55.62	2.40	60.42	60.75	60.41	60.53	0.32

Table D-9: MAPD Damage Index Relative to Zero Damage State for Adhesively Bonded Pipe Joint with ½-Debond for Tests 1-12

Test Set-up	Sensor 1 MAPD Index (%)					Sensor 2 MAPD Index (%)				
	Test 1	Test 2	Test 3	Average	COV (%)	Test 1	Test 2	Test 3	Average	COV (%)
1	53.86	52.46	54.06	53.46	1.63	49.88	52.97	48.42	50.42	4.60
2	73.85	85.73	91.18	83.58	10.60	37.75	38.00	41.03	38.93	4.69
3	52.52	50.27	53.75	52.18	3.38	49.33	49.78	47.88	49.00	2.03
4	51.50	48.68	50.42	50.20	2.83	57.66	53.05	43.96	51.56	13.52
5	72.95	83.29	76.83	77.69	6.73	76.66	69.03	74.03	73.24	5.29
6	53.51	56.95	61.43	57.30	6.93	50.27	52.75	51.23	51.42	2.44
7	53.17	53.57	53.46	53.40	0.39	52.97	46.77	45.35	48.36	8.38
8	87.98	96.41	74.54	86.31	12.78	39.96	39.75	38.93	39.55	1.37
9	49.89	52.67	53.91	52.15	3.94	41.11	41.63	40.62	41.12	1.22
10	50.87	52.34	54.16	52.46	3.14	48.26	42.04	43.32	44.54	7.38
11	79.95	79.83	80.96	80.25	0.77	45.67	46.45	45.92	46.02	0.87
12	67.33	73.07	55.06	65.15	14.12	45.91	41.47	42.28	43.22	5.47

Table D-10: MAPD Damage Index Relative to Zero Damage State for Adhesively Bonded Pipe Joint with ½-Debond for Tests 13-24

Test Set-up	Sensor 1 MAPD Index (%)					Sensor 2 MAPD Index (%)				
	Test 1	Test 2	Test 3	Average	COV (%)	Test 1	Test 2	Test 3	Average	COV (%)
13	49.76	50.91	48.06	49.58	2.89	40.83	49.45	44.98	45.08	9.55
14	69.81	68.11	79.21	72.38	8.26	43.66	44.29	43.26	43.74	1.19
15	41.80	41.59	43.39	42.26	2.32	46.36	48.49	46.55	47.14	2.50
16	48.09	47.28	50.05	48.47	2.94	60.66	60.15	55.84	58.88	4.50
17	64.51	83.56	70.69	72.92	13.33	65.84	69.78	72.18	69.27	4.62
18	59.35	62.36	66.01	62.57	5.33	50.45	51.21	49.89	50.52	1.32
19	46.21	47.74	48.76	47.57	2.70	51.11	46.08	46.77	47.99	5.68
20	70.14	76.88	69.36	72.13	5.74	43.43	41.58	42.56	42.52	2.17
21	46.36	45.62	56.87	49.62	12.68	46.72	46.95	47.53	47.07	0.89
22	46.39	46.76	46.49	46.55	0.42	49.72	48.55	52.05	50.11	3.56
23	67.14	61.97	67.87	65.66	4.90	46.24	48.26	50.05	48.18	3.96
24	65.41	67.64	56.82	63.29	9.03	43.90	45.88	46.32	45.37	2.84

Table D-11: CC Damage Index Relative to Zero Damage State for Adhesively Bonded Pipe Joint with ½-Debond for Tests 1-12

Test Set-up	Sensor 1 CC Index					Sensor 2 CC Index				
	Test 1	Test 2	Test 3	Average	COV (%)	Test 1	Test 2	Test 3	Average	COV (%)
1	0.6910	0.6464	0.7124	0.6833	4.93	0.7545	0.7700	0.7560	0.7601	1.12
2	0.7520	0.7436	0.7438	0.7465	0.64	0.7821	0.7826	0.7773	0.7806	0.37
3	0.7446	0.7535	0.7436	0.7472	0.73	0.7207	0.7294	0.7193	0.7232	0.76
4	0.7580	0.7753	0.7652	0.7661	1.13	0.7664	0.7644	0.7637	0.7648	0.18
5	0.6954	0.7223	0.7260	0.7146	2.34	0.7447	0.7671	0.7704	0.7607	1.84
6	0.7490	0.7425	0.7369	0.7428	0.82	0.7435	0.7318	0.7315	0.7356	0.93
7	0.6966	0.6850	0.6791	0.6869	1.30	0.7995	0.7890	0.7854	0.7913	0.93
8	0.7372	0.7116	0.7741	0.7410	4.25	0.8269	0.8292	0.8484	0.8348	1.41
9	0.7346	0.7195	0.7320	0.7287	1.11	0.7752	0.7633	0.7704	0.7696	0.77
10	0.7677	0.7624	0.7320	0.7540	2.56	0.7938	0.8020	0.7948	0.7969	0.56
11	0.7263	0.6856	0.7625	0.7248	5.31	0.8275	0.8204	0.8266	0.8248	0.47
12	0.7471	0.7208	0.7324	0.7334	1.80	0.7625	0.7532	0.7644	0.7600	0.79

Table D-12: CC Damage Index Relative to Zero Damage State for Adhesively Bonded Pipe Joint with ½-Debond for Tests 13-24

Test Set-up	Sensor 1 CC Index					Sensor 2 CC Index				
	Test 1	Test 2	Test 3	Average	COV (%)	Test 1	Test 2	Test 3	Average	COV (%)
13	0.7536	0.6905	0.7548	0.7330	5.02	0.7604	0.7609	0.7553	0.7589	0.41
14	0.8241	0.8280	0.8290	0.8271	0.31	0.7569	0.7695	0.7587	0.7617	0.89
15	0.7813	0.7772	0.7734	0.7773	0.51	0.7154	0.7199	0.7181	0.7178	0.32
16	0.7925	0.8024	0.7958	0.7969	0.64	0.7398	0.7324	0.7241	0.7321	1.08
17	0.8020	0.8138	0.8091	0.8083	0.73	0.7239	0.7147	0.7141	0.7176	0.77
18	0.7825	0.7791	0.7910	0.7842	0.79	0.7009	0.6932	0.7078	0.7006	1.04
19	0.7234	0.7282	0.7105	0.7207	1.27	0.7787	0.7798	0.7640	0.7742	1.14
20	0.7994	0.8057	0.8135	0.8062	0.87	0.7833	0.7914	0.7814	0.7854	0.67
21	0.7398	0.7352	0.7350	0.7366	0.37	0.7381	0.7358	0.7344	0.7361	0.25
22	0.8115	0.7894	0.7989	0.7999	1.39	0.7741	0.7690	0.7640	0.7690	0.66
23	0.8106	0.7925	0.8392	0.8141	2.89	0.8040	0.7950	0.7871	0.7953	1.06
24	0.7689	0.7670	0.7638	0.7666	0.34	0.7264	0.7177	0.7205	0.7215	0.61

Table D-13: RMSD Damage Index for ½-Debond Pipe Relative to the ¼-Debond Pipe for Tests 1-12

Test Set-up	Sensor 1 RMSD Index (%)					Sensor 2 RMSD Index (%)				
	Test 1	Test 2	Test 3	Average	COV (%)	Test 1	Test 2	Test 3	Average	COV (%)
13	43.03	43.22	42.67	42.97	0.64	38.58	36.65	36.56	37.26	3.06
14	42.52	43.08	44.29	43.30	2.09	35.87	35.67	37.16	36.23	2.24
15	50.22	48.21	49.00	49.15	2.06	38.80	38.49	39.21	38.83	0.92
16	37.48	37.02	37.28	37.26	0.61	29.50	29.91	29.28	29.56	1.09
17	38.50	37.05	37.95	37.84	1.93	33.21	32.09	30.77	32.02	3.82
18	44.87	45.10	45.73	45.23	0.97	36.90	38.03	38.51	37.81	2.19
19	43.77	43.70	43.77	43.75	0.09	36.79	37.80	36.91	37.17	1.47
20	43.64	41.50	41.19	42.11	3.16	36.06	37.63	33.45	35.71	5.91
21	48.67	49.74	49.75	49.39	1.26	39.99	40.70	40.35	40.35	0.88
22	36.90	38.70	38.43	38.01	2.55	29.07	30.61	29.19	29.62	2.90
23	38.13	37.78	37.88	37.93	0.48	35.80	32.68	32.35	33.61	5.65
24	45.67	47.11	45.87	46.21	1.70	39.11	40.99	40.40	40.17	2.39

Table D-14: RMSD Damage Index for ½-Debond Pipe Relative to the ¼-Debond Pipe for Tests 13-24

Test Set-up	Sensor 1 RMSD Index (%)					Sensor 2 RMSD Index (%)				
	Test 1	Test 2	Test 3	Average	COV (%)	Test 1	Test 2	Test 3	Average	COV (%)
13	48.34	49.77	49.15	49.08	1.46	33.59	35.61	35.00	34.73	2.99
14	44.45	43.64	44.18	44.09	0.93	33.10	33.15	34.19	33.48	1.84
15	47.01	50.30	49.35	48.89	3.46	38.78	40.50	41.41	40.23	3.32
16	38.97	39.39	37.75	38.70	2.20	32.21	32.67	33.50	32.79	1.98
17	36.61	36.35	35.89	36.28	1.02	29.30	30.86	30.93	30.36	3.04
18	40.89	42.04	40.53	41.15	1.91	38.54	38.49	37.93	38.32	0.89
19	48.64	46.99	51.22	48.95	4.36	37.13	39.11	38.88	38.38	2.83
20	44.26	42.04	44.19	43.50	2.90	36.63	34.15	36.12	35.63	3.68
21	51.74	51.44	52.15	51.78	0.68	43.22	43.57	42.87	43.22	0.81
22	40.83	39.89	40.38	40.37	1.17	33.51	34.87	33.96	34.11	2.03
23	38.86	35.76	37.21	37.27	4.16	32.71	28.56	30.17	30.48	6.86
24	43.58	41.74	43.59	42.97	2.48	38.77	38.38	40.27	39.14	2.55

Table D-15: MAPD Damage Index for ½-Debond Pipe Relative to the ¼-Debond Pipe for Tests 1-12

Test Set-up	Sensor 1 MAPD Index (%)					Sensor 2 MAPD Index (%)				
	Test 1	Test 2	Test 3	Average	COV (%)	Test 1	Test 2	Test 3	Average	COV (%)
13	34.54	37.39	35.16	35.70	4.20	41.98	36.90	38.24	39.04	6.75
14	40.84	46.98	50.03	45.95	10.19	28.13	28.72	31.19	29.35	5.54
15	60.50	48.82	50.02	53.11	12.09	38.24	39.85	41.04	39.71	3.53
16	30.84	28.24	31.18	30.09	5.33	29.59	26.63	32.51	29.58	9.94
17	35.62	34.57	33.11	34.43	3.66	27.22	25.96	25.91	26.36	2.82
18	31.52	32.50	35.10	33.04	5.61	42.45	42.53	43.76	42.91	1.71
19	38.66	36.42	40.00	38.36	4.71	43.72	46.43	42.05	44.07	5.02
20	48.33	46.62	39.98	44.98	9.81	30.80	32.60	31.09	31.50	3.07
21	60.11	51.53	55.37	55.67	7.72	40.65	40.39	39.98	40.34	0.84
22	33.01	30.63	34.16	32.60	5.52	27.09	26.90	28.40	27.47	2.97
23	34.68	34.84	30.63	33.39	7.14	30.74	27.30	26.94	28.33	7.41
24	35.10	39.08	35.78	36.65	5.81	41.40	44.34	48.66	44.80	8.16

Table D-16: MAPD Damage Index for ½-Debond Pipe Relative to the ¼-Debond Pipe for Tests 13-24

Test Set-up	Sensor 1 MAPD Index (%)					Sensor 2 MAPD Index (%)				
	Test 1	Test 2	Test 3	Average	COV (%)	Test 1	Test 2	Test 3	Average	COV (%)
13	44.396	47.776	45.610	45.93	3.73	35.533	38.416	36.493	36.81	3.99
14	35.868	34.551	34.742	35.05	2.03	41.696	40.607	45.914	42.74	6.56
15	32.105	34.805	33.720	33.54	4.05	36.719	41.861	42.502	40.36	7.85
16	31.490	32.759	29.728	31.33	4.86	35.515	35.138	42.284	37.65	10.68
17	31.817	31.435	31.122	31.46	1.11	35.559	38.851	39.693	38.03	5.74
18	29.344	29.601	29.374	29.44	0.48	58.271	75.750	59.840	64.62	14.97
19	47.279	46.991	49.176	47.82	2.48	35.643	40.471	38.846	38.32	6.41
20	33.456	32.906	34.230	33.53	1.98	42.520	42.683	37.310	40.84	7.48
21	37.517	35.283	35.751	36.18	3.26	36.556	37.989	38.185	37.58	2.37
22	33.266	30.816	33.021	32.37	4.17	37.169	37.097	33.567	35.94	5.73
23	36.802	32.787	35.981	35.19	6.03	39.965	32.432	37.338	36.58	10.45
24	32.589	29.712	31.136	31.15	4.62	47.582	48.187	62.325	52.70	15.83

Table D-17: CC Damage Index for ½-Debond Pipe Relative to the ¼-Debond Pipe for Tests 1-12

Test Set-up	Sensor 1 CC Index					Sensor 2 CC Index				
	Test 1	Test 2	Test 3	Average	COV (%)	Test 1	Test 2	Test 3	Average	COV (%)
13	0.7859	0.7975	0.7967	0.7934	0.82	0.8063	0.8284	0.8260	0.8203	1.48
14	0.8042	0.7892	0.7769	0.7901	1.73	0.8229	0.8238	0.8137	0.8201	0.69
15	0.8131	0.8269	0.8216	0.8205	0.85	0.7911	0.8006	0.7926	0.7948	0.64
16	0.8319	0.8530	0.8287	0.8379	1.57	0.8785	0.8817	0.8860	0.8821	0.42
17	0.8679	0.8764	0.8496	0.8646	1.59	0.8184	0.8353	0.8428	0.8322	1.50
18	0.8514	0.8373	0.8201	0.8362	1.88	0.8279	0.8132	0.8035	0.8149	1.51
19	0.7638	0.7698	0.7521	0.7619	1.19	0.8201	0.8123	0.8122	0.8149	0.56
20	0.7878	0.8047	0.8168	0.8031	1.81	0.8228	0.8169	0.8461	0.8286	1.86
21	0.8155	0.8056	0.8115	0.8109	0.62	0.7758	0.7652	0.7683	0.7698	0.71
22	0.8391	0.8373	0.8155	0.8306	1.58	0.8876	0.8829	0.8842	0.8849	0.27
23	0.8629	0.8703	0.8758	0.8697	0.74	0.8340	0.8458	0.8586	0.8461	1.45
24	0.8465	0.8035	0.8421	0.8307	2.85	0.7804	0.7536	0.7718	0.7686	1.78

Table D-18: CC Damage Index for ½-Debond Pipe Relative to the ¼-Debond Pipe for Tests 13-24

Test Set-up	Sensor 1 CC Index					Sensor 2 CC Index				
	Test 1	Test 2	Test 3	Average	COV (%)	Test 1	Test 2	Test 3	Average	COV (%)
13	0.8012	0.7875	0.8047	0.7978	1.14	0.8450	0.8331	0.8447	0.8409	0.81
14	0.8114	0.8489	0.8385	0.8329	2.32	0.8829	0.8848	0.8741	0.8806	0.65
15	0.8207	0.8134	0.8144	0.8162	0.49	0.8467	0.8381	0.8302	0.8383	0.99
16	0.8706	0.8602	0.8455	0.8588	1.47	0.8557	0.8526	0.8448	0.8510	0.66
17	0.8872	0.8744	0.8841	0.8819	0.76	0.8876	0.8771	0.8779	0.8808	0.66
18	0.8276	0.8390	0.8409	0.8358	0.86	0.8482	0.8490	0.8536	0.8503	0.34
19	0.8025	0.8124	0.7920	0.8023	1.27	0.8176	0.8125	0.7962	0.8087	1.38
20	0.8179	0.8300	0.8193	0.8224	0.80	0.8504	0.8664	0.8520	0.8563	1.03
21	0.7794	0.7856	0.7964	0.7871	1.10	0.8115	0.8105	0.8183	0.8134	0.52
22	0.8615	0.8409	0.8537	0.8520	1.22	0.8448	0.8337	0.8391	0.8392	0.66
23	0.8740	0.8913	0.8828	0.8827	0.98	0.8661	0.8931	0.8783	0.8791	1.54
24	0.8196	0.8313	0.8200	0.8236	0.80	0.8468	0.8458	0.8334	0.8420	0.89

Appendix E MATLAB Codes Developed for Processing the Mechanically Fastened Pipe Joint Experimental Results

piezoresponse.m

```
% THIS CODE REMOVES NON-RESPONSE DATA AND ANY OFFSET

clear;

format long;

% Command for entering the result file which is entered on the main MATLAB prompt
a = input('Enter baseline file name: ');

% 'points' is the number of data points acquired
points = 30000;
% 'rate' is the data acquisition rate
rate = 10000;
% 'length' controls the length of the retained results, depends on test setup
length = 10000;

% Loads piezoelectric sensor file into variable 'base_holder'
base_holder = load(a);

[a,aa] = size(base_holder);

% Determines the number of tests performed
number_tests = a/(2*points);

% Seperates the results of the different tests into different columns in variable 'base'
for j = 1:2*number_tests
   for i = 1:points
      base(i,j) = base_holder(i+(j-1)*points,1);
   end
end

base_holder = [];

% Seperates test data for the different tests into different variables
test1 = base(:,1:2);    % Test 1, sensor 1 & 2
test2 = base(:,3:4);    % Test 2, sensor 1 & 2
test3 = base(:,5:6);    % Test 3, sensor 1 & 2
test4 = base(:,7:8);    % Test 4, sensor 1 & 2

base = [];

% Puts voltage into proper scale, measured value was 6.5% of actual for sensor 2 only
```

```
test1(:,2) = test1(:,2)/0.065;  %Test 1, sensor 2
test2(:,2) = test2(:,2)/0.065;  %Test 2, sensor 2
test3(:,2) = test3(:,2)/0.065;  %Test 3, sensor 2
test4(:,2) = test4(:,2)/0.065;  %Test 4, sensor 2

% Determines first voltage value greater than 0.2 volts, used to determine start of test
st1 = find(abs(test1(:,1)) > 0.2);  % Test 1
st2 = find(abs(test2(:,1)) > 0.2);  % Test 2
st3 = find(abs(test3(:,1)) > 0.2);  % Test 3
st4 = find(abs(test4(:,1)) > 0.2);  % Test 4

% Determines start point of test, 200 chosen to eliminate any possibility of initial offsets
start1 = find(st1 > 200);   % Test 1
start2 = find(st2 > 200);   % Test 2
start3 = find(st3 > 200);   % Test 3
start4 = find(st4 > 200);   % Test 4

% Variable 'lag_points' is based on the time difference
% between the impact load and the sensor response
lag_points = 8;

% Removes all non-response data before the start of the test
test1(1:st1(start1(1,1),:)-lag_points,:) = [];  % Test 1
test2(1:st2(start2(1,1),:)-lag_points,:) = [];  % Test 2
test3(1:st3(start3(1,1),:)-lag_points,:) = [];  % Test 3
test4(1:st4(start4(1,1),:)-lag_points,:) = [];  % Test 4

% Eliminates results past time determined by variable 'length', non-response data
test1 = test1(1:length,1:2);   % Test 1
test2 = test2(1:length,1:2);   % Test 2
test3 = test3(1:length,1:2);   % Test 3
test4 = test4(1:length,1:2);   % Test 4

% Initialization of first time
time(1,1) = 0.0;

% Computes the time vector for the tests
for i = 2:length
   time(i,1) = time1(i-1,1) + 1/rate;
end

% Plots a comparison of the sensor responses for the four tests
% Figure(1) is sensor 1 for the four tests, Figure(2) is sensor 2 for the four tests
figure(1); plot(time, test1(:,1),time, test2(:,1),'-r',time, test3(:,1),'-y',time, test4(:,1),'-g' );...
```

```
figure(2); plot(time, test1(:,2),time, test2(:,2),'-r',time, test3(:,2),'-y',time, test4(:,2),'-g' );...

% Stores all four tests in one variable 'result'
result(:,1) = test1(:,1);   % Test 1, sensor 1
result(:,5) = test1(:,2);   % Test 1, sensor 2
result(:,2) = test2(:,1);   % Test 2, sensor 1
result(:,6) = test2(:,2);   % Test 2, sensor 2
result(:,3) = test3(:,1);   % Test 3, sensor 1
result(:,7) = test3(:,2);   % Test 3, sensor 2
result(:,4) = test4(:,1);   % Test 4, sensor 1
result(:,8) = test4(:,2);   % Test 4, sensor 2

% Saves the test results to a text file 'filename.txt'
save filename.txt result –ASCII
```

loadresponse.m

```
% THIS PROGRAM SORTS THE LOADING FILES FOR A GIVEN TEST SETUP BY
REMOVING NON-RESPONSE DATA

clear;

format long;

% Input for load file, the name is entered on the main MATLAB prompt
b = input('Enter baseline file name: ');

% Test data
points = 20000; % Number of data points
rate = 10000;   % Rate of data acquisition

% Loads the load file into variable 'base_holder'
base_holder = load(b);

% Determines the total number of points in the file and stores it in 'a'
[a,aa] = size(base_holder);

number_tests = a/points;        % Determines number of tests
col_in_data = number_tests+1;   % Determines the number of columns required for the
output file

% Loop seperates the tests into their own column and stores it in variable 'base'
for j = 1:number_tests
   for i = 1:points
      base(i,j) = base_holder(i+(j-1)*points,1);
   end
end

% Following commands determine the points greater than 0.09 volts for the start of the
test
st1 = find(base(:,1) > 0.09);   % Test 1
st2 = find(base(:,2) > 0.09);   % Test 2
st3 = find(base(:,3) > 0.09);   % Test 3
st4 = find(base(:,4) > 0.09);   % Test 4

% Converts the voltage to load (Newtons), and stores it in the variables 'load#'
load1 = base(:,1)*1000/9.96;    % Loading for test 1
load2 = base(:,2)*1000/9.96;    % Loading for test 2
```

```
load3 = base(:,3)*1000/9.96;   % Loading for test 3
load4 = base(:,4)*1000/9.96;   % Loading for test 4

% Variable 's#(1,1)' contains the start point of the test
% Comparison to 50 due to offset at very start of test in hammer voltage
s1 = find(st1 > 50);       % Test 1
s2 = find(st2 > 50);       % Test 2
s3 = find(st3 > 50);       % Test 3
s4 = find(st4 > 50);       % Test 4

% Removes data more than 1 second after first value greater than 0.9 volts
load1(st1(s1(1,1),1)+9999:points,:) = [];  % Test 1
load2(st2(s2(1,1),1)+9999:points,:) = [];  % Test 2
load3(st3(s3(1,1),1)+9999:points,:) = [];  % Test 3
load4(st4(s4(1,1),1)+9999:points,:) = [];  % Test 4

% Removes non-response data before loading applied
load1(1:st1(s1(1,1),1)-2,:) = [];  % 'load1' contatins 1 second worth of data for test 1
load2(1:st2(s2(1,1),1)-2,:) = [];  % 'load2' contatins 1 second worth of data for test 2
load3(1:st3(s3(1,1),1)-2,:) = [];  % 'load3' contatins 1 second worth of data for test 3
load4(1:st4(s4(1,1),1)-2,:) = [];  % 'load4' contatins 1 second worth of data for test 3

% Initialize the start time to zero
time(1,1) = 0.0;

% Loop computes the time vector for the loading history
for i = 2:10000
   time(i,1) = time(i-1,1) + 1/rate;
end

% Following commands plot the time history of the loading
figure(1); plot(time,load1);
figure(2); plot(time,load2);
figure(3); plot(time,load3);
figure(4); plot(time,load4);

% Following stores all load results into one variable 'force'
force(:,1) = load1;
force(:,2) = load2;
force(:,3) = load3;
force(:,4) = load4;

% Saves the variable 'force' to a text file 'filename.txt'
save filename.txt force –ASCII
```

normalize.m

```
% THIS PROGRAM NORMALIZES THE FOURIER SPECTRUMS FOR THE
MECHANICALLY FASTENED PIPE JOINTS

clear;

format long;

% File inputs to be entered on MATLAB main prompt
a = input('Enter the piezo file name: ');   % Piezoelectric response file
b = input('Enter the load file name: ');    % Load file

% Data acquisition rate
rate = 10000;

% Plot Controls, 'y' means plots, 'n' is do not plot
plot_fourier = 'y';
% Filter requirements, 'y' mean filter, 'n' means no filter required
filter_required = 'y';

% Loads the test files
p = load(a);    % Piezoelectric response stored in 'p'
force = load(b);    % load file stored in 'force'

[pr,pc] = size(piezo);
[fr,fc] = size(force);

%Following filters the data through function 'fullfilter'
if filter_required = 'y'
   filt_piezo = filterdata(piezo,pc);
else
   filt_piezo = piezo;
end

%Following performs the Fast Fourier transform through function 'fastfourier'
piezo_pow = fastfourier(filt_piezo);
force_pow = fastfourier(force);

%Following normalizes the piezoelectric response wrt the load results through function
'normalize'
norm = frf(piezo_pow,force_pow);

% Determines frequency scale for fourier plots
```

```
f = rate*(0:4096)/8192;

% Following loop plots the normalized Fourier spectrums
% Range of plot can be changed by changing the limits in the variable 'f' & 'norm'
if plot_fourier == 'y'
% Plots all three tests seperately on one subplot
   for i = 1:pc/2
      figure(8); subplot(pc/2,1,i); plot(f(1,55:2154),norm(55:2154,i));       % Sensor 1
      legend('First Sensor');
      figure(9); subplot(pc/2,1,i); plot(f(1,55:2154),norm(55:2154,i+pc/2));  % Sensor 2
      legend('Second Sensor');
   end
   % Plots all three test on a single plot, 'j' determines sensor
   % 'j = 1' plots sensor 1 for all tests on a single plot
   % 'j = 2' plots sensor 2 for all tests on a single plot
   for j = 1:2
     figure(16+j); plot(f(1,55:2154),norm(55:2154,j+3*(j-1)));...        % Test 1
                hold on;...
                plot(f(1,55:2154),norm(55:2154,j*2+2*(j-1)),'-r');...   % Test 2
                hold on;...
                plot(f(1,55:2154),norm(55:2154,j*3+(j-1)),'-g');...     % Test 3
                hold on;...
                plot(f(1,55:2154),norm(55:2154,j*4),'-y');              % Test 4
   end
end

% 'fourier' holds the desired Fourier range for damage index evaluation
% The range can be changed to norrow or enlarge evaluation window by changing the
row limits
fourier = norm(55:2154,:);

% Outputs the variable 'fourier' to the text file 'filename.txt'
save filename.txt fourier –ASCII
```

filterdata.m

```
% THIS FUNCTION FILTERS THE PIEZOELECTRIC RESPONSE

function filtered = testfilter(base,number)

rate = 10000;

% Selects filter: Butterworth bandpass filter
[c,d] = butter(filter order,[low cutoff frequency,high cutoff frequency]);

% Loop filters the data of all sensors
for i = 1:number
   base(:,i) = filter(c,d,base(:,i));
end

% 'filtered' passed back to main program with filtered responses
filtered = base;
```

fastfourier.m

```
% THIS FUNCTION COMPUTES THE 8192 POINT FFT OF THE INPUT

function fourier = fastfourier(base)

baseY = fft(base,8192);

% 'fourier' is variable passed back to main program with fft of data
fourier = baseY;
```

frf.m

```
%THIS FUNCTION COMPUTES THE FRF OF EACH EXPERIMENT

function normal = normalize(piezo,force)

[a,b] = size(piezo);
[c,d] = size(force);

for i = 1:d
   hold(:,i) = (piezo(:,i)./(force(:,i)));
   hold(:,i+d) = (piezo(:,i+d)./(force(:,i)));
end

normal = hold;
```

RMSDindex.m

```
% DETERMINES THE RMSD DAMAGE INDEX FOR THE LOOSENED JOINT
STATES RELATIVE TO THE FULLY TIGHTENED JOINT

clear;

format long;

% File inputs read directly into the program
% Input for the undamaged fourier spectrum
base_his = importdata('d:\thesis\test results\bolt joint\pvc\1.2x1.2m\damage\fourier3.txt');
% Inputs for the damaged fourier spectrums for the different tests
dam_four_his(:,1:8) = importdata('d:\thesis\test results\bolt
joint\pvc\1.2x1.2m\damage\fourier6.txt');
dam_four_his(:,9:16) = importdata('d:\thesis\test results\bolt
joint\pvc\1.2x1.2m\damage\fourier9.txt');
dam_four_his(:,17:24) = importdata('d:\thesis\test results\bolt
joint\pvc\1.2x1.2m\damage\fourier12.txt');
dam_four_his(:,25:32) = importdata('d:\thesis\test results\bolt
joint\pvc\1.2x1.2m\damage\fourier15.txt');
dam_four_his(:,33:40) = importdata('d:\thesis\test results\bolt
joint\pvc\1.2x1.2m\damage\fourier18.txt');
dam_four_his(:,41:48) = importdata('d:\thesis\test results\bolt
joint\pvc\1.2x1.2m\damage\fourier21.txt');

% 'num_comp' is the number of comparison files to enter, number of damaged files input
num_comp = 6;

% Computes the square of the individual points in the undamaged data: xi^2 in RMSD
equation
sq_four_base = (base_four_his).^2;

% Computes the sum of the squares of the individual points in the undamaged data:
sum(xi^2) in RMSD equation
for i =1:8
   sums_four(1,i) = sum(sq_four_base(:,i));
end

% Following loop calculates the difference in the individual points of the
% undamaged and damaged Fourier spectrums: (yi-xi) in the RMSD equation
for i = 1:num_comp
   for j = 1:8
      diff_four(:,j+8*(i-1)) = dam_four_his(:,j+8*(i-1))-base_four_his(:,j);
```

```
   end
end

% Determines the square of the differences found above: (yi-xi)^2 in RMSD equation
sq_four_diff = (diff_four).^2;

% Determines the sum of the squares found above: sum((yi-xi)^2) in RMSD equation
for i = 1:num_comp
   for j = 1:8
      sum_four_diff(1,j+8*(i-1)) = sum(sq_four_diff(:,j+8*(i-1)));
   end
end

% Computes the RMSD damage index for each of the tests
for i = 1:num_comp
   for j = 1:8
      RMDS(i,j) = sqrt(sum_four_diff(1,j+8*(i-1))./sums_four(1,j))*100;
   end
end

% Saves the RMSD damage indices to the text file 'filename.txt'
save filename.txt RMDS -ASCII
```

MAPDindex.m

```
% DETERMINES THE MAPD DAMAGE INDEX FOR THE LOOSENED JOINT
STATES RELATIVE TO THE FULLY TIGHTENED JOINT

clear;

format long;

% File inputs read directly into the program
% Input for the undamaged fourier spectrum
base_his = importdata('d:\thesis\test results\bolt joint\pvc\1.2x1.2m\damage\fourier3.txt');
% Inputs for the damaged fourier spectrums for the different tests
dam_four_his(:,1:8) = importdata('d:\thesis\test results\bolt
joint\pvc\1.2x1.2m\damage\fourier6.txt');
dam_four_his(:,9:16) = importdata('d:\thesis\test results\bolt
joint\pvc\1.2x1.2m\damage\fourier9.txt');
dam_four_his(:,17:24) = importdata('d:\thesis\test results\bolt
joint\pvc\1.2x1.2m\damage\fourier12.txt');
dam_four_his(:,25:32) = importdata('d:\thesis\test results\bolt
joint\pvc\1.2x1.2m\damage\fourier15.txt');
dam_four_his(:,33:40) = importdata('d:\thesis\test results\bolt
joint\pvc\1.2x1.2m\damage\fourier18.txt');
dam_four_his(:,41:48) = importdata('d:\thesis\test results\bolt
joint\pvc\1.2x1.2m\damage\fourier21.txt');

% 'num_comp' is the number of comparison files to enter, number of damaged files input
num_comp = 6;

% Following loop calculates the difference in the individual points of the
% undamaged and damaged Fourier spectrums: (yi-xi) in the MAPD equation
for i = 1:num_comp
   for j = 1:8
      diff_four(:,j+8*(i-1)) = dam_four_his(:,j+8*(i-1))-base_four_his(:,j);
   end
end

% 'N_four' will hold the number of data points in the Fourier spectrums: N in MAPD
equation
[N_four,p] = size(diff_four);

% Loop calculates the division of the difference in Fourier spectrums by the
% value of the undamaged spectrum: (yi-xi)/xi in MAPD equation
for i = 1:num_comp
```

```
   for j = 1:8
      div_diff_four(:,j+8*(i-1)) = diff_four(:,j+8*(i-1))./base_four_his(:,j);
   end
end

% Command takes the absolute value of the previous step
% absolute value of ((yi-xi)/xi) in MAPD equation
div_diff_four = abs(div_diff_four);

% Determines the sum of the above step for each test
% sum(absolute value of ((yi-xi)/xi)) in MAPD equation
for i = 1:num_comp
   for j = 1:8
      sum_four_diff(1,j+8*(i-1)) = sum(div_diff_four(:,j+8*(i-1)));
   end
end

% Computes the MAPD damage index
for i = 1:num_comp
   for j = 1:8
      MAPD(i,j) = sum_four_diff(1,j+8*(i-1))*100/N_four;
   end
end

% Saves the MAPD damage indices to the text file 'filename.txt'
save filename.txt MAPD -ASCII
```

CCindex.m

```
% DETERMINES THE CC DAMAGE INDEX FOR THE LOOSENED JOINT
STATES RELATIVE TO THE FULLY TIGHTENED JOINT

clear;

format long;

% File inputs read directly into the program
% Input for the undamaged fourier spectrum
base_his = importdata('d:\thesis\test results\bolt joint\pvc\1.2x1.2m\damage\fourier3.txt');
% Inputs for the damaged fourier spectrums for the different tests
dam_his(:,1:8) = importdata('d:\thesis\test results\bolt
joint\pvc\1.2x1.2m\damage\fourier6.txt');
dam_his(:,9:16) = importdata('d:\thesis\test results\bolt
joint\pvc\1.2x1.2m\damage\fourier9.txt');
dam_his(:,17:24) = importdata('d:\thesis\test results\bolt
joint\pvc\1.2x1.2m\damage\fourier12.txt');
dam_his(:,25:32) = importdata('d:\thesis\test results\bolt
joint\pvc\1.2x1.2m\damage\fourier15.txt');
dam_his(:,33:40) = importdata('d:\thesis\test results\bolt
joint\pvc\1.2x1.2m\damage\fourier18.txt');
dam_his(:,41:48) = importdata('d:\thesis\test results\bolt
joint\pvc\1.2x1.2m\damage\fourier21.txt');

% 'num_comp' is the number of comparison files to enter, number of damaged files input
num_comp = 6;

% computes the standard deviation of the undamaged and damaged data
std_base = std(base_his);
std_dam = std(dam_his);

% computes the mean of the undamaged and damaged data
mean_base = mean(base_his);
mean_dam = mean(dam_his);

% Determines the size of the data matrices
[N,n] = size(base_his);
[P,p] = size(dam_his);

% Following loops determine the difference between the individual points and the mean
% 'diff_base' is the difference for the undamaged data: (xi-x) in covariance equation
for i = 1:n
```

```
   diff_base(:,i) = base_his(:,i) - mean_base(1,i);
end

% 'diff_dam' is the difference for the damaged data: (yi-y) in covariance equation
for i = 1:p
   diff_dam(:,i) = dam_his(:,i) - mean_dam(1,p);
end

% Following loop computes the multiplication of the difference between the individual
data points and the overall
% mean for the individual points of the undamaged and damaged specimens: (xi-x)(yi-y)
in covariance equation
for i = 1:num_comp
   for j = 1:8
      multi_diff(:,j+8*(i-1)) = diff_dam(:,j+8*(i-1)).*diff_base(:,j);
   end
end

% Computes the sum of the differences found above for the individual tests: sum((xi-
x)(yi-y)) in covariance equation
for i = 1:num_comp
   for j = 1:8
      sum_multi_diff(1,j+8*(i-1)) = sum(multi_diff(:,j+8*(i-1)));
   end
end

% Computes the covariance in the data sets
Cov = sum_multi_diff/N;

% Following loop calculates the CC damage index for each test
for i = 1:num_comp
   for j = 1:8
      CC(i,j) = Cov(1,j+8*(i-1))/(std_base(1,j)*std_dam(1,j+8*(i-1)));
   end
end

% Saves the CC damage indices to the text file 'filename.txt'
save filename.txt CC -ASCII
```

preceeding.m

```
% PRECEEDING STATE DAMAGE INDEX EVALUATION
% This program computes the damage INDICES FOR ONE STATE OF DAMAGE
RELATIVE TO THE PROCEEDING STATE

clear;

format long;

% File inputs, directly read into the code
% First stage of damage
base_his = importdata('d:\thesis\test results\bolt joint\pvc\1.2x1.2m\damage\fourier4.txt');
% Second stage of damage
dam_his = importdata('d:\thesis\test results\bolt joint\pvc\1.2x1.2m\damage\fourier7.txt');

% 'num_comp' is the number of comparison files, half the number of damaged files input
num_comp = 1;

% **********SECTION 1 COMPUTES THE RELATIVE CC DAMAGE
INDEX**********

% Computes the standard deviation of the baseline and damaged data for each test: Used
in CC index
std_base = std(base_his);
std_dam = std(dam_his);

% Computes the mean of the undamaged and damaged data: Used in CC index
mean_base = mean(base_his);
mean_dam = mean(dam_his);

% Determines the size of the data sets, capital letter is number
% of data points, small letter is number of test sets
[N,n] = size(base_his);
[P,p] = size(dam_his);

% Following loops determine the difference between the individual points and the mean
% 'diff_base' is the difference for the undamaged data: (xi-x) in covariance equation
for i = 1:n
   diff_base(:,i) = base_his(:,i) - mean_base(1,i);
end

% 'diff_dam' is the difference for the damaged data: (yi-y) in covariance equation
for i = 1:p
```

```
   diff_dam(:,i) = dam_his(:,i) - mean_dam(1,i);
end

% Following loop computes the multiplication of the difference between the individual
data points and the overall
% mean for the individual points of the undamaged and damaged specimens: (xi-x)(yi-y)
in covariance equation
for i = 1:num_comp
   for j = 1:8
      multi_diff(:,j+8*(i-1)) = diff_dam(:,j+8*(i-1)).*diff_base(:,j);
   end
end

% Computes the sum of the differences found above for the individual tests: sum((xi-
x)(yi-y)) in covariance equation
for i = 1:num_comp
   for j = 1:8
      sum_multi_diff(1,j+8*(i-1)) = sum(multi_diff(:,j+8*(i-1)));
   end
end

% Computes the covariance in the data sets
Cov = sum_multi_diff/N;

% Following loop calculates the CC damage index for each test
for i = 1:num_comp
   for j = 1:8
      CC(i,j) = Cov(1,j+8*(i-1))/(std_base(1,j)*std_dam(1,j+8*(i-1)));
   end
end

% ********** END OF SECTION 1 **********

% ********** SECTION 2 COMPUTES THE RELATIVE MAPD DAMAGE INDEX
**********

% Following loop calculates the difference in the individual points of the
% undamaged and damaged Fourier spectrums: (yi-xi) in the MAPD equation
for i = 1:num_comp
   for j = 1:8
      diff_four(:,j+8*(i-1)) = dam_his(:,j+8*(i-1))-base_his(:,j);
   end
end
```

```
% 'N_four' will hold the number of data points in the Fourier spectrums: N in MAPD
equation
[N_four,p] = size(diff_four);

% Loop calculates the division of the difference in Fourier spectrums by the
% value of the undamaged spectrum: (yi-xi)/xi in MAPD equation
for i = 1:num_comp
   for j = 1:8
      div_diff_four(:,j+8*(i-1)) = diff_four(:,j+8*(i-1))./base_his(:,j);
   end
end

% Command takes the absolute value of the previous step
% absolute value of ((yi-xi)/xi) in MAPD equation
div_diff_four = abs(div_diff_four);

% Determines the sum of the above step for each test
% sum(absolute value of ((yi-xi)/xi)) in MAPD equation
for i = 1:num_comp
   for j = 1:8
      sum_four_diff(1,j+8*(i-1)) = sum(div_diff_four(:,j+8*(i-1)));
   end
end

% Computes the MAPD damage index
for i = 1:num_comp
   for j = 1:8
      MAPD(i,j) = sum_four_diff(1,j+8*(i-1))*100/N_four;
   end
end

% ********** END OF SECTION 2 **********

% ********** SECTION 3 COMPUTES THE RELATIVE RMSD DAMAGE INDEX
**********

% Computes the square of the individual points in the undamaged data: xi^2 in RMSD
equation
sq_four_base = (base_his).^2;

% Computes the sum of the squares of the individual points in the undamaged data:
sum(xi^2) in RMSD equation
for i =1:8
   sums_four(1,i) = sum(sq_four_base(:,i));
```

```
end

% Following loop calculates the difference in the individual points of the
% undamaged and damaged Fourier spectrums: (yi-xi) in the RMSD equation
for i = 1:num_comp
   for j = 1:8
      diff_four(:,j+8*(i-1)) = dam_his(:,j+8*(i-1))-base_his(:,j);
   end
end

% Determines the square of the differences found above: (yi-xi)^2 in RMSD equation
sq_four_diff = (diff_four).^2;

% Determines the sum of the squares found above: sum((yi-xi)^2) in RMSD equation
for i = 1:num_comp
   for j = 1:8
      sum_four_diff(1,j+8*(i-1)) = sum(sq_four_diff(:,j+8*(i-1)));
   end
end

% Computes the RMSD damage index for each of the tests
for i = 1:num_comp
   for j = 1:8
      RMDS(i,j) = sqrt(sum_four_diff(1,j+8*(i-1))./sums_four(1,j))*100;
   end
end

% ********** END OF SECTION 3 **********

% Following commands save the resulting relative damage indexes to text files
save CCpre.txt CC -ASCII          % Relative CC index to 'CCpre.txt'
save MAPDpre.txt MAPD_four -ASCII  % Relative MAPD index to 'MAPDpre.txt'
save RMDSpre.txt RMDS_four -ASCII  % Relative RMSD index to 'RMSDpre.txt'
```

Appendix F Damage Index Results for Mechanically Fastened 1.2x1.2m Cast Iron Pipe Joint

Table F-1: RMSD Damage Index Relative to the Undamaged State for Excitation Location 1

Degree Of Damage	Test 1	Test 2	Test 3	Test 4	Average	COV (%)
	Sensor 1					
1	7.49	7.16	7.14	7.10	7.22	2.45
2	13.47	13.05	12.42	13.51	13.11	3.85
3	17.82	18.11	17.19	18.89	18.00	3.91
4	25.23	24.38	25.38	25.28	25.07	1.85
5	33.73	33.95	33.97	33.71	33.84	0.41
6	60.38	60.94	60.55	60.17	60.51	0.54
	Sensor 2					
1	7.64	6.47	6.69	6.94	6.93	7.30
2	8.72	10.53	10.27	9.99	9.88	8.11
3	10.72	10.25	10.58	9.98	10.38	3.19
4	13.07	11.60	11.51	12.25	12.11	5.96
5	28.21	29.76	28.88	29.35	29.05	2.28
6	29.80	34.12	29.00	32.47	31.35	7.56

Table F-2: RMSD Damage Index Relative to the Undamaged State for Excitation Location 2

Degree Of Damage	Test 1	Test 2	Test 3	Test 4	Average	COV (%)
	Sensor 1					
1	7.69	8.50	8.58	8.46	8.31	4.97
2	10.82	10.85	10.98	11.54	11.05	3.04
3	14.17	13.84	14.55	14.58	14.28	2.44
4	22.85	21.75	22.16	23.13	22.48	2.81
5	29.50	29.52	29.38	29.92	29.58	0.80
6	58.63	58.44	58.24	58.64	58.48	0.33
	Sensor 2					
1	5.95	6.63	5.87	6.86	6.33	7.75
2	9.58	9.45	8.37	8.53	8.98	6.93
3	12.66	11.25	11.94	11.64	11.88	5.02
4	15.47	14.55	16.55	14.25	15.20	6.82
5	18.47	17.49	17.31	16.33	17.40	5.02
6	21.25	21.17	21.10	21.15	21.17	0.31

Table F-3: RMSD Damage Index Relative to the Undamaged State for Excitation Location 3

Degree Of Damage	Test 1	Test 2	Test 3	Test 4	Average	COV (%)
	Sensor 1					
1	7.48	7.59	7.65	7.70	7.60	1.22
2	9.42	9.06	9.21	9.78	9.37	3.32
3	10.56	10.83	11.31	11.05	10.94	2.93
4	16.16	15.83	15.84	16.72	16.14	2.58
5	34.74	35.33	34.74	35.71	35.13	1.35
6	58.34	58.15	58.29	58.59	58.34	0.32
	Sensor 2					
1	8.05	7.98	7.94	7.91	7.97	0.81
2	7.71	8.04	7.65	7.70	7.77	2.26
3	11.14	12.43	11.89	11.11	11.64	5.46
4	16.53	14.69	14.90	15.14	15.31	5.42
5	38.16	35.41	35.75	36.12	36.36	3.40
6	43.00	44.60	41.16	43.89	43.16	3.44

Table F-4: MAPD Damage Index Relative to the Undamaged State for Excitation Location 1

Degree Of Damage	Test 1	Test 2	Test 3	Test 4	Average	COV (%)
	Sensor 1					
1	12.44	11.73	11.66	11.46	11.82	3.61
2	22.70	22.15	22.28	23.18	22.58	2.06
3	26.12	25.70	25.92	26.51	26.06	1.31
4	39.05	38.94	38.88	39.06	38.98	0.22
5	53.27	53.94	54.00	53.19	53.60	0.80
6	65.17	66.96	65.74	64.32	65.55	1.69
	Sensor 2					
1	8.82	10.78	10.49	10.17	10.06	8.62
2	15.88	15.14	15.27	15.42	15.43	2.10
3	16.66	16.33	16.56	16.15	16.42	1.40
4	23.71	21.61	22.76	23.21	22.82	3.94
5	41.04	43.10	41.94	42.57	42.16	2.10
6	44.38	49.50	43.41	47.58	46.22	6.11

Table F-5: MAPD Damage Index Relative to the Undamaged State for Excitation Location 2

Degree Of Damage	Test 1	Test 2	Test 3	Test 4	Average	COV (%)
	Sensor 1					
1	11.80	11.40	10.97	13.13	11.82	7.89
2	18.54	18.55	17.90	18.85	18.46	2.18
3	21.72	20.94	21.15	22.28	21.52	2.80
4	34.13	34.05	34.08	34.30	34.14	0.32
5	43.63	43.62	44.26	43.45	43.74	0.81
6	62.76	63.53	64.57	62.71	63.39	1.38
	Sensor 2					
1	9.80	11.20	10.70	12.31	11.00	9.51
2	13.76	14.61	12.22	13.45	13.51	7.33
3	14.64	15.85	14.42	14.03	14.74	5.32
4	18.73	17.49	19.37	18.08	18.42	4.41
5	22.16	22.15	22.80	22.42	22.38	1.37
6	49.72	51.92	50.59	50.16	50.60	1.88

Table F-6: MAPD Damage Index Relative to the Undamaged State for Excitation Location 3

Degree Of Damage	Test 1	Test 2	Test 3	Test 4	Average	COV (%)
	Sensor 1					
1	11.90	12.30	12.05	12.15	12.10	1.39
2	20.95	20.43	21.51	21.32	21.05	2.26
3	22.14	22.12	22.12	22.19	22.14	0.16
4	39.42	37.53	38.08	40.67	38.92	3.63
5	62.28	58.91	59.96	64.27	61.35	3.91
6	72.68	71.65	72.42	73.81	72.64	1.23
	Sensor 2					
1	9.12	9.43	9.36	9.29	9.30	1.45
2	15.57	15.58	15.59	15.57	15.58	0.09
3	16.17	17.25	15.95	16.14	16.38	3.59
4	29.91	28.01	28.23	28.49	28.66	2.99
5	55.74	52.49	52.89	53.34	53.62	2.72
6	73.89	76.36	70.92	75.28	74.11	3.18

Table F-7: CC Damage Index Relative to the Undamaged State for Excitation Location 1

Degree Of Damage	Test 1	Test 2	Test 3	Test 4	Average	COV (%)
	Sensor 1					
1	0.9962	0.9962	0.9962	0.9962	0.9962	1.2E-06
2	0.9933	0.9933	0.9933	0.9933	0.9933	0.0E+00
3	0.9905	0.9905	0.9905	0.9905	0.9905	1.7E-06
4	0.9801	0.9801	0.9801	0.9801	0.9801	1.8E-06
5	0.9252	0.9252	0.9252	0.9252	0.9252	4.6E-06
6	0.6834	0.6834	0.6834	0.6834	0.6834	1.8E-05
	Sensor 2					
1	0.9961	0.9961	0.9961	0.9961	0.9961	0.0E+00
2	0.9975	0.9975	0.9975	0.9975	0.9975	0.0E+00
3	0.9969	0.9969	0.9969	0.9969	0.9969	0.0E+00
4	0.9967	0.9967	0.9967	0.9967	0.9967	0.0E+00
5	0.9696	0.9696	0.9696	0.9696	0.9696	0.0E+00
6	0.9519	0.9519	0.9519	0.9519	0.9519	1.3E-06

Table F-8: CC Damage Index Relative to the Undamaged State for Excitation Location 2

Degree Of Damage	Test 1	Test 2	Test 3	Test 4	Average	COV (%)
	Sensor 1					
1	0.9983	0.9983	0.9983	0.9983	0.9983	0.0E+00
2	0.9924	0.9924	0.9924	0.9924	0.9924	0.0E+00
3	0.9894	0.9894	0.9894	0.9894	0.9894	0.0E+00
4	0.9722	0.9722	0.9722	0.9722	0.9722	0.0E+00
5	0.9309	0.9309	0.9309	0.9309	0.9309	0.0E+00
6	0.7431	0.7431	0.7431	0.7431	0.7431	0.0E+00
	Sensor 2					
1	0.9979	0.9979	0.9979	0.9979	0.9979	1.2E-06
2	0.9984	0.9984	0.9984	0.9984	0.9984	0.0E+00
3	0.9959	0.9959	0.9959	0.9959	0.9959	0.0E+00
4	0.9914	0.9914	0.9914	0.9914	0.9914	0.0E+00
5	0.9896	0.9896	0.9896	0.9896	0.9896	0.0E+00
6	0.9779	0.9779	0.9779	0.9779	0.9779	0.0E+00

Table F-9: CC Damage Index Relative to the Undamaged State for Excitation Location 3

Degree Of Damage	Test 1	Test 2	Test 3	Test 4	Average	COV (%)
	Sensor 1					
1	0.9968	0.9968	0.9968	0.9968	0.9968	0.0E+00
2	0.9947	0.9947	0.9947	0.9947	0.9947	0.0E+00
3	0.9939	0.9939	0.9939	0.9939	0.9939	0.0E+00
4	0.9835	0.9835	0.9835	0.9835	0.9835	0.0E+00
5	0.9328	0.9328	0.9328	0.9328	0.9328	0.0E+00
6	0.7585	0.7585	0.7585	0.7585	0.7585	0.0E+00
	Sensor 2					
1	0.9957	0.9957	0.9957	0.9957	0.9957	0.0E+00
2	0.9962	0.9962	0.9962	0.9962	0.9962	0.0E+00
3	0.9945	0.9945	0.9945	0.9945	0.9945	0.0E+00
4	0.9905	0.9905	0.9905	0.9905	0.9905	0.0E+00
5	0.9685	0.9685	0.9685	0.9685	0.9685	0.0E+00
6	0.9347	0.9347	0.9347	0.9347	0.9347	0.0E+00

Table F-10: RMSD Damage Index Relative to the Proceeding State of Damage for Excitation Location 1

Degree Of Damage	Test 1	Test 2	Test 3	Test 4	Average	COV (%)
	Sensor 1					
1	7.49	7.16	7.14	7.10	7.22	2.45
2	9.69	9.08	8.46	9.69	9.23	6.39
3	7.47	7.43	7.33	7.47	7.43	0.94
4	12.03	11.99	12.03	12.30	12.09	1.18
5	33.69	33.01	32.33	33.68	33.18	1.95
6	48.27	48.51	48.28	48.19	48.31	0.28
	Sensor 2					
1	7.64	6.47	6.69	6.94	6.93	7.30
2	7.51	8.28	8.28	8.28	8.09	4.78
3	6.25	7.28	7.37	6.27	6.79	9.01
4	4.14	4.51	4.13	4.12	4.22	4.54
5	38.15	38.06	34.88	40.31	37.85	5.91
6	11.12	12.24	10.07	11.63	11.26	8.19

Table F-11: RMSD Damage Index Relative to the Proceeding State of Damage for Excitation Location 2

Degree Of Damage	Test 1	Test 2	Test 3	Test 4	Average	COV (%)
	Sensor 1					
1	7.69	8.50	8.58	8.46	8.31	4.97
2	7.32	7.55	7.36	7.29	7.38	1.60
3	5.08	4.85	5.30	5.55	5.19	5.81
4	12.45	13.65	13.31	12.48	12.97	4.65
5	16.69	16.56	17.02	16.85	16.78	1.19
6	46.03	46.03	46.02	46.02	46.03	0.01
	Sensor 2					
1	5.95	6.63	5.87	6.86	6.33	7.75
2	10.83	12.10	13.66	12.05	12.16	9.54
3	12.59	13.59	12.85	12.87	12.98	3.32
4	6.85	7.06	6.17	6.07	6.54	7.53
5	10.37	10.31	11.00	11.22	10.73	4.21
6	10.66	11.03	12.69	11.91	11.57	7.88

Table F-12: RMSD Damage Index Relative to the Proceeding State of Damage for Excitation Location 3

Degree Of Damage	Test 1	Test 2	Test 3	Test 4	Average	COV (%)
	Sensor 1					
1	7.48	7.59	7.65	7.70	7.60	1.22
2	8.21	7.95	7.96	8.52	8.16	3.29
3	9.87	9.70	10.94	9.87	10.09	5.66
4	14.13	14.33	14.82	14.12	14.35	2.27
5	25.33	25.33	25.33	25.33	25.33	0.00
6	43.10	42.80	42.76	43.10	42.94	0.44
	Sensor 2					
1	8.05	7.98	7.94	7.91	7.97	0.81
2	4.51	4.31	3.90	3.88	4.15	7.55
3	11.39	11.70	11.52	11.39	11.50	1.28
4	9.09	7.50	8.11	8.11	8.20	8.04
5	23.59	23.59	23.59	23.59	23.59	0.00
6	15.04	14.47	15.04	14.51	14.76	2.14

Table F-13: MAPD Damage Index Relative to the Proceeding State of Damage for Excitation Location 1

Degree Of Damage	Test 1	Test 2	Test 3	Test 4	Average	COV (%)
	Sensor 1					
1	12.44	11.73	11.66	11.46	11.82	3.61
2	15.92	15.34	15.33	15.92	15.63	2.17
3	11.76	11.74	12.16	11.76	11.86	1.73
4	19.68	19.68	20.18	19.96	19.88	1.22
5	53.57	52.74	50.62	53.56	52.62	2.65
6	49.19	49.95	49.24	48.79	49.29	0.97
	Sensor 2					
1	8.82	10.78	10.49	10.17	10.06	8.62
2	12.19	12.66	12.66	12.66	12.55	1.91
3	11.65	12.45	12.52	11.67	12.07	3.96
4	10.30	11.12	10.41	10.30	10.53	3.78
5	52.59	52.49	48.71	55.11	52.23	5.05
6	27.50	27.86	27.23	27.66	27.56	0.97

Table F-14: MAPD Damage Index Relative to the Proceeding State of Damage for Excitation Location 2

Degree Of Damage	Test 1	Test 2	Test 3	Test 4	Average	COV (%)
	Sensor 1					
1	11.80	11.40	10.97	13.13	11.82	7.89
2	18.38	17.56	19.32	18.87	18.53	4.06
3	11.75	12.29	11.85	11.99	11.97	1.94
4	16.15	16.33	16.26	16.16	16.23	0.52
5	27.45	27.14	27.87	27.67	27.53	1.14
6	43.21	43.61	43.44	43.41	43.42	0.38
	Sensor 2					
1	9.80	11.20	10.70	12.31	11.00	9.51
2	14.12	16.37	17.63	13.76	15.47	11.91
3	11.67	11.56	13.44	13.69	12.59	8.99
4	11.53	9.83	9.99	9.94	10.32	7.82
5	17.25	14.48	14.33	13.93	15.00	10.13
6	59.19	62.39	67.30	64.30	63.29	5.38

Table F-15: MAPD Damage Index Relative to the Proceeding State of Damage for Excitation Location 3

Degree Of Damage	Test 1	Test 2	Test 3	Test 4	Average	COV (%)
	Sensor 1					
1	11.90	12.30	12.05	12.15	12.10	1.39
2	18.95	18.68	18.71	19.16	18.88	1.19
3	20.83	20.57	22.41	20.83	21.16	3.97
4	32.23	31.45	30.70	32.76	31.78	2.84
5	42.07	42.07	42.07	42.07	42.07	0.00
6	44.13	44.25	44.27	44.13	44.20	0.16
	Sensor 2					
1	9.12	9.43	9.36	9.29	9.30	1.45
2	10.54	10.41	10.27	10.26	10.37	1.28
3	17.42	17.71	17.54	17.42	17.52	0.77
4	20.02	18.00	18.99	18.99	19.00	4.34
5	28.29	28.29	28.29	28.29	28.29	0.00
6	34.43	35.17	34.43	34.82	34.71	1.03

Table F-16: CC Damage Index Relative to the Proceeding State of Damage for Excitation Location 1

Degree Of Damage	Test 1	Test 2	Test 3	Test 4	Average	COV (%)
	Sensor 1					
1	0.9962	0.9962	0.9962	0.9962	0.9962	1.22E-06
2	0.9947	0.9947	0.9947	0.9947	0.9947	0.00E+00
3	0.9971	0.9971	0.9971	0.9971	0.9971	2.11E-06
4	0.9887	0.9887	0.9887	0.9887	0.9887	1.74E-06
5	0.9508	0.9508	0.9508	0.9508	0.9508	6.14E-06
6	0.7997	0.7997	0.7997	0.7997	0.7997	8.61E-06
	Sensor 2					
1	0.9961	0.9961	0.9961	0.9961	0.9961	0.00E+00
2	0.9976	0.9976	0.9976	0.9976	0.9976	0.00E+00
3	0.9987	0.9987	0.9987	0.9987	0.9987	0.00E+00
4	0.9978	0.9978	0.9978	0.9978	0.9978	0.00E+00
5	0.9765	0.9765	0.9765	0.9765	0.9765	0.00E+00
6	0.9940	0.9940	0.9940	0.9940	0.9940	1.22E-06

Table F-17: CC Damage Index Relative to the Proceeding State of Damage for Excitation Location 2

Degree Of Damage	Test 1	Test 2	Test 3	Test 4	Average	COV (%)
	Sensor 1					
1	0.9983	0.9983	0.9983	0.9983	0.9983	0.00E+00
2	0.9954	0.9954	0.9954	0.9954	0.9954	0.00E+00
3	0.9974	0.9974	0.9974	0.9974	0.9974	0.00E+00
4	0.9932	0.9932	0.9932	0.9932	0.9932	0.00E+00
5	0.9785	0.9785	0.9785	0.9785	0.9785	3.52E-06
6	0.8329	0.8329	0.8329	0.8329	0.8329	6.20E-06
	Sensor 2					
1	0.9979	0.9979	0.9979	0.9979	0.9979	1.22E-06
2	0.9981	0.9981	0.9981	0.9981	0.9981	0.00E+00
3	0.9952	0.9952	0.9952	0.9952	0.9952	0.00E+00
4	0.9973	0.9973	0.9973	0.9973	0.9973	0.00E+00
5	0.9978	0.9978	0.9978	0.9978	0.9978	0.00E+00
6	0.9922	0.9922	0.9922	0.9922	0.9922	1.73E-06

Table F-18: CC Damage Index Relative to the Proceeding State of Damage for Excitation Location 3

Degree Of Damage	Test 1	Test 2	Test 3	Test 4	Average	COV (%)
	Sensor 1					
1	0.9968	0.9968	0.9968	0.9968	0.9968	0.00E+00
2	0.9953	0.9953	0.9953	0.9953	0.9953	0.00E+00
3	0.9943	0.9943	0.9943	0.9943	0.9943	0.00E+00
4	0.9856	0.9856	0.9856	0.9856	0.9856	0.00E+00
5	0.9619	0.9619	0.9619	0.9619	0.9619	0.00E+00
6	0.8603	0.8603	0.8603	0.8603	0.8603	0.00E+00
	Sensor 2					
1	0.9957	0.9957	0.9957	0.9957	0.9957	0.00E+00
2	0.9986	0.9986	0.9986	0.9986	0.9986	0.00E+00
3	0.9952	0.9952	0.9952	0.9952	0.9952	0.00E+00
4	0.9959	0.9959	0.9959	0.9959	0.9959	0.00E+00
5	0.9879	0.9879	0.9879	0.9879	0.9879	0.00E+00
6	0.9858	0.9858	0.9858	0.9858	0.9858	0.00E+00

Appendix G Damage Index Results for Mechanically Fastened 1.8x0.6m Cast Iron Pipe Joint

Table G-1: RMSD Damage Index Relative to the Undamaged State for Excitation Location 1

Degree Of Damage	Test 1	Test 2	Test 3	Test 4	Average	COV (%)
	Sensor 1					
1	13.74	13.11	13.04	12.98	13.22	2.65
2	26.94	27.25	28.72	28.02	27.73	2.88
3	35.45	35.45	35.44	35.44	35.45	0.02
4	39.88	39.19	40.50	40.46	40.01	1.53
5	44.50	43.81	45.47	45.11	44.72	1.62
6	55.15	55.16	55.07	55.08	55.11	0.09
	Sensor 2					
1	15.08	14.41	14.76	13.97	14.55	3.27
2	17.94	17.86	17.77	17.44	17.75	1.23
3	25.43	25.38	26.34	26.30	25.86	2.04
4	27.39	27.36	27.53	28.35	27.66	1.68
5	27.50	28.60	28.07	28.11	28.07	1.60
6	30.90	28.74	30.13	29.02	29.70	3.37

Table G-2: RMSD Damage Index Relative to the Undamaged State for Excitation Location 2

Degree Of Damage	Test 1	Test 2	Test 3	Test 4	Average	COV (%)
	Sensor 1					
1	11.53	11.61	10.87	11.03	11.26	3.24
2	19.85	20.24	19.81	20.21	20.03	1.13
3	24.74	23.61	25.14	24.40	24.47	2.66
4	25.72	25.36	25.68	25.41	25.54	0.72
5	27.55	27.49	27.62	27.63	27.57	0.22
6	39.83	39.90	39.81	40.01	39.89	0.23
	Sensor 2					
1	15.55	16.58	15.21	14.88	15.56	4.73
2	24.60	25.00	23.61	23.21	24.11	3.46
3	24.01	24.97	23.77	24.03	24.19	2.20
4	29.19	29.68	29.28	29.22	29.34	0.78
5	36.86	37.44	35.38	35.43	36.28	2.85
6	37.35	39.47	36.85	36.34	37.50	3.67

Table G-3: RMSD Damage Index Relative to the Undamaged State for Excitation Location 3

Degree Of Damage	Test 1	Test 2	Test 3	Test 4	Average	COV (%)
	Sensor 1					
1	9.27	8.66	8.32	8.97	8.81	4.62
2	20.09	19.85	19.82	20.11	19.97	0.78
3	26.94	27.29	27.70	26.11	27.01	2.50
4	29.26	28.77	29.21	27.89	28.78	2.20
5	28.32	29.76	30.76	29.65	29.62	3.39
6	37.25	37.56	37.55	36.46	37.21	1.39
	Sensor 2					
1	12.45	13.75	12.15	13.13	12.87	5.55
2	13.55	13.57	13.68	15.95	14.19	8.30
3	20.77	23.56	20.12	20.11	21.14	7.78
4	27.67	32.62	27.58	28.34	29.05	8.26
5	30.99	34.44	31.65	31.74	32.21	4.74
6	38.71	36.13	37.05	35.97	36.97	3.40

Table G-4: RMSD Damage Index Relative to the Undamaged State for Excitation Location 4

Degree Of Damage	Test 1	Test 2	Test 3	Test 4	Average	COV (%)
	Sensor 1					
1	14.42	14.34	14.60	14.74	14.52	1.25
2	19.60	20.60	20.21	21.96	20.59	4.85
3	32.05	34.78	33.44	33.66	33.48	3.35
4	27.84	27.78	27.51	30.59	28.43	5.09
5	29.83	30.30	31.98	34.51	31.65	6.68
6	39.51	43.70	41.88	39.79	41.22	4.76
	Sensor 2					
1	10.15	10.95	10.70	10.57	10.59	3.15
2	16.38	15.52	17.91	14.17	15.99	9.80
3	17.56	20.01	20.00	16.47	18.51	9.64
4	22.07	21.66	24.30	22.57	22.65	5.12
5	24.48	25.17	27.44	28.32	26.35	6.93
6	31.01	26.69	29.60	33.87	30.29	9.87

Table G-5: RMSD Damage Index Relative to the Undamaged State for Excitation Location 5

Degree Of Damage	Test 1	Test 2	Test 3	Test 4	Average	COV (%)
	Sensor 1					
1	26.34	25.98	25.06	25.58	25.74	2.12
2	46.93	48.37	46.98	47.41	47.42	1.41
3	56.16	54.89	53.98	54.80	54.96	1.64
4	65.17	65.93	64.90	64.90	65.23	0.74
5	71.55	71.35	70.85	71.33	71.27	0.42
6	85.04	84.23	82.29	83.38	83.74	1.41
	Sensor 2					
1	14.35	14.42	14.01	14.56	14.33	1.63
2	15.72	15.00	15.75	15.11	15.39	2.55
3	16.11	17.47	16.76	17.38	16.93	3.73
4	18.66	19.75	18.20	18.64	18.81	3.51
5	23.42	22.78	22.76	23.05	23.00	1.34
6	33.22	37.38	33.92	34.61	34.78	5.23

Table G-6: MAPD Damage Index Relative to the Undamaged State for Excitation Location 1

Degree Of Damage	Test 1	Test 2	Test 3	Test 4	Average	COV (%)
	Sensor 1					
1	24.61	24.18	23.93	24.04	24.19	1.24
2	31.98	31.75	31.29	31.42	31.61	0.99
3	43.46	43.52	42.79	42.86	43.16	0.90
4	44.49	44.79	44.33	44.34	44.49	0.48
5	48.44	48.57	48.38	48.39	48.45	0.18
6	66.55	66.58	66.14	66.18	66.36	0.36
	Sensor 2					
1	17.79	17.50	17.64	17.38	17.58	1.00
2	22.06	21.92	21.78	21.22	21.75	1.70
3	28.06	27.26	27.66	27.30	27.57	1.34
4	31.28	30.40	30.16	29.95	30.45	1.91
5	36.91	36.83	36.83	36.88	36.86	0.10
6	52.58	48.22	51.14	48.88	50.20	4.02

Table G-7: MAPD Damage Index Relative to the Undamaged State for Excitation Location 2

Degree Of Damage	Test 1	Test 2	Test 3	Test 4	Average	COV (%)
	Sensor 1					
1	26.25	26.32	25.63	27.40	26.40	2.79
2	34.81	34.59	34.84	34.61	34.71	0.38
3	40.58	41.16	40.44	40.72	40.72	0.77
4	47.91	48.18	47.94	48.14	48.04	0.28
5	50.75	51.33	50.48	50.45	50.75	0.81
6	56.46	56.94	55.88	57.40	56.67	1.16
	Sensor 2					
1	26.70	28.37	26.06	25.38	26.63	4.81
2	31.44	31.93	30.04	29.36	30.69	3.90
3	32.90	34.30	32.52	32.93	33.16	2.36
4	53.61	54.33	53.76	53.67	53.84	0.62
5	83.50	84.69	80.27	80.38	82.21	2.71
6	119.95	125.15	118.62	117.25	120.24	2.87

Table G-8: MAPD Damage Index Relative to the Undamaged State for Excitation Location 3

Degree Of Damage	Test 1	Test 2	Test 3	Test 4	Average	COV (%)
	Sensor 1					
1	33.93	33.47	33.17	33.71	33.57	0.98
2	57.07	57.66	57.74	57.01	57.37	0.67
3	58.36	58.13	57.89	58.99	58.34	0.81
4	66.67	66.93	66.70	67.45	66.94	0.54
5	78.33	77.37	76.78	77.43	77.48	0.83
6	87.59	86.98	86.99	89.26	87.70	1.22
	Sensor 2					
1	18.16	19.18	17.92	18.71	18.49	3.06
2	18.29	18.40	18.65	22.14	19.37	9.56
3	25.55	27.73	25.05	25.04	25.84	4.95
4	35.19	39.19	35.12	35.72	36.30	5.36
5	49.07	51.85	49.62	49.69	50.06	2.46
6	73.01	69.96	71.07	69.77	70.95	2.10

Table G-9: MAPD Damage Index Relative to the Undamaged State for Excitation Location 4

Degree Of Damage	Test 1	Test 2	Test 3	Test 4	Average	COV (%)
	Sensor 1					
1	28.81	26.47	33.15	28.10	29.13	9.79
2	41.83	43.82	38.65	35.37	39.92	9.28
3	50.69	48.23	54.28	44.14	49.34	8.64
4	66.75	54.29	59.24	59.78	60.01	8.54
5	70.43	70.98	65.25	70.44	69.27	3.89
6	84.66	77.91	79.77	79.86	80.55	3.58
	Sensor 2					
1	22.64	27.70	23.98	25.83	25.04	8.81
2	28.80	30.01	33.71	28.53	30.26	7.88
3	36.26	36.32	37.69	34.58	36.21	3.52
4	76.67	65.65	66.04	74.05	70.60	7.93
5	79.47	75.34	83.55	83.08	80.36	4.74
6	94.51	98.81	94.44	102.91	97.67	4.14

Table G-10: MAPD Damage Index Relative to the Undamaged State for Excitation Location 5

Degree Of Damage	Test 1	Test 2	Test 3	Test 4	Average	COV (%)
	Sensor 1					
1	27.62	28.40	33.09	29.02	29.53	8.25
2	55.87	49.33	42.84	46.66	48.68	11.27
3	50.16	49.12	48.41	49.05	49.18	1.47
4	57.53	58.37	57.23	57.23	57.59	0.93
5	63.59	63.32	62.63	63.30	63.21	0.65
6	87.96	86.81	84.01	85.58	86.09	1.97
	Sensor 2					
1	22.12	21.98	22.13	21.96	22.05	0.40
2	24.15	26.73	23.68	24.43	24.75	5.48
3	26.08	27.20	26.61	27.12	26.75	1.93
4	35.80	37.03	35.12	35.77	35.93	2.23
5	46.06	45.49	45.48	45.74	45.69	0.59
6	84.21	90.79	85.36	86.47	86.71	3.31

Table G-11: CC Damage Index Relative to the Undamaged State for Excitation Location 1

Degree Of Damage	Test 1	Test 2	Test 3	Test 4	Average	COV (%)
	Sensor 1					
1	0.9888	0.9888	0.9888	0.9888	0.9888	0.0E+00
2	0.9563	0.9563	0.9563	0.9563	0.9563	0.0E+00
3	0.9166	0.9166	0.9166	0.9166	0.9166	0.0E+00
4	0.9112	0.9112	0.9112	0.9112	0.9112	0.0E+00
5	0.8970	0.8970	0.8970	0.8970	0.8970	1.4E-06
6	0.7910	0.7910	0.7910	0.7910	0.7910	0.0E+00
	Sensor 2					
1	0.9890	0.9890	0.9890	0.9890	0.9890	0.0E+00
2	0.9815	0.9815	0.9815	0.9815	0.9815	0.0E+00
3	0.9616	0.9616	0.9616	0.9616	0.9616	0.0E+00
4	0.9549	0.9549	0.9549	0.9549	0.9549	0.0E+00
5	0.9550	0.9550	0.9550	0.9550	0.9550	1.3E-06
6	0.9531	0.9531	0.9531	0.9531	0.9531	0.0E+00

Table G-12: CC Damage Index Relative to the Undamaged State for Excitation Location 2

Degree Of Damage	Test 1	Test 2	Test 3	Test 4	Average	COV (%)
	Sensor 1					
1	0.9935	0.9935	0.9935	0.9935	0.9935	0.0E+00
2	0.9813	0.9813	0.9813	0.9813	0.9813	0.0E+00
3	0.9743	0.9743	0.9743	0.9743	0.9743	0.0E+00
4	0.9704	0.9704	0.9704	0.9704	0.9704	0.0E+00
5	0.9584	0.9584	0.9584	0.9584	0.9584	0.0E+00
6	0.9104	0.9104	0.9104	0.9104	0.9104	0.0E+00
	Sensor 2					
1	0.9871	0.9871	0.9871	0.9871	0.9871	0.0E+00
2	0.9681	0.9681	0.9681	0.9681	0.9681	0.0E+00
3	0.9670	0.9670	0.9670	0.9670	0.9670	0.0E+00
4	0.9587	0.9587	0.9587	0.9587	0.9587	0.0E+00
5	0.9364	0.9364	0.9364	0.9364	0.9364	0.0E+00
6	0.9358	0.9358	0.9358	0.9358	0.9358	0.0E+00

Table G-13: CC Damage Index Relative to the Undamaged State for Excitation Location 3

Degree Of Damage	Test 1	Test 2	Test 3	Test 4	Average	COV (%)
	Sensor 1					
1	0.9962	0.9962	0.9962	0.9962	0.9962	0.0E+00
2	0.9797	0.9797	0.9797	0.9797	0.9797	0.0E+00
3	0.9701	0.9701	0.9701	0.9701	0.9701	0.0E+00
4	0.9698	0.9698	0.9698	0.9698	0.9698	0.0E+00
5	0.9736	0.9736	0.9736	0.9736	0.9736	0.0E+00
6	0.9414	0.9414	0.9414	0.9414	0.9414	0.0E+00
	Sensor 2					
1	0.9925	0.9925	0.9925	0.9925	0.9925	0.0E+00
2	0.9887	0.9887	0.9887	0.9887	0.9887	0.0E+00
3	0.9830	0.9830	0.9830	0.9830	0.9830	1.2E-06
4	0.9744	0.9744	0.9744	0.9744	0.9744	0.0E+00
5	0.9599	0.9599	0.9599	0.9599	0.9599	0.0E+00
6	0.9555	0.9555	0.9555	0.9555	0.9555	1.3E-06

Table G-14: CC Damage Index Relative to the Undamaged State for Excitation Location 4

Degree Of Damage	Test 1	Test 2	Test 3	Test 4	Average	COV (%)
	Sensor 1					
1	0.9927	0.9965	0.9930	0.9951	0.9943	1.8E-01
2	0.9792	0.9789	0.9790	0.9763	0.9783	1.4E-01
3	0.9629	0.9630	0.9653	0.9615	0.9632	1.6E-01
4	0.9600	0.9618	0.9608	0.9590	0.9604	1.2E-01
5	0.9590	0.9585	0.9589	0.9559	0.9581	1.5E-01
6	0.9257	0.9321	0.9271	0.9262	0.9278	3.2E-01
	Sensor 2					
1	0.9857	0.9959	0.9856	0.9919	0.9898	5.1E-01
2	0.9845	0.9898	0.9805	0.9777	0.9831	5.3E-01
3	0.9884	0.9882	0.9771	0.9840	0.9845	5.4E-01
4	0.9653	0.9749	0.9686	0.9697	0.9696	4.1E-01
5	0.9644	0.9634	0.9667	0.9513	0.9614	7.2E-01
6	0.9492	0.9632	0.9492	0.9503	0.9530	7.2E-01

Table G-15: CC Damage Index Relative to the Undamaged State for Excitation Location 5

Degree Of Damage	Test 1	Test 2	Test 3	Test 4	Average	COV (%)
	Sensor 1					
1	0.9666	0.9666	0.9666	0.9666	0.9666	0.0E+00
2	0.8720	0.8720	0.8720	0.8720	0.8720	0.0E+00
3	0.8217	0.8217	0.8217	0.8217	0.8217	0.0E+00
4	0.7165	0.7165	0.7165	0.7165	0.7165	1.7E-06
5	0.6343	0.6343	0.6343	0.6343	0.6343	1.4E-06
6	0.5923	0.5923	0.5923	0.5923	0.5923	0.0E+00
	Sensor 2					
1	0.9912	0.9912	0.9912	0.9912	0.9912	0.0E+00
2	0.9883	0.9883	0.9883	0.9883	0.9883	0.0E+00
3	0.9894	0.9894	0.9894	0.9894	0.9894	0.0E+00
4	0.9812	0.9812	0.9812	0.9812	0.9812	0.0E+00
5	0.9727	0.9727	0.9727	0.9727	0.9727	0.0E+00
6	0.9593	0.9593	0.9593	0.9593	0.9593	0.0E+00

Table G-16: RMSD Damage Index Relative to the Proceeding State of Damage for Excitation Location 1

Degree Of Damage	Test 1	Test 2	Test 3	Test 4	Average	COV (%)
	Sensor 1					
1	13.74	13.11	13.04	12.98	13.22	2.65
2	22.87	22.29	22.84	22.84	22.71	1.23
3	19.51	20.08	21.93	20.81	20.58	5.08
4	26.27	25.19	26.68	26.69	26.21	2.70
5	30.01	30.02	30.09	30.01	30.03	0.14
6	48.46	46.87	49.91	49.13	48.59	2.66
	Sensor 2					
1	15.08	14.41	14.76	13.97	14.55	3.27
2	6.79	6.41	6.82	6.82	6.71	2.97
3	10.76	10.75	11.07	11.76	11.08	4.30
4	16.58	16.19	17.12	17.04	16.73	2.59
5	5.10	4.93	4.86	5.00	4.97	2.05
6	23.62	22.27	24.26	21.25	22.85	5.90

Table G-17: RMSD Damage Index Relative to the Proceeding State of Damage for Excitation Location 2

Degree Of Damage	Test 1	Test 2	Test 3	Test 4	Average	COV (%)
	Sensor 1					
1	11.53	11.61	10.87	11.03	11.26	3.24
2	20.29	20.94	19.35	22.29	20.72	5.96
3	11.28	10.01	11.79	10.55	10.91	7.18
4	11.15	11.12	11.31	11.15	11.19	0.77
5	27.36	27.87	26.85	26.46	27.14	2.25
6	25.69	25.66	25.63	26.26	25.81	1.17
	Sensor 2					
1	15.55	16.58	15.21	14.88	15.56	4.73
2	10.24	10.07	10.03	10.05	10.10	0.95
3	4.74	4.85	4.85	4.11	4.64	7.66
4	9.35	8.04	10.24	9.35	9.24	9.82
5	11.62	11.64	11.13	11.14	11.38	2.51
6	10.10	10.63	10.51	10.24	10.37	2.33

Table G-18: RMSD Damage Index Relative to the Proceeding State of Damage for Excitation Location 3

Degree Of Damage	Test 1	Test 2	Test 3	Test 4	Average	COV (%)
	Sensor 1					
1	9.27	8.66	8.32	8.97	8.81	4.62
2	19.60	18.64	18.24	19.39	18.97	3.34
3	12.40	13.62	14.37	13.05	13.36	6.27
4	10.95	10.37	10.37	10.64	10.58	2.60
5	20.35	20.30	20.39	20.49	20.38	0.41
6	24.17	24.16	24.30	24.42	24.26	0.51
	Sensor 2					
1	12.45	13.75	12.15	13.13	12.87	5.55
2	9.39	9.37	9.28	10.01	9.51	3.52
3	15.76	16.20	15.05	14.91	15.48	3.90
4	9.71	10.92	10.27	10.92	10.46	5.63
5	9.44	9.63	9.29	9.39	9.44	1.50
6	10.46	10.46	10.34	9.53	10.20	4.42

Table G-19: RMSD Damage Index Relative to the Proceeding State of Damage for Excitation Location 4

Degree Of Damage	Test 1	Test 2	Test 3	Test 4	Average	COV (%)
	Sensor 1					
1	14.42	14.34	14.60	14.74	14.52	1.25
2	17.01	17.63	18.30	19.01	17.99	4.78
3	16.01	15.43	15.78	17.93	16.29	6.88
4	38.38	34.08	32.12	29.20	33.44	11.52
5	25.26	24.57	27.44	21.75	24.76	9.49
6	28.34	27.04	29.33	30.76	28.87	5.45
	Sensor 2					
1	10.15	10.95	10.70	10.57	10.59	3.15
2	12.96	11.57	10.60	12.10	11.80	8.35
3	15.47	12.75	14.18	13.04	13.86	8.94
4	34.79	29.46	29.94	34.20	32.10	8.68
5	20.49	21.34	21.96	21.86	21.41	3.14
6	19.42	19.19	23.25	20.55	20.60	9.04

Table G-20: RMSD Damage Index Relative to the Proceeding State of Damage for Excitation Location 5

Degree Of Damage	Test 1	Test 2	Test 3	Test 4	Average	COV (%)
	Sensor 1					
1	26.34	25.98	25.06	25.58	25.74	2.12
2	30.02	31.40	27.51	27.92	29.21	6.25
3	22.97	20.60	20.43	19.63	20.91	6.87
4	32.15	31.66	31.71	31.88	31.85	0.69
5	38.22	38.27	38.23	38.22	38.24	0.05
6	52.65	52.24	51.25	51.21	51.84	1.39
	Sensor 2					
1	14.35	16.42	14.01	14.56	14.83	7.29
2	14.33	13.60	13.80	11.80	13.38	8.23
3	6.21	6.10	6.73	6.71	6.44	5.11
4	9.35	9.00	9.96	9.38	9.42	4.22
5	9.39	9.01	9.44	9.13	9.24	2.22
6	14.28	16.72	16.62	16.68	16.08	7.46

Table G-21: MAPD Damage Index Relative to the Proceeding State of Damage for Excitation Location 1

Degree Of Damage	Test 1	Test 2	Test 3	Test 4	Average	COV (%)
	Sensor 1					
1	24.61	24.18	23.93	24.04	24.19	1.24
2	21.29	21.52	21.30	21.30	21.35	0.53
3	33.68	34.83	38.01	36.16	35.67	5.21
4	31.95	31.26	32.22	32.22	31.91	1.42
5	51.38	51.35	51.22	51.38	51.33	0.15
6	52.84	51.40	54.14	53.44	52.96	2.20
	Sensor 2					
1	17.79	17.50	17.64	17.38	17.58	1.00
2	16.68	17.11	16.65	16.65	16.77	1.33
3	18.85	18.85	19.63	20.51	19.46	4.06
4	17.71	17.76	19.37	20.89	18.93	8.01
5	3.43	3.94	3.59	3.43	3.60	6.64
6	44.37	39.98	41.90	39.00	41.31	5.73

Table G-22: MAPD Damage Index Relative to the Proceeding State of Damage for Excitation Location 2

Degree Of Damage	Test 1	Test 2	Test 3	Test 4	Average	COV (%)
	Sensor 1					
1	26.25	26.32	25.63	27.40	26.40	2.79
2	25.45	25.51	25.47	25.78	25.55	0.60
3	26.16	26.59	26.17	26.27	26.30	0.77
4	30.40	29.97	30.68	30.40	30.36	0.97
5	56.48	57.05	55.90	55.46	56.22	1.23
6	46.68	46.48	46.28	48.45	46.97	2.12
	Sensor 2					
1	26.70	28.37	26.06	25.38	26.63	4.81
2	17.78	17.73	17.75	17.81	17.77	0.19
3	10.11	9.96	9.96	10.44	10.12	2.21
4	20.12	18.93	20.91	20.12	20.02	4.08
5	25.21	25.25	23.55	23.65	24.41	3.85
6	21.48	22.14	22.02	21.70	21.83	1.38

Table G-23: MAPD Damage Index Relative to the Proceeding State of Damage for Excitation Location 3

Degree Of Damage	Test 1	Test 2	Test 3	Test 4	Average	COV (%)
	Sensor 1					
1	33.93	33.47	33.17	33.71	33.57	0.98
2	55.28	56.71	57.47	55.57	56.26	1.80
3	28.96	29.34	29.58	28.61	29.12	1.46
4	45.14	45.59	45.59	45.35	45.42	0.48
5	56.06	54.66	54.35	54.12	54.80	1.59
6	73.66	75.49	77.35	78.25	76.19	2.67
	Sensor 2					
1	18.16	19.18	17.92	18.71	18.49	3.06
2	13.17	13.57	12.88	13.89	13.38	3.31
3	13.29	15.47	13.02	14.41	14.05	7.98
4	25.03	25.98	25.45	25.98	25.61	1.78
5	27.71	27.69	27.80	27.73	27.73	0.17
6	34.63	28.86	32.26	31.18	31.73	7.56

Table G-24: MAPD Damage Index Relative to the Proceeding State of Damage for Excitation Location 4

Degree Of Damage	Test 1	Test 2	Test 3	Test 4	Average	COV (%)
	Sensor 1					
1	28.81	26.47	33.15	28.10	29.13	9.79
2	43.21	47.42	48.36	48.94	46.98	5.52
3	35.27	29.20	27.72	34.51	31.68	11.92
4	38.53	35.57	34.09	44.68	38.21	12.26
5	41.27	39.09	42.09	46.44	42.22	7.30
6	53.85	54.24	61.88	50.25	55.06	8.88
	Sensor 2					
1	22.64	27.70	23.98	25.83	25.04	8.81
2	17.00	13.95	14.53	17.56	15.76	11.33
3	17.23	17.92	16.66	13.56	16.34	11.78
4	48.36	48.02	54.06	47.70	49.54	6.12
5	34.75	30.15	30.39	35.86	32.79	8.98
6	40.14	37.44	32.86	31.85	35.57	10.96

Table G-25: MAPD Damage Index Relative to the Proceeding State of Damage for Excitation Location 5

Degree Of Damage	Test 1	Test 2	Test 3	Test 4	Average	COV (%)
	Sensor 1					
1	27.62	28.40	33.09	29.02	29.53	8.25
2	39.79	39.45	35.50	36.42	37.79	5.69
3	28.81	27.57	28.90	27.28	28.14	2.97
4	35.76	36.68	36.45	36.05	36.24	1.13
5	43.00	42.32	42.52	43.00	42.71	0.81
6	68.79	68.24	66.90	66.84	67.69	1.45
	Sensor 2					
1	22.12	21.98	22.13	21.96	22.05	0.40
2	27.49	26.75	26.95	24.92	26.53	4.19
3	17.34	17.61	16.97	16.98	17.22	1.79
4	24.07	24.06	24.27	24.18	24.14	0.41
5	34.78	34.62	34.79	34.70	34.72	0.23
6	62.77	72.05	66.31	66.38	66.88	5.74

Table G-26: CC Damage Index Relative to the Proceeding State of Damage for Excitation Location 1

Degree Of Damage	Test 1	Test 2	Test 3	Test 4	Average	COV (%)
	Sensor 1					
1	0.9888	0.9888	0.9888	0.9888	0.9888	0.0E+00
2	0.9759	0.9759	0.9759	0.9759	0.9759	0.0E+00
3	0.9776	0.9776	0.9776	0.9776	0.9776	0.0E+00
4	0.9713	0.9713	0.9713	0.9713	0.9713	0.0E+00
5	0.9425	0.9425	0.9425	0.9425	0.9425	0.0E+00
6	0.9102	0.9102	0.9102	0.9102	0.9102	0.0E+00
	Sensor 2					
1	0.9890	0.9890	0.9890	0.9890	0.9890	0.0E+00
2	0.9973	0.9973	0.9973	0.9973	0.9973	0.0E+00
3	0.9928	0.9928	0.9928	0.9928	0.9928	0.0E+00
4	0.9970	0.9970	0.9970	0.9970	0.9970	0.0E+00
5	0.9995	0.9995	0.9995	0.9995	0.9995	0.0E+00
6	0.9936	0.9936	0.9936	0.9936	0.9936	0.0E+00

Table G-27: CC Damage Index Relative to the Proceeding State of Damage for Excitation Location 2

Degree Of Damage	Test 1	Test 2	Test 3	Test 4	Average	COV (%)
	Sensor 1					
1	0.9935	0.9935	0.9935	0.9935	0.9935	0.0E+00
2	0.9843	0.9843	0.9843	0.9843	0.9843	0.0E+00
3	0.9942	0.9942	0.9942	0.9942	0.9942	0.0E+00
4	0.9928	0.9928	0.9928	0.9928	0.9928	0.0E+00
5	0.9683	0.9683	0.9683	0.9683	0.9683	0.0E+00
6	0.9639	0.9639	0.9639	0.9639	0.9639	0.0E+00
	Sensor 2					
1	0.9871	0.9871	0.9871	0.9871	0.9871	0.0E+00
2	0.9935	0.9935	0.9935	0.9935	0.9935	0.0E+00
3	0.9987	0.9987	0.9987	0.9987	0.9987	0.0E+00
4	0.9969	0.9969	0.9969	0.9969	0.9969	0.0E+00
5	0.9921	0.9921	0.9921	0.9921	0.9921	0.0E+00
6	0.9935	0.9935	0.9935	0.9935	0.9935	0.0E+00

Table G-28: CC Damage Index Relative to the Proceeding State of Damage for Excitation Location 3

Degree Of Damage	Test 1	Test 2	Test 3	Test 4	Average	COV (%)
	Sensor 1					
1	0.9962	0.9962	0.9962	0.9962	0.9962	0.0E+00
2	0.9845	0.9845	0.9845	0.9845	0.9845	0.0E+00
3	0.9956	0.9956	0.9956	0.9956	0.9956	0.0E+00
4	0.9942	0.9942	0.9942	0.9942	0.9942	0.0E+00
5	0.9779	0.9779	0.9779	0.9779	0.9779	0.0E+00
6	0.9684	0.9684	0.9684	0.9684	0.9684	0.0E+00
	Sensor 2					
1	0.9925	0.9925	0.9925	0.9925	0.9925	0.0E+00
2	0.9962	0.9962	0.9962	0.9962	0.9962	0.0E+00
3	0.9981	0.9981	0.9981	0.9981	0.9981	0.0E+00
4	0.9956	0.9956	0.9956	0.9956	0.9956	0.0E+00
5	0.9945	0.9945	0.9945	0.9945	0.9945	0.0E+00
6	0.9954	0.9954	0.9954	0.9954	0.9954	0.0E+00

Table G-29: CC Damage Index Relative to the Proceeding State of Damage for Excitation Location 4

Degree Of Damage	Test 1	Test 2	Test 3	Test 4	Average	COV (%)
	Sensor 1					
1	0.9927	0.9965	0.9930	0.9951	0.9943	1.8E-01
2	0.9810	0.9848	0.9824	0.9843	0.9831	1.8E-01
3	0.9926	0.9934	0.9943	0.9931	0.9934	7.2E-02
4	0.9852	0.9900	0.9919	0.9903	0.9893	2.9E-01
5	0.9811	0.9793	0.9808	0.9767	0.9795	2.1E-01
6	0.9704	0.9751	0.9693	0.9755	0.9726	3.3E-01
	Sensor 2					
1	0.9857	0.9959	0.9856	0.9919	0.9898	5.1E-01
2	0.9971	0.9971	0.9973	0.9945	0.9965	1.3E-01
3	0.9965	0.9984	0.9986	0.9967	0.9976	1.1E-01
4	0.9841	0.9913	0.9964	0.9933	0.9912	5.3E-01
5	0.9971	0.9948	0.9972	0.9935	0.9956	1.8E-01
6	0.9939	0.9962	0.9937	0.9962	0.9950	1.4E-01

Table G-30: CC Damage Index Relative to the Proceeding State of Damage for Excitation Location 5

Degree Of Damage	Test 1	Test 2	Test 3	Test 4	Average	COV (%)
	Sensor 1					
1	0.9673	0.9673	0.9673	0.9673	0.9673	0.0E+00
2	0.9537	0.9537	0.9537	0.9537	0.9537	0.0E+00
3	0.9743	0.9743	0.9743	0.9743	0.9743	0.0E+00
4	0.9318	0.9318	0.9318	0.9318	0.9318	0.0E+00
5	0.8988	0.8988	0.8988	0.8988	0.8988	0.0E+00
6	0.8813	0.8813	0.8813	0.8813	0.8813	0.0E+00
	Sensor 2					
1	0.9883	0.9883	0.9883	0.9883	0.9883	0.0E+00
2	0.9983	0.9983	0.9983	0.9983	0.9983	0.0E+00
3	0.9975	0.9975	0.9975	0.9975	0.9975	0.0E+00
4	0.9964	0.9964	0.9964	0.9964	0.9964	0.0E+00
5	0.9951	0.9951	0.9951	0.9951	0.9951	0.0E+00
6	0.9940	0.9940	0.9940	0.9940	0.9940	0.0E+00

Appendix H Damage Index Results for 1.2x1.2 m Mechanically Fastened PVC Pipe Joint

Table H-1: RMSD Damage Index Relative to the Undamaged State for Excitation Location 1

Degree Of Damage	Test 1	Test 2	Test 3	Test 4	Average	COV (%)
	Sensor 1					
1	7.07	7.90	7.45	7.45	7.47	4.54
2	9.02	9.49	9.29	9.28	9.27	2.07
3	12.89	13.06	12.84	12.77	12.89	0.98
4	20.68	21.75	22.62	22.49	21.89	4.07
5	30.76	30.76	30.31	30.37	30.55	0.79
6	36.32	36.30	36.06	35.88	36.14	0.58
	Sensor 2					
1	7.25	7.84	7.28	7.85	7.55	4.44
2	8.07	8.63	7.59	8.07	8.09	5.29
3	8.73	9.13	8.71	8.55	8.78	2.84
4	9.54	9.62	9.44	9.26	9.47	1.63
5	10.59	10.22	9.29	10.88	10.24	6.75
6	10.44	10.80	10.51	11.00	10.69	2.46

Table H-2: RMSD Damage Index Relative to the Undamaged State for Excitation Location 2

Degree Of Damage	Test 1	Test 2	Test 3	Test 4	Average	COV (%)
	Sensor 1					
1	4.53	4.20	4.34	4.16	4.31	3.87
2	7.32	7.60	7.71	7.47	7.53	2.21
3	12.24	12.54	13.40	13.44	12.91	4.69
4	24.82	26.99	25.23	29.26	26.57	7.60
5	31.38	31.67	32.75	32.72	32.13	2.21
6	39.96	36.84	37.78	38.44	38.26	3.43
	Sensor 2					
1	3.79	3.59	3.59	3.95	3.73	4.71
2	4.79	5.32	4.98	4.63	4.93	6.00
3	5.81	5.62	4.82	5.14	5.35	8.45
4	7.87	7.60	7.53	8.30	7.83	4.48
5	8.57	8.35	8.55	8.38	8.46	1.34
6	9.36	8.98	8.74	9.58	9.17	4.14

Table H-3: RMSD Damage Index Relative to the Undamaged State for Excitation Location 3

Degree Of Damage	Test 1	Test 2	Test 3	Test 4	Average	COV (%)
	Sensor 1					
1	8.34	7.92	9.15	8.99	8.60	6.64
2	11.77	11.46	12.38	12.26	11.97	3.57
3	23.36	24.98	25.71	25.57	24.91	4.32
4	49.76	48.98	48.94	48.77	49.11	0.89
5	53.90	53.18	53.14	52.98	53.30	0.77
6	58.75	60.42	58.27	62.12	59.89	2.92
	Sensor 2					
1	4.69	4.10	4.54	4.58	4.48	5.83
2	5.24	5.03	5.18	5.20	5.16	1.74
3	8.59	9.39	9.38	9.99	9.34	6.15
4	12.77	13.22	12.38	11.64	12.50	5.37
5	13.60	14.43	13.60	12.87	13.62	4.71
6	15.98	16.15	15.81	16.99	16.23	3.22

Table H-4: MAPD Damage Index Relative to the Undamaged State for Excitation Location 1

Degree Of Damage	Test 1	Test 2	Test 3	Test 4	Average	COV (%)
	Sensor 1					
1	14.99	15.50	12.91	12.91	14.07	9.69
2	20.48	21.80	20.32	22.81	21.35	5.52
3	26.44	26.46	27.62	27.61	27.03	2.49
4	34.99	35.86	39.93	38.90	37.42	6.33
5	41.26	41.31	43.60	43.12	42.32	2.87
6	59.23	59.11	64.01	62.97	61.33	4.13
	Sensor 2					
1	9.80	10.13	9.32	9.20	9.61	4.52
2	9.44	11.16	9.88	9.81	10.07	7.46
3	10.90	11.29	10.20	10.63	10.75	4.28
4	13.35	11.07	9.74	10.04	11.05	14.81
5	11.26	11.00	11.87	10.96	11.27	3.74
6	12.32	12.52	11.70	11.94	12.12	3.06

Table H-5: MAPD Damage Index Relative to the Undamaged State for Excitation Location 2

Degree Of Damage	Test 1	Test 2	Test 3	Test 4	Average	COV (%)
	Sensor 1					
1	9.50	9.72	9.71	8.64	9.39	5.45
2	25.04	24.65	23.92	21.43	23.76	6.83
3	39.28	40.40	34.73	38.73	38.29	6.44
4	65.66	74.89	66.18	75.35	70.52	7.54
5	72.75	70.93	73.13	72.80	72.40	1.38
6	93.68	80.70	76.94	81.02	83.08	8.79
	Sensor 2					
1	7.46	6.10	6.26	6.95	6.69	9.47
2	6.96	8.18	7.13	6.85	7.28	8.41
3	7.99	7.40	8.63	7.17	7.80	8.38
4	9.95	9.66	10.33	9.82	9.94	2.91
5	11.71	10.36	13.55	12.15	11.94	11.01
6	12.69	11.90	11.98	14.50	12.77	9.44

Table H-6: MAPD Damage Index Relative to the Undamaged State for Excitation Location 3

Degree Of Damage	Test 1	Test 2	Test 3	Test 4	Average	COV (%)
	Sensor 1					
1	15.16	14.90	15.69	15.58	15.33	2.39
2	22.03	21.89	22.33	22.27	22.13	0.94
3	37.10	39.09	39.74	39.62	38.89	3.16
4	55.54	54.87	54.83	54.68	54.98	0.69
5	57.45	56.89	56.86	56.74	56.98	0.55
6	100.11	98.24	104.15	95.27	99.44	3.74
	Sensor 2					
1	4.95	4.55	4.85	4.88	4.81	3.64
2	7.79	7.60	7.74	7.75	7.72	1.05
3	10.86	12.68	12.66	13.08	12.32	8.07
4	14.95	15.25	14.69	14.20	14.77	3.00
5	16.00	16.48	16.00	15.56	16.01	2.35
6	15.88	15.80	16.36	17.57	16.40	4.99

Table H-7: CC Damage Index Relative to the Undamaged State for Excitation Location 1

Degree Of Damage	Test 1	Test 2	Test 3	Test 4	Average	COV (%)
	Sensor 1					
1	0.9974	0.9974	0.9965	0.9965	0.9970	0.049
2	0.9955	0.9942	0.9962	0.9947	0.9952	0.088
3	0.9891	0.9891	0.9898	0.9898	0.9895	0.040
4	0.9699	0.9663	0.9637	0.9641	0.9660	0.294
5	0.9332	0.9332	0.9354	0.9354	0.9343	0.134
6	0.9070	0.9070	0.9091	0.9091	0.9080	0.131
	Sensor 2					
1	0.9979	0.9967	0.9972	0.9988	0.9976	0.093
2	0.9973	0.9973	0.9973	0.9973	0.9973	0.002
3	0.9933	0.9959	0.9959	0.9962	0.9953	0.134
4	0.9948	0.9948	0.9954	0.9954	0.9951	0.034
5	0.9952	0.9952	0.9946	0.9946	0.9949	0.033
6	0.9944	0.9944	0.9940	0.9940	0.9942	0.024

Table H-8: CC Damage Index Relative to the Undamaged State for Excitation Location 2

Degree Of Damage	Test 1	Test 2	Test 3	Test 4	Average	COV (%)
	Sensor 1					
1	0.9976	0.9980	0.9985	0.9985	0.9981	0.046
2	0.9963	0.9958	0.9955	0.9968	0.9961	0.056
3	0.9888	0.9883	0.9890	0.9874	0.9883	0.074
4	0.9590	0.9498	0.9553	0.9442	0.9521	0.680
5	0.9362	0.9309	0.9291	0.9308	0.9318	0.332
6	0.8919	0.9077	0.9069	0.9038	0.9026	0.808
	Sensor 2					
1	0.9981	0.9980	0.9987	0.9987	0.9984	0.038
2	0.9981	0.9983	0.9977	0.9984	0.9981	0.030
3	0.9959	0.9970	0.9976	0.9976	0.9970	0.083
4	0.9935	0.9949	0.9947	0.9925	0.9939	0.116
5	0.9922	0.9938	0.9920	0.9933	0.9928	0.087
6	0.9911	0.9923	0.9924	0.9903	0.9915	0.099

Table H-9: CC Damage Index Relative to the Undamaged State for Excitation Location 3

Degree Of Damage	Test 1	Test 2	Test 3	Test 4	Average	COV (%)
	Sensor 1					
1	0.9969	0.9969	0.9969	0.9969	0.9969	0.000
2	0.9926	0.9926	0.9926	0.9926	0.9926	0.000
3	0.9761	0.9731	0.9731	0.9731	0.9738	0.156
4	0.9233	0.9233	0.9233	0.9233	0.9233	0.000
5	0.8979	0.8979	0.8979	0.8979	0.8979	0.000
6	0.8746	0.8772	0.8817	0.8669	0.8751	0.709
	Sensor 2					
1	0.9987	0.9987	0.9987	0.9987	0.9987	0.000
2	0.9970	0.9970	0.9970	0.9970	0.9970	0.000
3	0.9956	0.9934	0.9934	0.9934	0.9939	0.114
4	0.9926	0.9926	0.9926	0.9926	0.9926	0.000
5	0.9916	0.9927	0.9929	0.9904	0.9919	0.118
6	0.9909	0.9909	0.9909	0.9909	0.9909	0.000

Table H-10: RMSD Damage Index Relative to the Proceeding State of Damage for Excitation Location 1

Degree Of Damage	Test 1	Test 2	Test 3	Test 4	Average	COV (%)
	Sensor 1					
1	7.07	7.90	7.45	7.45	7.47	4.54
2	9.29	8.35	7.64	8.24	8.38	8.16
3	7.97	7.29	8.27	7.25	7.70	6.58
4	13.73	13.51	14.13	14.28	13.91	2.55
5	12.53	12.24	11.31	11.78	11.97	4.47
6	11.21	11.11	11.15	11.15	11.15	0.35
	Sensor 2					
1	7.25	7.84	7.28	7.85	7.55	4.44
2	12.24	14.53	12.90	12.80	13.12	7.53
3	3.70	4.31	4.09	4.25	4.09	6.71
4	3.45	3.47	3.61	3.17	3.43	5.34
5	3.46	3.43	3.32	3.69	3.47	4.43
6	3.12	3.05	3.31	3.05	3.13	3.99

Table H-11: RMSD Damage Index Relative to the Proceeding State of Damage for Excitation Location 2

Degree Of Damage	Test 1	Test 2	Test 3	Test 4	Average	COV (%)
	Sensor 1					
1	4.53	4.20	4.34	4.16	4.31	3.87
2	7.22	8.16	8.44	8.84	8.17	8.44
3	11.01	10.83	10.97	11.23	11.01	1.52
4	15.60	17.26	17.47	17.95	17.07	5.97
5	17.38	15.95	14.06	16.43	15.96	8.76
6	16.98	14.00	14.00	15.66	15.16	9.54
	Sensor 2					
1	3.79	3.59	3.59	3.95	3.73	4.71
2	6.83	6.92	7.08	6.58	6.85	3.04
3	5.40	5.49	6.29	6.15	5.83	7.77
4	6.57	6.96	7.14	6.33	6.75	5.42
5	4.45	4.45	4.33	4.87	4.52	5.27
6	5.39	4.15	4.92	4.57	4.76	11.05

Table H-12: RMSD Damage Index Relative to the Proceeding State of Damage for Excitation Location 3

Degree Of Damage	Test 1	Test 2	Test 3	Test 4	Average	COV (%)
	Sensor 1					
1	8.34	7.92	9.15	8.99	8.60	6.64
2	5.92	5.92	5.92	5.92	5.92	0.00
3	11.73	13.53	13.20	13.20	12.92	6.22
4	24.94	22.95	22.14	22.14	23.04	5.73
5	10.82	10.82	10.82	10.82	10.82	0.00
6	15.37	15.08	16.40	15.21	15.51	3.88
	Sensor 2					
1	4.69	4.10	4.54	4.58	4.48	5.83
2	4.49	4.49	4.49	4.49	4.49	0.00
3	4.59	5.03	4.72	5.39	4.94	7.24
4	5.10	5.53	5.75	5.55	5.48	5.00
5	3.39	3.45	3.45	3.45	3.43	0.81
6	6.00	7.08	7.11	6.73	6.73	7.64

Table H-13: MAPD Damage Index Relative to the Proceeding State of Damage for Excitation Location 1

Degree Of Damage	Test 1	Test 2	Test 3	Test 4	Average	COV (%)
	Sensor 1					
1	14.99	15.50	12.91	12.91	14.07	9.69
2	25.01	26.98	24.63	20.72	24.33	10.78
3	15.04	14.72	16.07	14.74	15.14	4.20
4	38.28	36.09	34.40	34.46	35.81	5.10
5	23.32	20.66	20.24	21.40	21.41	6.37
6	45.19	44.90	45.04	45.04	45.04	0.26
	Sensor 2					
1	9.80	10.13	9.32	9.20	9.61	4.52
2	16.01	15.12	14.18	16.03	15.34	5.73
3	5.46	4.50	5.78	4.49	5.06	13.08
4	5.89	6.40	5.48	5.23	5.75	8.90
5	5.83	6.27	5.34	5.73	5.79	6.59
6	5.36	5.29	5.48	5.30	5.36	1.70

Table H-14: MAPD Damage Index Relative to the Proceeding State of Damage for Excitation Location 2

Degree Of Damage	Test 1	Test 2	Test 3	Test 4	Average	COV (%)
	Sensor 1					
1	9.50	9.72	9.71	8.64	9.39	5.45
2	23.88	26.22	23.15	27.16	25.10	7.56
3	16.58	16.54	16.64	15.81	16.39	2.39
4	28.02	32.42	28.30	32.49	30.31	8.20
5	31.82	30.85	25.91	29.00	29.40	8.85
6	56.27	54.07	50.34	53.43	53.53	4.58
	Sensor 2					
1	7.46	8.10	7.26	6.95	7.44	6.51
2	8.87	8.24	8.89	7.05	8.26	10.42
3	9.40	7.83	9.16	7.72	8.53	10.25
4	10.00	11.65	10.33	11.87	10.96	8.55
5	8.26	8.36	8.11	8.59	8.33	2.44
6	8.83	7.03	8.82	7.67	8.09	10.97

Table H-15: MAPD Damage Index Relative to the Proceeding State of Damage for Excitation Location 3

Degree Of Damage	Test 1	Test 2	Test 3	Test 4	Average	COV (%)
	Sensor 1					
1	15.16	14.90	15.69	15.58	15.33	2.39
2	13.70	13.70	13.70	13.70	13.70	0.00
3	23.20	23.84	23.54	23.54	23.53	1.10
4	25.44	24.69	24.18	24.18	24.62	2.42
5	21.63	21.63	21.63	21.63	21.63	0.00
6	48.21	46.32	53.90	44.18	48.15	8.66
	Sensor 2					
1	4.95	4.55	4.85	4.88	4.81	3.64
2	6.42	6.42	6.43	6.42	6.42	0.01
3	5.52	5.91	5.74	6.13	5.82	4.43
4	5.73	6.50	5.91	5.21	5.84	9.14
5	5.26	5.34	5.34	5.34	5.32	0.81
6	6.83	8.44	7.26	6.96	7.37	9.94

Table H-16: CC Damage Index Relative to the Proceeding State of Damage for Excitation Location 1

Degree Of Damage	Test 1	Test 2	Test 3	Test 4	Average	COV (%)
	Sensor 1					
1	0.9974	0.9974	0.9965	0.9965	0.9970	0.049
2	0.9937	0.9915	0.9951	0.9971	0.9944	0.239
3	0.9966	0.9972	0.9947	0.9972	0.9964	0.117
4	0.9892	0.9881	0.9866	0.9866	0.9876	0.130
5	0.9860	0.9891	0.9903	0.9907	0.9890	0.216
6	0.9906	0.9906	0.9906	0.9906	0.9906	0.000
	Sensor 2					
1	0.9948	0.9948	0.9954	0.9954	0.9951	0.034
2	0.9945	0.9894	0.9914	0.9977	0.9932	0.369
3	0.9987	0.9980	0.9974	0.9980	0.9980	0.051
4	0.9950	0.9977	0.9983	0.9979	0.9972	0.152
5	0.9953	0.9978	0.9980	0.9977	0.9972	0.128
6	0.9980	0.9980	0.9980	0.9980	0.9980	0.000

Table H-17: CC Damage Index Relative to the Proceeding State of Damage for Excitation Location 2

Degree Of Damage	Test 1	Test 2	Test 3	Test 4	Average	COV (%)
	Sensor 1					
1	0.9976	0.9980	0.9985	0.9985	0.9981	0.046
2	0.9964	0.9956	0.9967	0.9979	0.9967	0.095
3	0.9953	0.9954	0.9958	0.9947	0.9953	0.049
4	0.9852	0.9791	0.9827	0.9778	0.9812	0.344
5	0.9910	0.9895	0.9903	0.9903	0.9902	0.063
6	0.9798	0.9868	0.9865	0.9866	0.9849	0.344
	Sensor 2					
1	0.9981	0.9980	0.9987	0.9987	0.9984	0.038
2	0.9979	0.9975	0.9980	0.9985	0.9980	0.040
3	0.9974	0.9978	0.9975	0.9985	0.9978	0.052
4	0.9979	0.9953	0.9962	0.9956	0.9963	0.115
5	0.9983	0.9978	0.9978	0.9975	0.9979	0.035
6	0.9912	0.9974	0.9969	0.9975	0.9958	0.305

Table H-18: CC Damage Index Relative to the Proceeding State of Damage for Excitation Location 3

Degree Of Damage	Test 1	Test 2	Test 3	Test 4	Average	COV (%)
	Sensor 1					
1	0.9969	0.9969	0.9969	0.9969	0.9969	0.000
2	0.9966	0.9966	0.9966	0.9966	0.9966	0.000
3	0.9928	0.9913	0.9913	0.9913	0.9916	0.076
4	0.9789	0.9808	0.9808	0.9808	0.9803	0.098
5	0.9914	0.9914	0.9914	0.9914	0.9914	0.000
6	0.9840	0.9860	0.9829	0.9857	0.9846	0.148
	Sensor 2					
1	0.9987	0.9987	0.9987	0.9987	0.9987	0.000
2	0.9977	0.9977	0.9977	0.9977	0.9977	0.000
3	0.9984	0.9977	0.9977	0.9977	0.9978	0.036
4	0.9976	0.9975	0.9975	0.9975	0.9975	0.007
5	0.9980	0.9980	0.9980	0.9980	0.9980	0.000
6	0.9968	0.9955	0.9933	0.9972	0.9957	0.179

Appendix I Damage Index Results for Mechanically Fastened 1.8x0.6m PVC Pipe Joint

Table I-1: RMSD Damage Index Relative to the Undamaged State for Excitation Location 1

Degree Of Damage	Test 1	Test 2	Test 3	Test 4	Average	COV (%)
	Sensor 1					
1	2.06	2.44	2.54	2.43	2.37	8.85
2	6.28	5.92	6.54	5.60	6.09	6.74
3	8.72	8.93	8.77	9.59	9.00	4.44
4	10.11	10.24	9.33	9.77	9.86	4.14
5	13.73	13.19	12.43	12.49	12.96	4.78
6	19.79	19.36	18.36	17.67	18.79	5.11
	Sensor 2					
1	2.98	2.69	2.48	2.41	2.64	9.71
2	4.80	4.29	4.28	4.69	4.51	5.94
3	5.42	6.04	5.28	5.69	5.61	5.96
4	5.60	6.58	5.61	5.76	5.89	7.96
5	6.86	6.50	6.45	6.17	6.50	4.35
6	7.50	6.92	7.03	7.47	7.23	4.12

Table I-2: RMSD Damage Index Relative to the Undamaged State for Excitation Location 2

Degree Of Damage	Test 1	Test 2	Test 3	Test 4	Average	COV (%)
	Sensor 1					
1	2.59	2.30	2.31	2.60	2.45	6.91
2	4.58	4.80	4.67	4.33	4.59	4.30
3	7.52	7.39	7.47	7.52	7.48	0.81
4	10.21	8.97	8.85	8.86	9.22	7.15
5	14.93	14.49	14.09	13.63	14.28	3.90
6	21.82	20.36	19.13	18.74	20.01	6.92
	Sensor 2					
1	2.30	2.24	2.20	2.63	2.34	8.35
2	4.49	4.31	4.36	3.74	4.23	7.84
3	5.20	4.41	4.95	4.21	4.69	9.75
4	5.39	5.35	5.08	5.40	5.31	2.89
5	6.19	5.97	5.86	5.90	5.98	2.44
6	8.22	7.55	6.57	7.84	7.55	9.39

Table I-3: RMSD Damage Index Relative to the Undamaged State for Excitation Location 3

Degree Of Damage	Test 1	Test 2	Test 3	Test 4	Average	COV (%)
	Sensor 1					
1	2.11	2.51	2.47	2.27	2.34	7.88
2	3.73	3.71	3.74	4.20	3.85	6.15
3	7.87	7.13	8.14	8.38	7.88	6.89
4	10.64	11.26	10.26	12.40	11.14	8.41
5	15.80	14.83	15.61	16.70	15.73	4.90
6	21.80	22.56	22.18	23.45	22.50	3.13
	Sensor 2					
1	2.07	2.37	2.28	2.05	2.20	7.13
2	3.97	3.47	3.31	3.26	3.50	9.30
3	4.37	4.07	4.07	4.86	4.34	8.56
4	5.36	4.92	5.98	5.54	5.45	8.09
5	6.18	5.68	6.87	6.87	6.40	9.08
6	6.83	7.64	6.72	7.74	7.23	7.38

Table I-4: RMSD Damage Index Relative to the Undamaged State for Excitation Location 4

Degree Of Damage	Test 1	Test 2	Test 3	Test 4	Average	COV (%)
	Sensor 1					
1	3.61	3.60	3.22	3.04	3.37	8.51
2	4.93	5.95	5.09	5.73	5.42	9.05
3	10.28	9.51	8.97	9.12	9.47	6.20
4	12.99	12.35	14.00	13.17	13.13	5.20
5	22.35	20.96	19.20	20.36	20.72	6.32
6	27.20	29.08	27.15	26.86	27.57	3.68
	Sensor 2					
1	2.20	2.47	2.49	2.05	2.30	9.39
2	3.69	4.00	4.47	4.42	4.14	8.95
3	5.68	5.45	6.39	6.63	6.04	9.29
4	6.64	7.72	7.96	7.20	7.38	7.92
5	7.73	8.62	8.65	8.47	8.37	5.18
6	10.28	9.26	10.91	10.48	10.23	6.86

Table I-5: RMSD Damage Index Relative to the Undamaged State for Excitation Location 5

Degree Of Damage	Test 1	Test 2	Test 3	Test 4	Average	COV (%)
	Sensor 1					
1	2.17	2.16	2.21	2.05	2.15	3.24
2	5.48	5.28	5.56	5.70	5.51	3.13
3	8.81	7.38	8.75	8.93	8.47	8.58
4	8.76	9.41	9.24	10.86	9.57	9.46
5	11.39	10.70	11.06	11.03	11.04	2.53
6	17.43	18.71	16.68	17.27	17.52	4.87
	Sensor 2					
1	2.22	2.48	2.36	2.21	2.32	5.48
2	3.78	3.83	3.48	3.14	3.55	8.94
3	4.65	4.18	4.59	4.26	4.42	5.27
4	5.25	5.79	5.51	6.45	5.75	8.94
5	6.22	6.48	6.32	7.35	6.59	7.84
6	7.40	7.40	7.31	7.71	7.45	2.38

Table I-6: MAPD Damage Index Relative to the Undamaged State for Excitation Location 1

Degree Of Damage	Test 1	Test 2	Test 3	Test 4	Average	COV (%)
	Sensor 1					
1	7.83	7.26	6.45	7.75	7.32	8.69
2	25.11	26.86	25.01	23.36	25.09	5.71
3	31.86	31.43	28.03	29.57	30.22	5.85
4	38.23	37.69	35.18	36.09	36.80	3.83
5	43.76	41.56	40.33	40.03	41.42	4.09
6	74.05	65.66	59.81	62.22	65.43	9.51
	Sensor 2					
1	4.04	3.60	3.19	3.55	3.60	9.63
2	5.05	4.80	5.36	4.77	5.00	5.44
3	5.99	7.36	6.81	7.46	6.90	9.76
4	7.55	7.90	6.57	6.95	7.24	8.24
5	8.38	7.81	8.03	8.05	8.07	2.90
6	9.82	9.27	10.34	10.23	9.92	4.86

Table I-7: MAPD Damage Index Relative to the Undamaged State for Excitation Location 2

Degree Of Damage	Test 1	Test 2	Test 3	Test 4	Average	COV (%)
	Sensor 1					
1	11.06	12.08	13.51	11.06	11.93	9.73
2	21.35	23.88	25.92	22.45	23.40	8.44
3	31.04	33.81	37.93	32.05	33.70	9.02
4	36.83	37.77	44.62	38.34	39.39	8.99
5	45.88	48.44	51.02	46.10	47.86	5.02
6	77.01	79.75	83.51	81.02	80.32	3.37
	Sensor 2					
1	3.70	4.43	4.46	4.24	4.21	8.37
2	6.29	6.82	5.34	5.49	5.98	11.61
3	6.70	7.12	6.65	6.56	6.76	3.71
4	7.85	8.95	8.01	7.87	8.17	6.42
5	9.06	10.59	9.94	8.99	9.65	7.92
6	11.93	13.29	11.61	11.96	12.20	6.09

Table I-8: MAPD Damage Index Relative to the Undamaged State for Excitation Location 3

Degree Of Damage	Test 1	Test 2	Test 3	Test 4	Average	COV (%)
	Sensor 1					
1	7.93	8.10	7.30	9.29	8.15	10.18
2	15.84	16.43	15.57	18.31	16.54	7.47
3	23.33	23.97	22.09	25.34	23.68	5.72
4	30.35	34.02	29.70	32.48	31.64	6.27
5	38.40	39.95	38.43	43.31	40.02	5.77
6	57.84	64.19	59.82	65.03	61.72	5.59
	Sensor 2					
1	3.93	3.24	3.66	3.92	3.69	8.76
2	6.26	5.16	5.94	5.68	5.76	8.11
3	7.87	7.70	7.50	7.74	7.70	2.01
4	8.96	8.73	8.34	9.37	8.85	4.85
5	9.28	9.48	10.47	10.94	10.04	7.87
6	11.89	11.17	11.28	12.58	11.73	5.53

Table I-9: MAPD Damage Index Relative to the Undamaged State for Excitation Location 4

Degree Of Damage	Test 1	Test 2	Test 3	Test 4	Average	COV (%)
	Sensor 1					
1	10.89	9.60	9.26	9.07	9.71	8.45
2	17.28	21.92	18.32	18.93	19.11	10.41
3	21.88	24.37	22.29	22.14	22.67	5.04
4	28.20	31.01	31.73	28.25	29.80	6.17
5	37.65	41.87	43.74	37.42	40.17	7.82
6	48.98	51.58	51.05	47.53	49.79	3.77
	Sensor 2					
1	5.21	5.25	4.66	4.56	4.92	7.31
2	7.61	7.14	7.70	8.30	7.69	6.19
3	9.04	9.55	8.43	10.18	9.30	7.99
4	9.37	8.95	10.02	10.42	9.69	6.76
5	12.29	13.36	12.60	13.39	12.91	4.28
6	14.65	17.50	15.93	15.27	15.84	7.72

Table I-10: MAPD Damage Index Relative to the Undamaged State for Excitation Location 5

Degree Of Damage	Test 1	Test 2	Test 3	Test 4	Average	COV (%)
	Sensor 1					
1	13.42	14.48	16.11	14.28	14.57	7.72
2	25.82	30.89	29.70	32.37	29.69	9.45
3	30.45	35.76	28.38	33.21	31.95	10.07
4	33.02	38.78	32.96	38.42	35.80	9.06
5	44.45	50.49	40.87	51.15	46.74	10.57
6	55.06	59.86	54.39	48.80	54.53	8.31
	Sensor 2					
1	6.69	5.17	5.40	5.63	5.72	11.79
2	6.48	5.65	7.01	6.71	6.46	9.04
3	7.67	7.10	7.92	8.43	7.78	7.10
4	11.16	10.09	10.84	12.32	11.10	8.35
5	13.28	14.32	12.16	14.91	13.67	8.84
6	14.19	15.21	16.12	17.02	15.64	7.77

Table I-11: CC Damage Index Relative to the Undamaged State for Excitation Location 1

Degree Of Damage	Test 1	Test 2	Test 3	Test 4	Average	COV (%)
	Sensor 1					
1	0.9987	0.9988	0.9989	0.9987	0.9988	0.009
2	0.9968	0.9976	0.9977	0.9974	0.9974	0.041
3	0.9940	0.9944	0.9950	0.9945	0.9945	0.042
4	0.9932	0.9941	0.9933	0.9927	0.9933	0.057
5	0.9869	0.9889	0.9894	0.9893	0.9886	0.119
6	0.9774	0.9790	0.9796	0.9793	0.9788	0.102
	Sensor 2					
1	0.9983	0.9983	0.9988	0.9985	0.9985	0.026
2	0.9968	0.9973	0.9972	0.9976	0.9972	0.034
3	0.9971	0.9965	0.9972	0.9970	0.9970	0.032
4	0.9961	0.9965	0.9968	0.9969	0.9966	0.036
5	0.9943	0.9947	0.9949	0.9951	0.9948	0.034
6	0.9936	0.9942	0.9943	0.9948	0.9942	0.052

Table I-12: CC Damage Index Relative to the Undamaged State for Excitation Location 2

Degree Of Damage	Test 1	Test 2	Test 3	Test 4	Average	COV (%)
	Sensor 1					
1	0.9988	0.9986	0.9988	0.9987	0.9987	0.009
2	0.9980	0.9975	0.9978	0.9978	0.9977	0.019
3	0.9959	0.9955	0.9955	0.9956	0.9956	0.020
4	0.9948	0.9951	0.9945	0.9948	0.9948	0.025
5	0.9894	0.9892	0.9890	0.9894	0.9893	0.020
6	0.9784	0.9786	0.9783	0.9780	0.9783	0.026
	Sensor 2					
1	0.9987	0.9986	0.9987	0.9986	0.9987	0.005
2	0.9976	0.9972	0.9979	0.9976	0.9976	0.029
3	0.9972	0.9976	0.9977	0.9973	0.9974	0.024
4	0.9971	0.9972	0.9971	0.9969	0.9971	0.012
5	0.9955	0.9956	0.9961	0.9958	0.9958	0.025
6	0.9929	0.9935	0.9949	0.9941	0.9939	0.084

Table I-13: CC Damage Index Relative to the Undamaged State for Excitation Location 3

Degree Of Damage	Test 1	Test 2	Test 3	Test 4	Average	COV (%)
	Sensor 1					
1	0.9988	0.9989	0.9989	0.9982	0.9987	0.031
2	0.9981	0.9982	0.9981	0.9980	0.9981	0.012
3	0.9960	0.9965	0.9965	0.9943	0.9958	0.104
4	0.9912	0.9904	0.9920	0.9867	0.9901	0.239
5	0.9824	0.9843	0.9827	0.9800	0.9823	0.181
6	0.9667	0.9644	0.9650	0.9617	0.9644	0.218
	Sensor 2					
1	0.9986	0.9988	0.9988	0.9987	0.9987	0.012
2	0.9975	0.9979	0.9981	0.9980	0.9979	0.025
3	0.9973	0.9975	0.9975	0.9977	0.9975	0.015
4	0.9976	0.9975	0.9976	0.9971	0.9975	0.023
5	0.9954	0.9960	0.9963	0.9966	0.9961	0.048
6	0.9953	0.9962	0.9962	0.9962	0.9960	0.048

Table I-14: CC Damage Index Relative to the Undamaged State for Excitation Location 4

Degree Of Damage	Test 1	Test 2	Test 3	Test 4	Average	COV (%)
	Sensor 1					
1	0.9984	0.9981	0.9987	0.9987	0.9985	0.031
2	0.9974	0.9967	0.9976	0.9960	0.9969	0.071
3	0.9951	0.9956	0.9957	0.9950	0.9953	0.036
4	0.9894	0.9911	0.9911	0.9896	0.9903	0.092
5	0.9793	0.9781	0.9772	0.9795	0.9785	0.108
6	0.9633	0.9638	0.9627	0.9620	0.9629	0.081
	Sensor 2					
1	0.9987	0.9986	0.9988	0.9988	0.9987	0.011
2	0.9983	0.9981	0.9981	0.9979	0.9981	0.017
3	0.9980	0.9976	0.9978	0.9974	0.9977	0.026
4	0.9975	0.9976	0.9979	0.9974	0.9976	0.023
5	0.9967	0.9964	0.9963	0.9968	0.9965	0.023
6	0.9958	0.9956	0.9960	0.9960	0.9959	0.017

Table I-15: CC Damage Index Relative to the Undamaged State for Excitation Location 5

Degree Of Damage	Test 1	Test 2	Test 3	Test 4	Average	COV (%)
	Sensor 1					
1	0.9988	0.9988	0.9984	0.9987	0.9987	0.022
2	0.9980	0.9977	0.9973	0.9973	0.9976	0.035
3	0.9968	0.9967	0.9967	0.9967	0.9967	0.003
4	0.9961	0.9960	0.9961	0.9961	0.9961	0.006
5	0.9924	0.9922	0.9926	0.9928	0.9925	0.028
6	0.9832	0.9774	0.9824	0.9833	0.9816	0.286
	Sensor 2					
1	0.9986	0.9988	0.9980	0.9988	0.9985	0.038
2	0.9983	0.9984	0.9983	0.9981	0.9983	0.011
3	0.9983	0.9984	0.9980	0.9978	0.9981	0.026
4	0.9974	0.9976	0.9974	0.9955	0.9969	0.099
5	0.9961	0.9967	0.9962	0.9951	0.9960	0.067
6	0.9956	0.9959	0.9959	0.9958	0.9958	0.015

Table I-16: RMSD Damage Index Relative to the Proceeding State of Damage for Excitation Location 1

Degree Of Damage	Test 1	Test 2	Test 3	Test 4	Average	COV (%)
	Sensor 1					
1	2.06	2.44	2.54	2.43	2.37	8.85
2	4.62	3.98	4.76	4.65	4.50	7.88
3	5.84	5.42	5.74	5.85	5.71	3.54
4	5.95	6.09	6.21	5.92	6.04	2.27
5	7.55	6.15	6.94	6.84	6.87	8.35
6	10.53	10.04	9.56	9.91	10.01	4.01
	Sensor 2					
1	2.98	2.69	2.48	2.41	2.64	9.71
2	3.33	3.32	3.98	3.87	3.62	9.73
3	3.32	2.69	3.04	2.77	2.95	9.63
4	3.66	3.49	3.56	3.62	3.58	2.12
5	4.03	4.31	4.38	3.50	4.05	9.87
6	3.58	3.79	3.75	3.48	3.65	3.96

Table E-17: RMSD Damage Index Relative to the Proceeding State of Damage for Excitation Location 2

Degree Of Damage	Test 1	Test 2	Test 3	Test 4	Average	COV (%)
	Sensor 1					
1	2.59	2.30	2.31	2.60	2.45	6.91
2	4.74	4.18	3.91	3.86	4.18	9.67
3	4.78	4.86	4.05	4.51	4.55	8.05
4	7.34	7.00	7.85	8.56	7.69	8.84
5	7.67	9.33	8.08	7.90	8.24	9.01
6	10.13	9.86	9.37	9.37	9.68	3.89
	Sensor 2					
1	2.30	2.24	2.20	2.63	2.34	8.35
2	3.79	3.65	3.24	3.43	3.53	6.83
3	2.40	2.81	2.77	2.64	2.66	6.92
4	2.40	2.42	2.36	2.26	2.36	2.92
5	4.90	5.29	4.30	5.25	4.93	9.24
6	3.72	3.46	3.44	3.93	3.64	6.37

Table E-18: RMSD Damage Index Relative to the Proceeding State of Damage for Excitation Location 3

Degree Of Damage	Test 1	Test 2	Test 3	Test 4	Average	COV (%)
	Sensor 1					
1	2.11	2.51	2.47	2.27	2.34	7.88
2	2.85	2.80	3.13	3.42	3.05	9.45
3	4.45	4.91	5.61	4.85	4.96	9.75
4	9.83	8.73	10.16	9.40	9.53	6.50
5	8.48	8.30	9.38	8.49	8.66	5.63
6	9.90	11.62	9.90	10.12	10.38	7.97
	Sensor 2					
1	2.07	2.37	2.28	2.05	2.20	7.13
2	3.18	2.88	2.89	3.34	3.07	7.33
3	2.09	2.55	2.11	2.60	2.34	11.70
4	3.37	3.43	3.32	3.17	3.32	3.40
5	5.29	5.99	5.76	5.81	5.71	5.23
6	4.40	4.44	4.34	4.83	4.50	4.97

Table I-19: RMSD Damage Index Relative to the Proceeding State of Damage for Excitation Location 4

Degree Of Damage	Test 1	Test 2	Test 3	Test 4	Average	COV (%)
	Sensor 1					
1	3.61	3.60	3.22	3.04	3.37	8.51
2	5.14	4.62	4.07	4.45	4.57	9.75
3	6.20	6.34	6.86	5.51	6.23	8.94
4	7.88	6.67	7.45	6.97	7.24	7.36
5	12.43	10.37	10.68	10.15	10.91	9.50
6	8.22	9.30	9.47	8.30	8.82	7.41
	Sensor 2					
1	2.20	2.47	2.49	2.05	2.30	9.39
2	4.73	4.30	4.06	4.46	4.38	6.41
3	4.69	5.39	4.93	5.39	5.10	6.81
4	4.10	4.02	3.45	4.11	3.92	7.98
5	3.76	3.56	3.96	3.47	3.69	5.91
6	4.47	3.98	4.25	4.42	4.28	5.20

Table I-20: RMSD Damage Index Relative to the Proceeding State of Damage for Excitation Location 5

Degree Of Damage	Test 1	Test 2	Test 3	Test 4	Average	COV (%)
	Sensor 1					
1	2.17	2.16	2.21	2.05	2.15	3.24
2	4.00	4.10	4.34	4.43	4.22	4.78
3	5.74	6.42	6.36	5.46	5.99	7.82
4	4.86	5.11	5.10	5.17	5.06	2.68
5	6.08	6.12	5.22	6.42	5.96	8.69
6	8.06	8.86	8.03	9.87	8.70	9.94
	Sensor 2					
1	2.22	2.48	2.36	2.21	2.32	5.48
2	2.90	2.40	2.73	2.62	2.66	7.92
3	3.80	3.49	3.43	3.19	3.48	7.24
4	6.38	5.66	5.74	6.48	6.07	6.99
5	6.26	6.49	6.23	5.33	6.08	8.43
6	5.83	5.56	5.50	4.89	5.44	7.29

Table I-21: MAPD Damage Index Relative to the Proceeding State of Damage for Excitation Location 1

Degree Of Damage	Test 1	Test 2	Test 3	Test 4	Average	COV (%)
	Sensor 1					
1	7.83	7.26	6.45	7.75	7.32	8.69
2	23.79	19.89	23.35	22.71	22.43	7.82
3	12.95	11.89	14.79	12.91	13.14	9.17
4	22.98	22.89	23.72	21.79	22.85	3.48
5	20.67	18.92	19.96	20.39	19.99	3.83
6	59.54	74.48	60.64	63.34	64.50	10.61
	Sensor 2					
1	4.04	3.60	3.19	3.55	3.60	9.63
2	4.54	5.04	5.42	4.51	4.88	8.92
3	3.78	3.82	4.14	4.78	4.13	11.17
4	5.14	4.75	4.09	4.84	4.71	9.35
5	6.69	7.01	7.17	6.83	6.93	3.05
6	4.84	4.40	4.48	4.64	4.59	4.21

Table I-22: MAPD Damage Index Relative to the Proceeding State of Damage for Excitation Location 2

Degree Of Damage	Test 1	Test 2	Test 3	Test 4	Average	COV (%)
	Sensor 1					
1	11.06	12.08	13.51	11.06	11.93	9.73
2	15.77	14.91	16.18	14.74	15.40	4.47
3	18.55	16.95	19.26	19.16	18.48	5.77
4	19.38	17.66	16.11	16.02	17.29	9.14
5	32.14	26.94	25.72	28.29	28.27	9.84
6	65.91	71.58	68.86	67.05	68.35	3.62
	Sensor 2					
1	3.70	4.43	4.46	4.24	4.21	8.37
2	5.22	5.28	4.66	5.40	5.14	6.39
3	3.93	4.36	3.93	3.68	3.97	7.13
4	5.28	4.66	4.95	5.11	5.00	5.26
5	7.50	7.96	8.16	8.92	8.13	7.29
6	6.15	5.02	6.16	5.91	5.81	9.26

Table I-23: MAPD Damage Index Relative to the Proceeding State of Damage for Excitation Location 3

Degree Of Damage	Test 1	Test 2	Test 3	Test 4	Average	COV (%)
	Sensor 1					
1	7.93	8.10	7.30	8.29	7.90	5.44
2	13.83	12.76	13.68	13.74	13.50	3.68
3	14.27	11.91	12.71	14.55	13.36	9.44
4	14.80	16.89	17.75	15.48	16.23	8.23
5	21.09	20.06	18.35	19.85	19.84	5.70
6	37.90	42.46	41.61	38.31	40.07	5.75
	Sensor 2					
1	3.93	3.24	3.66	3.92	3.69	8.76
2	5.32	5.47	5.82	4.92	5.38	6.91
3	5.26	5.38	6.41	5.34	5.60	9.75
4	6.28	6.92	6.55	5.83	6.39	7.14
5	8.85	9.75	7.98	7.84	8.61	10.32
6	7.17	7.59	6.38	6.69	6.95	7.65

Table I-24: MAPD Damage Index Relative to the Proceeding State of Damage for Excitation Location 4

Degree Of Damage	Test 1	Test 2	Test 3	Test 4	Average	COV (%)
	Sensor 1					
1	10.89	9.60	9.26	9.07	9.71	8.45
2	13.98	14.58	13.77	15.10	14.36	4.21
3	22.36	20.75	20.45	24.98	22.13	9.36
4	22.73	20.62	21.26	20.58	21.30	4.72
5	29.96	25.93	27.29	30.59	28.44	7.73
6	50.16	42.04	51.42	46.02	47.41	8.98
	Sensor 2					
1	5.21	5.25	4.66	4.56	4.92	7.31
2	9.07	9.65	9.73	10.44	9.72	5.76
3	7.75	9.68	8.72	7.66	8.45	11.20
4	6.69	7.95	8.29	6.78	7.43	10.95
5	8.63	9.89	8.09	8.41	8.76	9.01
6	7.31	6.91	6.34	6.56	6.78	6.28

Table I-25: MAPD Damage Index Relative to the Proceeding State of Damage for Excitation Location 5

Degree Of Damage	Test 1	Test 2	Test 3	Test 4	Average	COV (%)
	Sensor 1					
1	13.42	14.48	16.11	14.28	14.57	7.72
2	18.53	19.21	19.15	18.91	18.95	1.63
3	38.31	35.00	36.27	30.32	34.97	9.69
4	19.88	19.92	20.22	21.99	20.50	4.89
5	16.19	18.09	16.42	18.35	17.26	6.47
6	26.63	25.21	26.20	27.39	26.36	3.45
	Sensor 2					
1	5.69	5.17	5.40	5.63	5.47	4.38
2	6.29	5.58	5.37	6.14	5.85	7.52
3	5.58	6.33	6.77	5.88	6.14	8.51
4	7.28	8.55	8.13	7.16	7.78	8.64
5	11.14	11.62	11.13	9.91	10.95	6.67
6	8.00	8.59	6.82	8.57	7.99	10.38

Table I-26: CC Damage Index Relative to the Proceeding State of Damage for Excitation Location 1

Degree Of Damage	Test 1	Test 2	Test 3	Test 4	Average	COV (%)
	Sensor 1					
1	0.9987	0.9988	0.9989	0.9987	0.9988	0.009
2	0.9975	0.9979	0.9979	0.9975	0.9977	0.020
3	0.9980	0.9978	0.9978	0.9978	0.9979	0.010
4	0.9971	0.9968	0.9964	0.9971	0.9968	0.034
5	0.9964	0.9965	0.9967	0.9968	0.9966	0.020
6	0.9943	0.9938	0.9942	0.9942	0.9941	0.019
	Sensor 2					
1	0.9983	0.9983	0.9988	0.9985	0.9985	0.026
2	0.9978	0.9975	0.9975	0.9975	0.9976	0.017
3	0.9984	0.9986	0.9981	0.9986	0.9984	0.025
4	0.9982	0.9984	0.9984	0.9983	0.9983	0.010
5	0.9979	0.9980	0.9979	0.9978	0.9979	0.008
6	0.9983	0.9982	0.9982	0.9981	0.9982	0.006

Table I-27: CC Damage Index Relative to the Proceeding State of Damage for Excitation Location 2

Degree Of Damage	Test 1	Test 2	Test 3	Test 4	Average	COV (%)
	Sensor 1					
1	0.9988	0.9986	0.9988	0.9987	0.9987	0.009
2	0.9982	0.9983	0.9981	0.9983	0.9982	0.010
3	0.9981	0.9980	0.9981	0.9981	0.9981	0.006
4	0.9961	0.9964	0.9963	0.9963	0.9963	0.011
5	0.9956	0.9958	0.9958	0.9954	0.9956	0.019
6	0.9943	0.9936	0.9936	0.9936	0.9937	0.035
	Sensor 2					
1	0.9987	0.9986	0.9987	0.9986	0.9987	0.005
2	0.9980	0.9980	0.9980	0.9981	0.9980	0.007
3	0.9986	0.9985	0.9988	0.9988	0.9986	0.014
4	0.9985	0.9985	0.9985	0.9985	0.9985	0.002
5	0.9980	0.9978	0.9979	0.9980	0.9979	0.010
6	0.9977	0.9979	0.9978	0.9978	0.9978	0.010

Table I-28: CC Damage Index Relative to the Proceeding State of Damage for Excitation Location 3

Degree Of Damage	Test 1	Test 2	Test 3	Test 4	Average	COV (%)
	Sensor 1					
1	0.9988	0.9989	0.9989	0.9982	0.9987	0.031
2	0.9984	0.9984	0.9983	0.9984	0.9984	0.007
3	0.9976	0.9982	0.9980	0.9974	0.9978	0.035
4	0.9960	0.9943	0.9957	0.9954	0.9954	0.074
5	0.9947	0.9950	0.9941	0.9942	0.9945	0.043
6	0.9937	0.9910	0.9926	0.9927	0.9925	0.114
	Sensor 2					
1	0.9986	0.9988	0.9988	0.9987	0.9987	0.012
2	0.9980	0.9982	0.9982	0.9983	0.9982	0.012
3	0.9986	0.9987	0.9981	0.9988	0.9985	0.032
4	0.9985	0.9976	0.9985	0.9983	0.9983	0.042
5	0.9977	0.9970	0.9978	0.9976	0.9975	0.035
6	0.9977	0.9976	0.9979	0.9980	0.9978	0.019

Table I-29: CC Damage Index Relative to the Proceeding State of Damage for Excitation Location 4

Degree Of Damage	Test 1	Test 2	Test 3	Test 4	Average	COV (%)
	Sensor 1					
1	0.9984	0.9981	0.9987	0.9987	0.9985	0.031
2	0.9980	0.9976	0.9979	0.9971	0.9977	0.038
3	0.9980	0.9973	0.9981	0.9978	0.9978	0.032
4	0.9962	0.9968	0.9967	0.9968	0.9966	0.032
5	0.9937	0.9934	0.9930	0.9936	0.9934	0.032
6	0.9944	0.9952	0.9946	0.9945	0.9947	0.037
	Sensor 2					
1	0.9987	0.9986	0.9988	0.9988	0.9987	0.011
2	0.9976	0.9981	0.9976	0.9977	0.9977	0.026
3	0.9986	0.9984	0.9985	0.9985	0.9985	0.007
4	0.9982	0.9987	0.9984	0.9986	0.9985	0.020
5	0.9978	0.9979	0.9972	0.9980	0.9977	0.036
6	0.9979	0.9982	0.9982	0.9983	0.9981	0.018

Table I-30: CC Damage Index Relative to the Proceeding State of Damage for Excitation Location 5

Degree Of Damage	Test 1	Test 2	Test 3	Test 4	Average	COV (%)
	Sensor 1					
1	0.9988	0.9988	0.9984	0.9987	0.9987	0.022
2	0.9981	0.9979	0.9979	0.9978	0.9979	0.013
3	0.9983	0.9985	0.9979	0.9984	0.9983	0.028
4	0.9975	0.9977	0.9973	0.9975	0.9975	0.014
5	0.9974	0.9973	0.9975	0.9972	0.9973	0.014
6	0.9952	0.9918	0.9949	0.9932	0.9938	0.162
	Sensor 2					
1	0.9986	0.9988	0.9980	0.9988	0.9985	0.038
2	0.9984	0.9985	0.9984	0.9982	0.9984	0.014
3	0.9985	0.9985	0.9984	0.9987	0.9985	0.011
4	0.9981	0.9984	0.9986	0.9980	0.9983	0.028
5	0.9981	0.9980	0.9982	0.9981	0.9981	0.009
6	0.9981	0.9963	0.9981	0.9972	0.9974	0.084

Appendix J Sample Input Files for FEA Analysis with NISA

Full Plate Model

```
**** NISA file:  DISPLAY VERSION - 12.0 : Release : 03-03-03  ****
** This NISA file is written out by DISPLAY-III FEA program
** All ** lines are comment cards except lines with **_DISP3_:
** labels which have special meanings and retained in NISA file
** for compatibility with DISP3 database. Pls do not modify them
****
**EXECUTIVE data deck
ANALYSIS = STATIC
BLANK COMMON = 81004
SOLV = FRON
FILE = int5lu5
SAVE = 26,27
*ELTYPE
 1,  4,   1
 2,  4,  10
 3,  7,   1
 4,  4,  30
*RCTABLE
    1,    8,1,    0
**_DISP3_: NAME =SHELL
 2.5000000E-01, 2.5000000E-01, 2.5000000E-01, 2.5000000E-01,
 2.5000000E-01, 2.5000000E-01, 2.5000000E-01, 2.5000000E-01,
    2,    8,1,    0
**_DISP3_: NAME =SHELL
 1.0000000E-15, 1.0000000E-15, 1.0000000E-15, 1.0000000E-15,
 1.0000000E-15, 1.0000000E-15, 1.0000000E-15, 1.0000000E-15,
*LAMANGLE
1,4
0.0,0.0,0.0,0.0
2,4
90.0,90.0,90.0,90.0
3,4
45.0,45.0,45.0,45.0
4,4
-45.0,-45.0,-45.0,-45.0
*LAMSEQ
**_DISP3_: 1,
15,0,2,1,2,2,1,2,2,1,2,2,1,2,2,1,2,2,2,2
3,3,3,1,1,1,4,4,4,2,2,2,1,1,1,1,1,1,1,1
1,1,1,1,1,1,1
**_DISP3_: 2,
81,0,2,1,2,2,1,2,2,1,2,2,1,2,2,1,2,2,1,2
2,1,2,2,1,2,2,1,2,2,1,2,2,1,2,2,1,2,2,1
```

```
2,2,1,2,2,1,2,2,1,2,2,1,2,2,1,2,2,1,2,2
1,2,2,1,2,2,1,2,2,1,2,2,1,2,2,1,2,2,1,2
2,1,2,3,3,3,1,1,1,4,4,4,2,2,2,3,3,3,1,1
1,4,4,4,2,2,2,3,3,3,1,1,1,4,4,4,4,4,4,1
1,1,3,3,3,2,2,2,4,4,4,1,1,1,3,3,3,2,2,2
4,4,4,1,1,1,3,3,3,2,2,2,4,4,4,1,1,1,3,3
3,2,2,2,1,1,1,1,1,1,1,1,1,1,1,1,1,1,1,1
1,1,1,1,1,1,1,1,1,1,1,1,1,1,1,1,1,1,1,1
1,1,1,1,1,1,1,1,1,1,1,1,1,1,1,1,1,1,1,1
1,1,1,1,1,1,1,1,1,1,1,1,1,1,1,1,1,1,1,1
1,1,1,1,1
*NODES
   1,,,, 0.00000E+00, 2.54000E+01, 6.75000E+00,    0
   2,,,, 8.46667E+00, 2.54000E+01, 6.75000E+00,    0
   3,,,, 1.69333E+01, 2.54000E+01, 6.75000E+00,    0
   ...
   ...
   ...
16786,,,, 4.91086E+02, 4.23333E+01, 0.00000E+00,    0
16787,,,, 4.99543E+02, 4.23333E+01, 0.00000E+00,    0
16788,,,, 5.08000E+02, 4.23333E+01, 0.00000E+00,    0
*ELEMENTS
   1,   3,   1,   1,   1
   1,   2,  12,  11,  41,  42,  52,  51,
   2,   3,   1,   1,   1
   2,   3,  13,  12,  42,  43,  53,  52,
   3,   3,   1,   1,   1
   3,   4,  14,  13,  43,  44,  54,  53,
   ...
   ...
   ...
16785, 16786, 16058, 16057, 16369, 16370, 15642, 15641,
 7489,   2,   3,   1,   1
16786, 16787, 16059, 16058, 16370, 16371, 15643, 15642,
 7490,   2,   3,   1,   1
 16787, 16788, 16060, 16059, 16371, 16372, 15644, 15643,
*MATERIAL
EX ,    1,0, 1.40000E+05,
EY ,    1,0, 9.10000E+03,
EZ ,    1,0, 9.10000E+03,
NUXY,    1,0, 3.50000E-01,
NUXZ,    1,0, 3.50000E-01,
NUYZ,    1,0, 3.00000E-01,
GXY ,    1,0, 7.20000E+03,
```

```
GXZ ,    1,0, 7.20000E+03,
GYZ ,    1,0, 6.31000E+03,
DENS,    1,0, 1.60000E-09,
EX  ,    2,0, 1.40000E+05,
EY  ,    2,0, 9.10000E+03,
EZ  ,    2,0, 9.10000E+03,
NUXY,    2,0, 3.50000E-01,
NUXZ,    2,0, 3.50000E-01,
NUYZ,    2,0, 3.00000E-01,
GXY ,    2,0, 7.20000E+03,
GXZ ,    2,0, 7.20000E+03,
GYZ ,    2,0, 6.31000E+03,
DENS,    2,0, 1.60000E-09,
EX  ,    3,0, 6.70000E+04,
EY  ,    3,0, 6.70000E+04,
EZ  ,    3,0, 5.40000E+04,
NUXY,    3,0, 3.00000E-01,
NUXZ,    3,0, 3.00000E-01,
NUYZ,    3,0, 3.00000E-01,
GXY ,    3,0, 2.58000E+04,
GXZ ,    3,0, 2.07000E+04,
GYZ ,    3,0, 2.07000E+04,
DENS,    3,0, 7.85000E-09,
EX  ,    4,0, 3.80000E+03,
EY  ,    4,0, 3.80000E+03,
EZ  ,    4,0, 3.80000E+03,
NUXY,    4,0, 3.00000E-01,
NUXZ,    4,0, 3.00000E-01,
NUYZ,    4,0, 3.00000E-01,
GXY ,    4,0, 1.46100E+03,
GXZ ,    4,0, 1.46100E+03,
GYZ ,    4,0, 1.46100E+03,
DENS,    4,0, 1.40000E-09,
*LDCASE, ID=    1
 0, 0, 1, 0,-1, 0, 1,   0.000,   0.000
*SPDISP
**_DISP3_: SPDISP, SET =     1
    1,UX  , 0.00000E+00,,,,,,,,    0
    1,UY  , 0.00000E+00,,,,,,,,    0
    1,UZ  , 0.00000E+00,,,,,,,,    0
   11,UX  , 0.00000E+00,,,,,,,,    0
   11,UY  , 0.00000E+00,,,,,,,,    0
   11,UZ  , 0.00000E+00,,,,,,,,    0
   21,UX  , 0.00000E+00,,,,,,,,    0
```

```
   21,UY  , 0.00000E+00,,,,,,,,    0
   21,UZ  , 0.00000E+00,,,,,,,,    0
   31,UX  , 0.00000E+00,,,,,,,,    0
   31,UY  , 0.00000E+00,,,,,,,,    0
   31,UZ  , 0.00000E+00,,,,,,,,    0
    ...
    ...
    ...
 16528,UX  , 0.00000E+00,,,,,,,,    0
 16528,UY  , 0.00000E+00,,,,,,,,    0
 16528,UZ  , 0.00000E+00,,,,,,,,    0
 16580,UX  , 0.00000E+00,,,,,,,,    0
 16580,UY  , 0.00000E+00,,,,,,,,    0
 16580,UZ  , 0.00000E+00,,,,,,,,    0
 16736,UX  , 0.00000E+00,,,,,,,,    0
 16736,UY  , 0.00000E+00,,,,,,,,    0
 16736,UZ  , 0.00000E+00,,,,,,,,    0
 16788,UX  , 0.00000E+00,,,,,,,,    0
 16788,UY  , 0.00000E+00,,,,,,,,    0
 16788,UZ  , 0.00000E+00,,,,,,,,    0
*PRESSURE
**_DISP3_: PRESSURE, SET =      1
   49,,,2,0,  0,     0.1,    0
   50,,,2,0,  0,     0.1,    0
   51,,,2,0,  0,     0.1,    0
   52,,,2,0,  0,     0.1,    0
    ...
    ...
    ...
  7334,,,2,0,  0,     0.1,    0
  7335,,,2,0,  0,     0.1,    0
  7336,,,2,0,  0,     0.1,    0
  7337,,,2,0,  0,     0.1,    0
*PRINTCNTL
AVND,-1
REAC,-1
VELO,-1
ACCE,-1
*POSTCNTL
NDSTRS,0
*ENDDATA
```

Initial Submodel

```
**** NISA file:  DISPLAY VERSION - 12.0 : Release : 03-03-03  ****
** This NISA file is written out by DISPLAY-III FEA program
** All ** lines are comment cards except lines with **_DISP3_:
** labels which have special meanings and retained in NISA file
** for compatibility with DISP3 database. Pls do not modify them
****
**EXECUTIVE data deck
ANALYSIS = STATIC
BLANK COMMON = 743953
SOLV = FRON
FILE = subint5lu5
SAVE = 26,27
*ELTYPE
 1,  4,   1
 2,  4,  10
 3,  7,   1
 4,  4,  30
*RCTABLE
   1,   8,1,   0
**_DISP3_: NAME =SHELL
 2.5000000E-01, 2.5000000E-01, 2.5000000E-01, 2.5000000E-01,
 2.5000000E-01, 2.5000000E-01, 2.5000000E-01, 2.5000000E-01,
   2,   8,1,   0
**_DISP3_: NAME =SHELL
 1.0000000E-15, 1.0000000E-15, 1.0000000E-15, 1.0000000E-15,
 1.0000000E-15, 1.0000000E-15, 1.0000000E-15, 1.0000000E-15,
*LAMANGLE
1,4
0.0,0.0,0.0,0.0
2,4
90.0,90.0,90.0,90.0
3,4
45.0,45.0,45.0,45.0
4,4
-45.0,-45.0,-45.0,-45.0
*LAMSEQ
**_DISP3_: 1,
15,0,2,1,2,2,1,2,2,1,2,2,1,2,2,1,2,2,2,2
3,3,3,1,1,1,4,4,4,2,2,2,1,1,1,1,1,1,1,1
1,1,1,1,1,1,1
**_DISP3_: 2,
81,0,2,1,2,2,1,2,2,1,2,2,1,2,2,1,2,2,1,2
2,1,2,2,1,2,2,1,2,2,1,2,2,1,2,2,1,2,2,1
```

```
2,2,1,2,2,1,2,2,1,2,2,1,2,2,1,2,2,1,2,2
1,2,2,1,2,2,1,2,2,1,2,2,1,2,2,1,2,2,1,2
2,1,2,3,3,3,1,1,1,4,4,4,2,2,2,3,3,3,1,1
1,4,4,4,2,2,2,3,3,3,1,1,1,4,4,4,4,4,4,1
1,1,3,3,3,2,2,2,4,4,4,1,1,1,3,3,3,2,2,2
4,4,4,1,1,1,3,3,3,2,2,2,4,4,4,1,1,1,3,3
3,2,2,2,1,1,1,1,1,1,1,1,1,1,1,1,1,1,1,1
1,1,1,1,1,1,1,1,1,1,1,1,1,1,1,1,1,1,1,1
1,1,1,1,1,1,1,1,1,1,1,1,1,1,1,1,1,1,1,1
1,1,1,1,1,1,1,1,1,1,1,1,1,1,1,1,1,1,1,1
1,1,1,1,1
*NODES
   1,,,, 0.00000E+00, 2.54000E+01, 6.75000E+00,    0
   2,,,, 4.23333E-01, 2.54000E+01, 6.75000E+00,    0
   3,,,, 8.46667E-01, 2.54000E+01, 6.75000E+00,    0
   4,,,, 1.27000E+00, 2.54000E+01, 6.75000E+00,    0
   ...
   ...
   ...
165372,,,, 9.23452E+01, 5.03767E+01, 0.00000E+00,    0
165373,,,, 9.27680E+01, 5.03767E+01, 0.00000E+00,    0
165374,,,, 9.31909E+01, 5.03767E+01, 0.00000E+00,    0
165375,,,, 9.36137E+01, 5.03767E+01, 0.00000E+00,    0
*ELEMENTS
   1,   3,   1,   1,   1
   1,   2,  23,  22, 442, 443, 464, 463,
   2,   3,   1,   1,   1
   2,   3,  24,  23, 443, 444, 465, 464,
   3,   3,   1,   1,   1
   3,   4,  25,  24, 444, 445, 466, 465,
   4,   3,   1,   1,   1
   4,   5,  26,  25, 445, 446, 467, 466,
   ...
   ...
   ...
 73983,   2,   3,   1,   1
 27342, 28498, 28519, 27363, 24380, 28162, 24950,  7077,
 73984,   2,   3,   1,   1
 28098, 28666, 28687, 28119, 23373, 25136, 28351, 24383,
 73985,   4,   4,   1,   1
 24380, 28162, 24950,  7077,  7518,
 73986,   4,   4,   1,   1
 23373, 25136, 28351, 24383, 23814,
*MATERIAL
```

```
EX ,    1,0, 1.40000E+05,
EY ,    1,0, 9.10000E+03,
EZ ,    1,0, 9.10000E+03,
NUXY,    1,0, 3.50000E-01,
NUXZ,    1,0, 3.50000E-01,
NUYZ,    1,0, 3.00000E-01,
GXY ,    1,0, 7.20000E+03,
GXZ ,    1,0, 7.20000E+03,
GYZ ,    1,0, 6.31000E+03,
DENS,    1,0, 1.60000E-09,
EX ,    2,0, 1.40000E+05,
EY ,    2,0, 9.10000E+03,
EZ ,    2,0, 9.10000E+03,
NUXY,    2,0, 3.50000E-01,
NUXZ,    2,0, 3.50000E-01,
NUYZ,    2,0, 3.00000E-01,
GXY ,    2,0, 7.20000E+03,
GXZ ,    2,0, 7.20000E+03,
GYZ ,    2,0, 6.31000E+03,
DENS,    2,0, 1.60000E-09,
EX ,    3,0, 6.70000E+04,
EY ,    3,0, 6.70000E+04,
EZ ,    3,0, 5.40000E+04,
NUXY,    3,0, 3.00000E-01,
NUXZ,    3,0, 3.00000E-01,
NUYZ,    3,0, 3.00000E-01,
GXY ,    3,0, 2.58000E+04,
GXZ ,    3,0, 2.07000E+04,
GYZ ,    3,0, 2.07000E+04,
DENS,    3,0, 7.85000E-09,
EX ,    4,0, 3.80000E+03,
EY ,    4,0, 3.80000E+03,
EZ ,    4,0, 3.80000E+03,
NUXY,    4,0, 3.00000E-01,
NUXZ,    4,0, 3.00000E-01,
NUYZ,    4,0, 3.00000E-01,
GXY ,    4,0, 1.46100E+03,
GXZ ,    4,0, 1.46100E+03,
GYZ ,    4,0, 1.46100E+03,
DENS,    4,0, 1.40000E-09,
*LDCASE, ID=     1
 0, 0, 1, 0,-1, 0, 1,   0.000,   0.000
*SPDISP
**_DISP3_: SPDISP, SET =      1
```

```
    1,UX  , 0.00000E+00,,,,,,,,     0
    1,UY  , 0.00000E+00,,,,,,,,     0
    1,UZ  , 0.00000E+00,,,,,,,,     0
   22,UX  , 0.00000E+00,,,,,,,,     0
   22,UY  , 0.00000E+00,,,,,,,,     0
   22,UZ  , 0.00000E+00,,,,,,,,     0
   43,UX  , 0.00000E+00,,,,,,,,     0
   43,UY  , 0.00000E+00,,,,,,,,     0
   43,UZ  , 0.00000E+00,,,,,,,,     0
   64,UX  , 0.00000E+00,,,,,,,,     0
   64,UY  , 0.00000E+00,,,,,,,,     0
   64,UZ  , 0.00000E+00,,,,,,,,     0
    ...
    ...
    ...
165333,UX  ,-8.00054E-02,,,,,,,,     0
165333,UY  , 4.38813E-03,,,,,,,,     0
165333,UZ  ,-1.31060E+00,,,,,,,,     0
165354,UX  ,-7.99807E-02,,,,,,,,     0
165354,UY  , 4.49702E-03,,,,,,,,     0
165354,UZ  ,-1.31021E+00,,,,,,,,     0
165375,UX  ,-7.99560E-02,,,,,,,,     0
165375,UY  , 4.60590E-03,,,,,,,,     0
165375,UZ  ,-1.30983E+00,,,,,,,,     0
*PRESSURE
**_DISP3_: PRESSURE, SET =      1
 11221,,,2,0,  0,      0.1,    0
 11222,,,2,0,  0,      0.1,    0
 11223,,,2,0,  0,      0.1,    0
 ...
 ...
 ...
 71580,,,2,0,  0,      0.1,    0
 73981,,,2,0,  0,      0.1,    0
 73982,,,2,0,  0,      0.1,    0
*PRINTCNTL
AVND,-1
REAC,-1
VELO,-1
ACCE,-1
*POSTCNTL
NDSTRS,0
*ENDDATA
```

Final Submodel

```
**** NISA file:  DISPLAY VERSION - 12.0 : Release : 03-03-03  ****
** This NISA file is written out by DISPLAY-III FEA program
** All ** lines are comment cards except lines with **_DISP3_:
** labels which have special meanings and retained in NISA file
** for compatibility with DISP3 database. Pls do not modify them
****
**EXECUTIVE data deck
ANALYSIS = STATIC
BLANK COMMON = 824817
SOLV = FRON
FILE = subres553
SAVE = 26,27
*ELTYPE
 1,  4,    1
 2,  4,   10
 3,  7,    1
*RCTABLE
    1,    8,1,    0
**_DISP3_: NAME =SHELL
 2.5000000E-01, 2.5000000E-01, 2.5000000E-01, 2.5000000E-01,
 2.5000000E-01, 2.5000000E-01, 2.5000000E-01, 2.5000000E-01,
    2,    8,1,    0
**_DISP3_: NAME =SHELL
 1.0000000E-15, 1.0000000E-15, 1.0000000E-15, 1.0000000E-15,
 1.0000000E-15, 1.0000000E-15, 1.0000000E-15, 1.0000000E-15,
*LAMANGLE
1,4
0.0,0.0,0.0,0.0
2,4
90.0,90.0,90.0,90.0
3,4
45.0,45.0,45.0,45.0
4,4
-45.0,-45.0,-45.0,-45.0
*LAMSEQ
**_DISP3_: 1,
15,0,2,1,2,2,1,2,2,1,2,2,1,2,2,1,2,2,2,2
3,3,3,1,1,1,4,4,4,2,2,2,1,1,1,1,1,1,1,1
1,1,1,1,1,1,1
**_DISP3_: 2,
81,0,2,1,2,2,1,2,2,1,2,2,1,2,2,1,2,2,1,2
2,1,2,2,1,2,2,1,2,2,1,2,2,1,2,2,1,2,2,1
2,2,1,2,2,1,2,2,1,2,2,1,2,2,1,2,2,1,2,2
```

```
1,2,2,1,2,2,1,2,2,1,2,2,1,2,2,1,2,2,1,2
2,1,2,3,3,3,1,1,1,4,4,4,2,2,2,3,3,3,1,1
1,4,4,4,2,2,2,3,3,3,1,1,1,4,4,4,4,4,4,1
1,1,3,3,3,2,2,2,4,4,4,1,1,1,3,3,3,2,2,2
4,4,4,1,1,1,3,3,3,2,2,2,4,4,4,1,1,1,3,3
3,2,2,2,1,1,1,1,1,1,1,1,1,1,1,1,1,1,1,1
1,1,1,1,1,1,1,1,1,1,1,1,1,1,1,1,1,1,1,1
1,1,1,1,1,1,1,1,1,1,1,1,1,1,1,1,1,1,1,1
1,1,1,1,1,1,1,1,1,1,1,1,1,1,1,1,1,1,1,1
1,1,1,1,1
*NODES
   1,,,, 0.00000E+00, 2.54000E+01, 6.75000E+00,    0
   2,,,, 4.23333E-01, 2.54000E+01, 6.75000E+00,    0
   3,,,, 8.46667E-01, 2.54000E+01, 6.75000E+00,    0
   4,,,, 1.27000E+00, 2.54000E+01, 6.75000E+00,    0
   ...
   ...
   ...
155082,,,, 7.49300E+01, 2.44700E+01, 0.00000E+00,    0
155083,,,, 7.53533E+01, 2.44700E+01, 0.00000E+00,    0
155084,,,, 7.57767E+01, 2.44700E+01, 0.00000E+00,    0
155085,,,, 7.62000E+01, 2.44700E+01, 0.00000E+00,    0
*ELEMENTS
   1,   3,   1,   1,   1
   1,   2,  23,  22, 442, 443, 464, 463,
   2,   3,   1,   1,   1
   2,   3,  24,  23, 443, 444, 465, 464,
   3,   3,   1,   1,   1
   3,   4,  25,  24, 444, 445, 466, 465,
   4,   3,   1,   1,   1
   4,   5,  26,  25, 445, 446, 467, 466,
   ...
   ...
   ...
100797,   2,   3,   1,   1
155081,155082, 91683, 91682,139205,139206, 84956, 84883,
100798,   2,   3,   1,   1
155082,155083, 91684, 91683,139206,139207, 85029, 84956,
100799,   2,   3,   1,   1
155083,155084, 91685, 91684,139207,139208, 85102, 85029,
100800,   2,   3,   1,   1
155084,155085, 91686, 91685,139208,139209, 85175, 85102,
*MATERIAL
EX ,    1,0, 1.40000E+05,
```

```
EY ,    1,0, 9.10000E+03,
EZ ,    1,0, 9.10000E+03,
NUXY,    1,0, 3.50000E-01,
NUXZ,    1,0, 3.50000E-01,
NUYZ,    1,0, 3.00000E-01,
GXY ,    1,0, 7.20000E+03,
GXZ ,    1,0, 7.20000E+03,
GYZ ,    1,0, 6.31000E+03,
DENS,    1,0, 1.60000E-09,
EX ,    2,0, 1.40000E+05,
EY ,    2,0, 9.10000E+03,
EZ ,    2,0, 9.10000E+03,
NUXY,    2,0, 3.50000E-01,
NUXZ,    2,0, 3.50000E-01,
NUYZ,    2,0, 3.00000E-01,
GXY ,    2,0, 7.20000E+03,
GXZ ,    2,0, 7.20000E+03,
GYZ ,    2,0, 6.31000E+03,
DENS,    2,0, 1.60000E-09,
EX ,    3,0, 6.70000E+04,
EY ,    3,0, 6.70000E+04,
EZ ,    3,0, 5.40000E+04,
NUXY,    3,0, 3.00000E-01,
NUXZ,    3,0, 3.00000E-01,
NUYZ,    3,0, 3.00000E-01,
GXY ,    3,0, 2.58000E+04,
GXZ ,    3,0, 2.07000E+04,
GYZ ,    3,0, 2.07000E+04,
DENS,    3,0, 7.85000E-09,
EX ,    4,0, 3.80000E+03,
EY ,    4,0, 3.80000E+03,
EZ ,    4,0, 3.80000E+03,
NUXY,    4,0, 3.00000E-01,
NUXZ,    4,0, 3.00000E-01,
NUYZ,    4,0, 3.00000E-01,
GXY ,    4,0, 1.46100E+03,
GXZ ,    4,0, 1.46100E+03,
GYZ ,    4,0, 1.46100E+03,
DENS,    4,0, 1.40000E-09,
*LDCASE, ID=    1
 0, 0, 1, 0,-1, 0, 1,   0.000,   0.000
*SPDISP
**_DISP3_: SPDISP, SET =     1
   1,UX  , 0.00000E+00,,,,,,,,    0
```

```
     1,UY  , 0.00000E+00,,,,,,,,     0
     1,UZ  , 0.00000E+00,,,,,,,,     0
    22,UX  , 0.00000E+00,,,,,,,,     0
    22,UY  , 0.00000E+00,,,,,,,,     0
    22,UZ  , 0.00000E+00,,,,,,,,     0
    43,UX  , 0.00000E+00,,,,,,,,     0
    43,UY  , 0.00000E+00,,,,,,,,     0
    43,UZ  , 0.00000E+00,,,,,,,,     0
    64,UX  , 0.00000E+00,,,,,,,,     0
    64,UY  , 0.00000E+00,,,,,,,,     0
    64,UZ  , 0.00000E+00,,,,,,,,     0
     ...
     ...
     ...
155043,UX  ,-7.80669E-02,,,,,,,,     0
155043,UY  ,-1.47251E-03,,,,,,,,     0
155043,UZ  ,-9.71662E-01,,,,,,,,     0
155064,UX  ,-7.80964E-02,,,,,,,,     0
155064,UY  ,-1.38902E-03,,,,,,,,     0
155064,UZ  ,-9.71888E-01,,,,,,,,     0
155085,UX  ,-7.81258E-02,,,,,,,,     0
155085,UY  ,-1.30552E-03,,,,,,,,     0
155085,UZ  ,-9.72113E-01,,,,,,,,     0
*PRESSURE
**_DISP3_: PRESSURE, SET =      1
 69121,,,2,0,  0,      0.1,    0
 69122,,,2,0,  0,      0.1,    0
 69123,,,2,0,  0,      0.1,    0
 ...
 ...
 ...
 93598,,,2,0,  0,      0.1,    0
 93599,,,2,0,  0,      0.1,    0
 93600,,,2,0,  0,      0.1,    0
*PRINTCNTL
AVND,-1
REAC,-1
VELO,-1
ACCE,-1
*POSTCNTL
NDSTRS,0
*ENDDATA
```